PETROGRAPHY AND PARAGENESIS OF DIAGENETIC MINERAL PHASES IN CHERTY AND DOLOMITIC SPICULITE STRATA, MISSISSIPPIAN, SOUTH-CENTRAL KANSAS

BY

Luis G. Montalvo Lliteras

Submitted to the graduate degree program in Geology
and the Graduate Faculty of the University of Kansas
in partial fulfillment of the requirements for the degree of
Master of Sciences

Advisory Committee:

_____
Luis A. Gonzalez, Chairperson

_____
Lynn Watney, Co-chairperson

_____
Jennifer Roberts, Committee member

Date defended: January 15, 2015

The Thesis Committee for Luis G. Montalvo Lliteras certifies that this is the approved version of the following thesis:

PETROGRAPHY AND PARAGENESIS OF DIAGENETIC MINERAL PHASES IN CHERTY AND DOLOMITIC SPICULITE STRATA, MISSISSIPPIAN, SOUTH-CENTRAL KANSAS

Advisory Committee:

_____

Luis A. Gonzalez, Chairperson

_____

Lynn Watney, Co-chairperson

_____

Jennifer Roberts, Committee member

Date Approved: January 15, 2015

ABSTRACT

Mississippian strata in four cores from three different locations in south-central Kansas (Rhodes field, Wellington field, and a "wildcat" well in Comanche county) were used to investigate the depositional environment, and the diagenetic history in variable cherty and dolomitic sponge-spicule-rich facies. The cores described comprises a series of lithofacies that are representative of inner-, mid and outer-ramp depositional environments, and depict conditions in which colonization of siliceous-sponges suppressed the deposition of carbonates. Paragenesis reveals that the most important and abundant diagenetic mineral phases are chert and dolomite, which partially to pervasively replaced the sediments early after they were deposited. Chertification was triggered in part by remobilization of silica from dissolution of siliceous sponge-spicule. Salinity measurements on fluid inclusions of early megaquartz revealed values consistent with seawater and evaporated seawater (early hypersalinity). This suggests that silicification processes (including chertification) began shortly after deposition of the sediments, and before complete lithification. Multiple phases of dolomite were described and are texturally different in the locations studied. Petrography and geochemistry data lead to the conclusions that primary dolomite (cD1 and wD1a) precipitation occurred in near-surface environments from potentially seawater-derived fluids and temporally associated with nodular cherts. Elevated concentrations of iron and manganese and void-filling textures characteristic of secondary dolomite phases indicate that secondary dolomitization occurred in the meteoric or subsurface realms. Two cases of regional scale events were described and include 1) an early event of nodular evaporite precipitation in the sediment column, and 2) a mineral assemblage of late stage cements comprising megaquartz, chalcedony (zebraic), baroque dolomite and calcite which has been indicated as a predictive mineral series to indicate hydrothermal fluid migration on Mississippian and adjacent units in the mid-continent by previous authors. Prospective hydrocarbon reservoirs involve facies rich in sponge-spicule debris that had undergone dissolution (either meteoric or hydrothermal), or pervasively dolomitized facies where intercrystaline porosity dominates.

ACKNOWLEDGEMENTS

I would like to express my very great appreciation to my advisor Dr. Luis A. Gonzalez and my Co-advisor Lynn Watney for giving me the opportunity to work on a project that fits my interests in geology. I thank them for the time, effort, guidance and support I received during the course of completing my research. In particular, I thank Dr. Luis A. Gonzalez for giving me the chance to pursue my master's degree in geology at such a great institution and excellent geology department; and Lynn Watney for sharing great amount of knowledge of the Mississippian. I also thank Dr. Robert Goldstein for sharing some ideas and his knowledge of the complicated diagenesis of the Mississippian. Thank you all, because without their knowledge this thesis project would not be the same.

I would like to express my thanks to the Department of Geology at The University of Kansas and the Society for Sedimentary Geology (SEPM) for their research grants and funding throughout this project; and the Kansas Geological Survey for sharing the cores used in this Project and the US Department of Energy (contract DE-FE0002056) for funding acquisition of the continuous core of the Mississippian in the Berexco Welllington KGS #1-32 borehole. I also like to thank the lab staff that made the collection of data for this research possible, in particular Dave Laflen (Kansas Geological Survey), Greg Cane (Keck Paleoenvironmental and Environmental Stable Isotope Laboratory at the University of Kansas), Wayne Dickerson (Department of Geology) and Nick Foster (Southeastern North Carolina Regional Microanalytical and Imaging Consortium in Fayetteville State University).

I would like to thank my undergraduate geology department at the University of Puerto Rico. Drs. Wilson Ramirez and Hernan Santos played a very important role on my early days in

geology by introducing me to the world of carbonate sedimentology. I thank them for their recommendations and convincing me that the University of Kansas was the perfect place for me as a carbonate geologist. I would not be a geologist today if it wasn't for them.

I wish to acknowledge the help given by many friends in the geology department that helped and supported me in different ways to complete this research. Especially to Alvin Bonilla, Michelle Mary, Ted Morehouse, "Abdul" and Michael Waynick.

It shouldn't be out of this list my family; they have supported me on taking this journey to the University of Kansas to pursue a master's degree in Geology. This has been one of my biggest challenges and achievements in my life.

TABLE OF CONTENTS

LIST OF FIGURES AND TABLES

INTRODUCTION

Mississippian cherty limestones of variable character and diagenetic history are locally prolific oil and gas reservoirs throughout southern Kansas and northern Oklahoma. Most of these reservoirs are collectively called the Mississippian "chat". These reservoirs are one of the most prolific pay zones in south-central Kansas yielding oil and gas rates up to 1500 bbl or 40 mmcf per day from depths of 909-1515 m (Montgomery et al., 1998, Watney et al., 2001). Characterization of the Mississippian reservoirs has been a difficult task due to a considerable variety and complexity in depositional origin and diagenetic history; multiple pore systems, and poor waterflood response (Montgomery et al., 1998). Relevant difficulties also result from variation in the visual textures of productive reservoirs, which for many years had been associated with a major regional unconformity that separates Pennsylvanian and Mississippian deposits (Merriam, 1963). Recent interpretations show that minor fluctuations in sea level intermittently exposed and submerged the sediments various times during their deposition, and these events are recorded as minor unconformities in the Mississippian (Mazzullo et al., 2009). Therefore diagenetic textures can be related to multiple events of sub-aerial exposures. In addition, recent studies have indicated that hydrothermal fluid migration is also responsible for porosity enhancement and cementation in Mississippian reservoirs in south-central Kansas and adjacent areas (King, 2013; Ramaker et al., 2014). These recent arguments make questionable earlier interpretations of diagenetic alterations and may account for a distribution of porosity that is independent of depositional stratigraphy. More importantly, the issue is what are prevailing processes that 1) account for the porosity and permeability that host the oil and gas accumulations and 2) contribute to the migration of oil and gas to locations that are being developed. The expert integration of the seismic and well data is strongly dictated by this a priori

knowledge. Refinements in the prediction of the location of hydrocarbon distribution are essential to improve the success in developing this complex play. For this reasons, reservoir characterization in the Mississippian in south-central Kansas requires a deliberate knowledge of diagenesis, because hydrocarbon-bearing units are tied to a specific set of diagenetic textures that improves reservoir quality.

Mississippian "chat" reservoirs are characterized by tripolitic cherts that exhibit low resistivities caused by the very high porosities and large amounts of bound water within the matrix microporosity (Colleary et al., 1997). This characteristic is observed in chert and interbedded chert and dolomite reservoirs (Montgomery et al., 1998). Most of the reservoirs also exhibit variable amounts of sponge-spicule molds, vuggy porosity and autoclastic chert breccia (Watney et al., 2001; Rogers et al., 2001; Mazzullo et al., 2009).

Chert reservoirs have been documented in North America in the Permian Basin and southern mid-continent (Saller et al., 1991; Ruppel and Hovorka, 1995; Rogers et al., 1995; Colleary et al., 1997; Montgomery et al., 1998; Saller et al., 2001; Watney et al., 2001; Franseen, 2006; Mazzullo et al., 2009; Watney et al., 2013). Many of them occur beneath unconformities and have been subaerially exposed. However, they are not restricted to specific depositional environments or water depths (Rogers and Longman, 2001). One major example is the Lower Devonian Thirtyone Formation in West Texas and New Mexico, described by Saller and others (1991, 2001) and Ruppel and Hovorka (1995). It is one of the largest chert-rich reservoir successions in the world found in gravity-flow deposits of sponge-spicule-rich sediments that are chertified. Dissolution of sponge-spicules, intercrystalline pores in the matrix of chert and fractures comprise most of the chert reservoir porosity in the Mississippian-age reservoirs. A worldwide example is the late Permian Kapp Starostin Formation on Spitsbergen, described by

Ehrenberg and others (2001), where porous spiculitic chert reservoirs are interbedded with limestones, shales and glauconitic sandstones. Here the porous spiculitic chert reservoirs have an overall high-porosity and widely varying permeability. Most of the porosity consists of moldic pores after sponge-spicules, interparticle pores in the matrix, fractures and vugs.

Diagenesis in the Mississippian system in Kansas is characterized by incipient stages of silicification and dolomitization, followed by dissolution, brecciation; silica and calcite cementation; and mineral stabilization related to meteoric diagenesis (Thomas, 1982; Watney et al., 2001; Rogers et al., 2001; Mazzullo et al., 2009; Ramaker et al., 2014). Later events of fracturing, stylolitization, dissolution and dolomitization are related to burial diagenesis and hydrothermal fluid migration (King et al., 2013; Ramaker et al., 2014). Most of the current understanding of diagenetic events is still immature and merits the implementation of geochemical techniques to explain the complexity of diagenesis. This study aims to improve our current understanding of diagenesis in Mississippian reservoirs by interpreting the timing and origin of diagenetic textures in Mississippian cores from the subsurface of south-central Kansas, via the use of petrographic descriptions coupled with standard geochemical analyses (stable isotopes, major- and trace-element concentrations, fluid inclusion analysis) to aid in the interpretation of paragenetic sequences.

METHODOLOGY

Four Mississippian cores (*Habaugh U.B. 15, George Michael 1-8, Wellington 1-32, Delaney No. 1*; Fig. 1; Table 1) from south-central Kansas and covering the Osagean-Meamecian-Chesterian time were described and divided into 13 different lithofacies. The objective of core description was to gain an understanding of the depositional environments of

the different lithofacies comprising the Mississippian system in the study area, and to recognize diagenetic textures visible at a core-scale. The lithological terminology of Dunham (1962) was used to describe carbonate textures. Additional criteria for describing lithofacies include: rock type, color, physical and biological sedimentary structures, fossil record, mineralogy and diagenetic textures visible on core samples.

The described cores were correlated to neighboring well logs (digital logs from the KGS database) to place the interpreted lithofacies into a spatial and relative time-stratigraphic framework. Raster logs from the interpreted cores were digitized for correlation purposes. The well logs were chosen based on quantity of petrophysical data and their favorable location to generate cross sections along the counties where the cores are located. The cross sections show the stratigraphic relationship between the four cores used in this study. The type of well log readings included include: gamma ray logs (GR), spontaneous potential log (SP), resistivity logs (ILD), neutron porosity logs (NPHI), bulk density logs (RHOB), density porosity logs (DPHI) and rock-composition logs from RHOmaa-NPHI or RHOmaa-Umaa calculations. Some of the well logs also contained core interpretations and/or geo-logs that were useful for correlation.

Approximately 120 polished and unpolished thin sections were prepared at the University of Kansas Geology Department to encompass features recognized during visual examination of core slabs. Thin sections were used for interpretations of lithofacies, depositional environment and diagenesis. Thin sections were impregnated with blue-dyed resin in order to recognized and differentiate porosity types. A portion of each thin section was stained with a solution of alizarin red S and potassium ferricyanide to differentiate between calcite, ferroan calcite, dolomite, and ferroan dolomite (Dickson, 1966). Standard transmitted light and reflected light microscopy was performed on a binocular microscope Olympus BX60 at the University of Kansas Geology

Department. Cathodoluminescence was performed using a Cambridge Image Technology LTD stage Clmk4 mounted on a Leitz SM-LUX-POL microscope at the University of Kansas Geology Department. Operating conditions for cathodoluminescence were: 14 kV acceleration potential and ~0.5mA gun current.

A paragenetic sequence was constructed for each of the areas studied from core and thin section petrography. Each location was considered separately for comparison purposes and recognition of localized and regional differences in paragenetic trends. The chronologic sequence of diagenetic textures was established by petrographic cross-cutting and super positional relationships.

Different geochemical methods were used to further refine the petrographic interpretations of different diagenetic mineral phases. These methods include stable isotopes, major- and trace-element concentrations, and fluid inclusion petrography and microthermometry. The procedures and parameters used for each analysis are described below.

Major- and trace-element concentrations

Ca, Mg, Fe, Mn, Sr and Na concentrations were obtained for dolomites on a fully automated JEOL JXA-8530F field emission electron analyzer at the Southeastern North Carolina Regional Microanalytical and Imaging Consortium (SENCR-MIC) in Fayetteville State University. Prior to analysis polished thin sections were carbon coated to ensure conductivity. In all analyses care was taken to avoid micron-sized pits or surface irregularities that were apparent in back scattered electron (BSE) images. Operating conditions were: 15 kv accelerating potential, 15-na beam current, 1 um spot-size and 60 seconds maximum counting time for each element.

Average calculated detection limits are as follows: Ca = 107 ppm, Mg = 89 ppm, Fe = 238 ppm, Mn = 149 ppm, Sr = 199 ppm, and Na = 48 ppm.

Stable isotopes

Selected calcite and dolomite phases were sampled and analyzed for their stable carbon ($\delta^{13}C$) and oxygen ($\delta^{18}O$) isotopic composition at the Keck Paleoenvironmental and Environmental Stable Isotope Laboratory (KPESIL) in the University of Kansas. All samples were digested with 100% phosphoric acid at 73°C in a KIEL IV single sample dosing system and the gas isotopic composition was measured with a ThermoFinnigan MAT 253 Dual Inlet system. Calcite and dolomite samples were collected under a binocular microscope from thin sections and polished slabs using a micro mill. All isotopic values are expressed in per mil (‰) and reported versus Vienna Peedee belemnite (VPDB) scale. Standards used for calibration of the isotopic data are: CA-14 (Sigma Aldrich Calcite #C4830-100G), NBS-19 Limestone (NIST Ref. Mat. 8544), CALX (internal calcite standard) and NIST Dolomite 88b. Analytical precisions are better than 0.05‰ for $\delta^{13}C$ and better than 0.10‰ for $\delta^{18}O$.

Fluid inclusion petrography and microthermometry

Fluid inclusion petrography and microthermometry was used to determine fluid composition and temperatures during diagenesis. Doubly polished thick sections were prepared using low-temperature techniques according to the methods described by Goldstein and Reynolds (1994). A small chip (less than 1 mm) of the prepared thick section was cut off to perform microthermometry analyses on a Linkam THMSG 600 heating/cooling stage, mounted on an Olympus BX60 binocular microscope at the University of Kansas Geology Department.

Fluid inclusions analyses were performed on early diagenetic megaquartz (cMGQZ-1) found on silicified evaporite nodules in the Cowley Formation from the *Harbaugh UB15* core.

GEOLOGIC SETTING

The cores used in this study are all located in south-central Kansas near the Kansas-Oklahoma state borderline. Specifically, two cores are from the *Rhodes* field in Barber County (*Habaugh U.B. 15, George Michael 1-8*), one is from the *Wellington* field in Sumner County (*Wellington 1-32*) and one well is from a "wildcat" area in Comanche County (*Delaney No. 1*; Fig. 1; Table 1). The *Delaney No. 1* core in the eastern most part of the Hugoton embayment lies west of the Pratt anticline (a southward-plunging extensions of the central Kansas uplift), which separates this core from the others to the east. The *Harbaugh*, *George Michael*, and *Wellington* cores all reside in the Sedgwick basin that is bounded by the Pratt Anticline on the west and the Nemaha Uplift on the east (Fig. 1). The stratigraphy of Mississippian rocks in the study area is predominantly restricted to Kinderhokian, Osagean and Lower Meramecian strata consisting of cherty partially dolomitized skeletal packestones and grainstones; and cherty partially dolomitized wackestones and mudstones (Watney et al., 2001; Fig. 2). Much of the skeletal constituents consist of siliceous-sponge spicules and heterozoan carbonates (specially crinoids; Watney et al, 2001; Franseen, 2006; Ramaker et al; 2014).

Mississippian sediments were deposited on a broad carbonate ramp that formed in a shallow tropical sea that covered most of present-day Kasnas and southern North America (Franseen, 2006; Fig. 3). The approximate paleolatitude of carbonate deposition in Kansas during the time was 20° south of the equator (Gutschik and Sandberg, 1983). During the Mississippian the relatively dry conditions were suitable for widespread deposition of carbonates

(Watney et al., 2001). The Mississippian carbonate ramp was characterized by an extensive wedge of carbonate sediments that prograded away from a northeast-trending transcontinental arch during the eustatic sea level rise in most of the Mississippian (Lane and De Keyser, 1980; Fig. 3). The ramp had a distally steepened southward dipping geometry that bordered the Anadarko Basin near the present Kansas-Oklahoma state borderline (Rankey, 2003). A deep seaway lay south of the ramp margin along a converging plate boundary between the North American and South American plates (Scotese, 1999).

The most prominent tectonic feature in the study area is a structural high known as the Central Kansas uplift-Pratt Anticline structure (Fig. 1). This tectonic uplift effectively separates two shallow basins: the Sedgwick basin to the east and the Hugoton embayment to the west. It was formed during the Late Mississippian-Early Pennsylvanian, when structural movement related to the collision between North America and South America (Ouachita Orogeny) resulted in fault-related uplift and tilting of the Mississippian strata (Gutschick and Sandberg, 1983). A period of eustatic sea-level fall in the late Mississippian accompanied the tectonic activity. This was followed by extensive erosion of the Mississippian strata that resulted in a regional unconformity that separates Mississippian and Pennsylvanian strata (Merriam, 1963; Montgomery et al., 1998; Watney et al., 2001; Franseen, 2006; Mazzullo et al., 2009; Ramaker et al., 2014). Thus, Mississippian rocks are absent along the crest of the central Kansas uplift (Merriam, 1963). Subcrop patterns beneath the unconformity show progressively older units toward the axis of the uplift trend (Merriam, 1963; Fig. 1). Other minor tectonic features in south-central Kansas are a series of local structural features consisting of southwest-plunging folds and northeast-southwest-oriented faults that began forming in the Early Mississippian and may have influenced depositional patterns during the time (Montgomery et al., 1998).

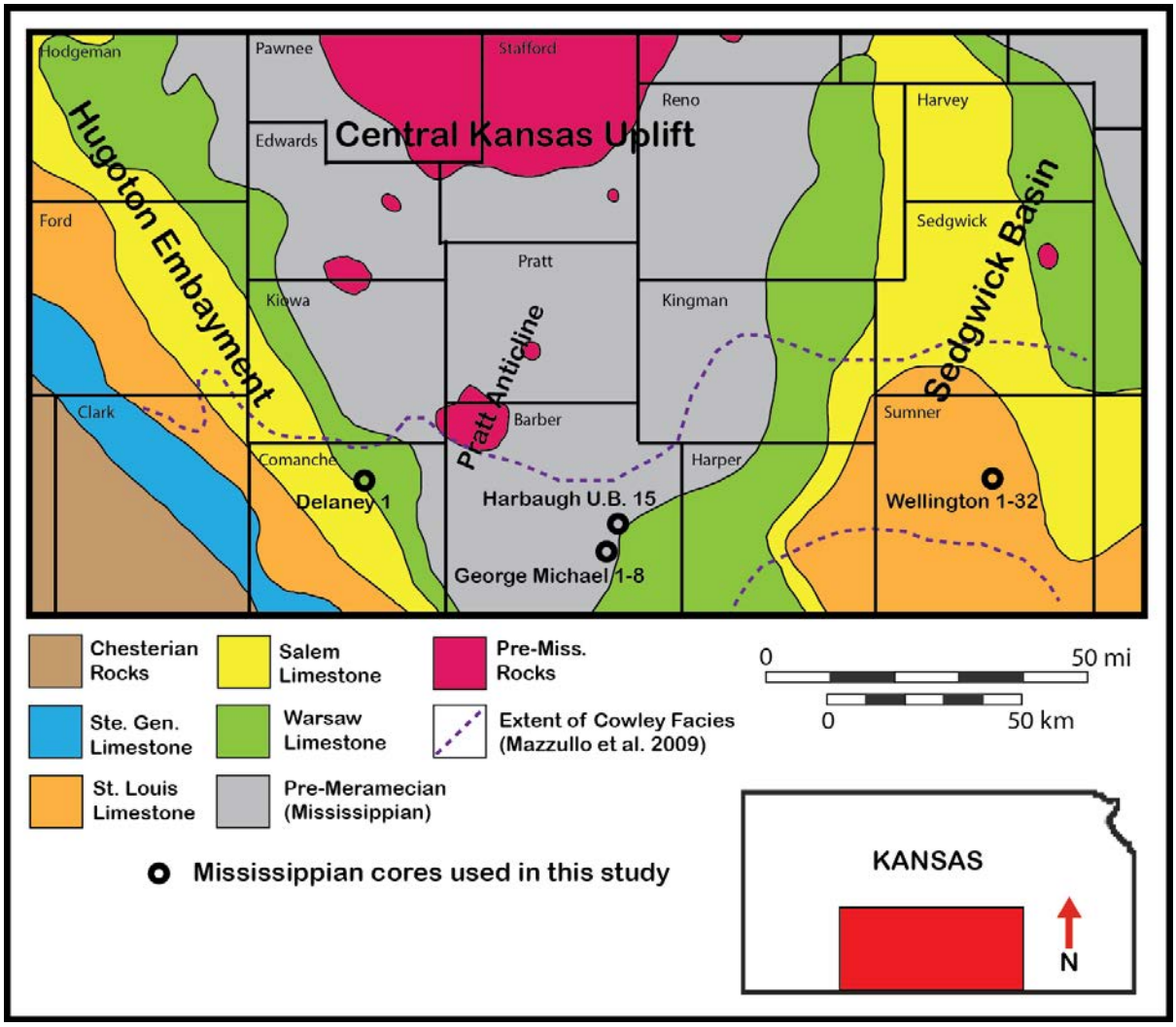

Figure 1. Pre-Pennsylvanian unconformity subcrop map of the study area. The locations of the four Mississippian cores used in this study are illustrated. Modified from Franseen (2006).

Well Name (Core)	Operator	API	County	Field	Location	Mississippian Interval on core
Delaney No. 1	Zenith Drilling Corp.	15-033-30101	Comanche	Wildcat*	T31S R18W, Sec. 36, C NE NW	5172 ft - 5220 ft
Harbaugh UB 15	Continental Oil Co.	15-007-01814	Barber	Rhodes Field	T33S R11W, Sec. 32, C SW SE NW	4540 ft - 4649 ft
George Michael 1-8	Nichols Drilling Co.	15-007-20121	Barber	Rhodes Field	T34S R11W Sec. 8, C NE SW	4572 ft - 4617 ft
Wellington 1-32	Berexco LLC	15-191-22591	Sumner	Wellington Field	T31S R1W, Sec. 32, NE SW NE NE	3568 ft - 4060 ft

Table 1. Core dataset used in this study. Mississippian Formations covered on cores was determined from correlation of the cores to adjacent type logs from the KGS website. "Wildcat wells" are wells drilled beyond the boundaries of an oil and gas field.

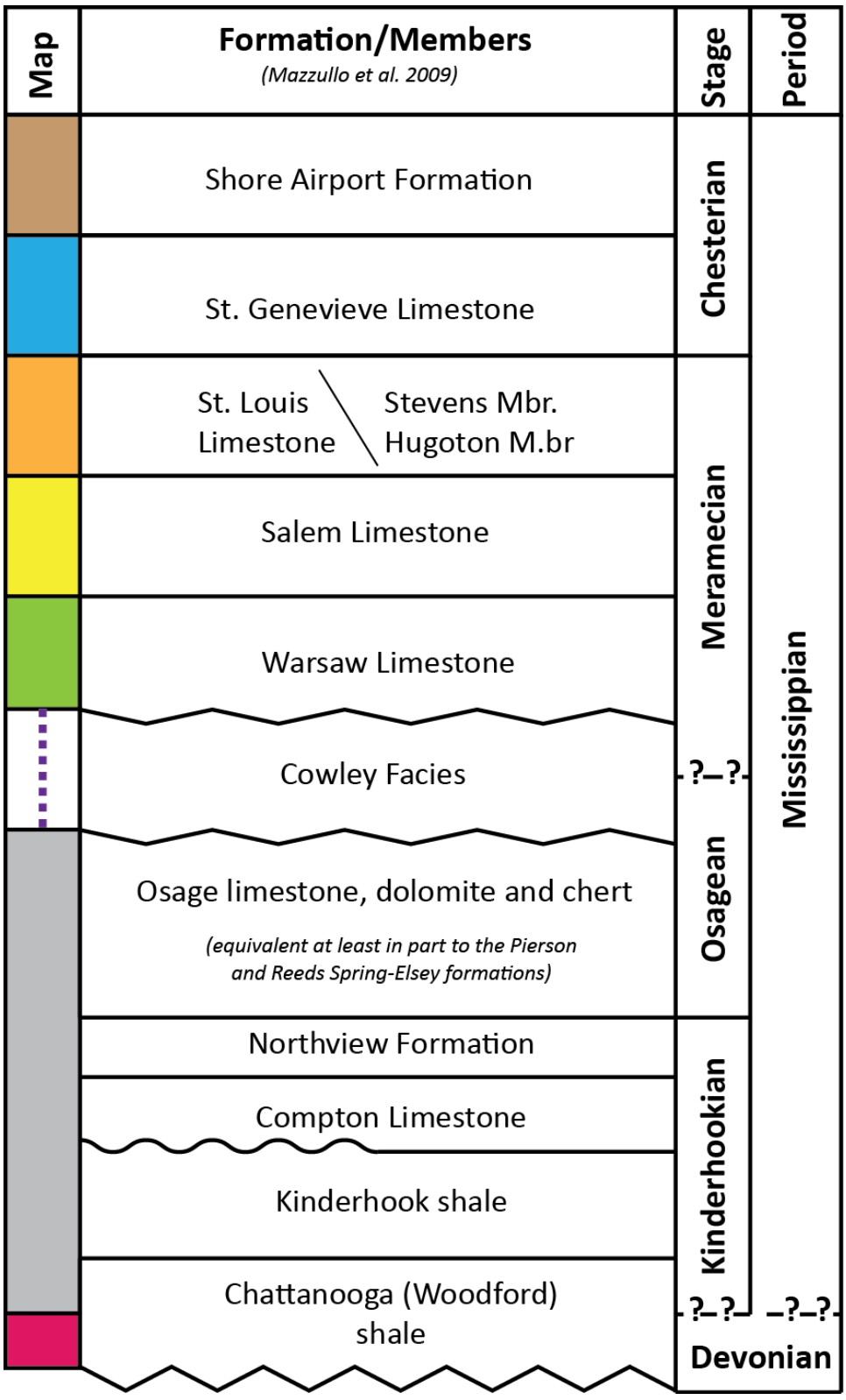

Figure 2. Mississippian stratigraphic units for the state of Kansas. Modified from Mazzullo and others (2009).

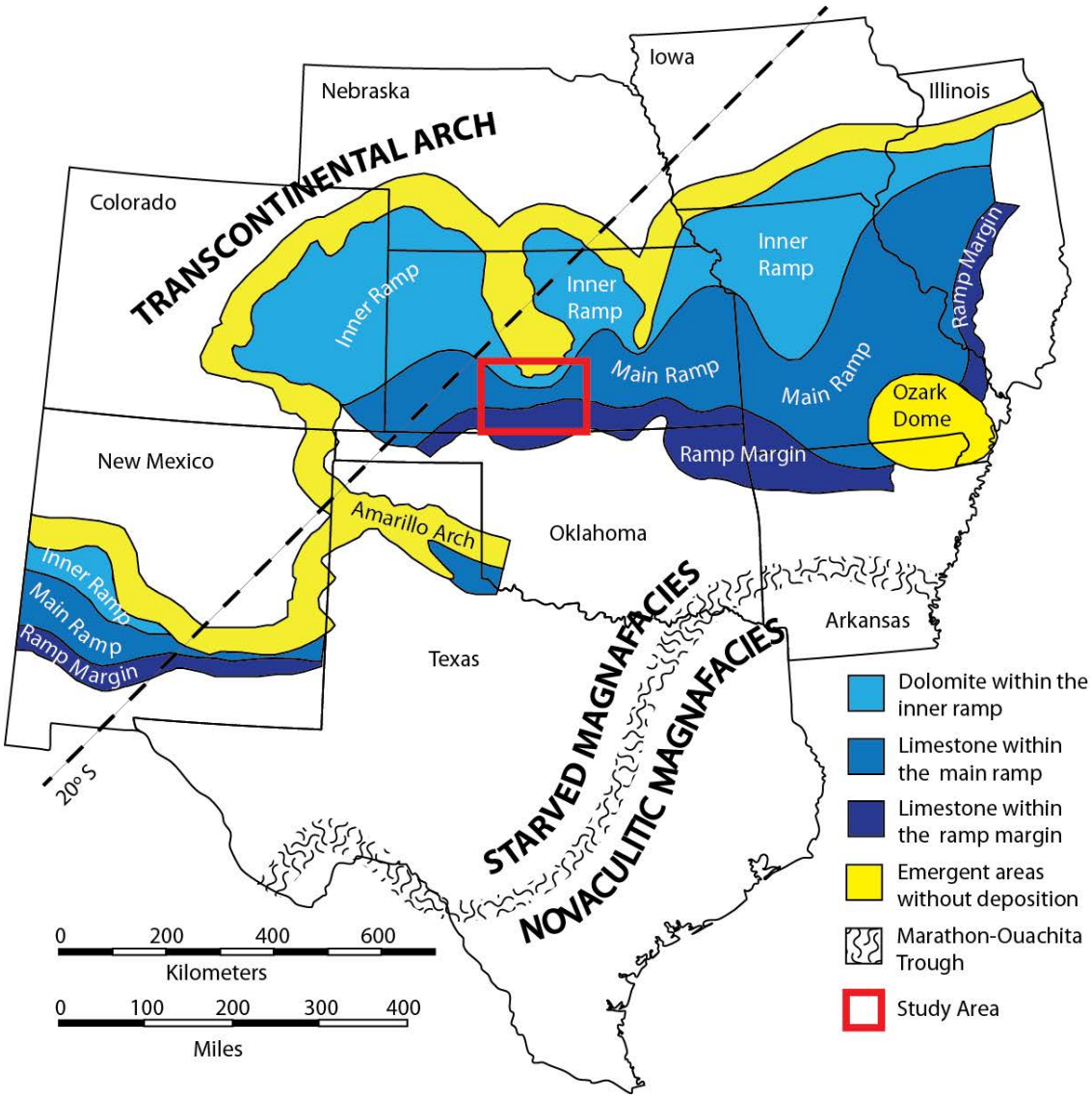

Figure 3. Paleogeographic map for the middle Mississippian (Osagean-Meramecian) in Kansas and bordering areas. The carbonate facies are divided into inner ramp, main ramp and ramp margin. Red square indicates the study area. Modified from Lane and De Keyser (1980).

SECTION 1. MISSISSIPPIAN LITHOFACIES: DESCRIPTIONS AND INTERPRATATIONS

The Mississippian subperiod, spanning about 359 to 323 million years ago, was dominated by carbonate deposition with minor periods when spiculite deposition suppressed the deposition of carbonates, and was intermittently exposed to erosion and weathering during multiple sea-level lowstands (Mazzullo et al. 2009). Mississippian strata in the study area are divided into 13 different lithofacies. Not all lithofacies are present on each core, but they are all representative of varying water depths and depositional settings that existed in the inner-, mid- and outer-ramp sections of the carbonate ramp that bordered the Anadarko basin in its relative south-central Kansas location during the Mississippian. Figures 4 thru 7 illustrate the distribution of lithofacies and diagenetic textures visible on core slabs for each of the cores studied. Figures 8 thru 20 illustrate examples of each lithofacies in hand sample and thin section.

Lenticular spiculite wacke/packestone (LSW/P)

Description: This facies comprises discontinuous lenticular beds of sponge-spicule rich marlstone, termed spiculite, interbedded with wispy thinly to thickly laminated shale (Fig. 7). It is the most common lithology found in the Cowley formation (Mazzullo et al., 2009). Similar facies have been called lenticular-, nodular- and flasser-bedded spiculites by Mazzullo and others (2009) and marlstones by Costello and others (2013), due to its peculiar sedimentary structure and the presence of a combination of clay, carbonate and silica in the matrix. In the cores described the thickest section of this facies covered more than 30 feet (Fig. 5 and 6). It is characterized by the predominance of skeletal fragments, primarily monaxon siliceous-sponge spicules derived from demosponges; but may contain disarticulated crinoid and fenestrae bryozoan fragments that are commonly silicified (Fig. 7C). Spiculite lenses are tan to dark brown

and the enclosing shale ranges down section from pale olive green to dark gray (Mazzullo et al., 2009). Spiculite lenses range from wackestones to packestones (Dunham, 1962), and are partially to completely replaced by fabric-retentive chert that in many cases resulted in chert nodules (Fig. 8B, 8C). Spiculite lenses are mainly massive but occasional ripple cross-sratification and sediment sorting is observed. The relatively low resistivity of this facies reflects the silica component in the rock (Fig. 1). A few samples appear dolomitized. Dolomite is present as scattered finely to medium-crystalline dolomite rhombs that partially replaces the matrix of spiculites lenses. Silica nodules after evaporites are abundant on this lithofacies. Framboidal clusters of pyrite are locally found. Trace fossils, possibly *planolites* and *chondrites,* are present in some samples and are more commonly observed on the shale portion (Mazzullo et al., 2009).

Lenticular spiculites typically contain vuggy, moldic (from leached siliceous-sponge spicules), micro- and fracture porosity (Fig, 9D). A porosity of 13% was calculated from point counting estimates of photomicrograph. Some of the moldic pores and irregular cavities are cemented with chalcedony and calcite. Some spiculite lenses where porosity dominates tend to have a much darker color (dark brown). The particular dark color can be the result of diagenetic overprint during weathering, hydrothermal alteration (Ramaker et al., 2014), hydrocarbon staining, or a combination of these (Fig. 8C). Some of this facies are brecciated and the amount brecciation increases with proximity to an unconformity. Transported fragments of weathered and faintly laminated cherty spiculite have been found within this lithofacies**.**

Interpretation: The water depth and temperature regimes where sponge-spicule rich deposits are found is still a subject of much controversy. Gammon et al. (2000) suggested that these deposits should be associated to marine environments with low hydrodynamic energy, normal salinity, high nutrients and high supply of silica that allows for prolific silicification and accelerated

growth. Upwelling of silica-bearing ocean waters onto shallower ramp areas during the Mississippian time has been suggested by Lowe (1975) as a plausible source of nutrients that contributed to the distribution of spiculite-rich deposits. The prevalence of demosponges over any other organism in this facies may reflect this conditions. Mazzullo and others (2009) interpreted lenticular-, nodular- or flasser-bedded spiculites and shales to be deposited in shallow to progressively deeper, moderate to low energy, medial-ramp environments.

The frequency of shale to lenticular spiculite cannot be formed by episodic storm waves. The presence of numerous intra-Mississippian unconformities suggests that sediments were subjected to hydraulic reworking and winnowing many times near an exposed area (Mazzullo et. al, 2009; Rogers, 2001). The lenticular bedding can be the result of periodic winnowing of the sediments by fair-weather wave base during sea-level lowstands. This is suggested by the well-sorted texture observed in many spiculite lenses. In turn, the shale represents the background sedimentation during quiet times and the wispy laminations are mostly the result of soft sediment compaction.

An alternative explanation is that the lenticular spiculites are in fact siliceous-sponge colonies. Once a sponge colony dies and the sponge tissue disintegrates the more resistant spicules accumulate in-place forming small pods of spicules within the sediment. Rogers and others (1995) concluded that spiculitic chert reservoirs in the Glick field, Kansas represent sponge mats and bioherms. Kopaska-Merkel and others (2013) described bedded sponge-microbial boundstone in Mississippian deposits in Alabama and interpreted them as biohermal structures formed at shallow water below normal wave base. However, no evidence of biological growth was found in the cores studied. The sponge microbial mound facies described by Kopaska-Merkel et al. (2013) had thrombolite and pelloidal textures suggestive of microbial

encrustation and biological binding that preserved the biological structure of in-place sponge-spicules. Such textures are absent in the cores studied, which can explain why the sponge-spicules don't preserve their original structure, and instead have the appearance of pods of skeletal debris. This alternative better explains the frequent intercolation of shale and lenticular spiculite in this lithofacies.

The abundance of shale, the presence of variable skeletal fragments, occasional ripple cross sratification and the presence of bioturbated textures suggest that this facies was deposited in a marine subtidal, mid- to outer-ramp environment. Sedimentary structures and disarticulation of some skeletal fragments indicates that some of these sediments were periodically winnowed by the action of waves, most likely fair-weather waves.

Bioclastic crinoidal packe/grainstone (BCP/G)

Description: A tan to dark grey, massively to gradded bedded and moderately sorted bioclastic packestone to grainstone (Dunham, 1962) texture characterizes this facies (Fig. 9). Skeletal debris consists dominantly of crinoid and fenestrate bryozoan fragments; with a minor content of bivalves (brachiopod and pelecipods), solitary rugose corals, foraminifers and ostracods (Fig. 9). Skeletal fragments are disarticulated but not abraded. Much of the original carbonate mineralogy remains except for some partial silicification of skeletal fragments. This facies occur locally within spiculite-dominated strata and typically show an erosional contact (scoured) with the sediment below (Watney et al., 2001; Fig. 1). The thickest bed found on the studied cores was 7 ft thick (Fig. 4), but similar facies have been recorded to reach 14 ft thick by Mazzullo and others (2009). Low porosity (0-5%) is indicated by thin-section and core observations. Most of the porosity is occluded by calcite spar that is typically found as a syntaxial overgrowth cement on

crinoid fragments. Stylolites and grain-to-grain pressure solution also reduced some of the porosity generating a tight fabric. It typically has high resistivity values that are indicative of the heavily compacted and cemented fabric (Fig. 5).

Interpretation: Echinoderm-dominated facies in Osagean strata of Schaben field, Ness County Kansas were interpreted by Franseen (2006) as inner-ramp deposits in relatively shallow subtidal, normal-marine conditions with fluctuating energy. Ramaker and others (2014) interpreted similar echinoderm-rich bioclastic wackestones and packestones in Osagean strata of Cherkoee County, Kansas to represent deposition in a subtidal normal-marine environment, below fair-weather wave base that were periodically agitated during storm events. Others (Johnson and Bud, 1994; Witzke et al., 1990) have also interpreted similar grainstone facies in Mississippian strata as sediments deposited during storm events. Skeletal deposits from shallow waters (above wave base) can be broken by wave action and subsequently be dumped down slope as small-scale debris flows (Rogers, 2001). The predominance of coarse skeletal debris, interbedding with shales and spiculites, and frequent graded bedding and scour features suggest that these lithofacies were deposited during episodic high-energy conditions. The absences of structures that indicate hydraulic reworking of sediments suggest that this facies was deposited below fair-weather wave base. The sediment was most probably transported from shallow areas into ramp-margin settings by seaward flowing storm-surge currents.

Nodular and bedded cherty spiculite (NBCS)

Description: This facies are characterized by dark brown spiculitic packestones (Dunham, 1962) with little to no shale content (Fig. 10). It mainly consists of grain-supported siliceous-sponge spicules that are pervasively replaced with microcrystalline quartz and chalcedony (Fig. 10C).

Most of the matrix consists of microcrystalline quartz and silicified clay minerals (Fig. 10D). It is commonly associated with porcelaneous cherts, breccias and subaerial exposure surfaces (Fig. 4). Some samples are autobrecciated and contain an extensive amount of vuggy and inter-granular porosity. Convoluted chert nodules ranging from millimeter to centimeter size with a grayish mottled texture and faint cross laminations are scattered in the matrix and show extensive dissolution along the rims, where solution-enlarged vugs are dominant (Fig. 10). The predominance of dissolution textures in this facies indicates an extensive history alteration under subaerial and subsurface processes (i.e. weathering, karsting and hydrothermal dissolution). Costello and others (2013) described similar dark colored spiculitic packestone facies with abundant moldic and intergranular porosity, from Osagean and Meramecian strata in south-central Kansas, and interpreted them as "weathered cherts" referring to the highly altered texture of the rock. The "weathered chert" of Costello and others (2013) has a mineralogical composition of more than 80% quartz. Scanning electron microscope images also suggest that this facies is mainly composed of quartz (Fig. 10D).

Interpretation: The absence of shale laminations, the grain-supported texture, faint cross lamination and consistent proximity to subaerial exposure surfaces suggest that these sediments were probably deposited in a ramp margin setting that is shallower than the LSW/P facies. Cross-laminated and proximity to exposure surfaces leads us to believe that these facies correspond to the bedded spiculite described by Mazzullo and others (2009). Bedded spiculite were characterized as the principal oil and gas reservoir within the Cowley Formation; deposited in moderate-energy, shallow water, inner-ramp settings. Cross-laminated microporous cherts in the Dollarhide field in West Texas are interpreted as sponge-spicule-rich sands that were deposited in sub-marine channels and fans on the slope, prior being pervasively chertified. However, no

evidence for channel-like deposition was found in the cores studied. The proximity of these lithofacies to unconformities and the autobrecciated texture is also suggestive of shallower conditions. Petrographic descriptions and comparisons supports the idea that this facies were deposited in shallow water inner-ramp settings where sponge-spicules where agitated by the action of fair-weather wave base during times of sea-level lowstands prior to sub aerial exposure of the sediments.

Porcelaneous chert (PC)

Description: This lithology is characterized by a hard and dense chert with a grayish white matte surface texture that may look dull or mottled (Fig. 11). It forms irregular chert beds that occur at proximities to lenticular spiculites where shale is not abundant. In the cores studied the thickness ranged from a couple of inches to about a foot thick. Siliceous sponge-spicules are unrecognizable on hand sample but silhouettes can be identified on thin section on a microcrystalline and cryptocrystalline quartz matrix (Fig. 11B). Siliceous sponge-spicules appear to be the main component of this facies prior to pervasive replacement with chert. No evidence of precursor carbonate fragments was found in porcelaneous chert beds. Moldic and vuggy porosity was rarely found in porcelaneous cherts and microporosity was visible in thin sections (Fig. 11B).

Interpretation: The formation of dense porcelaneous chert is the result of pervasive chertification during rapid growth and amalgamation of various chert nodules within the sediment, particularly sponge-spicule-rich sediments. The mottled texture of chert may be formed during multiple generations of chert growth (Mazzullo et al., 2009). This can lead to the formation of irregular and discontinuous chert beds that can have a wide range in sizes (a few inches to a few feet

thick). Conspicuous and discontinuous layers of chert has been described Mazzullo and others (2011) in outcrops of the Reeds Springs formation, a temporal correlative of the Cowley Formation studied in this paper. In the Reeds Spring they are usually associated with medium to dark gray mudstones. Dense chert beds in the cores studied occur randomly within lenticular spiculites, shales and breccias. The replacement nature of porcelaneous chert indicates that the depositional environment is linked to the sediment it replaced. The predominance of siliceous sponge-spicules in this facies suggests that they are preferential sites for nucleation and prolonged nodule growth, leading to the formation of a porcelain-like chert bed.

Cherty sucrosic dolomite (CSD)

Description: This facies consists of light yellowish brown, rather uniform, pervasively dolomitized lime-mud with scattered convoluted dark gray brecciated chert nodules (Fig. 12). It's characterized by a sponge-spicule-rich wackestone fabric (Dunham, 1962). This facies is pervasively dolomitized (up to 80% dolomite) and exhibits a sucrosic appearance (Fig. 12). Porosity in this facies reaches 30% based on point counting estimates of photomicrographs and petrophysical calculations from Watney and others (2013). High porosities are particularly a factor of dolomite intercrystalline porosity; but molds (after sponge-spicules), vugs and minor fractures are also present (Fig. 12). Dolomite occurs as finely to medium-crystalline cloudy to clear rhombs (Fig. 12). Chert nodules are composed of microcrystalline quartz with sponge-spicules replaced with the same. While sponge-spicules are preserved in chert nodules, sponge-spicules have leached out outside of the nodules (Fig. 12). Chert nodules contain a tripolitic (micro-porous) rim that's also indicative of silica dissolution. No sedimentary structure was visible in core samples cause they might have been overprinted during dolomitization. According

to Watney and others (2013) this facies is up to 50 ft thick in over 4 to 5 miles and represents the main reservoir facies of the Wellington field found below the brecciated chert facies (Fig. 12).

Interpretation: The presence of anastomosing chert nodules rich in sponge-spicules probably represent selective replacement. Much like in the LSW/P facies, these chert nodules formed where sponge-spicules accumulated. No evidence of a biogenic framework or a sedimentary structure that is diagnostic of the depositional environment was seen. Sponge-spicules showed no preferred orientation or good sediment sorting. Through comparison to the LSW/P facies, characteristics identifiable on core and thin sections suggest that the CSD facies was deposited in a similar environment; a marine subtidal, mid- to outer-ramp environment where the sediment was periodically winnowed by the action of fair-weather waves. Similarly it is possible that the presence of sponge-spicule rich chert nodules represent in-situ accumulations of sponge-spicule colonies that where chertified. The dolomite in this facies is secondary and its origin is not related to the depositional environment of this facies

Bioclastic mudstone/wackestone (BM/W)

Description: A light olive gray color, nonparallel wavy to lenticular bedding and a slightly dolomitized lime-mud matrix with scattered skeletal debris characterize the texture of this facies. Bedding occurs as alternating dark gray and olive gray cm-scaled wavy discontinuous beds. Skeletal debris consists of siliceous-sponge spicules and scattered disarticulated crinoids, bryozoans, brachiopods and ostracodes (Fig. 13). Lenses rich in sponge-spicules are chertified and exhibit a tripolitic texture. Dolomite is scarce in this facies, and occurs as scattered finely to medium-crystalline dolomite rhombs replacing the lime-mud matrix. Brecciated and collapsed, silicified and calcified evaporite nodules ranging from less than 1 cm to 4 cm are found.

Bioturbation is recorded as *phycosiphon* burrows that are deformed to oval shapes as a result of sediment compaction (Fig. 13). Compaction also resulted in stylolitization. This facies is poorly chertified and slightly argillaceous. Minor fractures, sponge-spicule molds and vugs are the main pore types in this facies. Occasional mm-scaled black shale streaks are found.

Interpretation: The diverse marine skeletal fragments, the wavy character of the bedding, the presence of bioturbation and the occurrence of shale streaks are suggestive of a marine, relatively quiet-water subtidal environment below fair-weather wave base. The moderately bioturbated texture is also indicative of an environment that was oxic and rich in nutrients. The presence of shale streaks and laminated clay-rich intervals are indicative of quiescence in deposition. The dolomite in this facies is secondary and its origin is not related to the depositional environment of this facies.

Cherty and dolomitized argillaceous mudstone/wackestone (CDAM/W)

Description: This facies is characterized by olive grey to dark grey, wavy laminated, dolomitized argillaceous lime-mud, lacking skeletal grains (Fig. 10). It is differentiated from the BM/W facies by a darker color, a moderate argillaceous content and abundant anastomosing to rounded dark grey dense-chert nodules reaching up to 15 cm in diameter (Fig. 14). Identified skeletal components consist of leached sponge-spicules and scattered disarticulated crinoids, bryozoans and brachiopods. The argillaceous lime-mud matrix is replaced by finely- to medium-crystalline dolomite rhombs (Fig. 14). Nodular chert crosscuts laminations in the sediment and deforms the surrounding sediment, indicating a replacement origin (Fig. 14). Laminations may be imparted by mm-scaled shale streaks. Bioturbation commonly occurs as compacted *phycosiphon* burrows (Fig. 14). Porosity occurs as molds, vugs and minor fractures. Authigenic pyrite “framboids” are

enclosed in dark grey chert nodules and within the dolomitized matrix. This pyrite is interpreted to form very early, prior chertification and dolomitization of the sediments according to the paragenetic relationships explained in a later section.

Interpretation: This facies are found stratigraphically adjacent to the BM/W facies (Fig. 6). The similarity in sedimentary structures to the BM/W facies, but the lack of skeletal grains and moderate clay content suggest that this facies are found down slope relative to the BM/W facies. The presence of early crystals of pyrite within the sediments is also suggestive of anaerobic and euxinic conditions that are more common in quiet and deeper marine environments (Taylor and Macquaker, 2000). No sedimentary structure that would indicate hydraulic reworking of sediments was described. Based on the arguments described above it is interpreted that this facies represent a marine subtidal condition, below fair-weather wave base in outer ramp settings.

Nodular and bedded dolomitized argillaceous wackestone (NBDAW)

Description: This facies consists of olive grey to dark grey, bedded and highly bioturbated, dolomitized argillaceous wackestones with abundant elongated silica nodules that contain relict evaporite textures (Fig. 15). Silicified evaporite nodules (SEN) raging from less than a cm to 30 cm in size, is the most characteristic feature of this facies (Fig. 15). The matrix consists of dolomitized lime-mud and clay (Fig. 15). Authigenic quartz is found cementing the intercrystalline and vuggy porosity in the dolomitized matrix. The authigenic quartz cement can easily be confused by silt- to fine-grained detrital quartz due to its abundance and sometimes rounded appearance. The very clear translucent texture with no evidence of sedimentary abrasion is also suggestive of an authigenic origin. Skeletal fragments are rare and primarily consist of siliceous sponge-spicules. Finely to medium-crystalline dolomite rhombs replaces most of the

matrix. Bedding is present as cm-scaled wavy, parallel beds with alternating light and darker color. *Phycosiphon* and cylinder to elliptical shaped sub-vertical burrows, possibly *skolithos* (elongated cylinder) or *planolites* (circular to elliptical), were identified in core slabs (Fig. 15). Some silicified evaporate nodules have an elongated sinuous shape that appears to occur along burrowed structures (Fig. 15). Some nodules appear autobrecciated and the sediments surrounding the nodules are typically deformed.

Interpretation: The presence of parallel wavy bedding with no evidence of wave or current reworking, the abundance of bioturbation and scarcity of sekeltal grains is suggestive of a marine subtidal environment below storm wave base. Evaporites in this facies do not represent evaporative conditions under supratidal environments because none of the sedimentary structure indicates this. Thin section examination suggests that the silt-sized quartz particles are most probably authigenic in origin and are probably related to the precipitation of early-megaquartz and/or chert, explained in section 3. The dolomite and silicified evaporite nodules in this facies are secondary and are not related to the depositional conditions of this facies.

Dolomitized lenticular bioclastic wacke/packestone (DLBW/P)

Description: Slightly disarticulated and unabbraded diverse skeletal fragments on a gray to light-gray dolomitized and argillaceous lime-mud matrix characterize this facies (Fig. 16). The most obvious texture of this facies is the well-sorted bioclastic wacke-packestone lenses (Fig. 16). Sponge-spicules, crinoids and bryozoans with variable abundances comprise the skeletal grains in the bioclastic lenses (Fig. 16). The matrix is replaced by finely to medium crystalline dolomite rhombs. Wavy, wispy and occasional cross-stratified laminations were found in core slabs. Burrow structures occur as elliptical shaped sub-vertical coarse-grained patches and are probably

planolites. Anastomosing light grey to dark grey tripolitic chert nodules were identified on core slabs, and occurs where siliceous-sponge spicules dominate.

Interpretation: These facies are essentially similar in sedimentary structures to the LSW/P facies. The bioclastic lenses are well-sorted, they have a diverse skeletal composition (although siliceous-sponge spicules dominate) and are interbedded in a fine-grained matrix just like in the LSW/P facies. The well-sorted texture may indicate some degree of periodic hydraulic reworking and mixing of sediments. It differs from the LSW/P facies by a lower content of chert and a higher content of dolomite. Through comparison to the LSW/P facies, it is interpreted that the DLBW/P facies was deposited in a marine subtidal, mid- to outer-ramp environment where the sediment was periodically winnowed by the action of fair-weather waves. The bioclastic lenses, particularly rich in sponge spicules, can also represent in-situ remnants of siliceous-sponge colonies similar to those observed in the LSW/P facies.

Argillaceous dolomite (AD)

Description: This facies is characterized by a dark brownish-grey to black, pervasively dolomitized argillaceous and organic-rich matrix with little identifiable skeletal grains. It is very tight with almost no porosity visible on core slabs (Fig. 17). Occasional micro-porosity and partially leached sponge-spicules are found. Faint wavy laminations can sometimes be identified. The matrix is replaced by subhedral fineley- to medium-crystalline dolomite rhombs. Contrary to other facies where dolomitization tends to improve porosities, in this facies a planar-s hypidiotopic mosaic results in a tight fabric with low intercrystalline porosity (Fig. 17; Sibley and Gregg, 1987). Accessory minerals include: ovoid-shaped, internally featureless glauconite crystals and framboidal pyrite clusters. Occasional silt-sized authigenic quartz is also found.

Phycosiphon burrows are abundant. Concentrations of organic matter occur as dark redish-brown smears and spots in the matrix visible in thin sections. Black shale seams ranging from a few millimeters to centimeters are also found. Horsetail dissolution seams can sometimes impart laminated textures seen in hand-sample and thin-section. Silicified evaporate nodules are found but very rare.

Interpretation: The predominance of fine-grained sediments, particularly clays, and lack of skeletal grains is suggestive of outer ramp settings, where sedimentation occurs by settling of fine-particles that are in suspension. The abundance of authigenic pyrite and glauconite are also suggestive of outer-ramp settings, and indicate anaerobic and reducing conditions. Glauconite in particular, is regarded as an indicator of slow-sedimentation rates (Harris and Whiting; 2000). The absence of wave and current induced structures also suggest a subtidal environment below storm-wave base. All the characteristics described above are consistent with a ramp margin, quiet-water subtidal environment, below the influence of wave action. Of all the facies this one represents the most distal and deepest of the ramp facies described on core. The tight nature of this facies indicates that it can represent a potential intra-Mississippian caprock.

Chert breccia (CB)

Description: This facies mainly consists of grain-supported breccias with angular to sub-angular clasts of variable chert lithologies including: porcelaneous chert, tripolitic chert and cherty bioclastic wacke-packestone, in a clay or shale groundmass (Fig. 18). Autobrecciated fabrics also occur and are differentiated by a clast-supported texture and individual clasts still found in the same place of fracturing (in-situ brecciated; Fig. 18). In some breccias, the clasts have vuggy, moldic and micro-porosity, in many cases constrained to the rims of individual clasts (Fig. 18).

Most of the breccias are found below the Mississippian-Pennsylvanian unconformity, but other facies can also be found brecciated when adjacent to intra-Mississippian unconformities (Fig. 4, 5, and 6).

Interpretation: Brecciated chert facies are very common at the top of Mississippian strata in south-central Kansas and their origin is well known (Montgomery et al., 1998; Rogers, 2001; Watney et al., 2001; Mazzullo et al., 2009; Mazzullo et al., 2011; Watney et al., 2013; Ramaker et al., 2014). The brecciated chert facies form by one or a combination three different process: collapsing of material after karst dissolution, sedimentary reworking and autobrecciation. Grain-supported breccias found directly below the Mississippian-Pennsylvanian unconformity consist of the brecciated Mississippian intervals commonly referred to as the "chat" (Montgomery et al., 1998). The "chat" intervals forms after the accumulation of the insoluble residues of leached Mississippian carbonates after karsting (Montgomery et al., 1998; Rogers, 2001; Watney et al., 200; Mazzullo et al., 2009). Ramaker and others (2014) referred to similar facies as solution-collapse breccias. Subsequent reworking of brecciated intervals is described on cores and increases toward the top of the Mississippian-Pennsylvanian unconformity where chert conglomerate facies are found. Autobrecciated fabrics may occur directly below the "chat" intervals where sedimentary reworking did not occur after fracturing and dissolution of the rock, or where brecciation results from loading and compaction instead of weathering processes.

Bryozoan bafflestone (BB)

Description: This facies is characterized by calcite-cemented patches of bryozoans that form a baffled framework, with pods of bioclastic wacke-packestones trapped between the cemented bafflers (Fig. 19). Bryozoans are mostly of the fenestrate and trepostone type. The baffled

framework is formed by piled-up plates of bryozoan fronds surrounded with isopachous radial, fibrous to bladed calcite cement (Fig. 19B). The abundance of isopachous cements sometimes makes the individual bryozoan plates appear isolated from one another (Fig. 19B). This facies is also highly cemented with masses of sparry calcite cements, which resembles *stromatactis* (Fig. 19C). Some of the sparry calcite may form intraskeletal geodal textures. Bioclastic pods consist of disarticulated and unabraded skeletal debris in grain-support; mostly bryozoans, crinoids, brachiopods and ostracods, with a micrite and/or peloidal matrix (Fig. 19D). There is no evidence of microbial encrustation or binding, however some of the skeletal fragments may show variable degrees of micritization. Some skeletal fragments may be replaced with chert. Quartz geodes were also identified on core samples. Most of the porosity is occluded with variable calcite cementation and stylolites or micro-stylolites are commonly found. This facies where only found in the *Delaney No. 1* core (Fig. 7).

Interpretation: Bryozoans are suspension feeders that generally require a stable substrate such as rock, shells and sediment grains (Feldman et al., 1993; Flügel, 2004). The preservation of fragile bryozoan fronds with calcite cements resulted in a baffling network of bryozoans, where disarticulated skeletal debris was trapped in between bafflers. Early cementation of sediments and skeletal debris could have provided a strong substrate for further bryozoan growth. The calcite spar masses made up of isopachous crusts of calcite cement found in inter-particle pore space are similar to *stromatactis*, although lacking the characteristic flat to undulate smooth lower surface and digitate upper surfaces (Bourque and Boulvian, 1993). *Stromatactis* has been widely found in Paleozoic carbonate-mounds and their origin is still enigmatic (Burke and Lasemi, 1995; Lazar et al., 2011,). They have been interpreted as cementation of reticulated cavity systems on carbonate mounds and most recently it was suggested to represent calcification

of siliceous sponge and organic matter diagenesis (Neuweiler et al., 2001). However no evidence of siliceous sponges is present in the BB facies. No physical sedimentary structures that suggest a continuous sediment drift or bioturbation were found in BB facies. The presence of micrite within the skeletal debris also indicates that these facies have been poorly washed and reworked. All the implications described above suggest that this facies could possibly correspond to an end-member of a Waulsortian-like bryozoan mound. Waulsortian mounds, described in many parts of the world, consists of bedded to massive, carbonate mud-rich, crinoidal-bryozoan-microbial facies surrounded by bedded, crinoidal packe-grainstones on the mound flanks, that deep steeply away from the mound core (Wilson, 1975).

Bryozoan reef mounds are common features in the geological record that occur within mid-ramp, slope paleoenvironments. Jobe and Saller (1995) describe the presence of similar early-cemented bryozoan boundstones showing characteristics of a bryozoan baffled network in the upper Harrodsburg limestone in the Illinois basin, and interpreted them as bryozoan mounds. Similar bryozoan mound facies in the Illinois and Williston basin have been called “platestones” in the past and are characterized by fenestral bryozoan plates in a loosely packed meshwork with ponded sediment and locally stabilized by isopachous cements (Burke and Lasemi, 1995). All of the ancient carbonate mounds are lithologically similar with bryozoans and crinoids as the dominant skeletal components. They are early cemented and they contain *stromatactis*-like structures. In modern environments bryozoan mounds occur on cool water areas with temperate carbonate sedimentation in upper slope settings, such as those described by James et al. (2000) in the Great Australian Bight. By comparison between previous studies and previous arguments, it leads us to interpret the bryozoan bafflestone as internal mound facies of a bryozoan mound deposit within the inner- and mid- ramp settings. With just one core it is difficult to conclude that

these are in-fact bryozoan mound deposits. Most studies rely on outcrop studies or well-log correlations to determine the presence of any concave up build-up, which is the most diagnostic criteria for, carbonate mounds.

Bryozoan packe/grainstone (BP/G)

Description: This facies is characterized by massive beds of packestones or grainstones composed of broken fragments of fenestrae bryozoans and crinoids with a minor component of brachiopods and ostracods (Fig. 20). Skeletal grains are in grain-support with inter-particle spaces cemented with isopachous calcite cements (Fig.20B). Micrite or peloidal sediments were not found in this facies. In contrast to the Bryozoan bafflestone, the fenestrate bryozoan fronds are broken and disoriented in a tightly packed and cemented mosaic (Fig. 16B). Individual beds may show sediment grading. This facies where only found in the *Delaney No. 1* core where they occur interbedded with bryozoan bafflestones (Fig. 7).

Interpretation: Bryozoan grainstones and packestones have been interpreted as flank facies of bryozoan mounds in the Illinois basin and Willinston basin (Jobe and Saller, 1995; Burke and Lasemi 1995). Bryozoan mound flank facies are dominated by resedimented material (mainly skeletal debris) broken off from the build-up and transported down the slope like small-scale debris flows (Giles, 1998). They are well-bedded and many show graded laminations. Contrary to the mound internal facies, flank facies are dominated by disarticulated grains, primarily bryozoans and crinoids.

Based on the association of bryozoan packe/grainstones to bryozoan bafflestones, it is interpreted that the grainstones represent episodic transport of broken skeletal grains from the edges of the mound. The lack of preserved skeletal fragments and the grain-supported fabric with

absence of mud indicates deposition by strong currents. Biohermal buildups keep up with the increase in water depth that results in the characteristic dome shape of bryozoan mounds, and the patch reef-like distribution in ramp settings. It is implicit that these mounds confronted storm waves that provided enough energy to break off skeletal constituents from the mound and winnowed the fine-grained sediments. Moreover, sediment grading also indicates episodical deposition of sediments by small-scale debris flows.

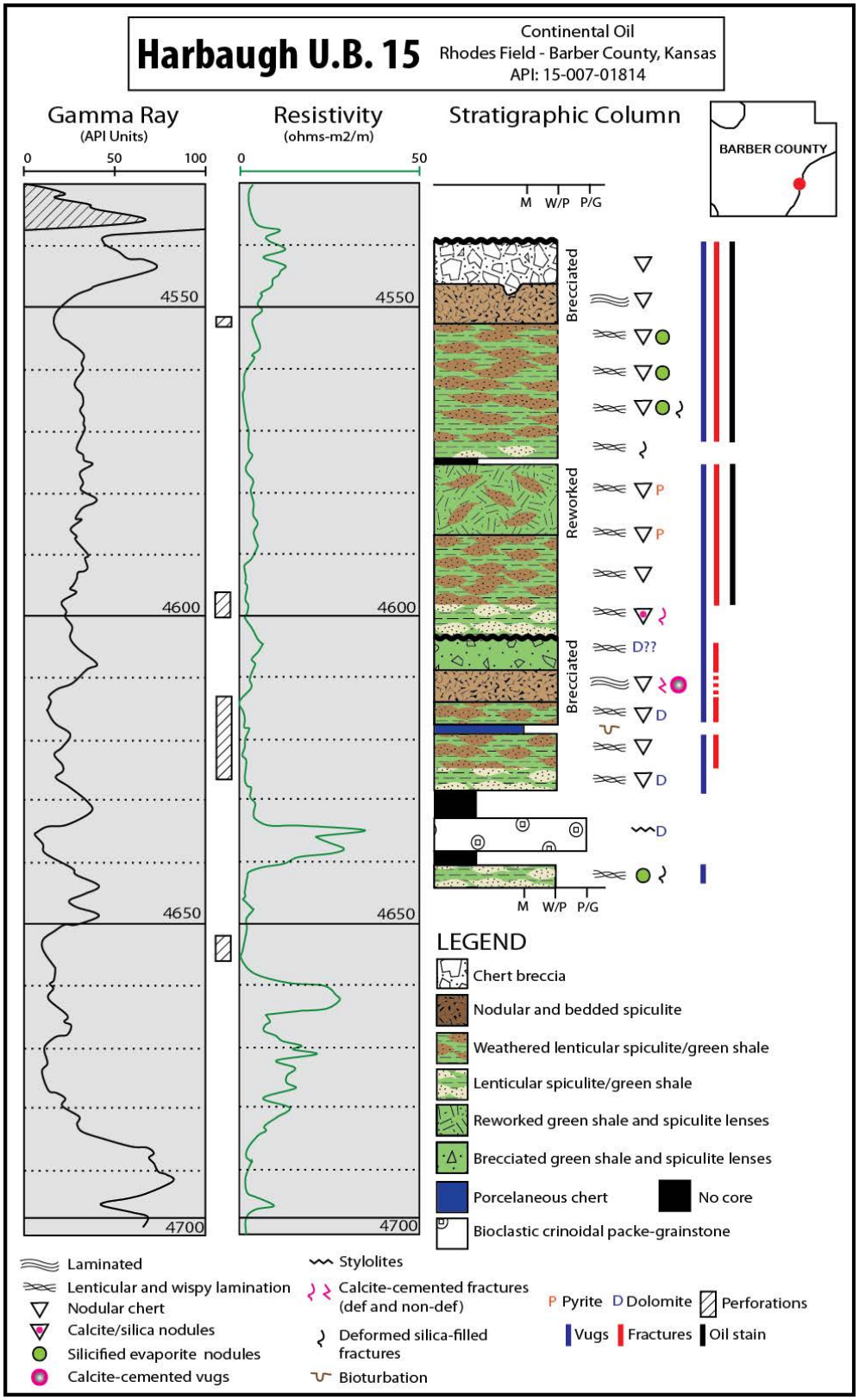

Figure 4. Well logs, lithofacies and diagenetic descriptions for well *Harbaugh U.B. 15* from the Rhodes field, Barber County, Kansas.

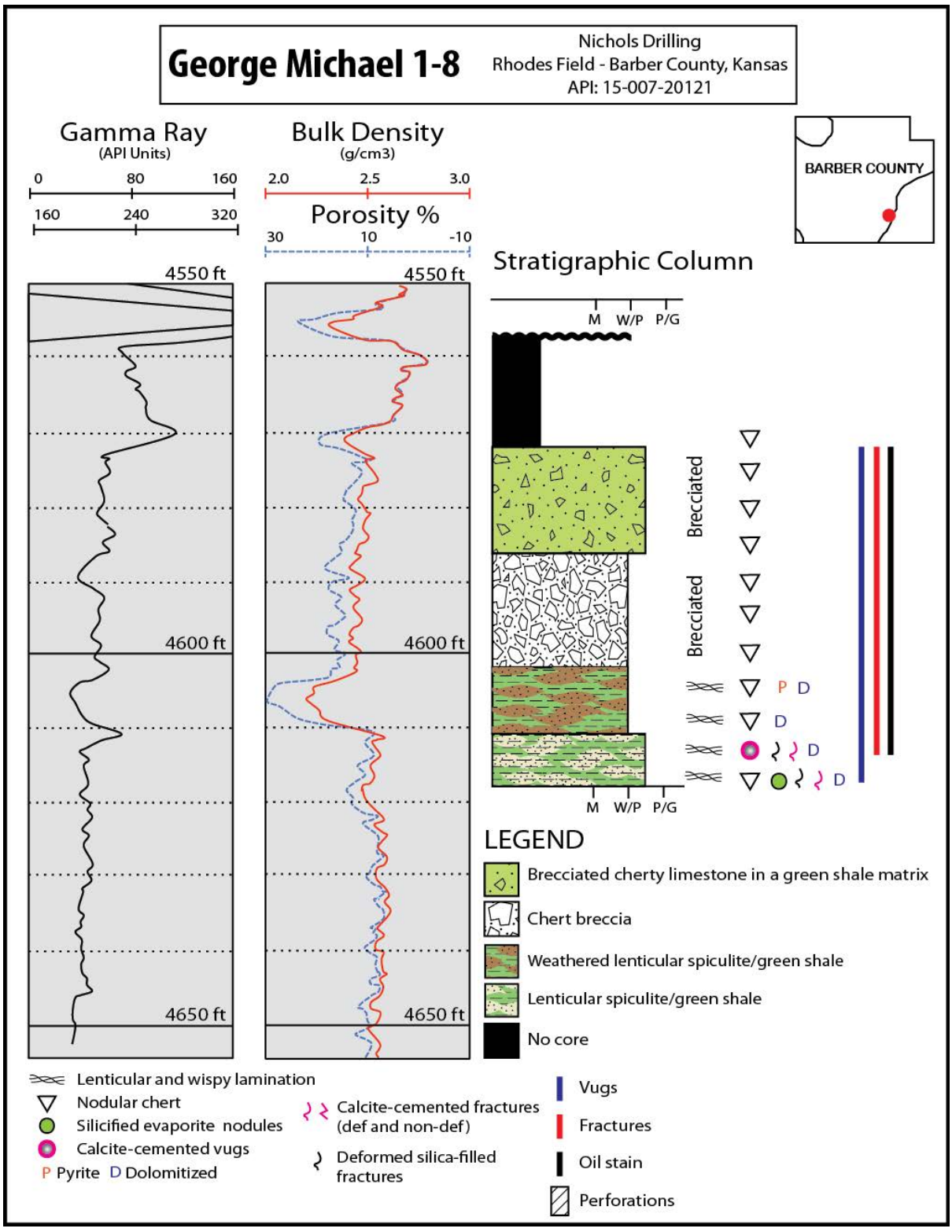

Figure 5. Well logs, lithofacies and diagenetic descriptions for well *George Michael 1-8* from the Rhodes field, Barber County, Kansas.

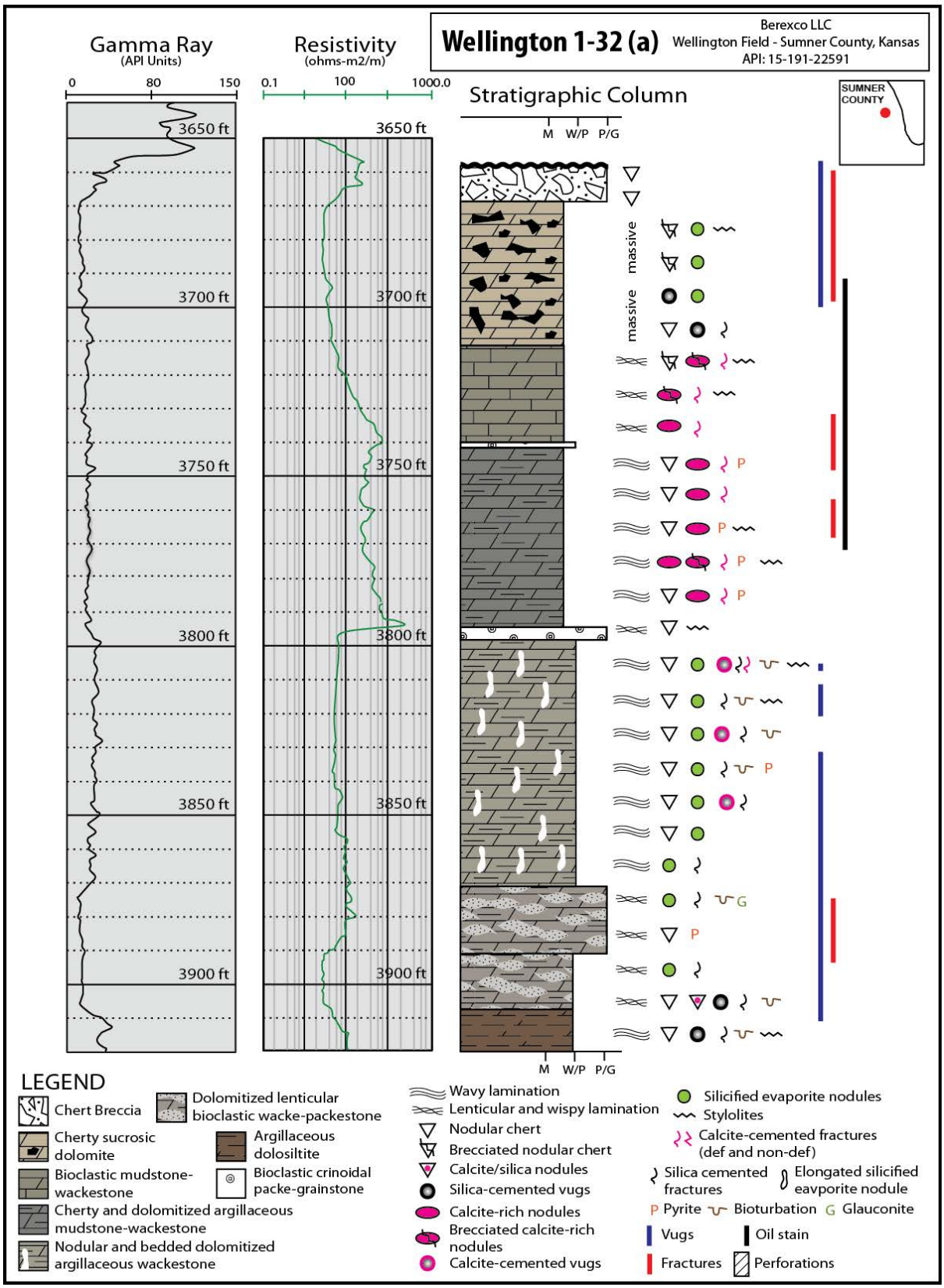
Wellington 1-32 (a)
Berexco LLC
Wellington Field - Sumner County, Kansas
API: 15-191-22591
Gamma Ray
(API Units)
0
80
150
Resistivity
(ohms-m2/m)
0.1
100
1000.0
Stratigraphic Column
M W/P P/G
SUMNER COUNTY
3650 ft
3700 ft
3750 ft
3800 ft
3850 ft
3900 ft
massive
massive
P
G
LEGEND
Chert Breccia
Dolomitized lenticular bioclastic wacke-packestone
Cherty sucrosic dolomite
Argillaceous dolosiltite
Bioclastic mudstone-wackestone
Bioclastic crinoidal packe-grainstone
Cherty and dolomitized argillaceous mudstone-wackestone
Nodular and bedded dolomitized argillaceous wackestone
Wavy lamination
Lenticular and wispy lamination
Nodular chert
Brecciated nodular chert
Calcite/silica nodules
Silica-cemented vugs
Calcite-rich nodules
Brecciated calcite-rich nodules
Calcite-cemented vugs
Silicified evaporite nodules
Stylolites
Calcite-cemented fractures (def and non-def)
Silica cemented fractures
Elongated silicified eavporite nodule
P Pyrite
Bioturbation
G Glauconite
Vugs
Oil stain
Fractures
Perforations

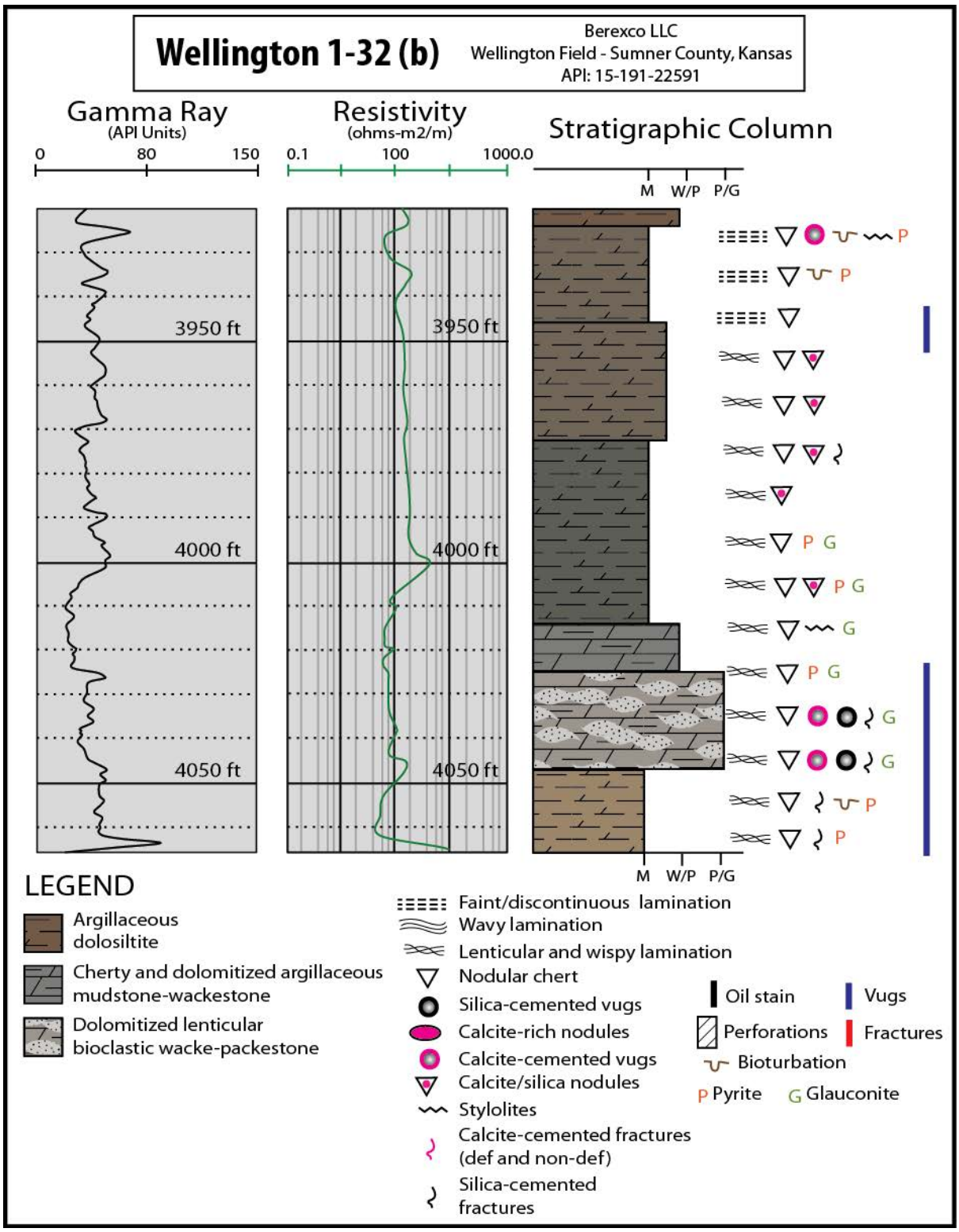

Figure 6. Well logs, lithofacies and diagenetic descriptions for well *Wellington 1-32* from the Wellington field, Barber County, Kansas.

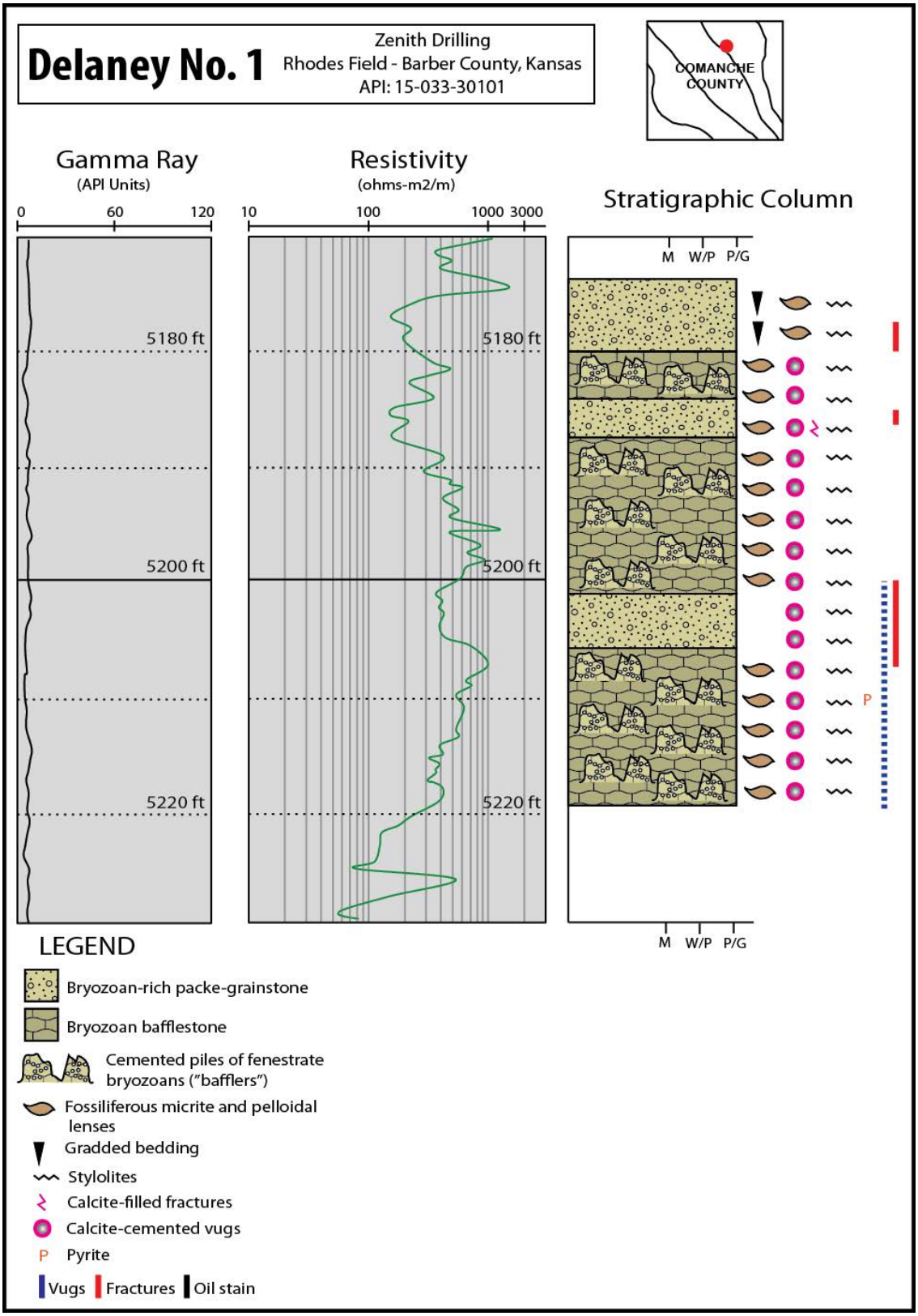

Figure 7. Well logs, lithofacies and diagenetic descriptions for well *Delaney No.1*; "wildcat well", Barber County, Kansas.

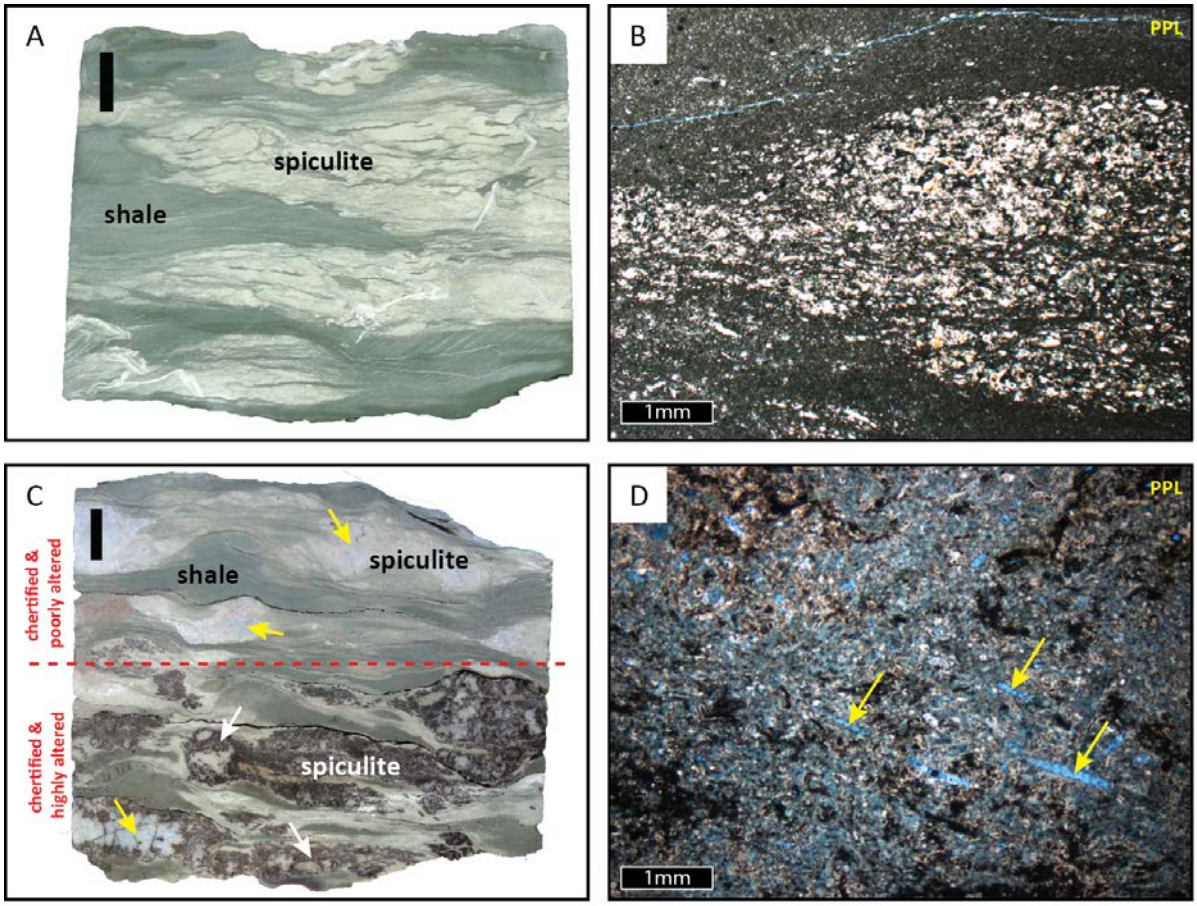

Figure 8. Scale bar on slab photos is 1 cm. **A**) Core slab of interbedded green shale and lenticular spiculite wacke/packestone. Note that the green shale looks wispy laminated inside the spiculite lenses. Spiculite lenses result from winnowing of siliceous-sponge spicule debris by waves creating small pods where the coarse material accumulates. (*Harbaugh U.B.15, 4642 ft*). **B**) Photomicrograph of illustrating a lens of sponge spicule debris surrounded by the green shale matrix. Note that the lens consists of disarticulated and broken siliceous-sponge spicules. The original hollow siliceous spicules are cemented and replaced with microcrystalline quartz. (*Harbaugh U.B.15, 4643 ft*). **C**) Core slab of interbedded green shale and lenticular spiculite wacke/packestone. This sample is similar to A but it has undergone significant diagenetic alteration. Pervasive silicification of spiculite lenses results in the formation of chert nodules (yellow arrows). After weathering and possibly hydrothermal alteration of the chert nodules, they generate extensive micro-porosity trough dissolution and etching of the silica matrix. Some refer to this micro-porous chert texture (white arrows) as tripolite (Costello et. al 2012; Ramaker et al., 2014). (*Harbaugh U.B.15, 4594 ft*). **D**) Photomicrograph illustrating a highly porous spiculite lens after leaching of siliceous-sponge spicules (yellow arrows) and the cherty matrix. Note that after impregnation with blue epoxy the micro-porous chert sections get are stained blue. (*Harbaugh U.B.15, 4566 ft*).

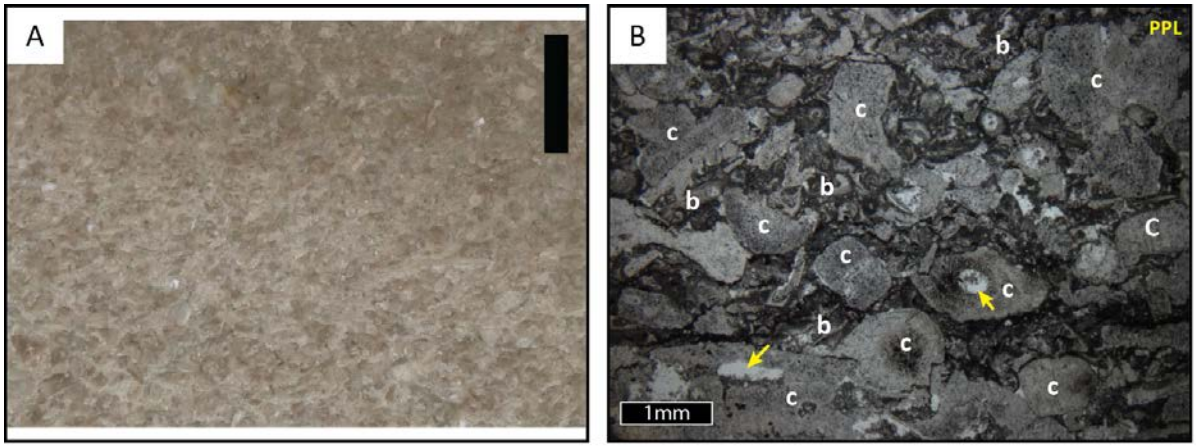

Figure 9. Scale bar on slab photos is 1 cm. **A**) Polished core slab of a boiclastic crinoidal packe/grainstone. Note the grainy texture of the rock that is dominated by skeletal fragments, primarily crinoids and bryozoans. (*Harbaugh U.B.15, 4634 ft*). **B**) Photomicrograph of bioclastic crinoidal packe/grainstone. The rock consists of tightly packed, moderately sorted skeletal debris, mostly crinoids (c) and bryozoans (b). A large part of the skeletal grains is replaced with syntaxial calcite that occluded a lot of the original porosity in the rock (yellow arrow). (*Harbaugh U.B.15, 4635 ft*).

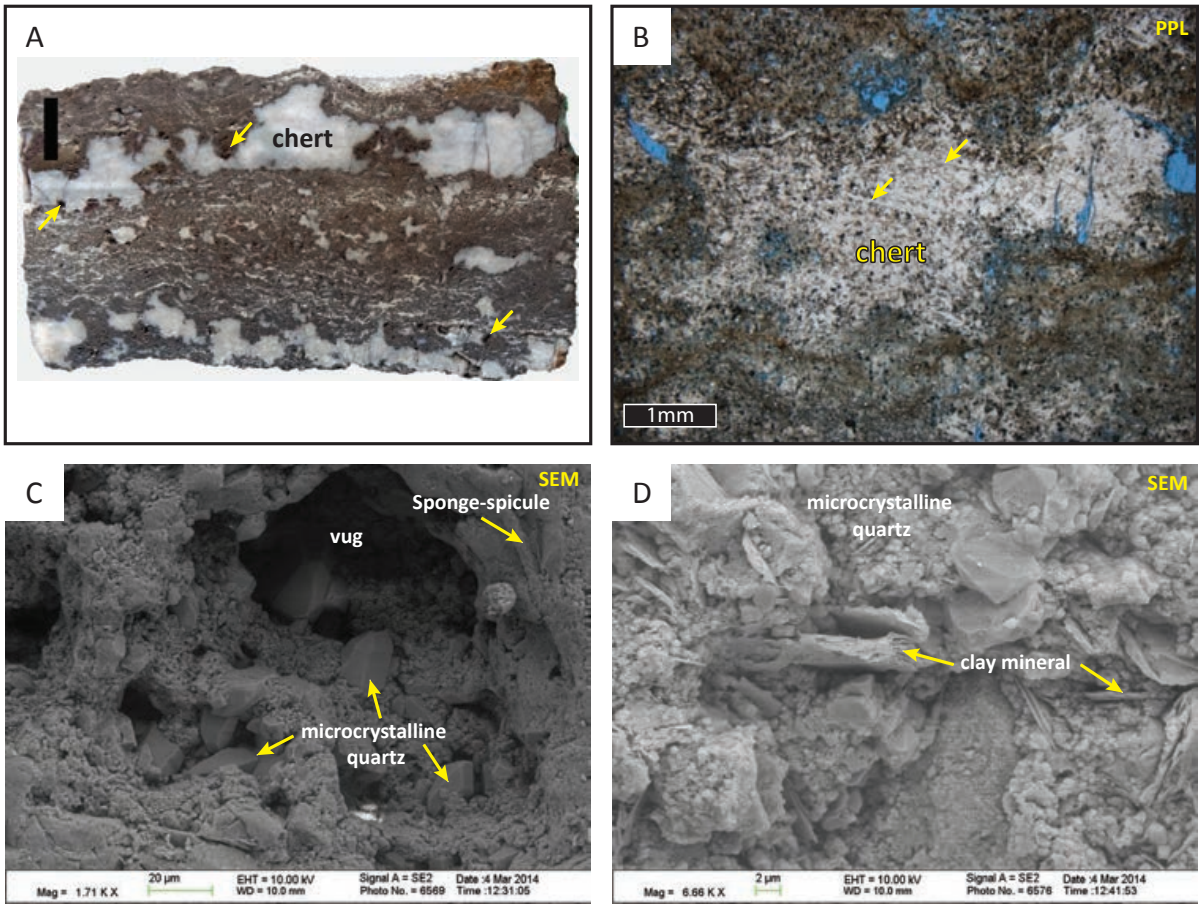

Figure 10. Scale bar on slab photos is 1 cm. **A**) Core slab of a nodular and bedded cherty spiculite. The convoluted chert nodules with a grayish mottled texture and faint cross laminations represent remnants of a dense chert after extensive weathering and dissolution. A large amount of vuggy porosity (yellow arrows) is also present. (*Harbaugh U.B.15, 4612ft*). **B**) Photomicrograph of an anastomosing chert nodule. The nodule consists of tightly packed siliceous-sponge spicules (yellow arrows) that are now difficult to discern from one another after extensive replacement with microcrystalline quartz. Also note the abundance of vuggy porosity and some micro-porosity. (*Harbaugh U.B.15, 4614 ft*). **C)** Scanning electron microscope photomicrograph bedded cherty spiculite. The illustration shows the abundance of microcrystalline quartz found inside the vuggy porosity surrounding a chert nodule. Also shown is the a remnant of a sponge spicule after extensive silicification and dissolution. (*Harbaugh U.B.15, 4553 ft*). **D)** Scanning electron microscope photomicrograph bedded cherty spiculite. The illustration shows the dark brown matrix composed mainly of microcrystalline quartz and silicified clay minerals. (*Harbaugh U.B.15, 4553 ft*).

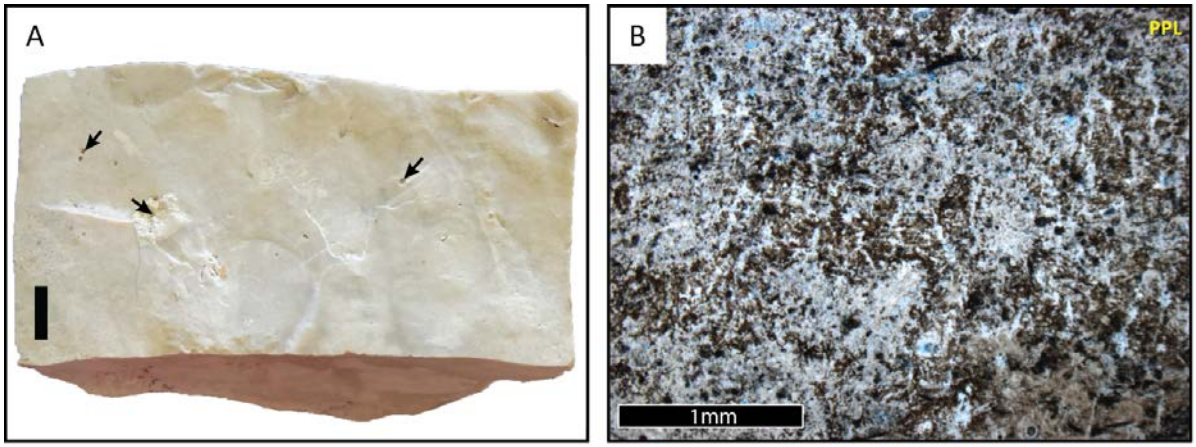

Figure 11. Scale bar on slab photos is 1 cm. **A**) Core slab of porcelaneous chert. It is characterized by a hard and dense chert with a grayish white, dull and matte surface texture. Vuggy porosity is indicated with the arrows. (*Harbaugh U.B.15, 4618 ft*). **B**) Photomicrograph of porcelaneous chert. Siliceous sponge-spicules silhouettes ("ghosts") can be identified on a microcrystalline and cryptocrystalline quartz matrix. Note that some sections are micro-porous. (*Harbaugh U.B.15, 4614ft*).

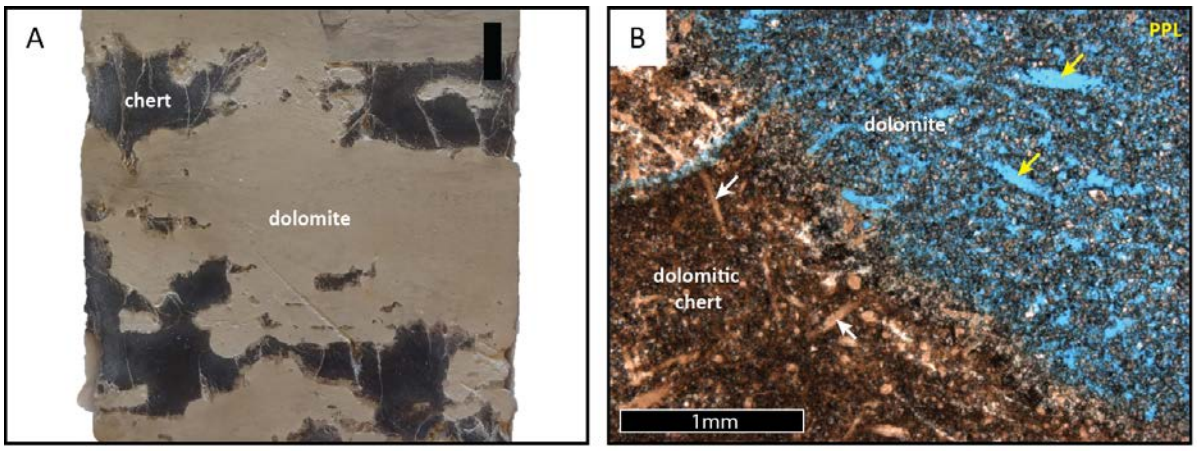

Figure 12. Scale bar on slab photos is 1 cm. **A)** Core slab of a cherty sucrosic dolomite. Sedimentary features have been masked during dolomitization. Convoluted dark gray chert nodules are scattered in the matrix and appear autobrecciated (*Wellington 1-32, 3671 ft*). **B)** Photomicrograph of cherty sucrosic dolomite. Note the large amount of intercrystalline pores and moldic pores (yellow arrows) after siliceous-sponge spicules. The chert nodules are partially replaced with dolomite and the sponge-spicules inside the nodules (white arrows) are preserved with microcrystalline quartz. Porosity is low inside the chert nodules (*Wellington 1-32, 3671.8 ft*).

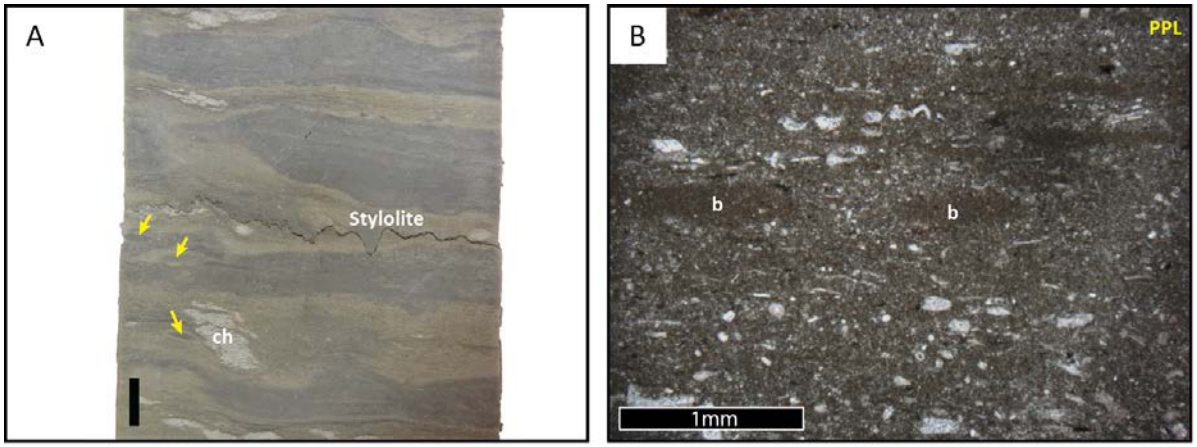

Figure 13. Scale bar on slab photos is 1 cm. **A)** Core slab of a bioclastic mudstone/wackestone with alternating dark gray and olive gray cm-scaled wavy discontinuous bedding. *Phycosiphon* burrows filled with darker sediment (yellow arrows) are deformed to oval shapes as a result of sediment compaction. Tripolitic chert (ch) lenses are also found. (*Wellington 1-32, 3714 ft*). **B**) Photomicrograph of bioclastic mudstone-wackestone. Note the presence dissarticulated skeletal debris scattered on a micrite matrix. Oval-shaped, fine-grained lenses are *Phycosiphon* burrows (b). (*Wellington 1-32, 3724.5 ft*).

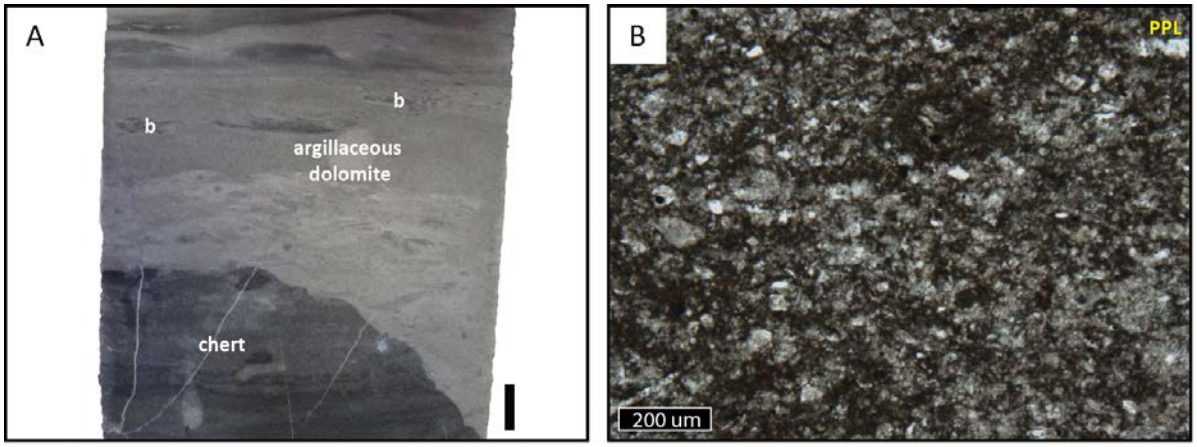

Figure 14. Scale bar on slab photos is 1 cm. **A**) Core slab of a cherty and dolomitized argillaceous mudstone/wackestone. Note the dark gray chert nodule at the bottom of the sample preserving the wavy laminations that can be traced outside the nodule. Patches of *Phycosiphon* burrows (b) rework the sediments and creates breaks in the laminations. (*Wellington 1-32, 3779 ft*). **B**) Photomicrograph of the matrix in CDAM/W facies illustrating the abundance of euhedral dolomite rhombs lying on an argillaceous matrix. (*Wellington 1-32, 3772.3 ft*).

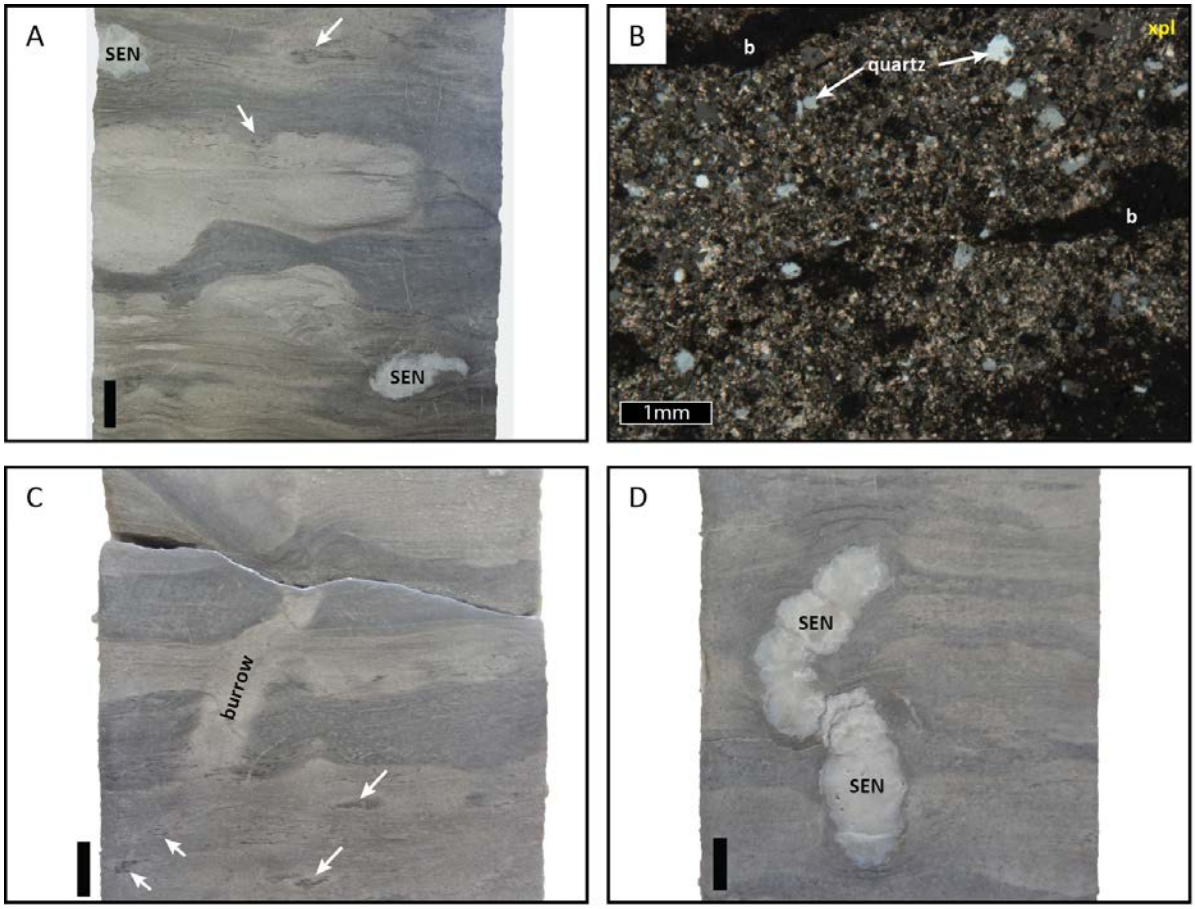

Figure 15. Scale bar on slab photos is 1 cm. **A**) Core slab of nodular and bedded dolomitized argillaceous wackestone. The bedding is present as cm-scaled wavy beds alternating in color from light to dark gray. Wispy laminations can also be identified. Silicified evaporite nodules (SEN) are found scattered in the matrix and they range widely in size (mm- to cm-sized). *Phycosiphon* burrows are pointed with the arrows. (*Wellington 1-32, 3808 ft*). **B**) Photomicrograph of the matrix NBDAW facies illustrating the silt-sized sub-rounded quartz grains and dolomite rhombs that are enclosed in a clay matrix. Burrowed (b) sections in the matrix are also observed. (*Wellington 1-32, 3807.5 ft*). **C**) Core slab of nodular and bedded dolomitized argillaceous wackestone. In this slab a vertical, cylinder-like burrow, possibly *skolithos* or *planolites* is cross-cutting the sediment beds. *Phycosiphon* burrows are pointed with the white arrows. (*Wellington 1-32, 3817 ft*). **D**) Core slab of nodular and bedded dolomitized argillaceous wackestone. In this sample various SEN are arranged in a vertical pattern that seems to previously be a burrow. Numerous examples like this one occur on this facies, and it is possible that burrowed sections where the preferred paths for evaporative fluids to precipitate nodular evaporites. Note the characteristic "chicken wire" texture of the nodules. (*Wellington 1-32, 3816 ft*).

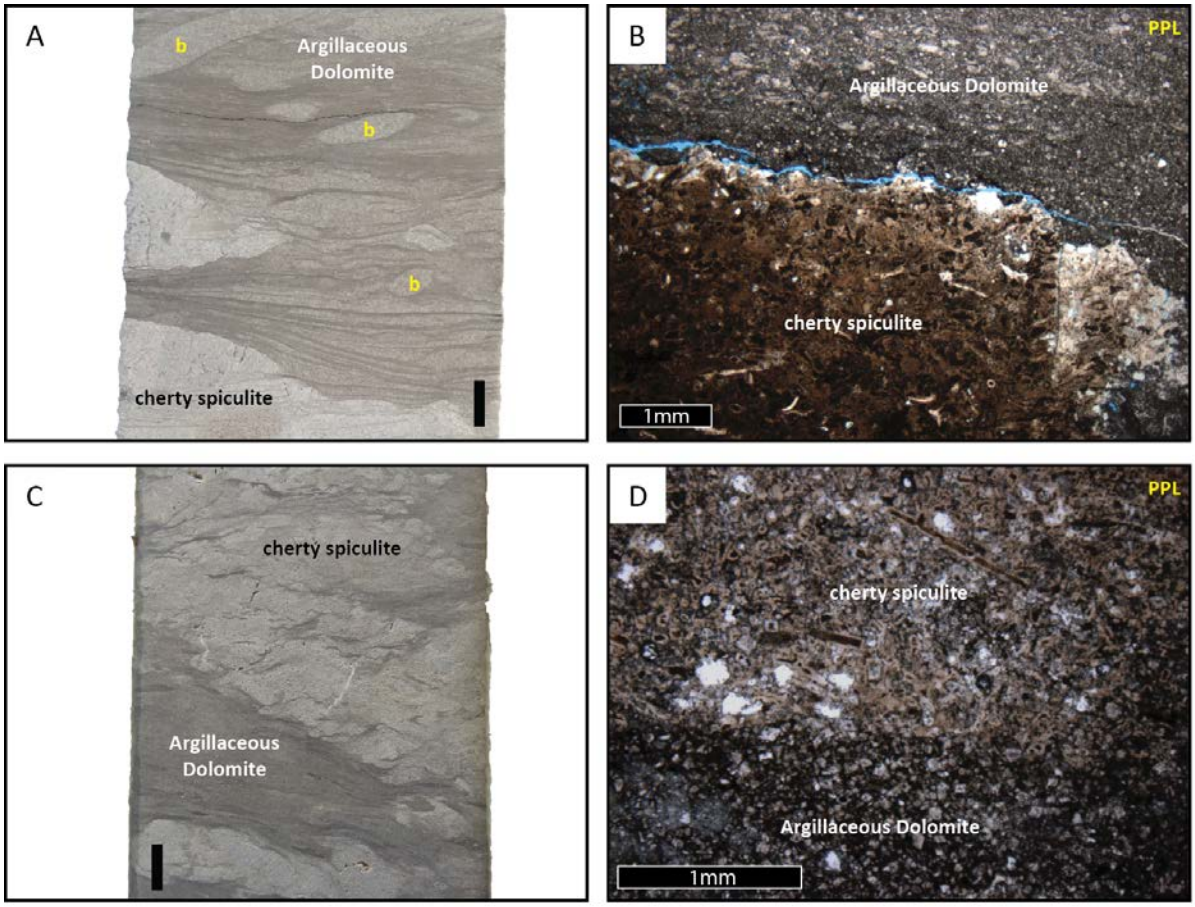

Figure 16. Scale bar on slab photos is 1 cm. **A**) Core slab of dolomitized lenticular bioclastic wacke/packestone. Lentcular beds of cherty spiculite are scattered in an argillaceous dolomite matrix that is laminated. Burrow (b) structures occurs as elliptical shaped sub-vertical coarse-grained patches and are probably *planolites*. (*Wellington 1-32, 3886 ft*). **B**) Photomicrograph of dolomitized lenticular bioclastic wacke/packestone. This section shows the contact between the argillaceous dolomite matrix (top) and a cherty spiculite lens (bottom). Note that the spiculite lens is highly chertified and poorly dolomitized. In the other hand, the argillaceous lime-mud matrix is highly dolomitized. (*Wellington 1-32, 3872.75 ft*). **C**) Core slab of dolomitized lenticular bioclastic wacke/packestone. Similar to C but it is found deeper in the same core. (*Wellington 1-32, 4033 ft*). **D**) Photomicrograph of dolomitized lenticular bioclastic wacke/packestone. This section shows the contact between the argillaceous dolomite matrix (bottom) and a cherty spiculite lens (top). Note the lenses are dominated by siliceous-sponge spicule debris. (*Wellington 1-32, 4045.9 ft*).

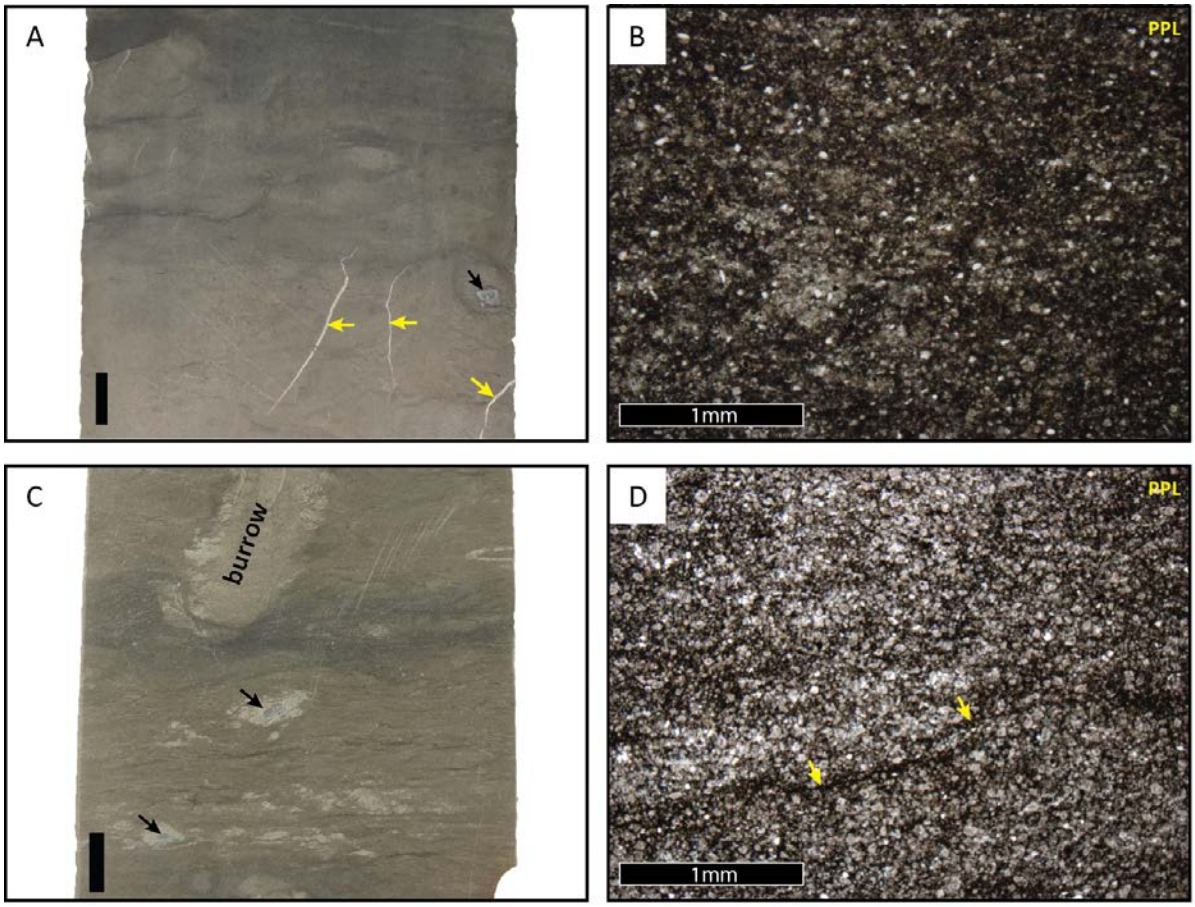

Figure 17. Scale bar on slab photos is 1 cm. **A**) Core slab of an argillaceous dolomite. Note the faintly wavy laminated texture. Chert nodules (black arrow) are found in this facies but are usually less than 2 cm big. White vertical streaks are chertified fractures (yellow arrows). (*Wellington 1-32, 3972 ft*). **B**) Photomicrograph of an argillaceous dolomite. Note that this facies are very tight and consists of silt-sized quartz and euhedral to subhedral dolomite rhombs in an argillaceous matrix. (*Wellington 1-32, 3967.4 ft*). **C**) Core slab of an argillaceous dolomite. Note the presence of vertical burrows and scattered cherty spiculite lenses (black arrows). (*Wellington 1-32, 4054 ft*). **D**) Photomicrograph of an argillaceous dolomite. Note that horsetail dissolution seams can be identified in thin sections and they sometimes impart laminations (yellow arrows). (*Wellington 1-32, 4052.9 ft*).

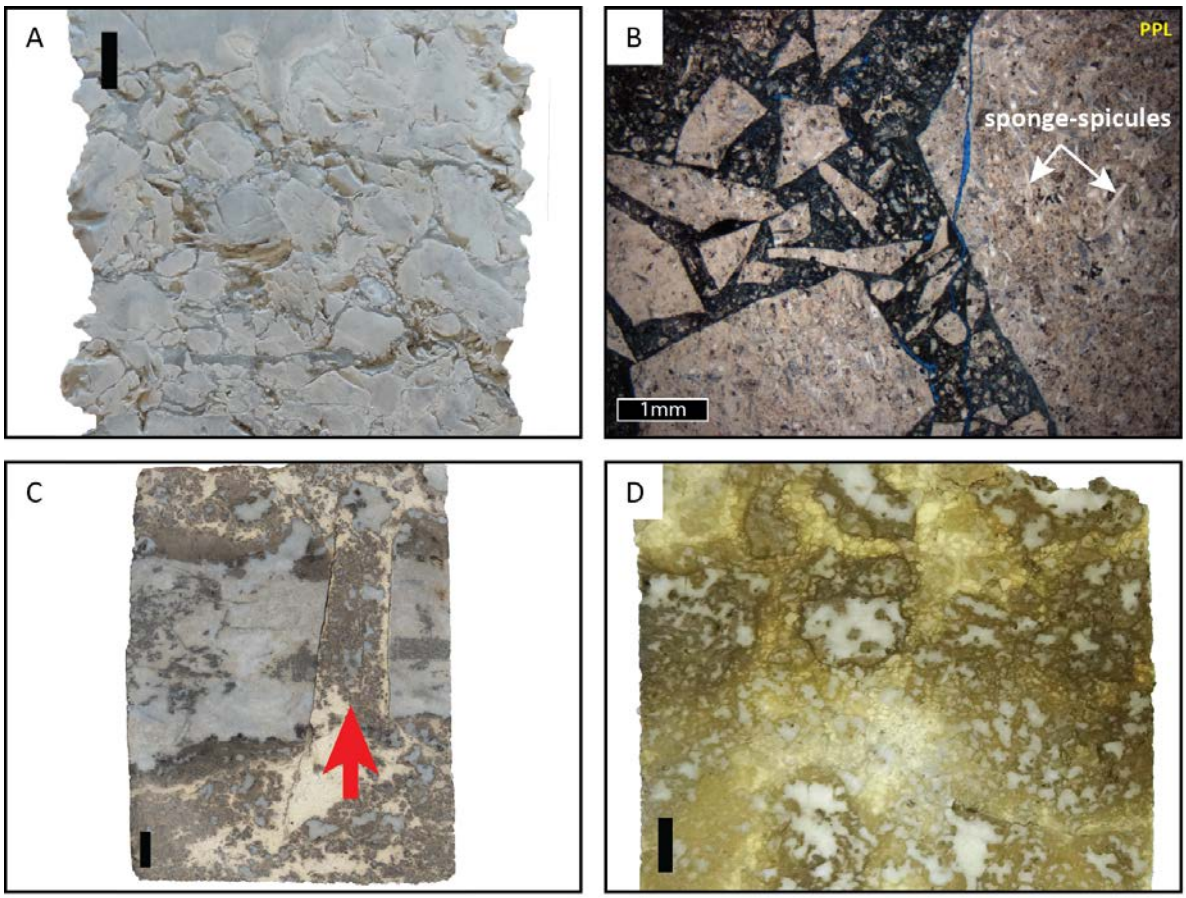

Figure 18. Scale bar on slab photos is 1 cm. **A**) Core slab of a chert breccia. This breccia consists of grain-supported angular to sub-angular chert clasts on a shaly matrix. (*Wellington 1-32, 3668 ft*). **B**) Photomicrograph of a breccia consisting of angular cherty spiculite clasts floating on a silicified clay matrix. (*Harbaugh U.B.15, 4588 ft*). **C**) Core slab of a chert breccia. Note the abundance of chert clasts varying largely in size and floating on a clay-rich matrix. Autobrecciation is suggested from the large gray mottled clast that has fractured but remains relatively in-place. The fracture is filled with brecciated material (red arrow). (*George Michael 1-8, 4592 ft*). **D**) Core photograph of a chert breccia consisting of grain-supported angular to sub-angular chert clasts on a clayey silicified matrix. (*Harbaugh U.B.15, 4547 ft*).

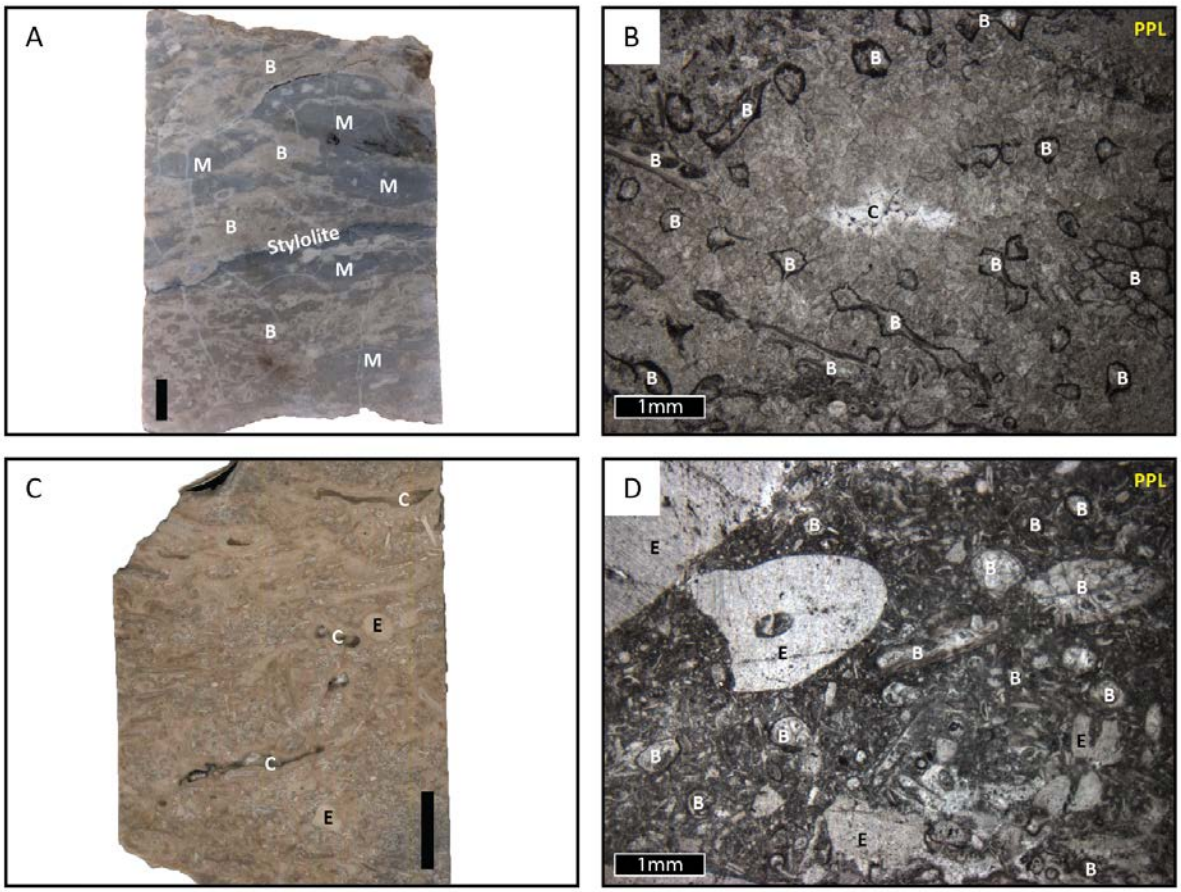

Figure 19. Scale bar on slab photos is 1 cm. **A**) Core slab of a bryozoan bafflestone. Note the patchy texture of these facies consisting of in-place cemented bryozoans (B) with interstitial pods of bioclastic wacke-packestones (M). (*Delaney no. 1, 5202 ft*). **B**) Photomicrograph showing fenestrate bryozoan plates piled-up and cemented with isopachous radial fibrous to bladded calcite. Early calcite cementation of amalgamated bryozoan plates results in the formation of sediment barriers ("bafflers") where the bioclastic sediment is trapped. (*Delaney no. 1, 5181 ft*). **C**) Polished core slab of a bryozoan bafflestone. Note the presence of scattered crinoid fragments (E) and sparry calcite masses (C) that resembles *stromatactis*. (*Delaney no. 1, 5217 ft*). **D**) Photomicrograph showing a bioclastic wacke-packestones pods. Pods consists of skeletal debris in a micrite or pellodial matrix. Skeletal grains are mostly fenestrate bryozoans (B) and crinoids (E) with a minor component of brachiopods and ostracods (*Delaney no. 1, 5195 ft*).

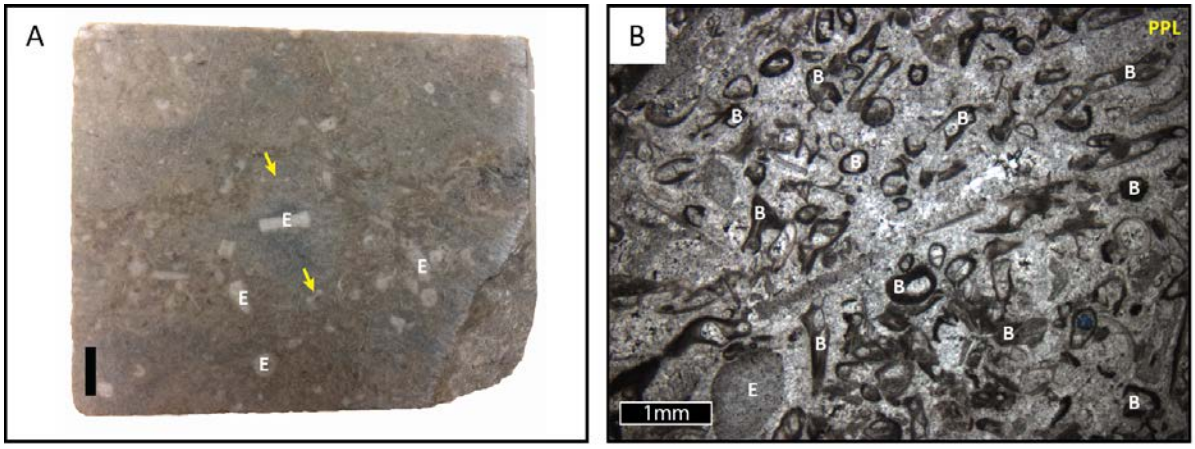

Figure 20. Scale bar on slab photos is 1 cm. **A**) Core slab of a bryozoan packe/grainstone. Crinoid fragments (E) and fenestrate bryozoans (yellow arrows) are the main skeletal grains in this facies and are easily identifiable in hand-sample. (*Delaney no. 1, 5214 ft*). **B**) Photomicrograph showing a bryozoan packestone composed of broken fragments of fenestrate bryozoans (B) and crinoids (E) in various orientations. (*Delaney no. 1, 5205 ft*).

SECTION 2. STRATIGRAPHIC SETTING

The different lithofacies described on core belong to distinct sections of the Mississippian carbonate ramp, each with its own characteristic paleogeographic and sedimentologic conditions. The stratigraphic setting of each core within the ramp (Fig. 21) was established from core-to-well log correlations and the distribution of different lithofacies described above.

Harbaugh U.B. 15 and George Michael 1-8

The *Harbaugh U.B. 15* and *George Michael 1-8* cores are found in the Rhodes field in Barber County, Kansas just south of the Pratt anticline (Fig. 1). Both cores comprise similar Mississippian lithofacies including: lenticular spiculite wacke/packestone with corresponding shaly interbeds, bioclastic crinoidal packe/grainstone, nodular and bedded cherty spiculite, porcelaneous chert, and chert breccias. Continental Oil Co. drilled the *Harbaugh U.B. 15* well in T33S R11W, Sec. 32 C SW SE NW in Barber County, Kansas (Fig. 1). Nichols Drilling Co. drilled the *George Michael 1-8* well in T34S R11W, Sec. 8 C NE SW in Barber County, Kansas (Fig. 1). Correlating of type logs logs to both cores indicates that the cored strata belong to the Osage stage in the Mississippian (Fig. 21 and 22). The interpreted facies in both cores corresponds to the Cowley Formation, dated by Mazzullo and others (2009) as late Osagean to early Meramecian according to stratigraphic relationships and positioning.

The Cowley Formation is restricted to an east-west belt 15 to 75 miles wide north of the Oklahoma border in south-central Kansas (Goebel, 1968). It is an unconformity-bounded unit that overlies Osagean limestones and cherts, and underlies Meramecian strata (Mazzullo et al., 2009). A cherty, tripolitic, fine-grained limestone rich in sponge-spicules that's commonly interbedded with shale or siltstones and is locally dolomitic characterizes the Cowley Formation

(Mazzullo et al., 2009; Evans and Newell, 2013). Deposition of the Cowley represents a period during which carbonate deposition was mostly suppressed by deposition of a thick section of spiculites on shallow- to deep-water settings of the ramp (Mazzullo et al., 2009). The Cowley Formation is described as a coarsening and thickening upward unit that gradually changes from dark grey to green shales and finally to bedded spiculites in a distal-to-proximal direction (Mazzullo et al., 2009). These gradations are concurrent with increasing abundance upward of spiculite material relative to shale, and represent sedimentological signatures of shallowing-upward facies tracts.

The Cowley Formation in the cores is dominated by variably tripolitic cherty spiculites interbedded with green shales, and local thin interbeds of bioclastic limestones. These facies are variably dolomitized but never pervasively. The Formation is capped by a residual chert breccia, also known as the "chat", which represents post-depositional erosion and weathering (Montgomery et al., 1998; Watney et al., 2001; Mazzullo et al., 2009; Evans and Newell, 2013). The distribution of the "chat" is manifested by the high-porosity and low resistivity interval at the top-most section of the Mississippian (Fig 22). An increase of chert towards the "chat" was observed in the cores and compositional partitioning of well logs also indicates a similar trend (Fig. 22). In contrast, most of the lower unit consists of dolomitic cherty limestones that are increasingly shaly with depth (Fig. 22). It can be inferred from compositional partitioning of well logs that the section becomes gradually more dolomitic and shaly in a down-dip trend. The same can be inferred from the cores described in Rhodes field, where only the distal core (*George Michael 1-8*) showed an identifiable amount of dolomite and only in the lowest portion of the core. The predominance of green shale and the presence of lenticular, nodular and bedded cherty spiculites close to "chat" intervals, suggest that the strata described in the *Harbaugh U.B. 15* and

George Michael 1-8 cores corresponds to the shallowest facies (inner- to mid-ramp) of a spiculite-dominated carbonate ramp.

Wellington 1-32

The *Wellington KGS 1-32* core was drilled as part of an intensive characterization and modeling effort at the Wellington Field to evaluate suitability for CO_2-enhanced oil recovery in the Mississippian and CO_2 storage in the underlying Arbuckle strata supported by US Department of Energy contract DE-FE0002056. The well was drilled by Berexco LLC on T31S R1W, Sec. 32 NE SW NE NE in Sumner County, Kansas and the complete Mississippian section (top to bottom) was cored from 3658 ft to 4064 ft. In the *Wellington KGS 1-32* core, the Kinderhookian and Osage are missing due to erosion (Watney personal com.) but are comprised of argillaceous dolosiltite that rests unconformably on the Simpson Group (*Fig 23*). The Mississippian at Wellington is entirely Meramec age and may include younger Chesterian-age strata (Watney, personal com.). The strata believed to be a variation of "Cowley Formation" equivalent strata comprised of various lithofacies including: chert breccia, cherty sucrosic dolomite, bioclastic mudstone/wackestone, dolomitized lenticular boclastic wacke/packestone and the three variables of dolomitic argillaceous facies (*cherty and dolomitized argillaceous mudstone/wackestone*, *nodular and bedded argillaceous wackestone*, *and argillaceous dolomite*). All the lithofacies throughout the entire Mississippian section of the *Wellington* core are dolomitized and chertified to some degree with the majority being pervasively dolomitized. This is in contrast to the less dolomitic tripolitic cherts described in the cores at Rhodes field in Barber County, Kansas.

The Mississippian strata in the Wellington field has been interpreted by Watney et al. (2013) as a succession of shallowing upward parasequences, each capped by the porous and less argillaceous dolomitized lenticular boclastic wacke/packestone lithofacies. These sediments accumulated and thickened on top of a paleotopographic high on a structural trend that lies approximately 20 miles west of the Nemaha Uplift (Fig. 1; Watney et al., 2013). No evidence of subaerial exposure is found throughout the entire Mississippian section in the *Wellington KGS 1-32*. The only exception is the uppermost portion, equivalent to the weathered "chat", where the sedments have been karstified and brecciated during the end of the Mississippian. Unlike the Mississippian strata in the vicinity of the Pratt anticline where the "chat" are the main pay zone, in the Wellington field the porous strata are confined to the higher topographic areas in the thicker dolomitic facies. A 20 ft thick cherty sucrosic dolomite with high intercrystalline porosity (30% porosity) found directly below the "chat" is the main pay zone in the Welligton field (Watney et al. 2013). Two additional porous intervals of spicultic packstone are present below this pay zone, the middle zone being wet and the lowermost zone near the base of the Mississippian with oil saturation. The increase in porosity (neutron porosity) observed in the lowermost shaly section is not considered effective porosity because clay and shales tend to increase the response of neutron logs.

The erosion at the base of the Mississippian in the Wellington KGS 1-32 core may be localized in the axis of the Sedgwick basin. The shaly strata that accumulated along the lower ramp may have bypassed high reaches of the shelf when they more frequently exposed. The strata in the *Wellington KGS 1-32* are correlated to the Cowley Formation, but are younger (Meramec or possibly Chester in age) than the strata that Mazzullo and others (2009) described as the Cowley limited to post-Osage and pre-Mermec. Evidence for this includes time-

equivalence of the strata (Fig 23), the predominance lithofacies that indicate the presence widespread siliceous-sponge colonies and the presence of disseminated glauconite grains that are characteristic of the Cowley Formation in southeastern Kansas (Goebel, 1968). In comparison to the Cowley depositional model from Mazzullo and others (2009), the lithofacies described in the *Welllington KGS 1-32* corresponds to the deepest facies (mid- to outer-ramp) of a spiculite-dominated carbonate ramp.

Delaney No. 1

Zenith Drilling Corp. drilled the *Delaney No. 1* well in T31S R18W, Sec. 36 C NE NW of Comanche County, Kansas (Fig. 1). The well is considered a "wildcat" well, meaning that it does not lie within a specific oil and gas field. The cored interval covers the Mississippian from 5172 ft to 5220 ft deep and comprises two lithofacies: Bryozoan bafflestone and Bryozoan packe/grainstones. Both of this facies are believed to be representative of bryozoan mounds that were common during the early and mid Mississippian (Harbaugh, 1957). On geo-logs interpreted by Zenith Drilling Corp., these lithologies were described as "unusual" for the Osage, and possibly representing localized "bioherms?". The *Delaney no. 1* core sits on the uppermost ramp where the shelf breaks (Fig 25). Correlation of the *Delaney No. 1* to surrounding type logs suggests that the stratigraphic section in the core belongs to the Osage (Fig. 24).

The Osage Limestone on the studied region dramatically thins towards the central Kansas uplift where it disappears and undergoes a change from cherty, argillaceous "Cowley" facies to shelf carbonate. Contrary to the "Cowley" facies, the lithofacies described in *Delaney No. 1* core contained no dolomite and only a few fossils appeared silicicified. Based on lithofacies interpretation suggesting the presence of bryozoan mounds and the relative up-dip ramp setting,

the cored section is interpreted as a local bioherm that developed along the inner ramp flexure prior to Cowley deposition. These bioherms resulted in local buildups that were eventually covered by the Cowley deposition. The location of bryozoan mounds within the paleoramp indicates that they were a potential source for deposition of resedimented carbonates (bioclastic facies) that are found in down-dip sections equivalent to the Cowley Formation.

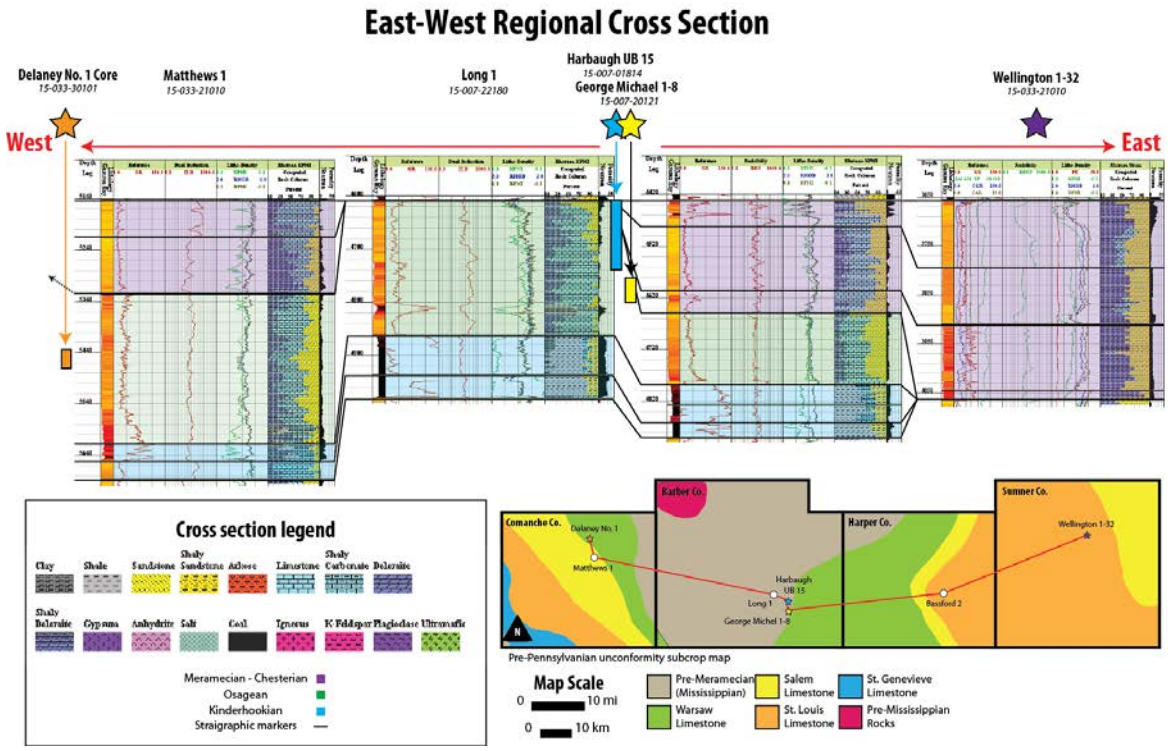

Figure 21. East-west trending cross section in south-central Kansas (Comanche, Barber, Harper and Sumner Co.) showing the structural, stratigraphic and petrophysical character of the Mississippian. The approximate stratigraphic position of the Mississippian interval studied in cores is shown (orange star and orange rectangle – *Delaney No. 1*; blue star and blue rectangle – *Harbaugh UB 15*; yellow star and yellow rectangle – *George Michael 1-8*; purple star – *Wellington 1-32*). Cross section is flattened to the Mississippian top. Well logs are not to scale. All well logs are modified versions from Kansas Geological Survey online databases (<*http://maps.kgs.ku.edu/co2/*> and <*http://www.kgs.ku.edu/PRS/Ozark/Summary/*>).

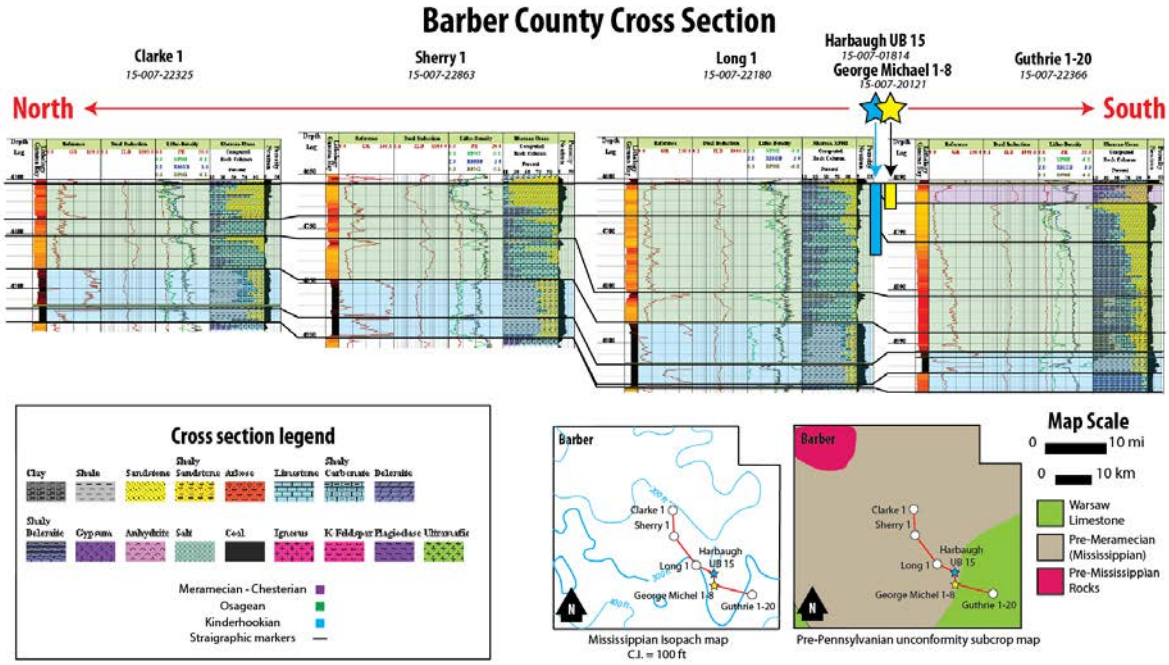

Figure 22. North-south trending cross section in Barber County showing the structural, stratigraphic and petrophysical character of the Mississippian. The approximate stratigraphic position of the Mississippian interval studied in cores is shown (blue star and blue rectangle – *Harbaugh UB 15*; yellow star and yellow rectangle – *George Michael 1-8*). Cross section is flattened to the Mississippian top. Well logs are not to scale. All well logs are modified versions from Kansas Geological Survey online databases (<*http://maps.kgs.ku.edu/co2/*> and <*http://www.kgs.ku.edu/PRS/Ozark/Summary/*>).

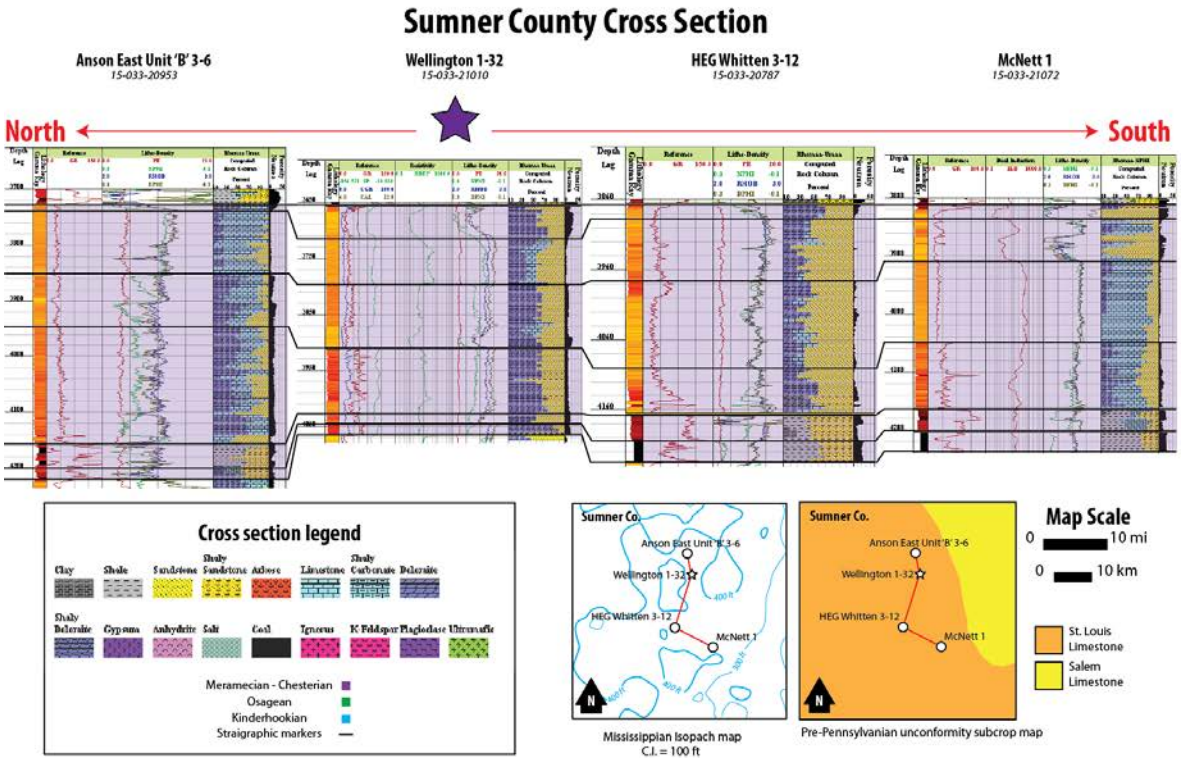

Figure 23. North-south trending cross section in Sumner County showing the structural, stratigraphic and petrophysical character of the Mississippian. Note that a full suite of digital logs from the *Wellington 1-32* (purple star) was used for this cross section. Cross section is flattened to the Mississippian top. Well logs are not to scale. All well logs are modified versions from Kansas Geological Survey online databases (<*http://maps.kgs.ku.edu/co2/*> and <*http://www.kgs.ku.edu/PRS/Ozark/Summary/*>).

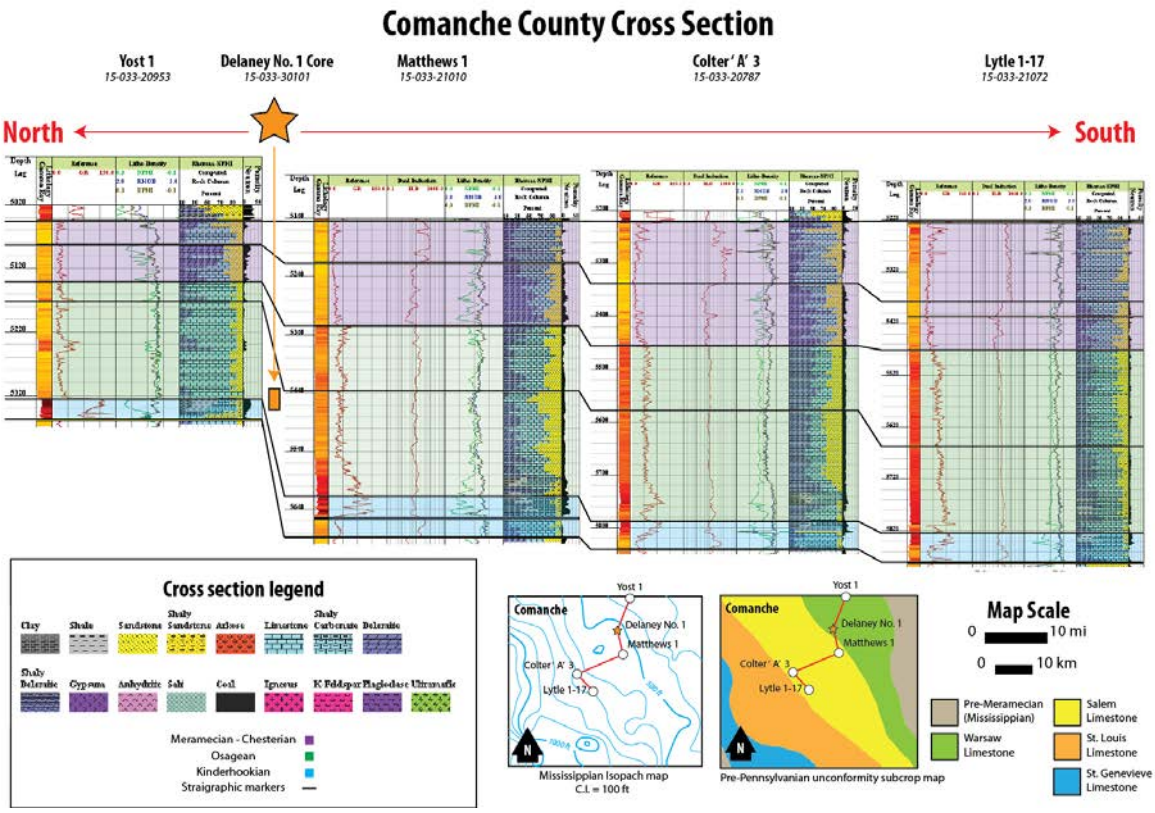

Figure 24. North-south trending cross section in Comanche County showing the structural, stratigraphic and petrophysical character of the Mississippian. The approximate stratigraphic position of the Mississippian interval cored in the *Delaney No. 1* core (orange star and orange rectangle) is also shown. Cross section is flattened to the Mississippian top. Well logs are not to scale. All well logs are modified versions from Kansas Geological Survey online databases (<*http://maps.kgs.ku.edu/co2/*> and <*http://www.kgs.ku.edu/PRS/Ozark/Summary/*>).

SECTION 3. MISSISSIPPIAN DIAGENESIS: PARAGENETIC SEQUENCES

Paragenetic sequence of the Mississippian (Cowley Formation) in the Rhodes Field, Barber County, Kansas

Cores: Harbaugh U.B. 15 and George Michael 1-7

Diagenesis in the Cowley Formation has been studied by Mazzullo and others (2009), but a paragenetic sequence was not put together to show the chronological order of different diagenetic alterations and mineral phases. It was a very simplified explanation, mainly focused on chertification and ignoring many stages of cementation, replacement and burial effects on rock textures. Core and thin section analysis from the *Harbaugh UB-15* and *George Michael 1-8* cores, suggest that the paragenetic sequence of the Cowley Formation consist of 26 stages of diagenetic (Fig. 25). The different stages are grouped into Mississippian, meteoric and burial diagenesis. The Mississippian period consists of the stages that occurred during deposition of the sediments before exposure to subaerial environments and meteoric diagenesis. The meteoric time period consist of diagenesis related to sub-aerial exposure and formation of karst. The burial time period consist of the events that occurred once deposition of the Pennsylvanian sediments started and continuous burying of the Mississippian till present day. The onset of hydrothermal diagenesis is assumed by petrographic assimilation with the events described by King (2012) and Ramaker and others (2014) in adjacent Mississippian strata.

Stage 1: Deposition. This stage consists of the formation of different sediment fabrics during deposition. These fabrics where later modified by bioturbation, resedimentation and diagenetic alteration.

Stage 2: Pyrite (cPY). Pyrite is rarely found within the Cowley and only occurs as clusters of pyrite "framboids" enclosed in chert nodules (Fig. 26A). It is inferred that it was formed early, prior to silicification (stage 7-8) of the sediments.

Stage 3: Evaporite precipitation (cEV). Scattered silicified evaporite nodules (SEN) are found in both cores through the entire Cowley Formation. SEN are generally rounded to sub-rounded and can reach diameters up to 5 cm (Fig. 26B). Although the nodules consist of different phases of silica, remnant lath-like inclusions suggest an evaporite precursor (anhydrite or gypsum; Fig. 26C). These nodules are not restricted to a particular lithology, but most commonly occur on fine-grained bioturbated facies at all depths in both cores. They are rarely found within the Mississippian karst breccias. They tend to displace the surrounding sediment (Fig. 26B) and when multiple nodules are grouped together they create a "chicken wire" texture that's typical of nodular evaporites. This texture indicates that the evaporites precipitated before the sediments lithified. The SEN's are found in facies that contained no sedimentary structures indicative of supratidal or shallow water evaporative conditions. It is still unclear how nodular evaporites form in subtidal sediments but others have documented this phenomenon in the past (Chowns et al., 1974; Milliken, 1979). It is possible that restricted conditions existed in shallower regions of the ramp where hypersaline brines concentrated and descended trough the sediment column to precipitate evaporites in subtidal sediments. The existence of hypersalline fluids during early diagenesis is suggested from fluid inclusions salinities of early megaquartz phases described in section 4.

Stage 4: Quartzine (cQZN). The first type of silica that replaces the evaporite nodules is in most cases quartzine also known as length-slow chalcedony. It silica phase occurs as spheluritic fibers of chalcedony along the outer rims of the nodules (Fig. 26D). It is easily distinguished by a

golden-brown color in thin section (plane-polarized light) and a milky color in hand-sample (Fig. 26D). The brownish coloration in chalcedony can be the result of incorporated organic matter in the crystal lattice (Hattori et al., 1998). Quartzine is a common early stage during silicification of evaporites and it is considered a diagnostic mineral phase of an evaporite precursor (Milliken, 1979).

Stage 5-6: Flamboyant quartz (cFQZ). The second most common type of silica that replaces evaporite nodules is "flamboyant quartz" also known as leutecite. Irregular to elongate fanning quartz crystals with unrecognizable crystal boundaries and undulose extinction characterizes the falmboyant quartz fabric (Fig. 27A). Hesse (1990) describes it as an intermediate between equant and fibrous quartz types. Flamboyant quartz and megaquartz typically occur together in a random mosaic, which indicates that they are temporally associated.

Stage 5-6: Megaquartz (cMGQZ-1). Megaquartz is the most abundant silica phase replacing evaporite nodules (Fig. 26D) and it is characterized by medium to coarsely crystalline equant crystals with strongly undulose extinction. Remnant evaporite lath-like inclusions and abundant fluid inclusions typically give the Megaquartz a cloudy appearance (Fig. 26D). This last characteristic is what differentiates the early megaquartz phase (cMGQZ-1) from the later one (cMGQZ-2). Salinity and petrography of fluid inclusions suggest that cMGQZ-1 precipitated from seawater and evaporated seawater before the onset of meteoric diagenesis under probably reduced conditions. A discussion of fluid inclusion data from cMGQZ-1 is presented on the next section 4.

Stage 7-8: Chertification. This stage consists of the events that resulted in partial to complete replacement of carbonates, spiculites and associated shales by microcrystalline and

cryptocrystalline quartz (chert). Chertification was entirely replacive because the loose-packing of bioclastic aggregates and sedimentary structures are preserved in dense chert beds and chert nodules (Fig. 27B, 27C, 27D). A replacive origin is also supported by the occurrence of bioclasts across the junction between chert nodules and the surrounding sediments. In order to preserve primary sedimentary textures (laminations and cross stratification), chertification must occur prior to subaerial exposure, reworking, weathering and erosion of the sediments. Mazzullo and others (2008) indicated that cherts in the Cowley precipitated from marine and a mixture of freshwater-marine pore-fluids, as indicated by the isotopic signature of oxygen in cherts. This also implies that chert precipitation was an early event.

Stage 7-8: Dolomitization. Finely to medium-crystalline dolomite rhombs characterized by a planar-euhedral, idiotopic mosaic texture (Sibley and Gregg, 1987) is found partially replacing the argillaceous and calcareous matrix of spiculites (Fig. 28A). Most of the dolomite rhombs vary in size from 20-50 μm but can be as large as 160 μm. The exact time relationship between chertification and dolomitization is still inconclusive. Dolomite is absence on SEN, but may be found in the chert nodules suggesting that dolomitization possibly occurred in between both events of silica precipitation. Also, dolomite within the nodules seemed to be enclosed in the chert rather than be replacing the chert. Dolomite is more abundant in the matrix of spiculitic sediments than in chert nodules. Staining with a solution of alizarin red S and potassium ferricyanide reveals three crystal growth zones in dolomite: two ferroan dolomite zones (stained blue) with an intermediate non-ferroan zone (Fig. 28B; Dickson, 1965). Analyzing the dolomite under cathodoluminescence confirms more than three zones of luminescence involving dissolution and overgrowth of a primary dolomite phase (Fig. 28C, 28D). The first dolomite phase (cD1) is characterized by a dolomite rhomb that is non-ferroan (as revealed from staining)

and exhibits a dully to bright luminescent under CL. The cores and some outer surfaces of cD1 are partially dissolved. The second phase of dolomite (cD2) is a cement that occurs on the partially dissolved cores of cD1 and staining reveals a ferroan composition. The third and fourth phase of dolomite (cD3 and cD4) occurs as an overgrowth on the irregular outer surfaces of cD1. Both cD3 and cD4 also stain blue indicating a ferroan composition. Under cathodoluminescence it is difficult to observe the boundary between cD3 and cD4 but SEM photomicrographs reveals the limit between the zones (Fig. 28C). The exact timing between the dolomite phases cD1, cD2, cD3 and cD4 are difficult to resolve from petrography. Overall, individual dolomite crystals are absent on later stage cements and some crystals are cross-cut by fractures and stylolites which also indicates that dolomite is an early precipitate. A more detailed description of the different dolomite phases is discussed on section 4 with the aid of trace- and minor- element data to provide an insight of the paragenesis of the different dolomite phases.

Stage 9-10: Karstification. Before Pennsylvanian deposition, the Mississippian system was exposed to meteoric conditions (Duren, 1960; Euwer, 1965; Thomas, 1982; Rogers et al., 1995; Montgomery et al., 1998; Watney et al., 2001; Mazzullo et al., 2009). During this time dissolution of carbonate material occurred, which created microkarst features (breccia, vuggy-, moldic-, cavern- and fracture-porosity; Fig. 29A) below sub-aerial exposure surfaces

Stage 9-10: Brecciation. Weathering during meteoric diagenesis resulted in the formation of solution-collapsed breccias (Fig. 29). Cavities filled with brecciated material with little evidence of reworking suggest that the breccias formed in-place by dissolution of carbonate material and accumulation of residual cherts (Fig. 29A, 29B). Brecciated fabrics are very common in the Cowley Formation and are not exclusive of the pre-Pennsylvanian unconformity. Short periods of subaerial exposure during the Mississippian have resulted in similar fabrics found trough the

entire stratigraphic section (Mazzullo et al., 2009). Stages 9-10 are interpreted to occur at the same time and cross-cut all previous stages. Stages 9-10 represent the onset of meteoric diagenesis consisting of the overall weathering, erosion and reworking of the sediments at the end of the Mississippian.

Stage 11: Silica dissolution. Etched and micro-porous (tripolitic) sections along the peripheries of chert clasts and chert nodules suggest that dissolution of silica occurred after brecciation (Fig. 29A, 29C and 29D). The dissolved sections are cross-cut by fractures that are filled with sediments and cements. Dissolution of remaining unstable silica, such as opal-a in sponge-spicules, also occurred during this stage and generated vuggy- and moldic-porosity.

Stage 12: Fracturing #1. The dissolved rims of chert nodules and chert clasts are cross-cut by fractures. These fractures are not related to the brecciation event because no dissolution occurred within these fractures, indicating that they post-date the dissolution of silica. The fractures are filled with sediments and later cements (Fig. 29D).

Stage 13-14-15: Chalcedony cement (cCDN). Micro-botryoidal "length-fast chalcedony" is found cementing the exterior rims of chert nodules and lining the fractures (stage 12) of the nodules (Fig. 30A, 30D). This cement can also occur as radiating splays of chalcedony (Fig. 30A).

Stage 13-14-15: Sediment infill. Sediment is found in fractures formed on stage 12 that cut across chert nodules and clasts (Fig. 29D). Sediment may also be found on vuggy and moldic pores generated in previous stages (stages 9-10 and 11).

Stage 13-14-15: Clay cementation. Micro laminated clay cement is found on fractures and vugs (Fig. 30B). Petrographic association of chalcedony, sediment infill and clay cementation (stages 13-14-15) on similar features suggests that all events are temporally associated.

Stage 16: Calcite overgrowth (cCC1). The first evidence of calcite cementation occurs as syntaxial overgrowths on crinoid fragments (Fig. 30C). The syntaxial overgrowths helped to preserve the skeletal components during grain-to-grain pressure dissolution. cCC1 appears dull under cathodoluminescence (CL) and exhibits no compositional zoning. Stable isotope data collected on cCC1 are discussed in section 4.

Stage 17. Calcite cementation (cCC2). Void-filling equant to drusy blocky calcite cement with deformation twins is found along fractures, intra-particle porosity and sponge-spicule molds (Fig. 30D, 31). Some of these fractures are outlined with cCDN suggesting that cCC2 was precipitated afterwards (Fig. 30D, 30A). Calcite cement cCC2 takes a pink to lilac stain in alizarin red S and potassium ferricyanide solution a ferroan composition (Dickson, 1965). No zonation was visible on stained samples, however three generations of crystal growth can be described under CL (Fig. 30A, 30B). The firs zone (cCC2-a) consists of dully-luminescent calcite that outlines the cavities. The second zone (cCC2-b) consists of adjoined calcite crystals fringing the previous zone showing numerous concentric bands of alternating bright luminescence and dull luminescence that appear to get thicker and brighter with advancing crystal growth. The third zone (cCC2-c) consists of poorly dully-luminescent calcite with no visible compositional zoning cementing the rest of the cavities. This zoning can result from fluctuations in pore fluids during crystal precipitation or variations in the rates of trace element partitioning into calcite (Boggs and Krinsley, 2006). The abundance of luminescent zones, the association with fractures and other

meteoric cements (chalcedony), and the drusy texture are all indicative of calcite precipitation from meteoric phreatic fluids. Stable isotope data collected in cCC2 are discussed in section 4.

Stage 18. Calcite cementation (cCC3). Calcite is also found replacing silica on SEN (Fig. 30D). A coarsely crystalline poikilotopic calcite crystal with twinning characterizes cCC3. Under crossed polarized light it exhibits a patchy texture that is pronounced by discontinuous twinning. This calcite takes a lilac stain in alizarin red S and potassium ferricyanide solution indicating a ferroan composition (Dickson, 1965). cCC3 exhibits a homogeneous poorly dull-luminescence in CL. No evidence of compositional zoning was found on cCC3. Isotopic values (section 4) along with petrography suggest that cCC1, cCC2 and cCC3 are all different calcite precipitates and each post dates the other respectively.

Stage 19-20: Grain-to-grain pressure dissolution. Close packing, minor deformation of skeletal grains and sutured (dissolved) grain contacts are found in bioclastic crinoidal grainstones (Fig. 32A). Significant compaction is necessary to generate pressure dissolution textures and it's interpreted to occur during burial conditions.

Stage 19-20: Stylolitization. Stylolitization is observed in grainstones while formation of horsetail dissolution seams are observed on fine-grained facies such as wackestones. Both textures are the result of burial compaction. Stages 19 and 20 initiated after the onset of burial diagenesis because significant stress are needed to generate these textures.

Stage 21: Calcite dissolution. Moldic pores after calcite bioclasts are found in spiculites. Some of the molds are cemented with late stage megaquartz (cMGQZ-2; Fig. 32B) but not with early chalcedony (cCDN) or calcite cements (cCC1, cCC2 and cCC3). For this reason it is interpreted

that the dissolution of calcite bioclasts took place after chalcedony and early calcite precipitation, and prior the precipitation of late stage megaquartz.

Stage 22: Megaquartz 2 (cMGQZ-2). Clear equant megaquartz occurs as a void-filling cement in cavities inside silicified evaporite nodules and calcareous skeletal molds (Fig. 32B, 33C). It occurs as an overgrowth of early megaquartz cements (cMGQZ-1; Fig. 32C). Evaporite lath-like inclusions are absent in cMGQZ-2 indicating that it precipitated after evaporite replacement concluded. King (2012) described similar megaquartz in SEN's from the *Wellington 1-32* core. King (2012) interpreted precipitation temperatures of ~90 °C from fluid inclusion microthermometry of two-phase aqueous-gas fluid inclusions in the megaquartz and suggested a hydrothermal origin. cMGQZ-2 is interpreted as a late stage precipitate due to the petrographical and paragenetic associations to the hydrothermal stages described by King (2012).

Stage 23: Zebraic chalcedony (cZCH). An overgrowth of zebraic chalcedony typically follows cMQZ-2. It occurs as a fringing cement of constant thickness within cavities of silicified evaporite nodules (Fig. 32C). This silica cement exhibits a golden-brown color in plane polarized light and a milky color in hand-sample (Fig. 32C). Zebraic chalcedony is characterized by fanning crystals with undulose extinction and unrecognizable crystal boundaries forming a pattern under crossed polarizers that resembles the skin of a zebra (Fig. 32C). Evaporite lath-like inclusions are absent in cZCH. Superposition of this cement on cMGQZ-2 indicates that it precipitated afterwards.

Stage 24: Fracturing #3. Late stage baroque dolomite (cBD) and calcite cement (cCC4) are found on fractured chert nodules suggesting that fracturing occurred prior to their precipitation.

Stage 25: Baroque dolomite (cBD). Baroque dolomite is observed as a void-filling cement found inside fractures and vugs before a late stage calcite cement (cCC4; Fig. 32D). Baroque dolomite was only seen on two thin-sections and is characterized by a light yellowish color (plane polarized light), curved crystal faces, undulose extinction and a cloudy appearance. These petrographic characteristics are indicators of dolomite precipitation at elevated temperatures typically between ~60-150 °C within the oil window (Radke & Mathis, 1980). Baroque dolomite is non-luminescent under CL and stains blue when reacted to a solution of alizarin red S and potassium ferricyanide, indicating that the dolomite is ferroan (Dickson, 1965).

Stage 26: Calcite Cement #4 (cCC4). A blocky calcite cement precipitated after baroque dolomite in chert nodule fractures (Fig. 32D). cCC4 is also found cross-cutting earlier chalcedony cements (cCDN). It has a poorly dull luminescence in CL and stains lilac when reacted to a solution of alizarin red S and potassium ferricyanide, indicating a ferrous composition (Dickson, 1965).

Paragenetic sequence of the Mississippian (Meramecian-Chesterian) in the Wellington Field, Sumner County, Kansas

Cores: Wellington 1-32

Diagenesis in the *Wellington 1-32* core has been partially studied by King (2012). King (2012) focused on understanding the thermal history of late stage mineral phases. On this section we study the complete paragenesis of the Mississippian in the *Wellington 1-32*, in particular the early stages that are not explained by King (2012). For further details on the later stages of diagenesis refer to King (2012). Petrographic interpretations suggest that the paragenesis of the Mississippian cored in the *Wellington 1-32* consist of 28 major stages (Fig. 33). All stages are grouped into Mississippian, meteoric and burial time periods relative to their interpreted time of

occurrence. The onset of hydrothermal conditions was placed after interpretations of fluid inclusion microthermometry by King (2012) from late stage mineral phases in the *Wellington 1-32*.

Stage 1: Deposition. This stage consists of the formation of different sediment fabrics during deposition. These fabrics where later modified by bioturbation, resedimentation and diagenetic alteration.

Stage 2: Pyrite (wPY1). Pyrite crystals forming spheroidal clusters (*framboidal pyrite*) typically occur within fine-grained facies (Fig. 9B). They may occur trapped within chert nodules and silica cements. It is therefore inferred that it was formed prior to precipitation of diagenetic silica phases and probably related to the replacement of organic matter as it can be inferred from the framboidal shape.

Stage 3: Glauconite (GL). Isolated, ovoid-shaped, internally featureless, dark-green glauconite crystals can be found in organic-rich, dolomitic and argillaceous facies (Fig. 34A). The lack of roundness and association with organic-rich sediments suggests an authigenic origin. Authigenic glauconite is representative of stagnant and slow sedimentation conditions (Flügel, 2004).

Stage 4: Evaporite #1 (wEV1). Nodules with similar textures to the SEN found in the *Harbaugh UB 15* and *George Michael 1-8* are found in the *Wellington 1-32* (Fig. 34C, 34D, 36A, 36B, 36C). SEN's in the *Wellington 1-32* tend to occur along burrowed sections. The burrowed sediments where probably a preferential pathway for hypersaline fluids to seep thru and precipitate evaporites in subtidal sediments. The deformation of the sediments around the SEN and the replacement with early silica cements indicates that evaporite precipitation occurred after sediment deposition and before silicification.

Stage 5. Quartzine (wQZN). Quartzine (length-slow chalcedony) is the first type of silica that replaces the evaporite nodules. It occurs along the outer rims of the nodules as spheluritic fibers of chalcedony (Fig. 35B). It is differentiated from other silica phases in the nodules by a golden-brown color in plane-polarized light and a milky color in hand specimen (Fig. 35B). The particular occurrence of wQZN in the rims of SEN suggests that this stage represents the onset of silicification of nodular evaporites and Mississippian limestone.

Stage 6-7. Flamboyant quartz (wFQZ). Flamboyant quartz typically follows quartzine on silicified evaporite nodules (Milliken, 1979). wFQZ may or may not contain evaporite inclusions but it shows polymorphic fabrics that are suggestive of evaporite replacement (Fig. 35B). It occurs in a random mosaic with megaquartz. Typically one mineral overgrows the other but no definite series of events can be defined. This fabric indicates that both minerals are temporally associated.

Stage 6-7. Megaquartz (wMGQZ-1). Megaquartz is the most common phase of silica replacing evaporites. It occurs as medium to coarsely crystalline euhedral quartz crystals characterized by undulose extinction with abundant evaporite and fluid inclusions (Fig. 35B, 36C). It may form a drusy mosaic fabric that is typical of Megaquartz replacement (Hesse, 1990). This megaquartz is petrographically similar to the megaquartz found in SEN in the Cowley Formation. It is interpreted that this quartz formed at similar conditions, prior to meteoric diagenesis on a reduced environment under the influence of seawater and evaporated seawater (see section 4).

Stage 8-9: Chertification. Early replacement of the sediments by microcrystalline and cryptocrystalline quartz (chert) also occurred in the facies described in the *Wellington 1-32* core. Preservation of primary sedimentary structures, loose packing of bioclastic aggregates (e.g.

sponge-spicules) inside convoluted chert nodules and deformation of the sediments surrounding the nodules is indicative that chertification occurred early before the sediments where completely lithified (Fig. 35D).

Stage 8-9: Dolomitization. Dolomite rhombs are pervasively replacing the matrix of fine-grained lithofacies (mudstones, wackestones and their argillaceous varieties) in the *Wellington 1-32* core (Fig. 36A and 36B). Dolomite size varies from finely to medium crystalline (20-120 μm). Overall, crystal size increases with increasing amount of dolomite in the matrix. On the basis of crystal boundaries two major dolomite fabrics can be differentiated: planar-euhedral idiotopic mosaic and planar-subhedral hypidiotopic mosaic (Sibley and Gregg, 1987). Idiotopic fabrics are more nicely developed where a micrite matrix supports most of the dolomite rhombs or where porosity dominates the intercrystalline space. Hypidiotopic fabrics are nicely developed in the lower portions of the *Wellington 1-32* core where facies are tight and seem more pervasively dolomitized. Dolomite rhombs in hypidiotopic fabrics tend to have cloudy cores and limpid rims. None of the dolomite appeared to be replaced with silica. Dolomite rhombs are however, found inside chert nodules but are scarce and more widely spread than in the matrix. Dolomite does not replace siliceous sponge-spicules and calcareous fossils. Moldic pores after siliceous sponge-spicules are not cemented with dolomite either which indicates that dolomite predates silica dissolution. When reacted with a solution of alizarin red S and potassium ferricyanide, the outer edges of the dolomite rhombs take a blue stain, indicating the presence of iron in the rims of individual rhombs (Dickson, 1965; Fig. 36B). This suggests that at least two dolomite phases must have been precipitated: an early non-ferroan phase (wD1a) and a subsequent ferroan phase (wD1b; Fig. 36B and 36C). Under CL most of the dolomite rhombs showed no luminescence. However the outer edges of some dolomite crystals may show some very dull luminescence. A

very few of the largest rhombs show a luminescent core that may or may not be dissolved (37D). The origin of this luminescent core is still unclear. Distorted crystal surfaces and cracks may also show some bright luminescence that can be the result some etching and dissolution in these areas. Some dolomite rhombs have dirty and pitted cores. The dirty appearance is imparted by undissolved inclusions of the precursor $CaCO_3$ (see section 4). The absence of dolomite crystals replacing late stage cements and the presence of dolomite inside chert nodules suggests it occurred early in the paragenesis at some time close to chertification. Dolomite rhombs are found cross-cut by stylolites and dissolution seams which also confirms dolomite precipitated prior the onset of burial diagenesis. However, it is also possible that the overgrowth wD1b occurred at a much later stage than this. The lack of cross-cutting relationships makes it difficult to determine under what conditions the wD1b phase was precipitated. A more detailed description of the different dolomite phases will be discussed on Section 4.

Stage 10-11: Karst. Before Pennsylvanian deposition, the Mississippian system was exposed to meteoric conditions (Duren, 1960; Euwer, 1965; Thomas, 1982; Rogers et al., 1995; Montgomery et al., 1998; Watney et al., 2001; Mazzullo et al., 2009). During this time dissolution of carbonate material occurred, which generated vuggy-, moldic, fracture- and cavernous-porosity; brecciated textures and other features indicative of karstification.

Stage 10-11: Brecciation. Sub-aerial exposure and weathering of the Mississippian strata resulted in the formation of solution-collapsed breccias along a karstified Mississippian surface. This event was responsible for the regional brecciated fabrics found directly below the pre-Pennsylvanian unconformity in south-central Kansas (Watney et al., 2001; Mazzullo et al., 2009). Stages 10-11 represents the onset of meteoric diagenesis and are interpreted to occur during the same time.

Stage 12: Silica dissolution. Weathering in sub-aerial exposure conditions created vugs and sponge-spicule molds that are cemented on later stages. Where the dissolution was extensive, irregular shaped solution-enlarged vugs where formed. Dissolution along the peripheries of chert nodules and chert clasts is also interpreted to occur during this event.

Stage 13-14: Void-Filling Dolomite (wD2). A medium crystalline (140-180 μm), void filling, planar-e dolomite cement is found on chert fractures and solution-enlarged vugs (Fig. 37A; Sibley and Gregg, 1987). This dolomite is much coarser than wD1 and is generally a limpid dolomite. A blue stain when reacted with a solution of alizarin red S and potassium ferricyanide indicates a ferrous dolomite composition (Dickson, 1965). No luminescence was observed under CL. Based on petrography and geochemical constraints discuss in section 4 wD2 is interpreted as a meteoric precipitate. The relationship between wCDN and wD2 is still unknown.

Stage 13-14: Chalcedony #1 (wCDN). Length-slow chalcedony commonly occurs along the cavity walls in fractures, sponge-spicule molds and vugs (Fig. 37B, 37C). wCDN has a golden-brown color in plane-polarized light and a milky color in hand sample. Some samples obtain a blue stain during impregnation with blue epoxy indicating the presence of micropores. wCDN is typically followed by calcite cement (wCC1) that completely occludes the remaining space in the cavities.

Stage 15-16. Calcite cement (wCC1). wCC1 exhibits a drusy texture and occludes the cavities after a lining of chalcedony (Fig. 37C). By superposition, it is interpreted that it postdates the chalcedony cement. This calcite shows a dull luminescence under CL and no evidence of compositional zoning was found.

Stage 15-16. Calcite overgrowth (wCC2). wCC2 occurs as syntaxial overgrowths on crinoids (Fig. 37D). It exhibits a poorly dull-luminescence under CL and no compositional zoning was found. This cement preserved many of the skeletal fragments during burial compaction. The exact timing and relationship between stages 15-16 is still unknown but are both considered to occur before the onset burial diagenesis.

Stage 17-18-19: Grain to grain pressure solution. Close packing and deformation of skeletal grains with sutured grain-to-grain contacts are typically found in packstones and grainstones. These textures are indicative of compaction during burial.

Stage 17-18-19: Fracturing #1. Vertical fractures that terminate on dissolution seams are interpreted to occur during stresses of burial compaction.

Stage 17-18-19: Stylolitization. Stylolitization is found in packestones and grainestones while the formation of horsetail dissolution seams is found on muddy, clayey and shaly intervals (Fig. 38A, 38B). Stages 15-16-17 represent the onset burial conditions in the paragenesis because significant stress is needed to generate these features.

Stage 20. Calcite cement (wCC3). Blocky equant calcite cement is found on vertical fractures formed during stage 17-18-19 (Fig. 13C). Under CL it exhibits a very dull patchy luminescence.

Stage 21: Megaquartz (wMGQZ-2). A late phase of megaquartz occurs as a cement on brecciated fabrics, vugs and cavities inside SEN. It is characterized by euhedral quartz crystals with undulatory extinction (Fig. 38D). It typically occurs as an overgrowth after early megaquartz (wMGQZ-1) and flamboyant quartz. Both megaquartz are easy to differentiate in SEN because the later one doesn't have evaporite inclusions. King (2012) interpreted precipitation temperatures of ~90 °C from fluid inclusion microthermometry of two-phase gas

and aqueous liquid fluid inclusions in this megaquartz. The temperature record on megaquartz confirms that it is a late-stage cement and represents the onset of hydrothermal alterations (King, 2012).

Stage 22-23-24: Zebraic chalcedony #4 (wZCH). An overgrowth of zebraic chalcedony occurs in the megaquartz (Fig. 38D). This occurs on cavities where megaquartz surfaces are exposed to pore fluids. Superposition of wZCH on wMGQZ-2 also suggest it formed at high temperatures during burial.

Stage 22-23-24: Baroque dolomite (wBD). Scarce rhombs of baroque dolomite can be found after megaquartz but prior to late-stage calcite (wCC4). The saddle shaped crystals are characterized by curved terminations and undulose extinction under crossed polarized light (Fig. 39A). King (2012) noted a presence of hydrocarbon inclusions in baroque dolomites. The time relationship between cZCH and Baroque dolomite is still inconclusive because no petrographic cross-cutting relationship was found between both.

Stage 22-23-24: Hydrocarbon emplacement. Apparent primary hydrocarbon fluid inclusions are found in baroque dolomites (King, 2012), which indicate that petroleum migration occurred before or during the precipitation of baroque dolomite.

Stage 25: Fracturing #2. Fracturing is interpreted from the occurrence of late-stage calcite cement (wCC4) along fractures of brecciated chert and silicified evaporite nodules.

Stage 26-27-28: Calcite cement (wCC4). Coarsely crystalline equant spar cements are found on fractures and cavities after wZCH (Fig. 38D). It appears light yellow in transmitted light and displays deformation twins. It has a dull luminescence on CL. wCC4 stains lilac in a solution of alizarin red S and potassium ferricyanide indicating a ferrous calcite cement (Dickson, 1965).

Stage 26-27-28: Evaporite #2 (wEV2). A late stage evaporite precipitation is suggested by coarsely crystalline poikilotopic tabular crystals that reduce pore space after precipitation of megaquartz (wMGQZ-2; Fig. 39B). No time relationship is found between wEV2 and wCC4. Isolated microcrystalline lath-like evaporites within the argillaceous and dolomitic matrix are also found and are probably related to this event.

Stage 26-27-28: Pyrite precipitation #2 (wPY2). Some of the dolomite rhombs have cores replaced with pyrite (40C). This is interpreted as a replacement pyrite because it obtains the same rhombic shape of the dolomite (polymorphic). It may also be found replacing tripolitic chert lenses (40D). It is still inconclusive the exact time of this pyrite phase but it is tentatively interpreted as an event that occurred sometime during reducing conditions in the burial realms. The relative timing between stages 26-27-28 is still unclear because no petrographic cross-cutting relationship was observed.

Paragenetic sequence of the Mississippian (Osage) in the Delaney area, Barber County, Kansas

Cores: Delaney No. 1 (wildcat well)

Diagenesis in the Delaney core is particularly dominated by early diagenesis in the marine and meteoric environments. The relationship between the different diagenetic alterations and the pre-Pennsylvanian unconformity are not clearly defined because the cored interval does not cover the Mississippian top. Petrographic interpretations suggest that the diagenetic alterations in the *Delaney No. 1* consist of 12 major stages (Fig. 40). All stages are grouped into Mississippian, meteoric and burial time periods relative to their interpreted genesis.

Stage 1: Deposition. This stage consists of the formation of different sediment fabrics during deposition. These fabrics where later modified by resedimentation and diagenetic alteration.

Stage 2: Micritization. Partial micritization of skeletal fragments, particularly bryozoans is interpreted to occur during a marine environment (Fig. 41A, 41B). It occurs as a cloudy micritic replacement of skeletal fragments, particularly bryozoans They formed after smaller organisms create micro-borings on the surface of skeletal fragments and the pores are then filled with aphanocrystalline high-Mg calcite. Micritization of bioclasts is a common diagenetic process affecting carbonate grains and mostly takes place on the shallow sea floor or just below (MacIntyre et al. 2000; Reid and McIntyre, 2000).

Stage 3: Recrystallization of lime mud. Most of the syndepositional marine lime mud was recrystallized into calcite microspar. Microspar can be found on lenses and interparticle porosity that was filled with mud and is now recrystallized. The occurrence of this texture is very minor since the lithofacies are primarily grainy (packestones and grainstones).

Stage 4: Radiaxial syntaxial calcite cement (dRSCC). This cement is characterized by very cloudy columnar calcite with concentral boundaries, curved twins and undulose extension (Fig. 41C, 41D). It occurs as fringing rims up to 800 micrometers thick and shows polygonal compromise boundaries (Fig. 41C, 41D). It is the most common cement in the *Delaney No.1* core and in most cases completely surrounds fenestrae bryozoan fragments and occludes inter-particle and large intra-particle cavities. The lack of compacted unsupported grainstones formed by very delicate skeletal grains (bryozoans) indicates that dRSCC is an early cement. Under cathodoluminescence dRSCC's can divided into two zones (Fig. 42). The first has a bright patchy luminescent (dRSCC-a), which may suggest neomorphic alteration since marine precipitated cements are tipcally non-luminescent (Abassi and Adabi. 2009; Swei and Tucker, 2012). The second dRSCC zone is dull luminescent (dRSCC-b). No other petrographic evidence is found to confirm such an alteration. During diagenesis (neomorphic alteration) the dRSCC

may have picked up Mn, if it was available and the pore-fluids where reducing. Truncation of dRSCC by marine sediments further supports the interpretation of a marine origin (Fig. 43B). Stable isotopes for this cement phase are discussed in section 4.

Stage 5: Blocky calcite cement (dCC1). This cement is characterized by a calcite that commonly occurs as a cloudy to clear, drusy mosaic void-filling precipitate in primary intra-granular porosity, fractures and inter-particle cavities after dRSCC (Fig. 18A). Commonly occurs as overgrowths of dRSCC (Fig. 43A). Geopetal fabrics are also formed from this cement. Under cathodoluminescence three different crystal growth zones can be identified (Fig. 42). The first zone (dCC1-a) is characterized by a non-luminescent overgrowth of dRSCC with variable thickness. The second zone (dCC1-b) is a very thin bright luminescent band fringing the previous zone with a consistent thickness. The third zone is characterized by a mosaic of blocky calcite with a dull-luminescence (dCC1-c). This cement is cross-cut by vertical fractures and stylolites that are interpreted to occur during burial. The blocky and drusy mosaic texture are characteristics of meteoric-phreatic calcite cements and and the formation before burial textures suggests that this cement pre-dates burial diagenesis. Stable isotopes for this cement phase are discussed in section 4.

Stage 6: Chertification. Although chertification is close to absent in this core, partial and selective replacement of skeletal fragments, particularly brachiopod fragments, by microcrystalline and cryptocrystalline quartz (chert) was found in some of the analyzed samples (Fig. 43C).

Stage 7: Calcite dissolution. Bivalve moldic porosity and the absence of prismatic layers on brachiopod fragments suggest that dissolution of unstable calcite occurred (Fig. 43D). It is likely that such dissolution occurred after marine conditions ended and meteoric conditions started.

Stage 8: Chalcedony (dCDN). Fibrous radial chalcedony is found on vuggy pores on skeletal fragments (Figure 45A). The vuggy pores are interpreted to occur during stage 7so chalcedony must postdate calcite dissolution.

Stage 9: Fracturing #1. Randomly oriented fractures cross-cut skeletal fragments and previous cements; and are cemented with clear blocky calcite (dCC2) (Fig. 44B, 44C). Such fractures are similar to autobrecciated textures documented in other Mississippian regions. These fractures are interpreted to occur from in-situ brecciation during meteoric conditions.

Stage 10: Blocky calcite cement (dCC2). This cement is characterized by a clear blocky calcite that occurs along fractures (stage 9) that cross-cut dRSCC and dCC1 (Fig. 44B, 44C). Contrary to dCC2 this cement does not have a cloudy texture. Formation before burial textures and after marine cements suggest that this dCC2 precipitated under meteoric conditions.

Stage11-12: Stylolitization. Stylolitization occurs by burial compaction of the sedimnets. Stylolites cross-cut all previous cements (Fig. 44D).

Stage 11-12: Fracturing. Vertical fractures that cross-cut fossil fragments and previous cements are interpreted to occur under stresses of burial compaction. Stages 11 and 12 initiated after the onset of burial diagenesis because significant stress are needed to generate such texture.

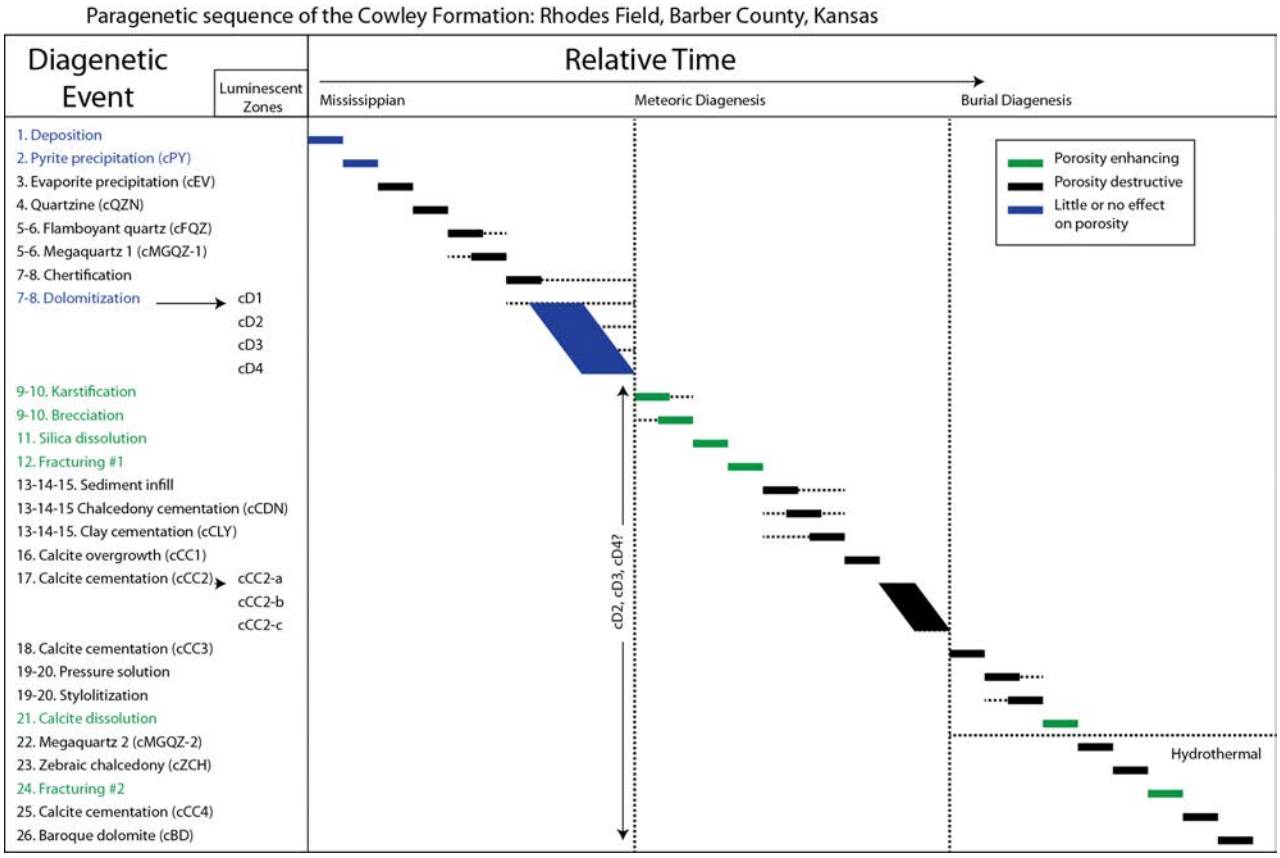

Figure 25. Paragenesis of the Mississippian Cowley Formation in Rhodes field, Barber County, Kansas.

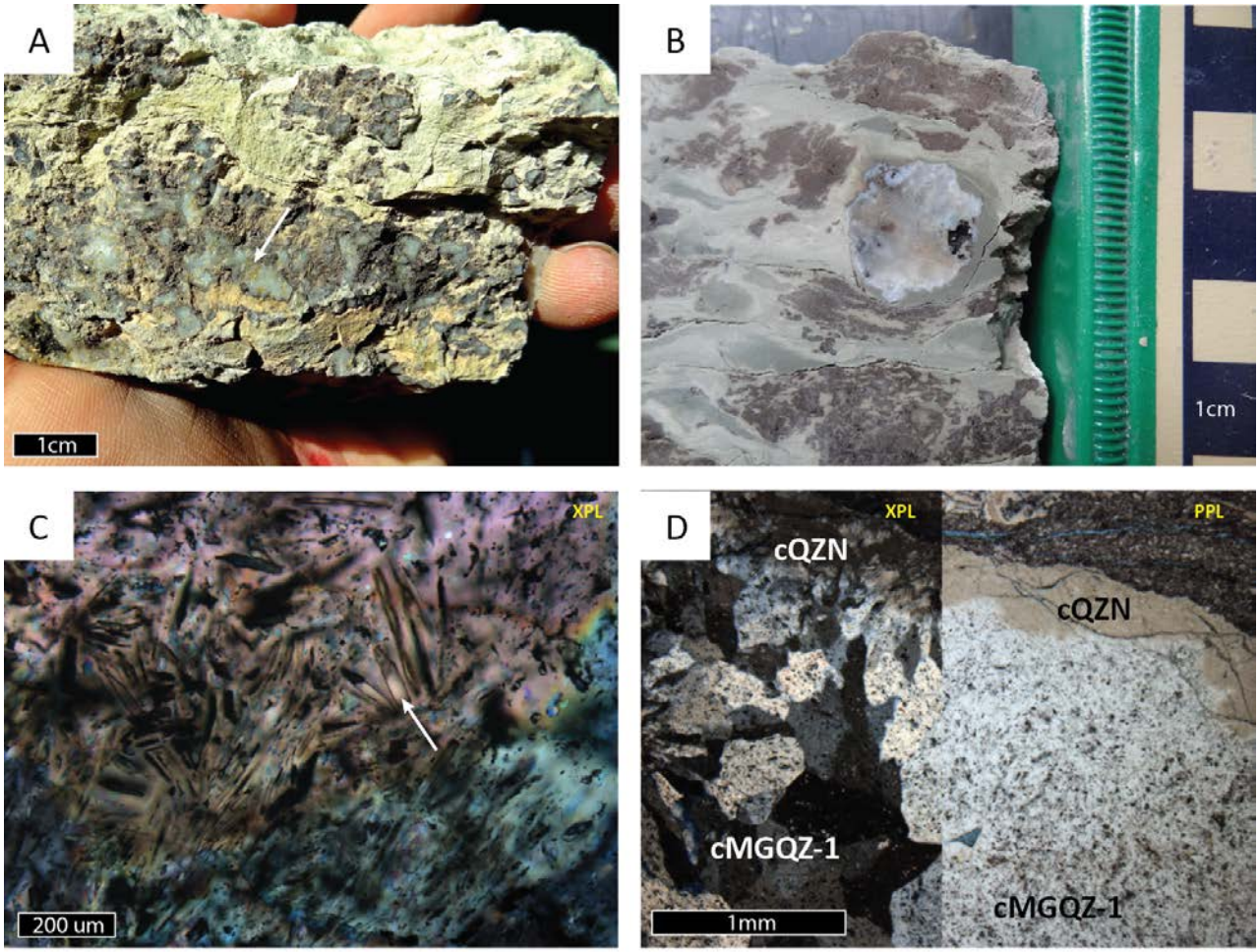

Figure 26. A) Core photograph of framboydal pyrite clusters inside chert nodules (*Harbaugh U.B.15, 4583 ft*). **B**) Core photograph of a silicified evaporite nodule on a weathered cherty spiculite lens. Note the Sub-rounded appearance of the SEN and the translucent to milky crystalline texture. Clusters of similar nodule generate a chicken wire texture. Also note how the surrounding sediment is displaced by nodule growth. (*Harbaugh U.B.15, 4561 ft*). **C**) Photomicrograph illustrating the presence of lath-like anhydrite inclusions (white arrow) inside crystals of megaquartz. (*Harbaugh U.B.15, 4564.5 ft*). **D**) Photomicrograph illustrating a cross sectional view along a silicified evaporite nodule. Note the presence of quartzine (cQZN) on the nodule rim and the presence of megaquartz (cMGQZ-1) on the inner portions of the nodule. Megaquartz crystal size increases towards the interior of the nodule, forming a drusy mosaic. The cloudy texture of megaquartz is caused by the abundance of anhydrite lath inclusions with a different color of interference and identified at higher magnifications. (*Harbaugh U.B.15, 4641 ft*).

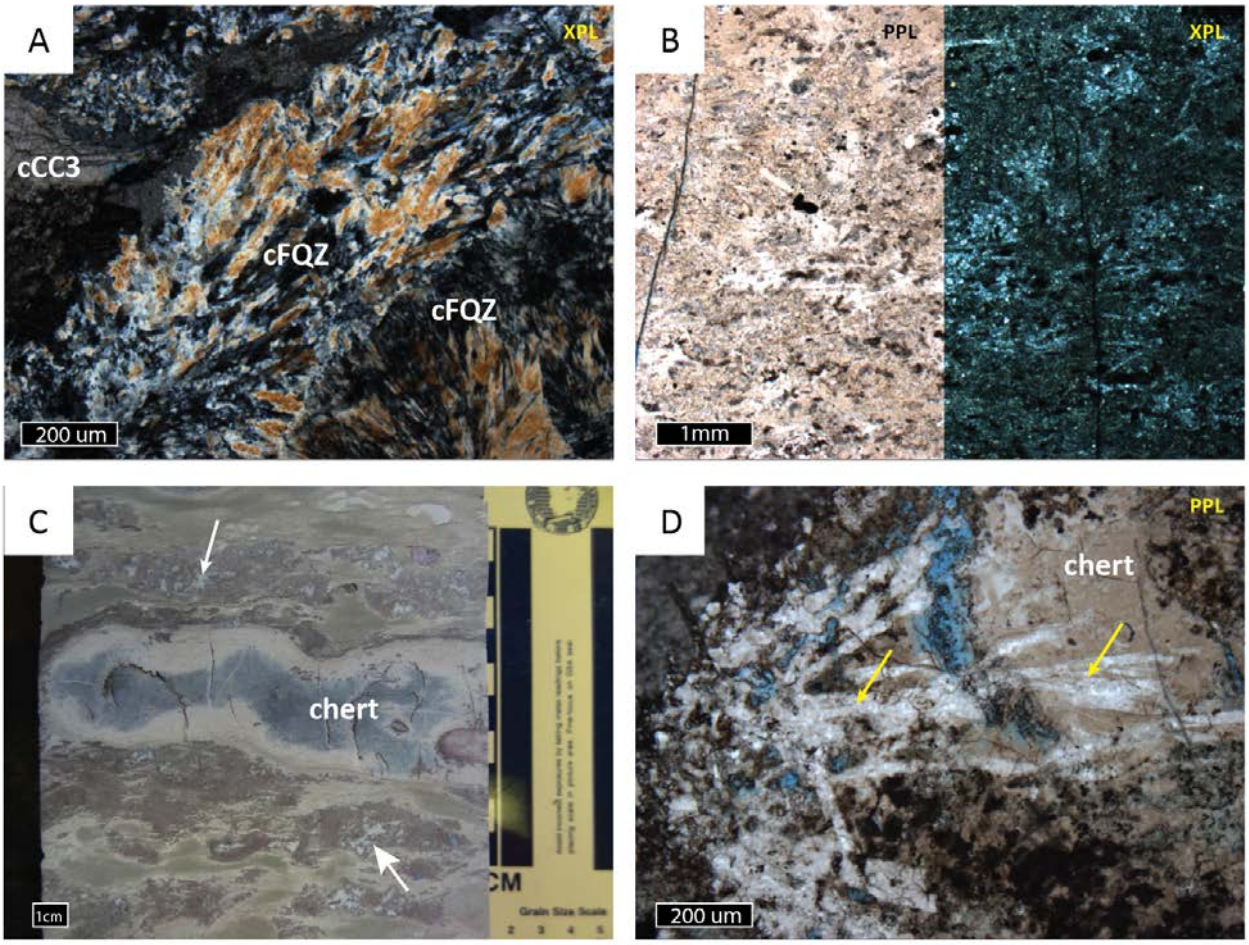

Figure 27. A) Photomicrograph of flamboyant quartz (cFQZ) replacing an evaporite nodule. Note the polymorphic texture resembling evaporite laths. Flamboyant quartz is replaced by calcite (cCC3) on the middle left corner. (*Harbaugh U.B.15, 4583 ft*). **B**) Photomicrograph of microcrystalline quartz or "chert". Note the dense microcrystalline quartz fabric replacing bioclastic fragments (mainly sponge-spicules) as well as the matrix. (*Harbaugh U.B.15, 4653 ft*). **C**) Core photograph illustrating a dense greyish-blue chert nodule. Note how the surrounding sediment is displaced by nodule growth. Note the weathered rims of the chert nodule (tripolitic rims). Remnants of chert nodules after weathering are identified with white arrows. (*George Michael 1-8, 4613 ft*). **D)** Photomicrograph illustrating microcrystalline quartz or "chert" replacing evaporite lath-like crystals (yellow arrows). (*Harbaugh U.B.15, 4614 ft*).

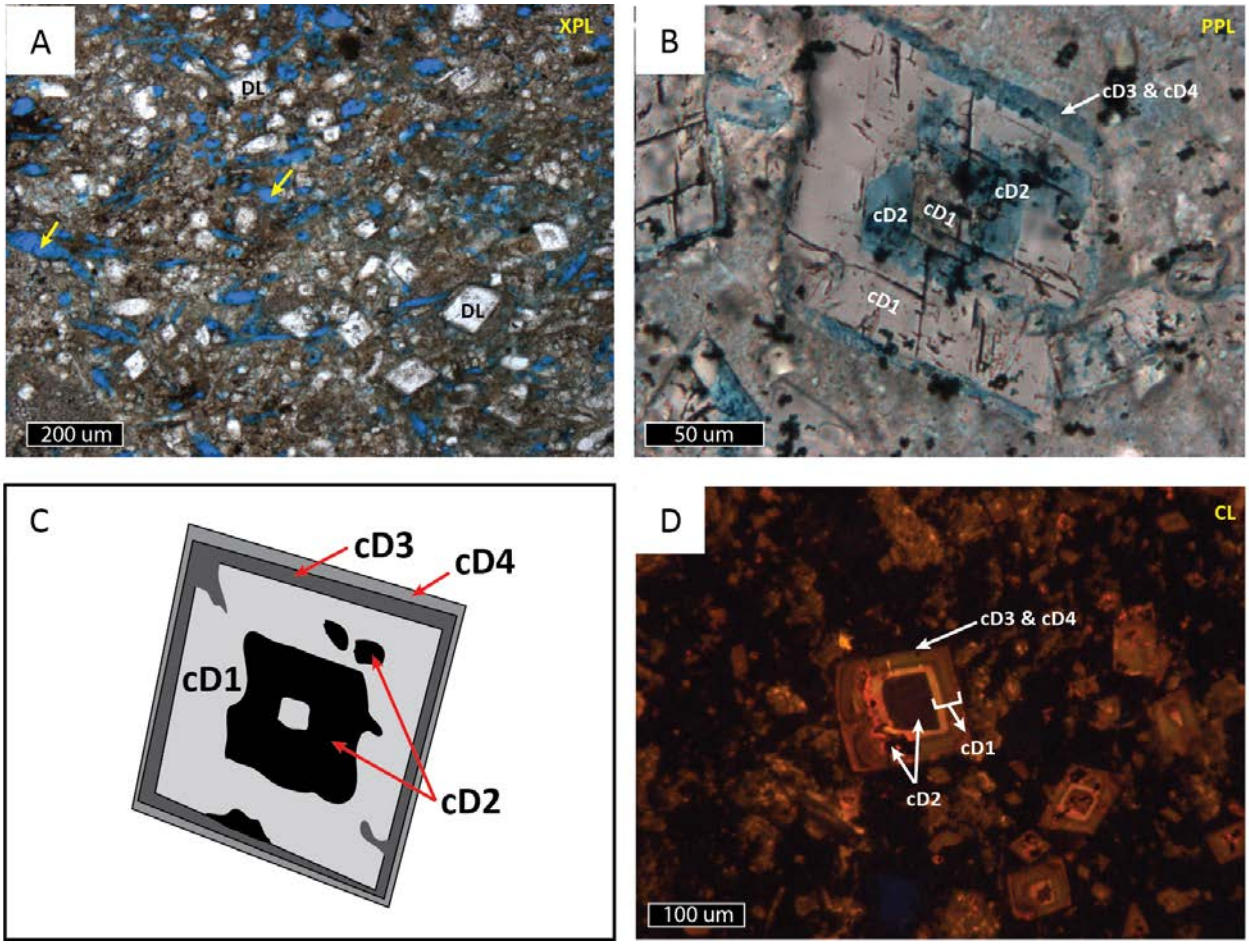

Figure 28. A) Photomicrograph illustrating the finely crystalline to medium crystalline (20-140 μm) dolomite rhombs (DL) observed in the Cowley Formation. Note that most of the crystals are euhedral (idiotopic texture) and are scattered in the matrix. Yellow arrows point at sponge-spicule molds. (*George Michael 1-8, 4610 ft*). **B)** Photomicrograph illustrating dolomite rhombs after being etched and stained with a solution of alizarin red S and potassium ferricyanide. Dolomtie portions stained blue (cD2, cD3 and cD4) indicate the presence of iron, while clear portions (cD1) indicate the absence of iron (Dickson, 1965). Note the presence of blue-stained patches of cD2 that crosscut cD1. These patches represent precipitation of ferroan dolomite (cD2) after dissolution of non-ferroan cD1. (*George Michael 1-8, 4611 ft*). **C)** Schematic diagram of the different dolomite phases and their morphologies within a single dolomite rhomb as seen under cathodoluminescence and backscattered electron images. **D)** Different dolomite phases under cathodoluminescence. Four luminescent zones can be identified. cD1 has a bright to dull-luminescence while the other phases are non-luminescent (cD2, cD3, cD4). The lack of luminescence in cD2, cD3 and cD4 is caused by the concentration of Iron revealed in stained samples. (*George Michael 1-8, 4614*).

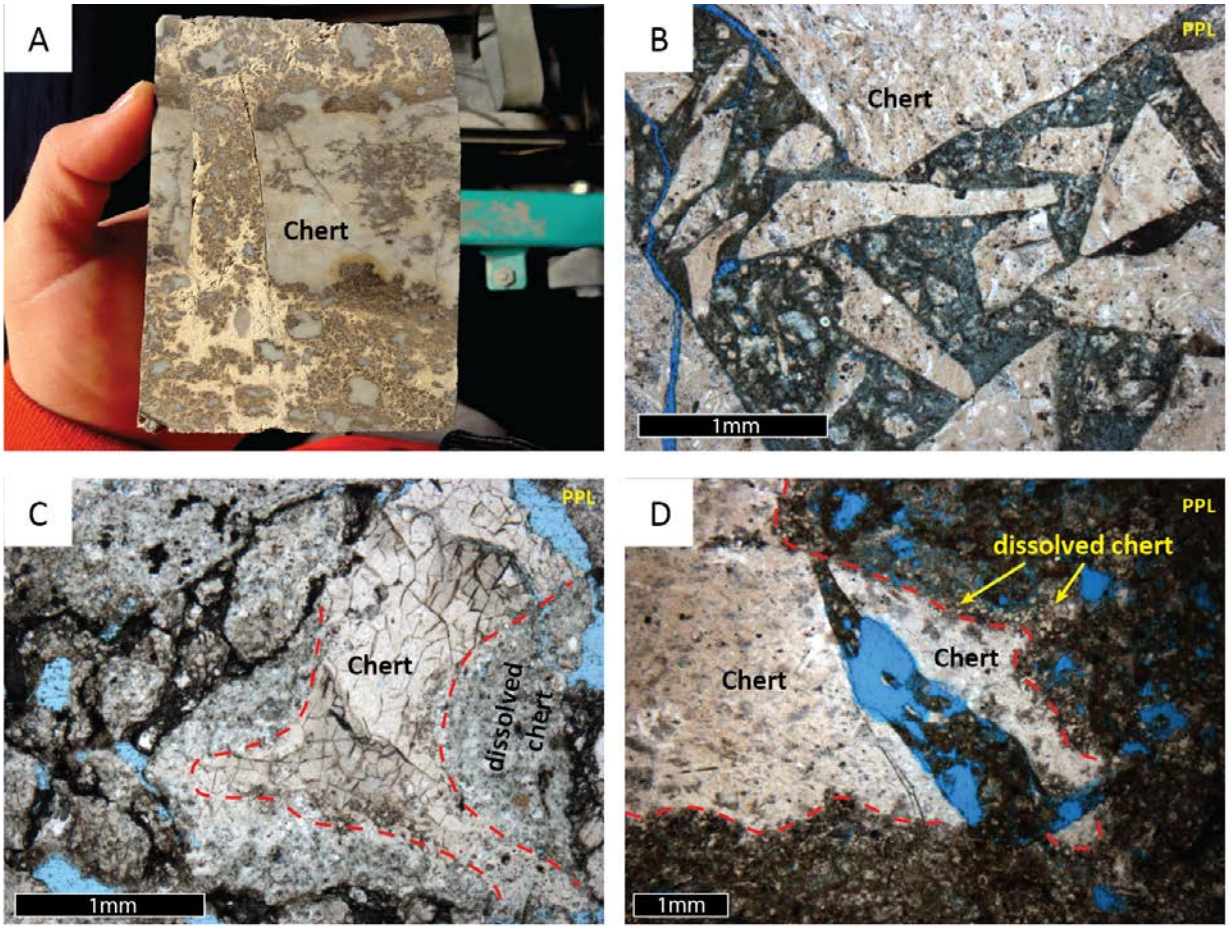

Figure 29. A) Core photograph of chert breccia. Note the abundance of chert clasts varying largely in size and floating on a clay-rich matrix. Autobrecciation is suggested by the abundance of clasts that have been fractured in-place. Brown areas are tripolitic (microporous chert). (*George Michael 1-8, 4593 ft*). **B**) Photomicrograph of brecciated chert. (*George Michael 1-8, 4588 ft*). **C**) Photomicrograph illustrating weathered clasts of sponge-spicule-rich chert breccia. The red dashed line separates the porous chert border (tripolitic) from the non-weathered chert in the interior of the clast. This results from silica weathering, generating porosity trough dissolution. (*Harbaugh U.B.15, 4544 ft*). **D**) Photomicrograph illustrating a weathered chert clast. Note the porous chert rims around the clast. Inside the fracture the clast was not altered by dissolution and sediment filled the fracture. This suggests that dissolution occurred early after some brecciation while the sediment was still loose trough the fractures. (*Harbaugh U.B.15, 4553 ft*).

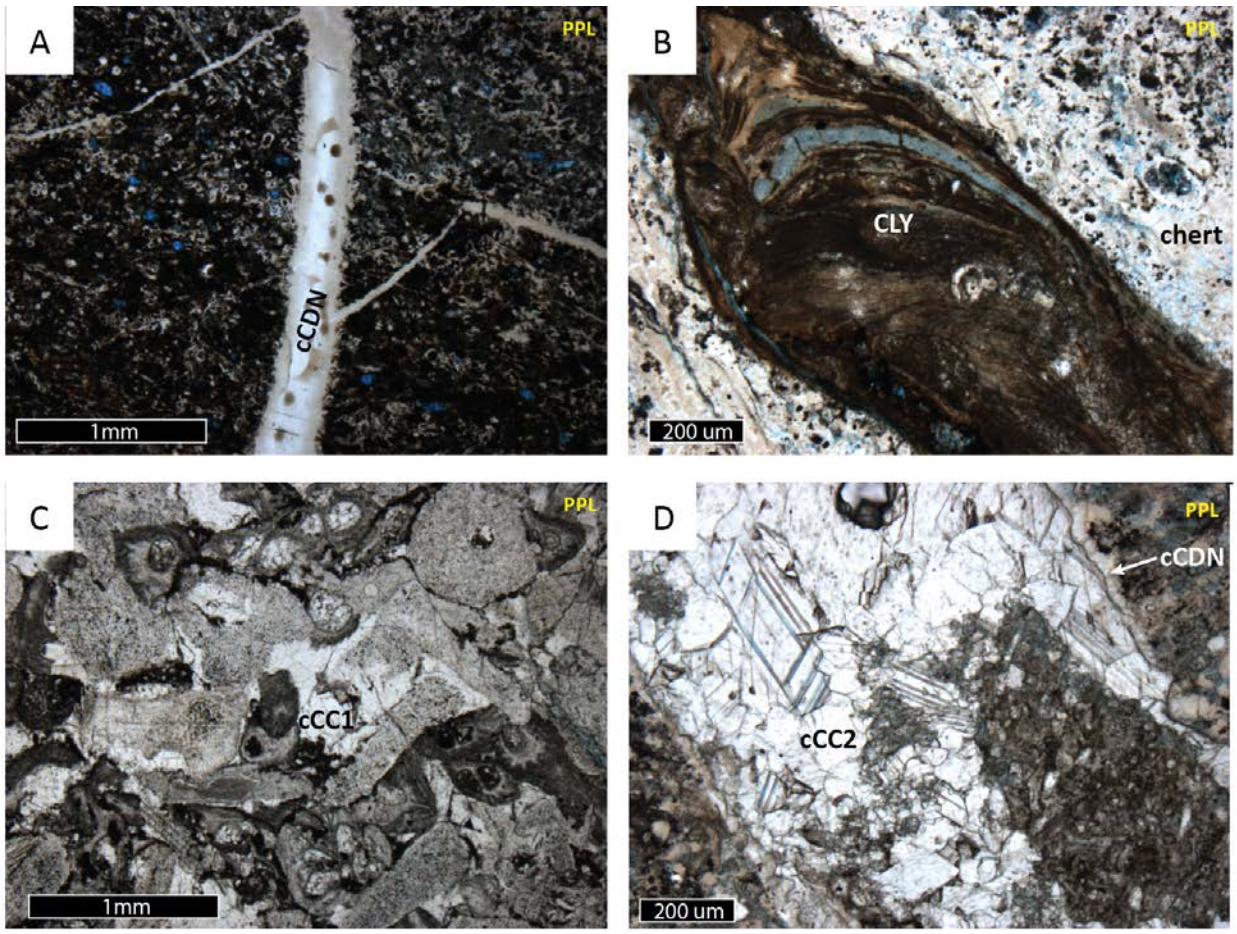

Figure 30. A) Photomicrograph of a brecciated sponge-spicule rich marlstone. Note the cementation of fractures with fibrous "length-slow chalcedony" and radiating splays of chalcedony (cCDN). Note the fibrous chalcedony lining the fractures followed by a microbotryoidal chalcedony completely cementing the rest of the fracture, both interpreted as one event; cDN. (*Harbaugh U.B.15, 4607 ft*). **B**) Photomicrograph illustrating the presence of micro-laminated clay cement (CLY) in the matrix of a brecciated chert. (*George Michael 1-8, 4572 ft*). **C**) Photomicrograph of a bioclastic crinoidal grainstone. Note the presence of syntaxial calcite overgrowth (cCC1) on echinoderm fragments. (*Harbaugh U.B.15, 4632 ft*). **D**) Drusy blocky calcite cement (cCC2) precipitates after a lining of length-slow chalcedony (CDN) in a irregular cavity. (*George Michael 1-7, 4617 ft*).

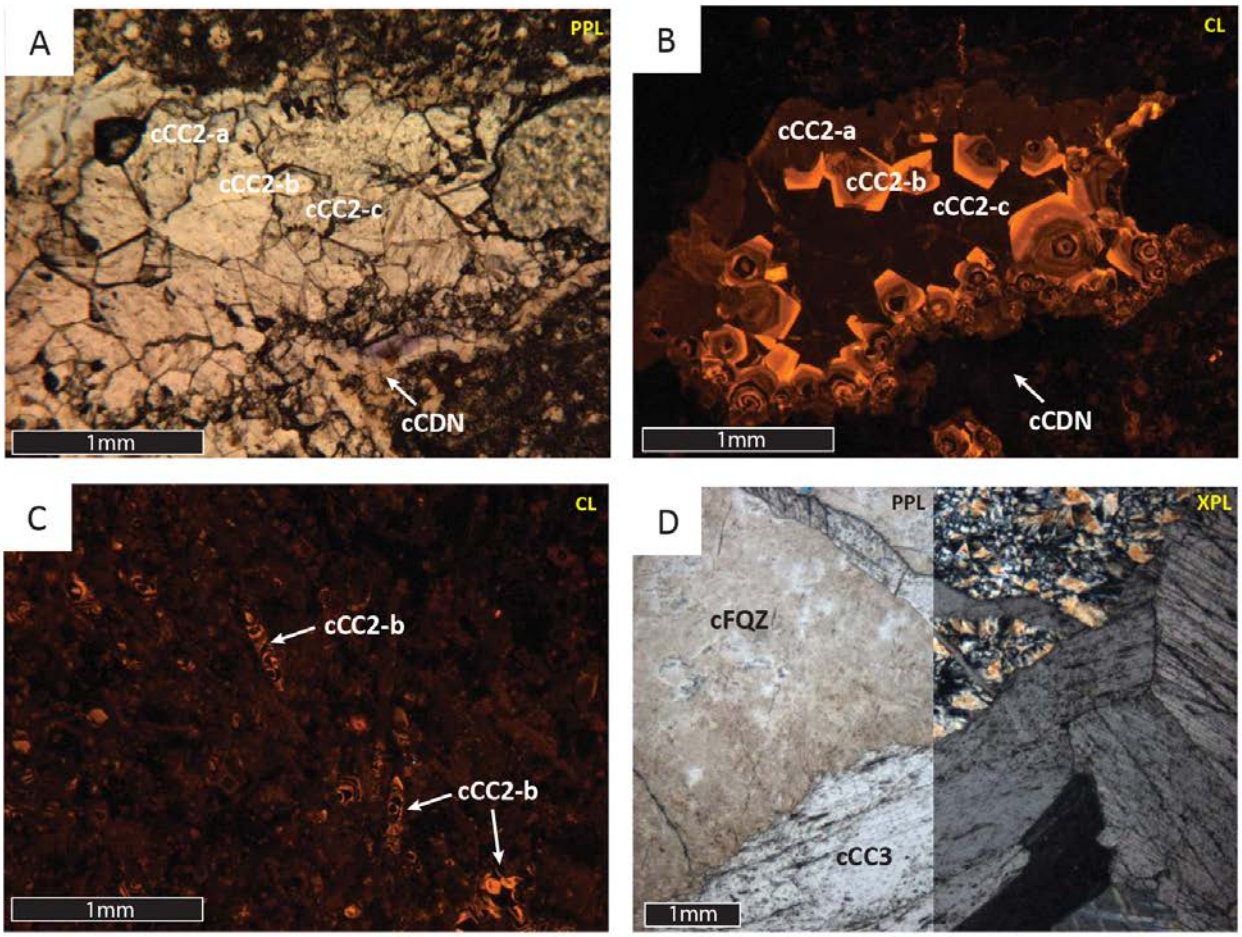

Figure 31. A) Photomicrograph of blocky calcite cement (cCC2) in plane polarized light. Note the occurrence of fibrous length-slow chalcedony (cCDN) lining the irregular cavity before calcite. (*George Michael 1-7, 4617 ft*). **B)** Same as A, but under cathodoluminescence. Note the presence of three major zones (cCC2-a, cCC2-b and cCC2-c) differentiated by luminescent characteristic. (*George Michael 1-7, 4617 ft*). **C)** Photomicrograph illustrating sponge-spicule molds that are cemented with calcite (cCC2) under cathodoluminescence. The interchanging pattern of luminescencent and non-luminescent zones is similar to the cCC2-b zonation in blocky calcite cement cCC2. (*George Michael 1-7, 4616 ft*). **D)** Coarsely crystalline poikilotopic calcite cement (cCC3) after flamboyant quartz in a silica-replaced evaporite nodule. Note that calcite occurs in fractures along the silicified nodule. In some areas calcite seemed to replace the flamboyant quartz (cFQZ) in the SEN's. Thin section was impregnated with blue epoxy (*Harbaugh U.B.15, 4600 ft*).

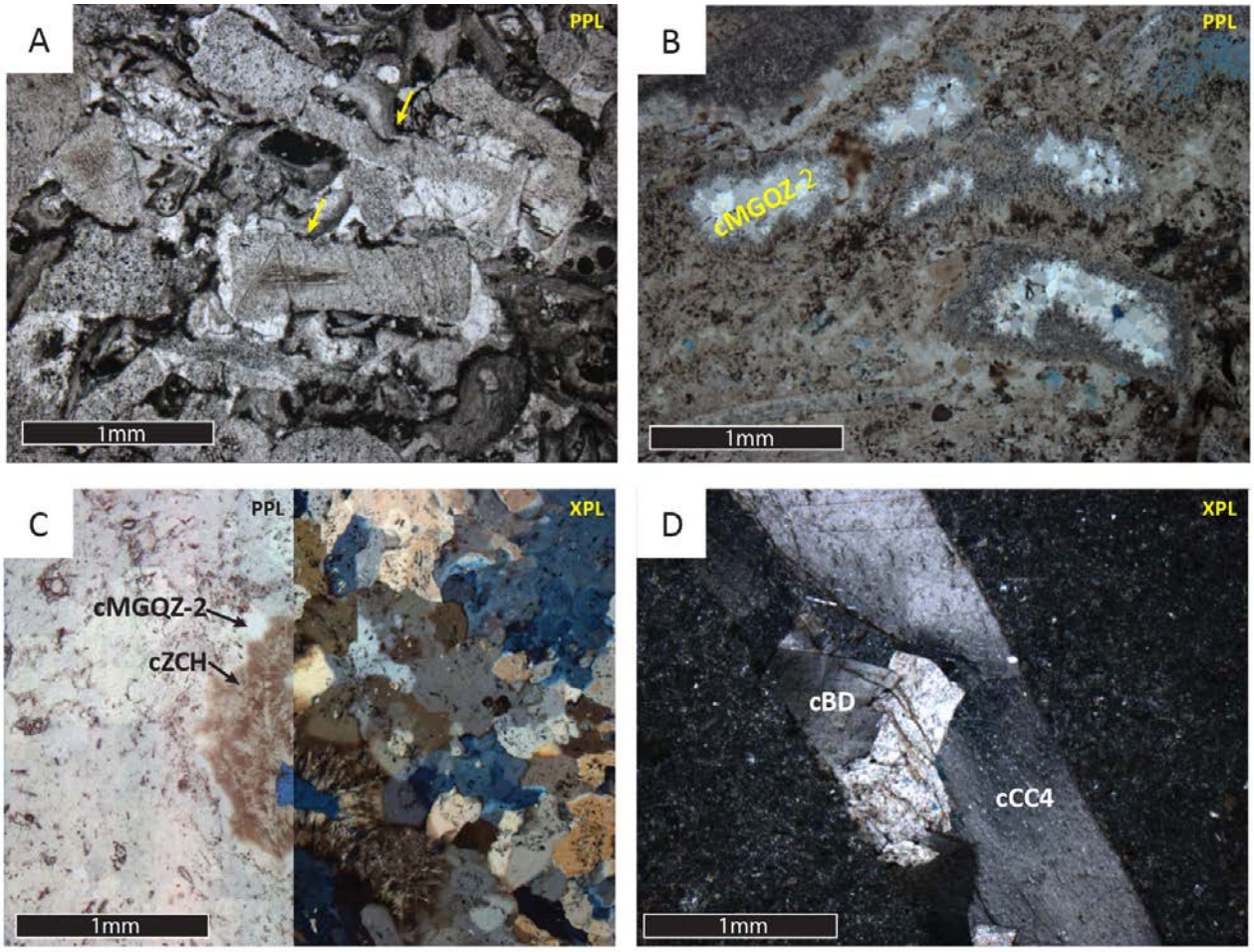

Figure 32. A) Photomicrograph of a bioclastic crinoidal grainstone. Note the heavily compacted texture of the different skeletal fragments. Pressure solution along grains is shown with yellow arrows. Thin section was impregnated with blue epoxy (*Harbaugh U.B.15, 4632 ft*). **B**) Photomicrograph illustrating partially dissolved crinoid columns enclosed in chert. Note that the cavities have been cemented with late stage megaquartz (cMGQZ-2). (*George Michael 1-7, 4580 ft*). **C**) Photomicrograph of a SEN. Note that the nodule is dominated by early megaquartz (cMGQZ-1) with abundant anhydrite inclusions. A cavity in the nodule has been filled with an overgrowth of clear megaquartz (cMGQZ-2) followed by zebraic chalcedony (cZCH) over the previous megaquartz cement (cMGQZ-1). cMGQZ-2 and cZCH are interpreted as hydrothermal due to the petrographical and paragenetic similarities to the hydrothermal stages described by King, 2012 (*Harbaugh U.B.15, 4564.5 ft*). **D**) Baroque dolomite (cBD) followed by blocky calcite cement (cCC4) in a chert fracture. Thin section photomicrograph was taken in crossed-polarized light. (*Harbaugh U.B.15, 4626 ft*).

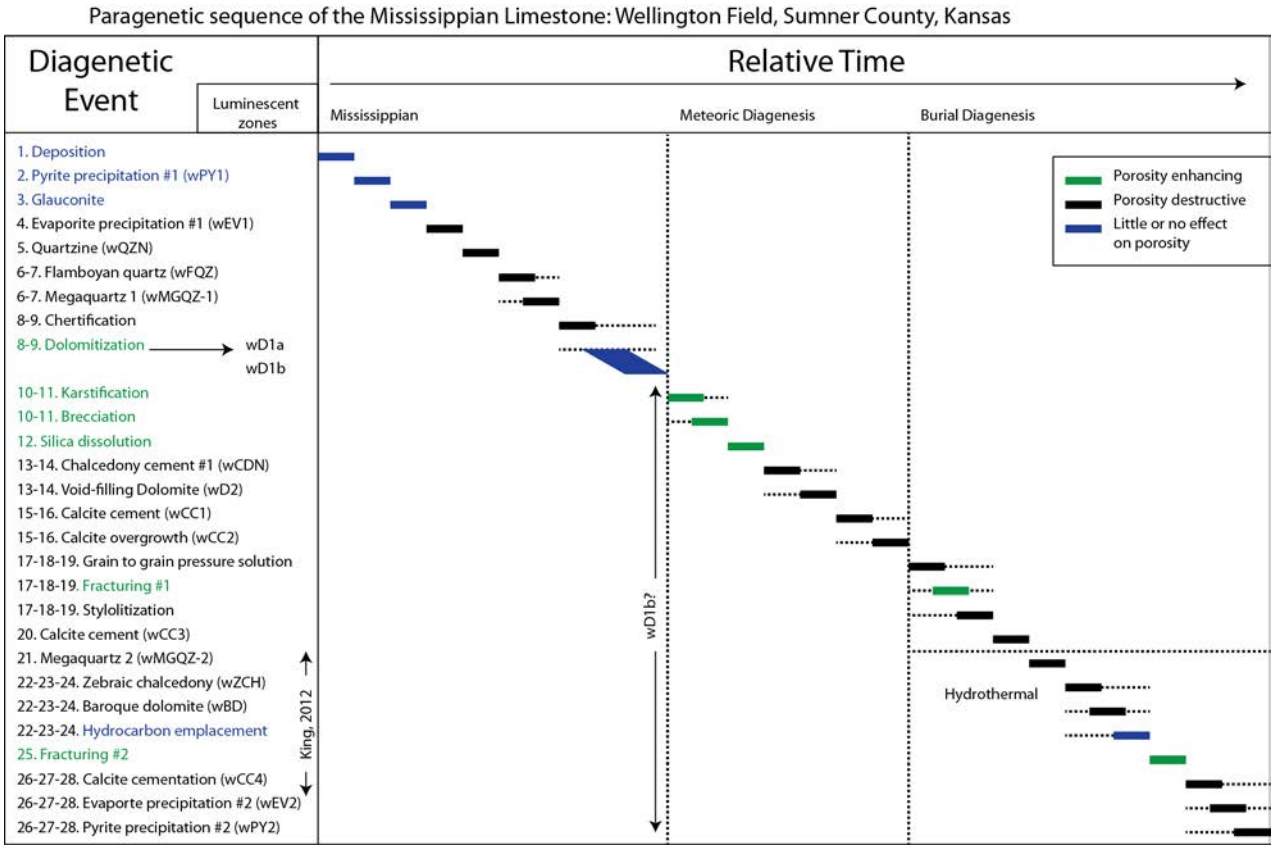

Figure 33. Paragenesis of the Mississippian Limestone in the Wellington field, Sumner County, Kansas.

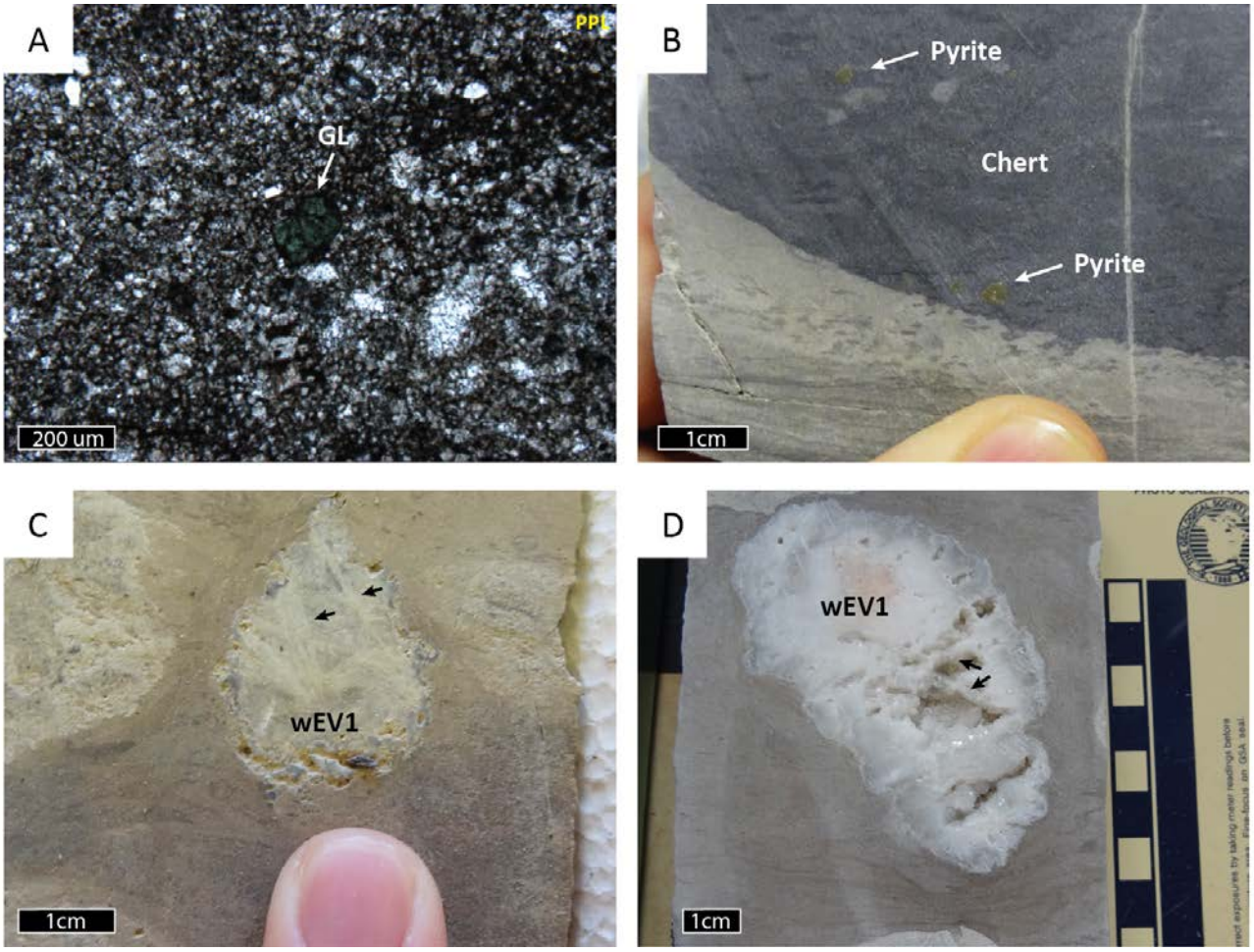

Figure 34. A) Photomicrograph illustrates an isolated, ovoid-shaped and internally featureless glauconite crystal in the matrix of an argillaceous dolosiltite. Thin section was impregnated with blue epoxy and photomicrograph was taken in plane-polarized light (*Wellington 1-32, 4026.4 ft*). **B)** Core photograph of framboidal pyrite clusters trapped inside a chert nodule. Note that sedimentary textures can be traced across the chert-sediment boundary. This texture suggests that chert nodules have a replacement origin. (*Wellington 1-32, 3770 ft*). **C)** Core photograph illustrates an example of a silicified evaporite nodule. Note the presence of randomly oriented tabular silica-polymorphs (black arrows) that resemble evaporite rosettes. This texture is typical in nodular evaporites and its sometimes preserved after silicification. Also note the displacement of the sediments around the nodule. (*Wellington 1-32, 3695 ft*). **D)** Core photograph illustrates an example of a silicified evaporite nodule. Tabular anhydrite silica-polymorphs are pointed with black arrows. Also note the displacement of the sediments around the nodule. (*Wellington 1-32, 3873 ft*).

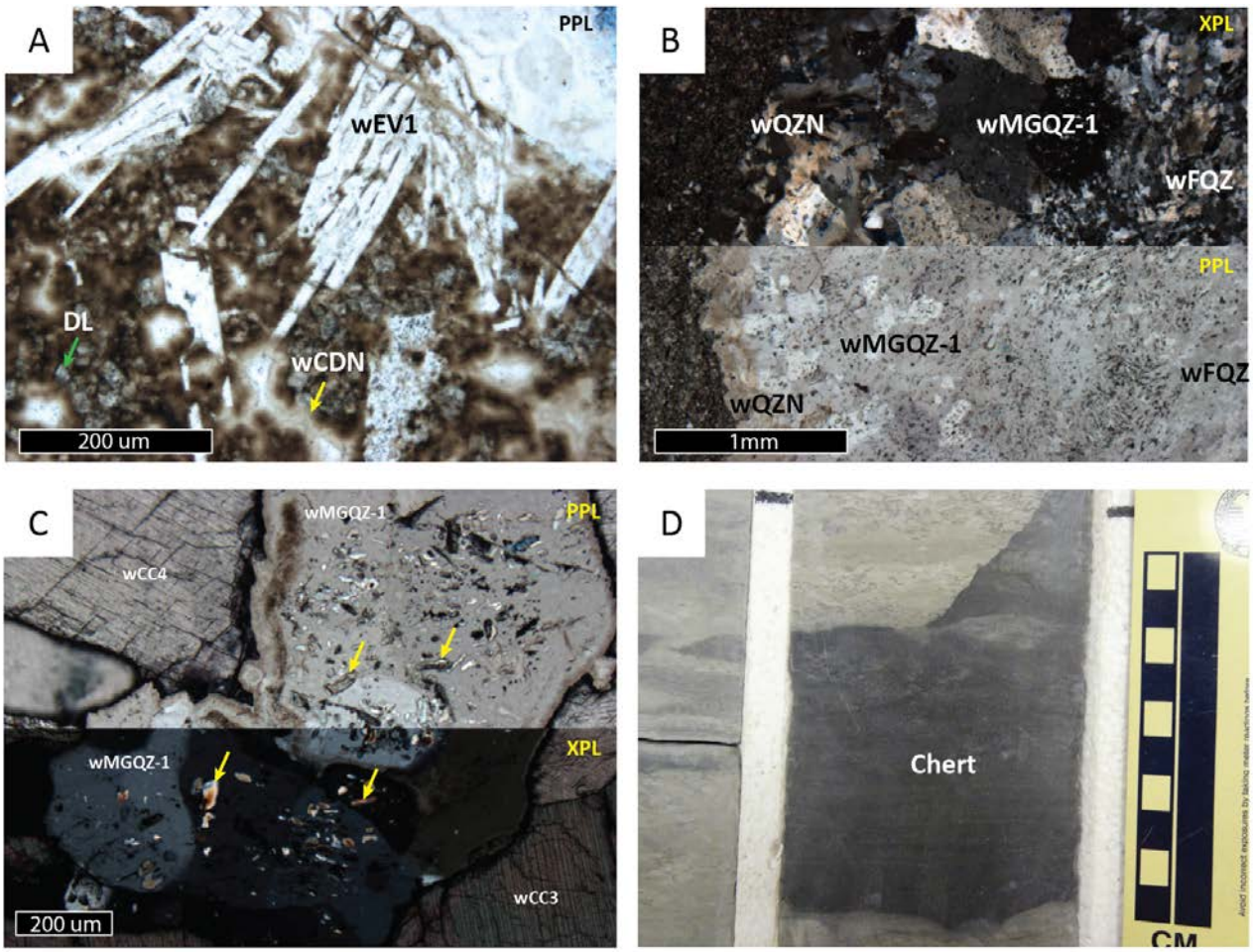

Figure 35. A) Photomicrograph illustrating silica polymorphs of evaporite laths enclosed in a chert nodule. This texture indicates that evaporites precipitated prior to chertification. (*Wellington 1-32, 3680.7 ft*). **B)** Photomicrograph illustrating a cross section across a silicified evaporite nodule (SEN). Note that the silica phases consist of quartzine (wQZN) on the edges and megaquartz (wMGQZ-1) or flamboyant quartz (wFQZ) on the interior of the nodules. Note the cloudy appearance of wMGQZ-1 due to the presence of anhydrite inclusions (*Wellington 1-32, 3823.3 ft*). **C)** Photomicrograph illustrating anhydrite inclusions inside a crystal of megaquartz (wMGQZ-1). Note the lath-like shape, and the difference in relief and interference color of anhydrite crystals (yellow arrow) from quartz. (*Wellington 1-32, 3790 ft*). **D)** Core photograph of an argillaceous dolomite replaced with chert. Note that sedimentary textures (i.e. lamination and bioturbation) can still be discerned inside the chert nodule. This indicates that chertification was a replacement event rather than a void filling cement (*Wellington 1-32, 3769 ft*).

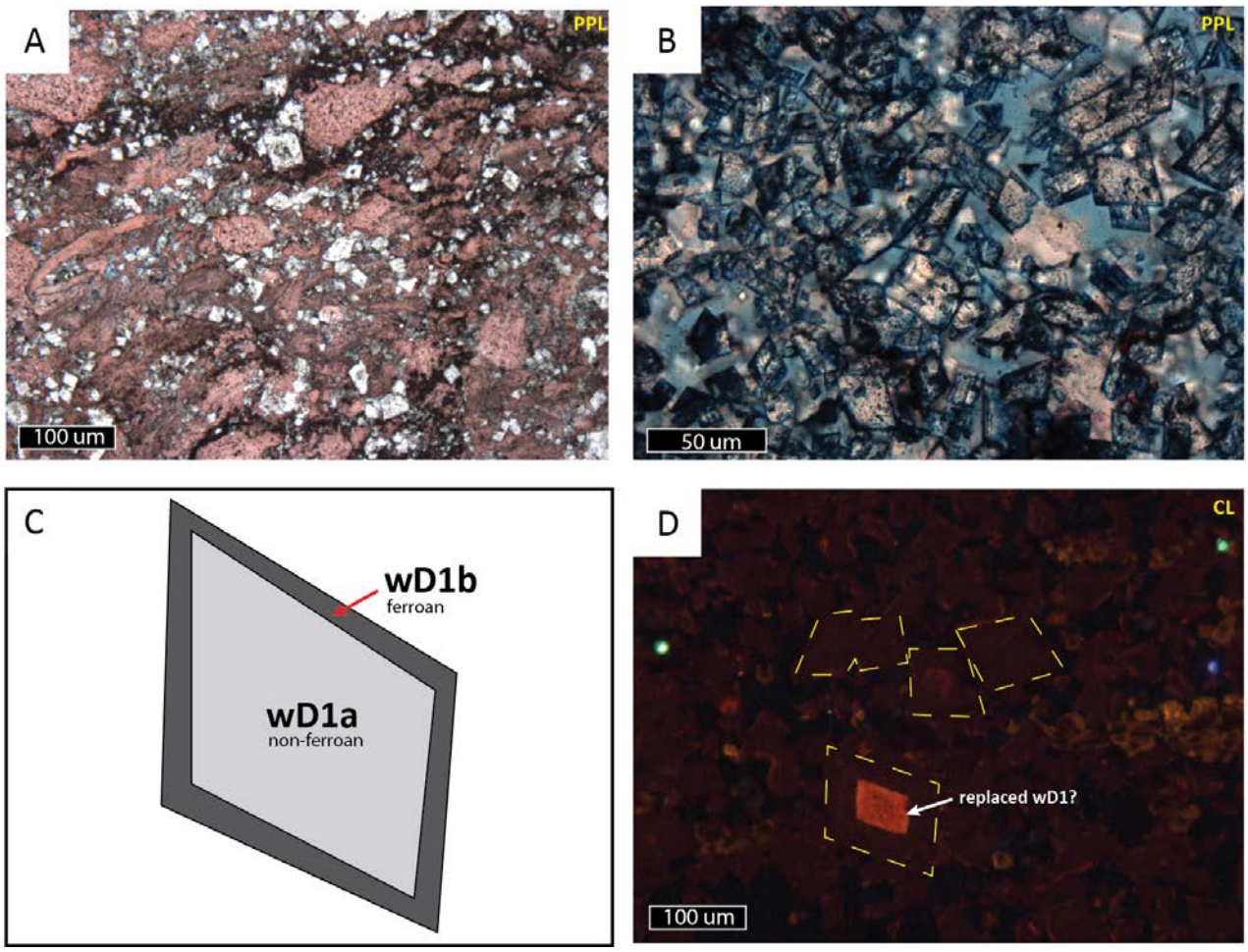

Figure 36. A) Photomicrograph illustrating dolomite rhombs (wD1) that preferentially replaces the matrix and not the calcareous fossil fragments (stained red). (*Wellington 1-32, 3883.5 ft*). **B)** Photomicrograph illustrating dolomite rhombs after being stained with a solution of alizarin red S and potassium ferricyanide. Note that dolomite edges are stained blue and the dolomite cores are not stained. This suggests that the edges of dolomite rhombs are ferroan (Dickson, 1965). Backscattered electron images and trace element data revealed that the blue-stained edges actually represent a second dolomite phase (wD1b) with an iron-rich composition (see section 4). (*Wellington 1-32, 3671.8 ft*). **C)**. Schematic diagram of the different dolomite phases and their morphologies within a single dolomite rhomb as seen under cathodoluminescence and backscattered electron images. **D)** Photomicrograph illustrating the dolomite texture under cathodoluminescence. Note that the most of the dolomite rhombs are non-luminescent. Some of the crystal edges may show a dull luminescence. A very few of the coarser dolomite rhombs may contain a luminescent core that probably represents replacement or recrystallization of the wD1b phase. However, dolomite rhombs with luminescent cores were very rarely found in the samples studied. (*Wellington 1-32, 3982.4 ft*).

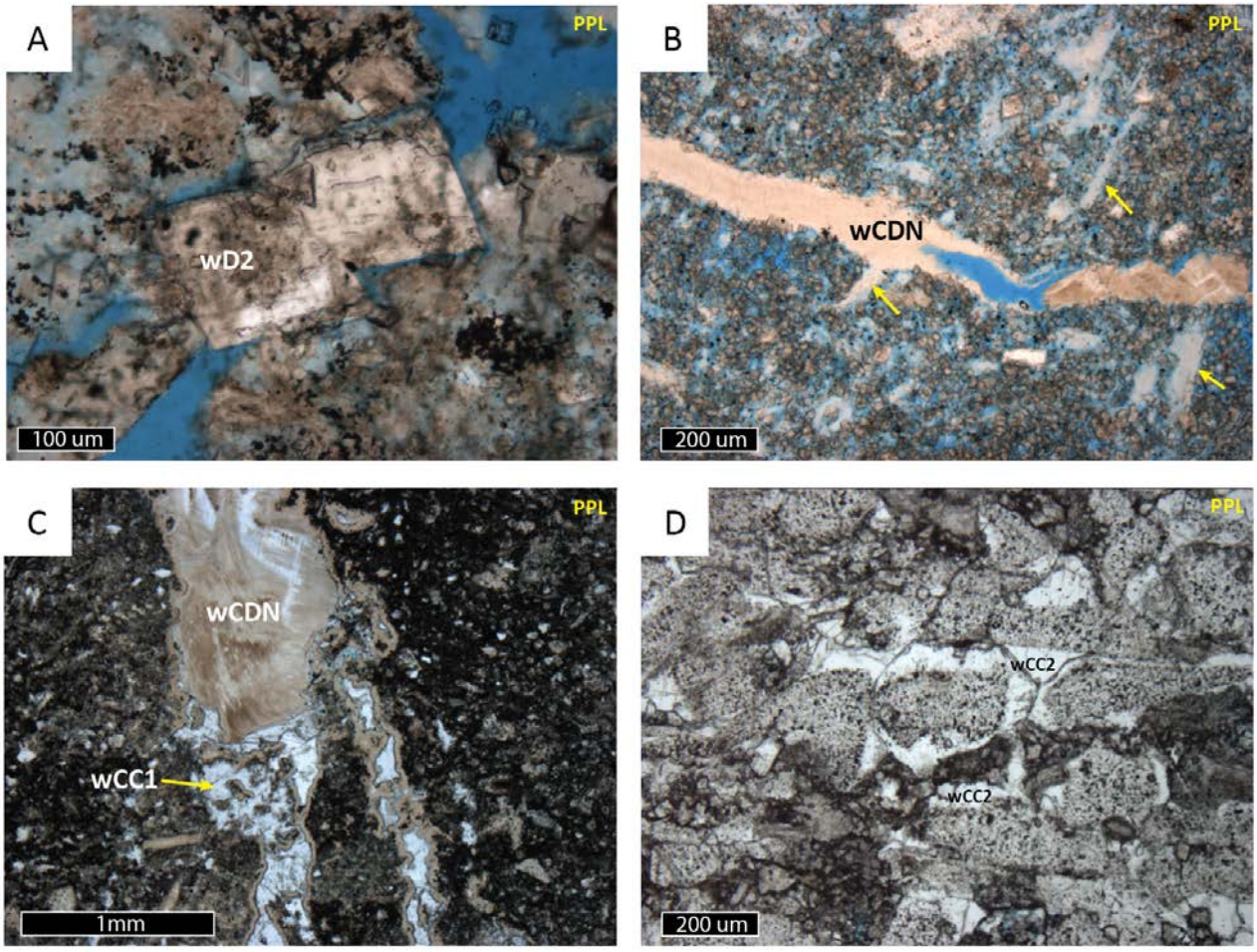

Figure 37. A) Photomicrograph illustrating the medium crystalline, void-filling dolomite cement (wD2). Note that the dolomite rhombs are coarser than wD1 rhombs. This dolomite cement occurs along chert fractures and solution-enlarged vugs. **B)** Photomicrograph illustrating a cement of chalcedony (wCDN) cementing a fracture that is cross-cutting the cherty-dolomitic matrix. Note that sponge-spicules are chertified (yellow arrows). (*Wellington 1-32, 3694.6 ft*). **C)** Photomicrograph illustrating a cavity lining of chalcedony (wCDN) followed by void-filling blocky calcite cement (wCC2). Also note that smaller vugs were cemented with wCDN. (*Wellington 1-32, 3867 ft*). **D)** Photomicrograph illustrating a syntaxial overgrowth of calcite (wCC2) on echinoderm fragments. (*Wellington 1-32, 3876.5 ft*).

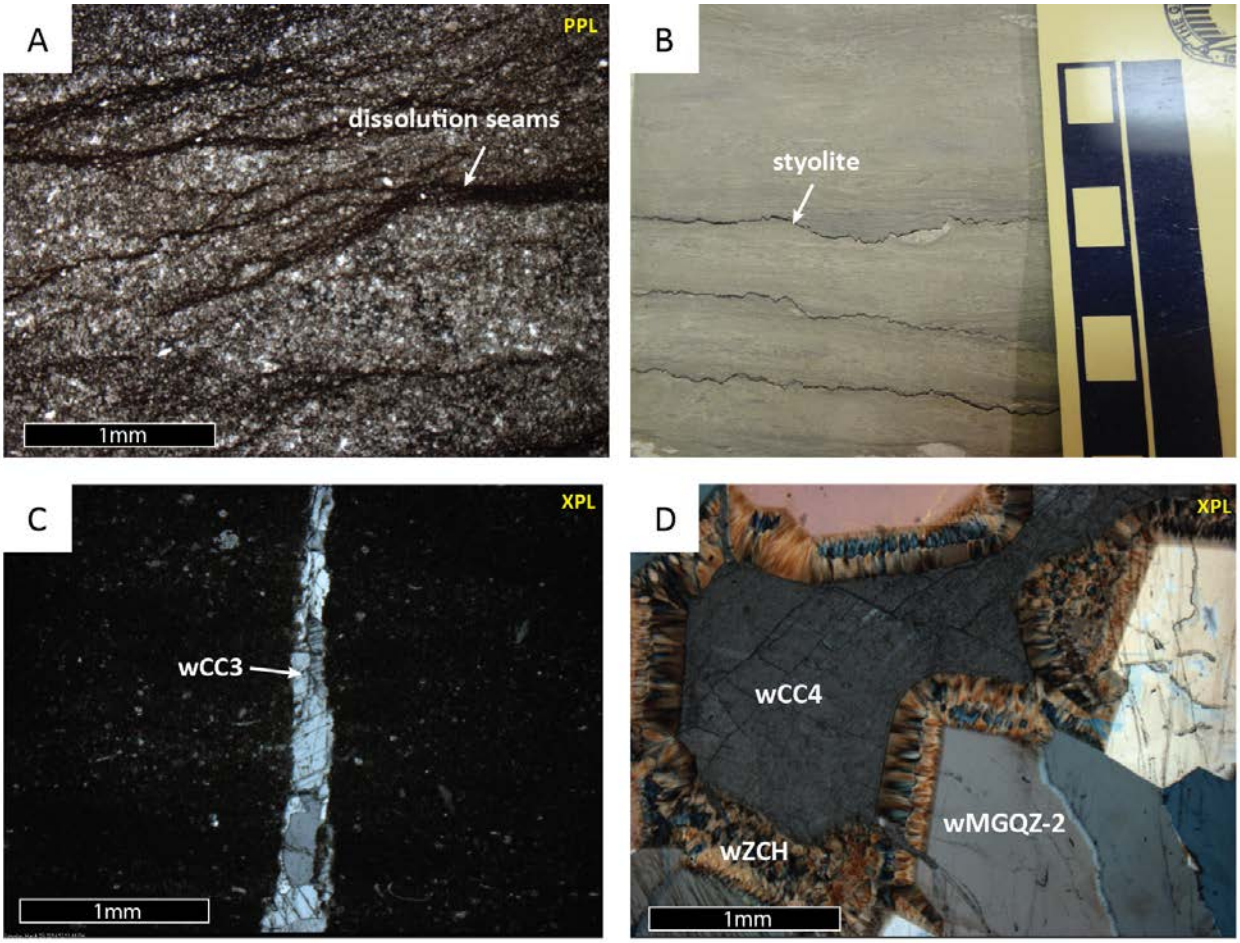

Figure 38. A) Photomicrograph illustrating horsetail dissolution seams found in fine-grained facies. Where abundant, these seams can create an apparent wispy lamination. (*Wellington 1-32, 4016.4 ft*). **B)** Core photograph illustrating the formation of stylolites. Stylolites form the same way as dissolution seams but occur on coarse-grained and dense (highly cemented or chertified) facies. (*Wellington 1-32, 3715 ft*). **C)** Photomicrograph illustrating a void-filling blocky calcite cement (wCC3) on a vertical fracture. These fractures terminate on dissolution seams and/or stylolites. (*Wellington 1-32, 3724.5 ft*). **D)** Photomicrograph illustrating the occurrence of clear megaquartz (wMGQZ-2) with an overgrowth of zebraic chalcedony (wZCH) cementing a cavity of a silicified evaporite nodule. A cement of void-filling blocky calcite (wCC4) is found after zebraic chalcedony (wZCH). All of the three cement phases are interpreted to occur under hydrothermal conditions (King , 2012). (*Wellington 1-32, 3857.5 ft*).

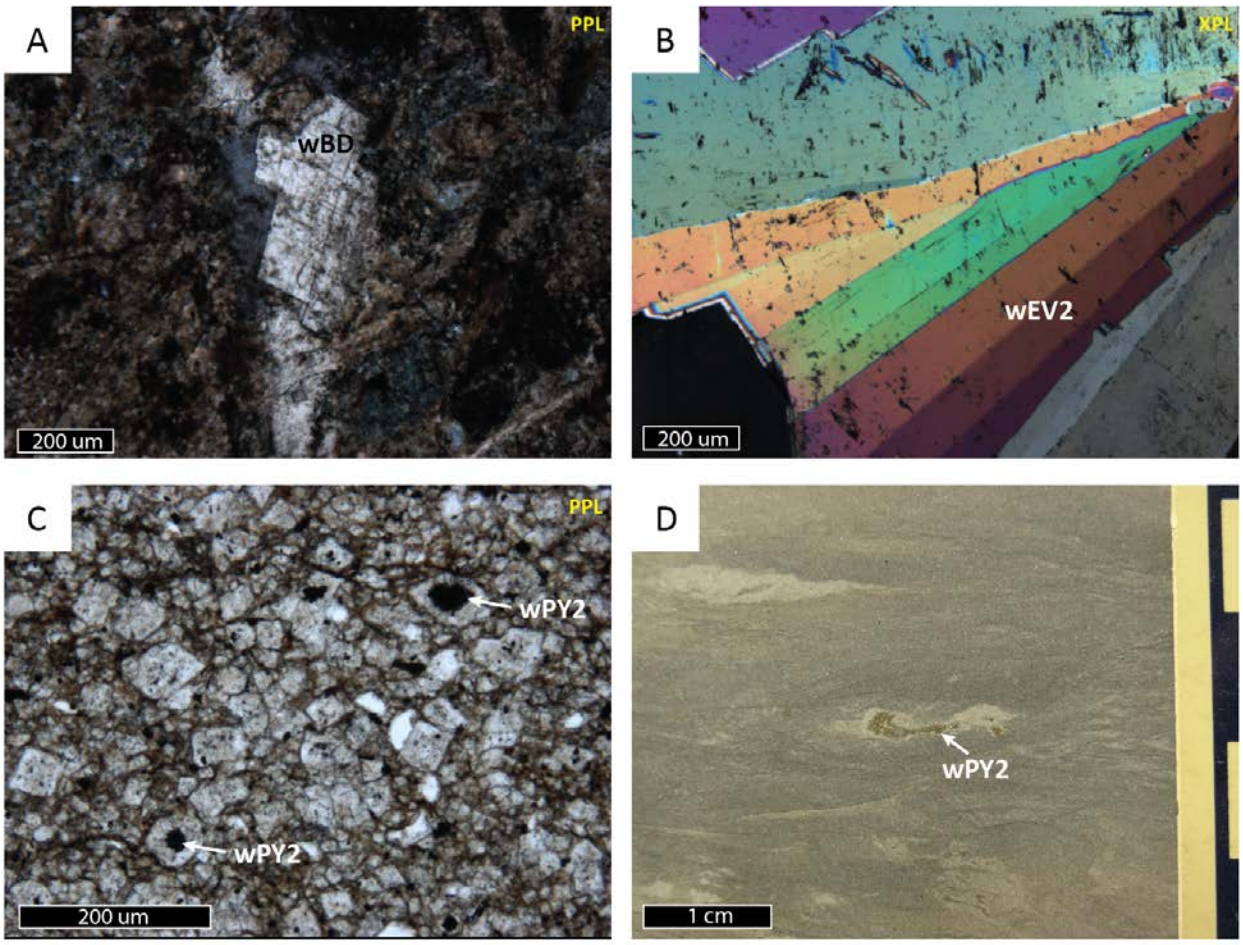

Figure 39. A) Photomicrograph illustrating cement of baroque dolomite (wBD) on an irregular cavity of microporous (triploitic) chert. Baroque dolomite is characterized by curved crystal faces and it's coarser that the early dolomite (*Wellington 1-32, 3867 ft*). **B)** Photomicrograph illustrating the coarsely crystalline tabular anhydrite (wEV2) that reduces pore space after precipitation of megaquartz (wMGQZ-2). None of the earlier cements are found in anhydrite. (*Wellington 1-32, 3694.6 ft*). **C)** Photomicrograph illustrating pyritized dolomite cores. This pyrite (wPY2) precipitated after dolomite and chert but the lack of cross cutting relationships with later stages in the paragenesis makes it difficult to tell exactly when it formed. It is likeley that it precipitated during burial when reducing conditions are prone to precipitate iron oxides. (*Wellington 1-32, 4049.4 ft*). **D)** Core photograph of the same interval as C, illustrating the occurrence of a pyritized (wPY2) cherty ltripolitic lens. Note the tendency of a polymorphic crystal shape characteristic of pyrite (wPY2). (*Wellington 1-32, 4049.5 ft*).

Paragenetic sequence of the Mississippian Limestone: *Delaney No. 1 core*, Comanche County, Kansas

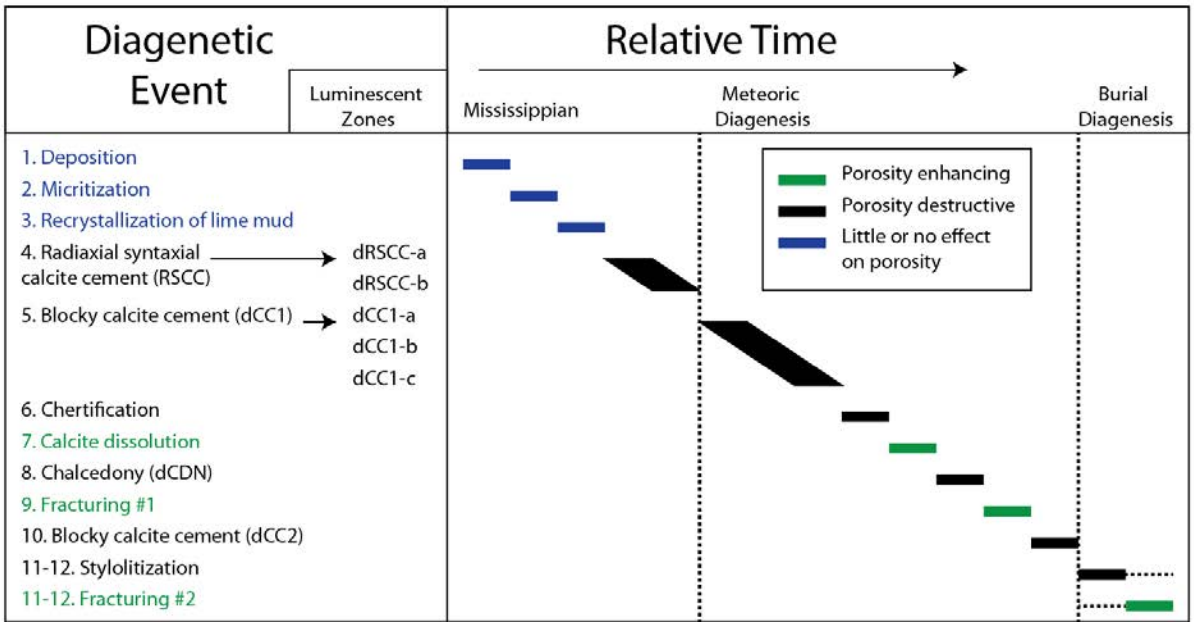

Figure 40. Paragenesis of the Mississippian Limestone in the Delaney No. 1 core location.

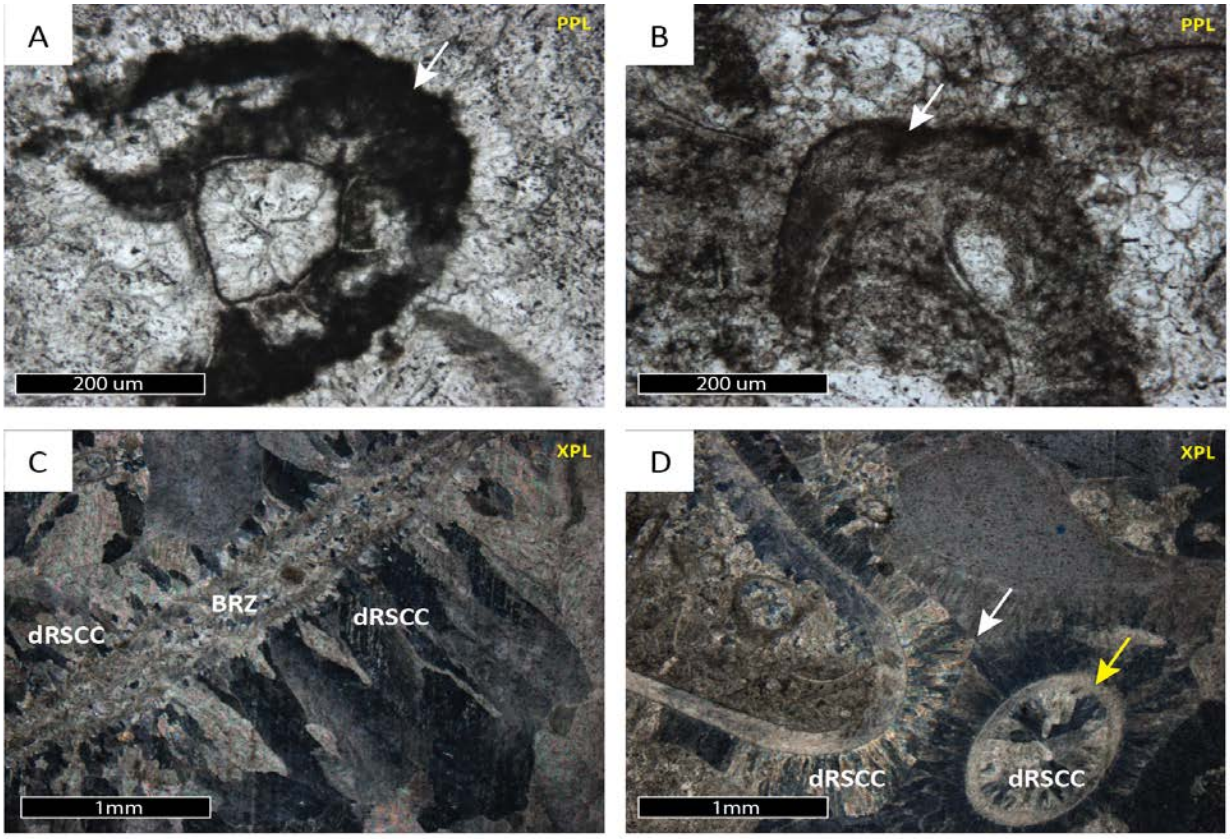

Figure 41. A) Photomicrograph illustrating the micritization (white arrow) of a bryozoan fragment. (*Delaney No. 1. 5181 ft*). **B)** Photomicrograph illustrating partial micritization (white arrow) of a bryozoan fragment. (*Delaney No. 1. 5175 ft*). **C)** Photomicrograph illustrating a radiaxial syntaxial calcite cement (dRSCC) on a bryozoan-rich packestone. dRSCC is characterized by very cloudy columnar calcite with concentral boundaries, curved twins and undulose extension. dRSCC crystal size varies greatly with some crystals reaching up to 1 mm length. Note that dRSCC occurs as a fringing cement enclosing bryozoan (BRZ) fragments. (*Delaney No. 1. 5195 ft*). **D)** Photomicrograph illustrating a radiaxial syntaxial calcite cement (dRSCC) on a bryozoan-rich packestone. Note the sharp triple crystal junction (white arrow), which suggest a fast cementation. Also note the occurrence of dRSCC on intra-skeletal pore space, in this case an ostracod fragment (yellow arrow). (*Delaney No. 1. 5195 ft*).

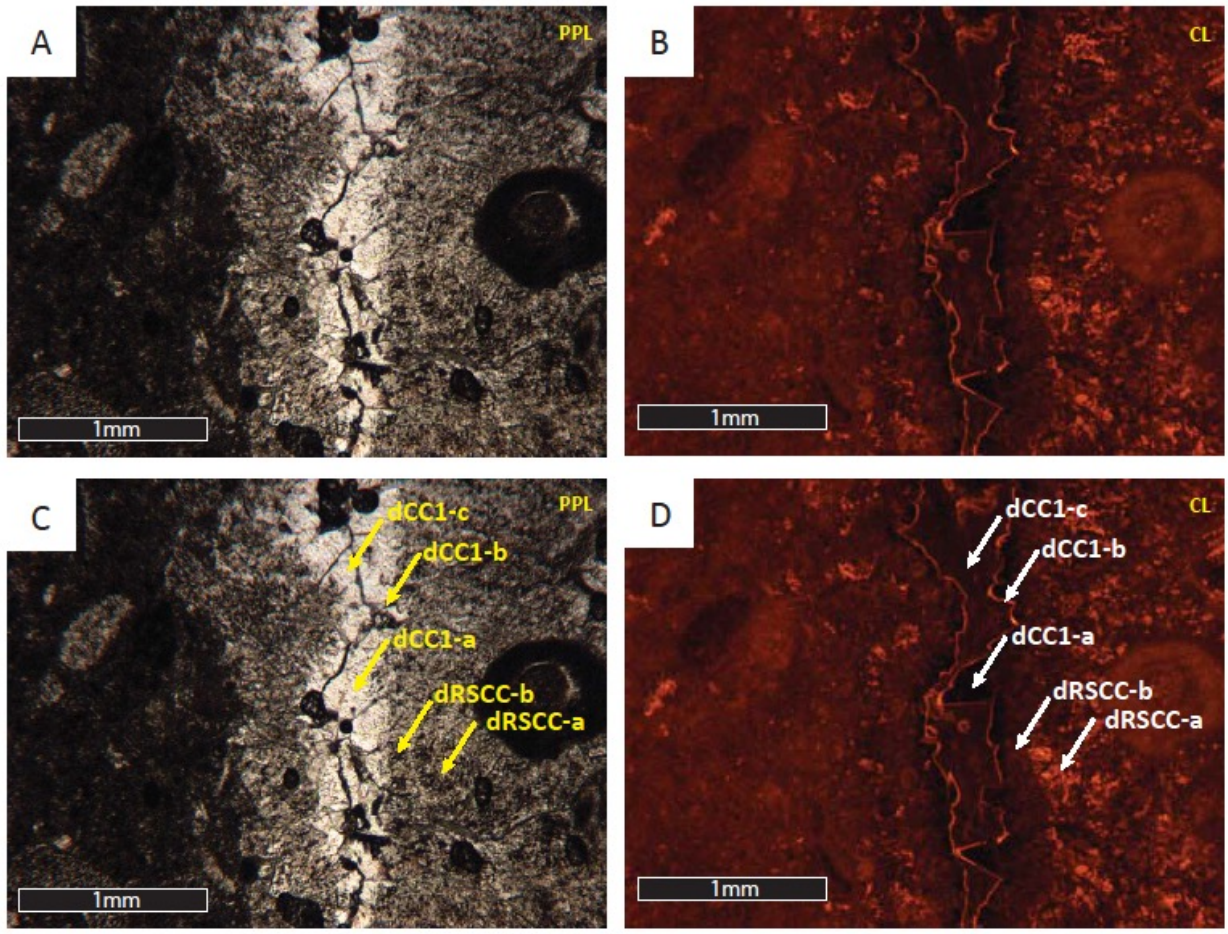

Figure 42. A) Plane polarized light photomicrograph illustrating two different calcite cements inside cavities and fractures on bryozoan packestones and grainstones. Blocky calcite cement (BCC) is characterized by a void-filling clear calcite cement that generates a drusy mosaic in primary intragranular porosity, fractures and interparticle cavities after RSCC. (*Delaney No. 1. 5205 ft*). **B)** Same as A, but under cathodoluminescence. (*Delaney No. 1. 5205 ft*). **C)** Same as A. The arrows indicate the crystal zones with different luminescence shown in D. (*Delaney No. 1. 5205 ft*). **D)** Same as A, but under cathodoluminescence. (*Delaney No. 1. 5205 ft*). Note that RSCC contains two luminescent zones. RSCC-1 has a patchy bright luminescence and RSCC-2 has a dull luminescence. The Patchy luminescence on RSCC-1 might indicate some alteration of the calcite cement (neomorphism). BCC can be divided into three zones based on luminescence. BCC-1 is non-luminescent, BCC-2 is a very thin bright luminescent band fringing the BCC-1 zone and BCC-3 is dully-luminescent zone that completely fills the rest of the cavity. (*Delaney No. 1. 5205 ft*).

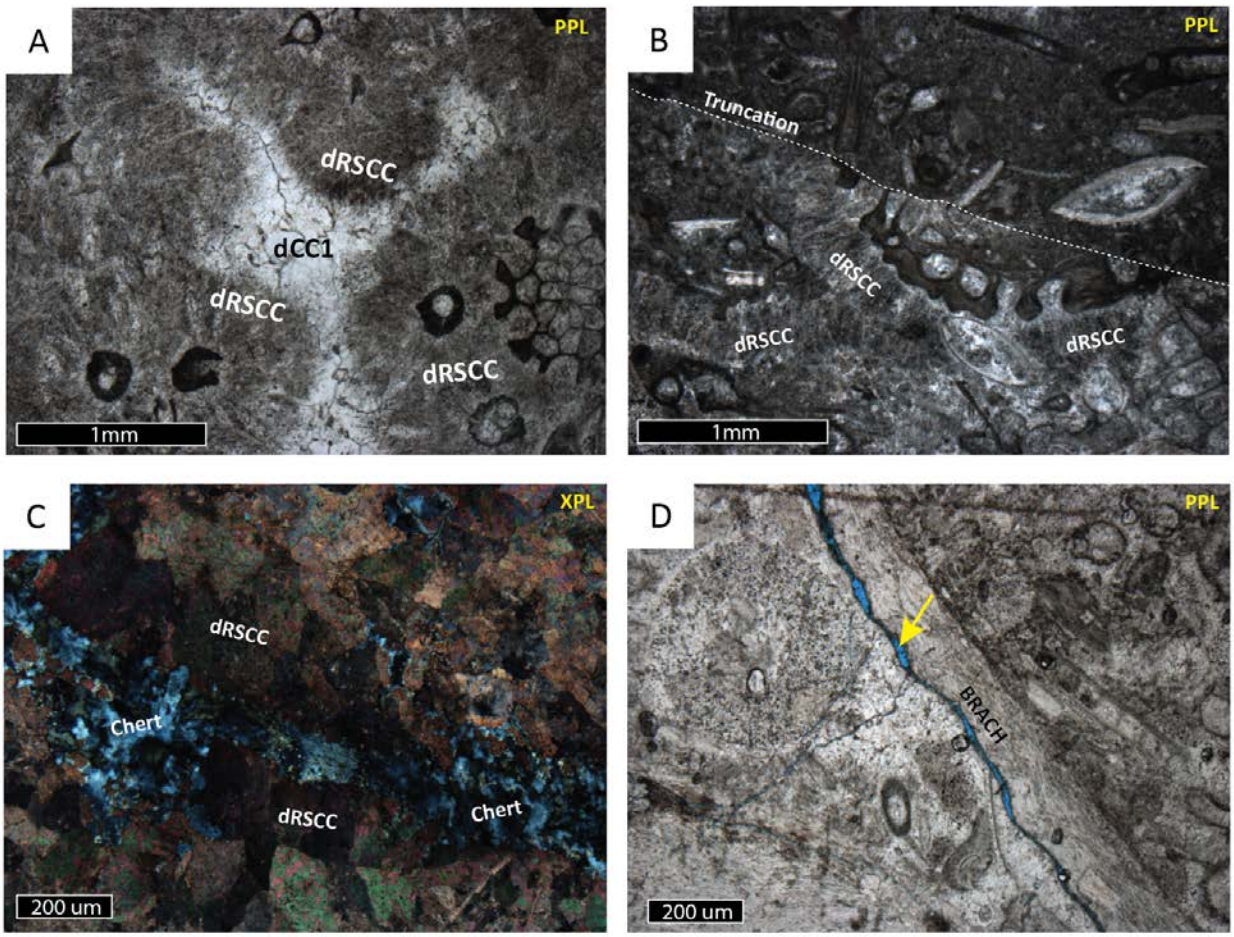

Figure 43. A) Photomicrograph illustrating dCC1 cementing the remaining interparticle porosity in a Bryozoan-rich packestone after dRSCC. Note that dCC1 is differentiated from dRSCC by a clear appeareance and a drusy texture. **B)** Photomicrograph of a truncated surface on a skeletal packestone. Notice that the truncated surface (dashed line) cross cuts a radiaxial fibrous calcite cement. The truncated surface is overlained by marine sediments. This indicates that RSCC precipitated prior erosion and reworking of marine sediments and confirms that RSCC is a very early marine cement. (*Delaney No. 1. 5205 ft*). **C)** Photomicrograph illustrating a RSCC that has been replaced with microcrystalline quartz (chert). Thin section was stained with alizarin red S. (*Delaney No. 1. 5186 ft*). **D)** Photomicrograph illustrating a brachiopod fragment with a dissolved prismatic layer. This suggests that dissolution of unstable calcite occurred. (*Delaney No. 1. 5175 ft*).

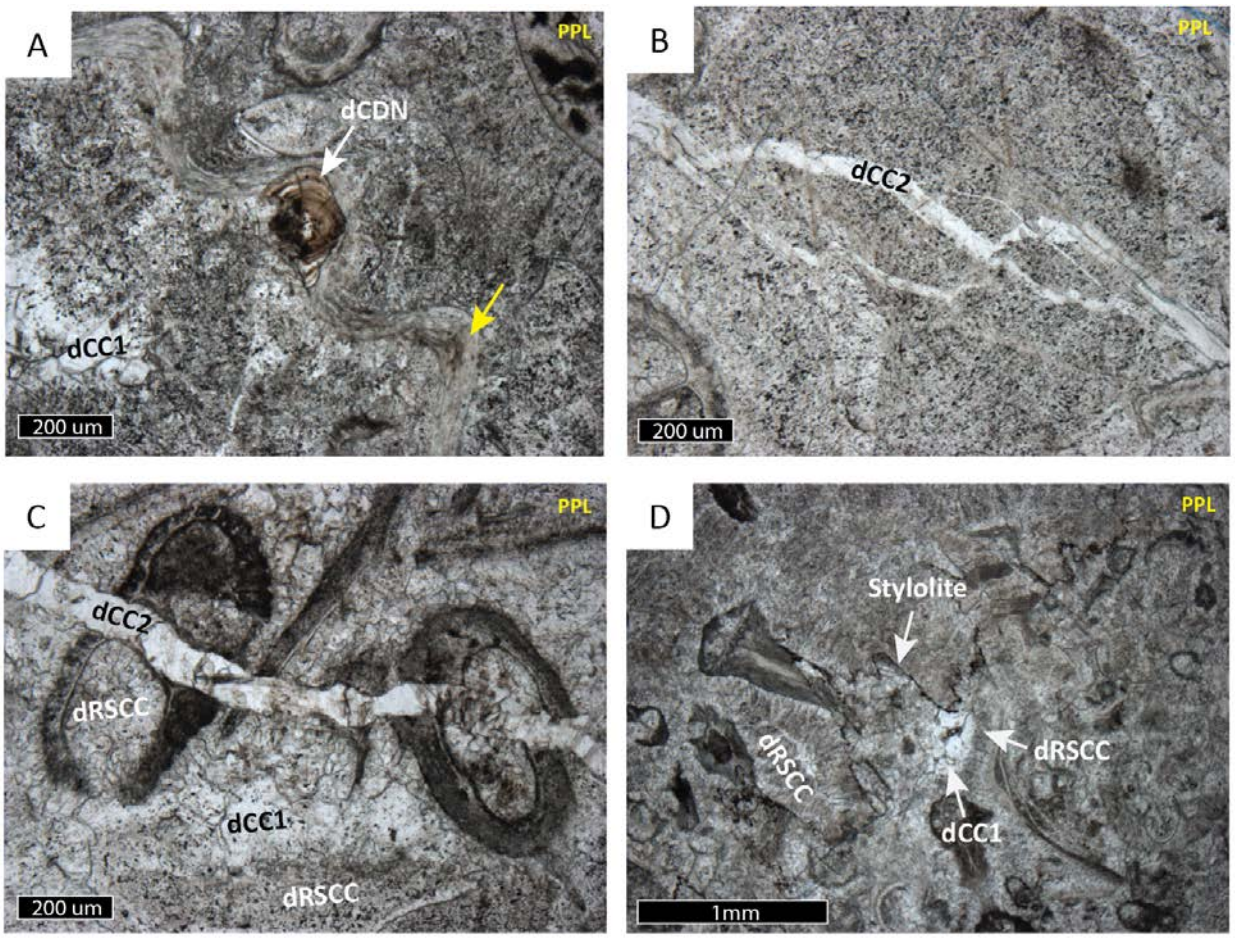

Figure 44. A) Photomicrograph of BCC occurring on a fracture. Notice that the fracture cross cuts skeletal fragments (*Delaney No. 1. 5176 ft*). **B)** Photomicrograph of BCC occurring on a fracture. Notice that the fracture cross cuts skeletal fragments cemented with RSCC. (*Delaney No. 1. 5176 ft*). **C)** Photomicrograph illustrating the paragenetic relationship between RSCC and BCC. Note that skeletal fragments (bryozoans) are enclosed with a fringing RSCC and the remaining space is filled with BCC. (*Delaney No. 1. 5181 ft*). **D)** Photomicrograph illustrating a stylolite that cross-cut RSCC and BCC. (*Delaney No. 1. 5181 ft*).

SECTION 4. GEOCHEMISTRY: STABLE ISOTOPE, ELEMENTAL CONCENTRATION AND FLUID INCLUSION DATA OF DIAGENETIC MINERAL PHASES

Rhodes field calcites

Cores: Harbaugh UB 15 and George Michael 1-8

Four generations of calcite cements (cCC1, cCC2, cCC3 and cCC4) in the Rhodes field Mississippian section were identified on thin section and core slabs, and have been petrographically described on section 3. All calcite generations are differentiated by petrographic characteristics and stable isotopic values (Fig. 45). The first generation of calcite precipitation occurs as a syntaxial calcite overgrowth (stage 16: cCC1) on echinoderm fragments. cCC1 have $\delta^{18}O$ values ranging from $^{-}4.88‰$ to $^{-}4.38‰$ PDB and $\delta^{13}C$ values ranging from $^{-}2.46$ to $^{+}2.19‰$ PDB (Fig. 45). The second generation of calcite precipitation occurs as a void-filling drusy calcite cement (stage 17: cCC2) in fractures, vugs and moldic pores after sponge-spicules. cCC2 have $\delta^{18}O$ values ranging from $^{-}5.98‰$ to $^{-}4.82‰$ PDB and $\delta^{13}C$ values ranging from $^{-}7.68‰$ to $^{-}0.28‰$ PDB (Fig. 45). The third generation of calcite precipitation occurs as coarsely crystalline poikilotopic calcite replacing siliceous cements on silicified evaporite nodules (stage 18: cCC3). cCC3 have $\delta^{18}O$ values ranging from $^{-}8.24$ to $^{-}7.59‰$ PDB and $\delta^{18}C$ values ranging from $^{-}6.09‰$ to $^{-}5.46‰$ PDB (Fig. 45). The last generation of calcite precipitation occurs as a blocky calcite cement that post-dates precipitation of Baroque dolomite (stage 25: cCC4). cCC4 has $\delta^{18}O$ and $\delta^{18}C$ values approximate to $\sim^{-}8.99‰$ PDB and $\sim^{-}1.34‰$ PDB respectively.

cCC1 and cCC2 have overlapping $\delta^{18}O$ values with highly variable $\delta^{13}C$ values. In comparison to marine Mississippian carbonate values ($\delta^{13}C \sim^{+}4.0‰$ PDB and $\delta^{18}O \sim^{-}1.5‰$

PDB; Meyers and Lohmann, 1985), the negative $\delta^{18}O$ values of both cements suggest low-temperature precipitation from depleted mixed marine-freshwater fluids. cCC1 and cCC2 $\delta^{13}C$ values are all below Mississippian marine carbonate values (Meyers and Lohmann, 1985). The large range of $\delta^{13}C$ with relative constant $\delta^{18}O$ suggests that precipitation of calcite took place from fluids deriving initial carbon from decomposing organic matter and undergoing progressive rock-water interactions. The relatively more positive $\delta^{13}C$ values of cCC1 indicate an influence of recycled carbon from locally dissolved calcite, possibly from calcareous skeletal fragments that cCC1 overgrowths. cCC1 is only found on bioclastic crinoidal packe/grainstones that are dominated by calcareous skeletal fragments, contrary to cCC2 which is found on spiculites dominated by a mixture of clay, silica and lime mud. Overall, the linear trend formed by both cements is similar to a *meteoric calcite line*, defined by relatively invariant oxygen isotopic values and more variable carbon isotopic values (Lohmann, 1988). Such trends reflect the narrow range of precipitation $\delta^{18}O$ from fresh groundwater systems (Lohmann, 1988). Petrographic crosscutting relationships indicate that the precipitation of calcite (cCC1 and cCC2) occurred shortly after subaerial exposure, which confirms the presence of freshwater influence during precipitation. Stable isotopes from cCC1 and cCC2 are consistent with the petrographic interpretations and indicate that calcite precipitation occurred under meteoric phreatic conditions.

Isotopic values of cCC3 are more depleted with respect to cCC1 and cCC2. Depleted $\delta^{18}O$ values suggest an increment in temperature with continuous burial. The negative $\delta^{13}C$ values are inconsistent with Mississippian marine carbonate values. Based on isotopic values and petrography cCC3 is interpreted to occur under shallow burial conditions.

Of all cements cCC4 shows the most depleted $\delta^{18}O$ value. From petrography it is evident that it postdates the precipitation of Baroque dolomite. This indicates that the depleted values are

the result of increased temperatures. This is consistent with petrographic interpretations suggesting that cCC4 precipitated under burial conditions.

Wellington field calcites

Core: Wellington 1-32

Four generations of calcite precipitation where identified on the *Wellington 1-32* core. Only two generations were large enough to be sampled for stable isotope analysis. Both of these can be differentiated by petrographic and isotopic characteristics. The first calcite cement occurs as a drusy cement (stage 15-16; wCC1) that precipitated along vugs and fractures after chalcedony cements. wCC1 have $\delta^{18}O$ values ranging from $^{-}9.37$ to $^{-}8.39$‰ PDB and $\delta^{13}C$ values ranging from $^{-}1.07$ to $^{+}1.18$‰ PDB (Fig. 46). The second cement sampled occurs as an equant spar calite cement (stage26-27-28; wCC4) after the precipitation of zebraich chalcedony (wZCH) and hydrothermal megaquartz (wMGQZ-2). wCC4 have $\delta^{18}O$ values ranging from $^{-}8.26$ to $^{-}7.19$‰ PDB and $\delta^{13}C$ values ranging from $^{+}1.12$ to $^{+}1.40$‰ PDB (Fig. 46).

Petrographic observations suggest that wCC1 predates wCC4. wCC1 has more depleted values and a higher variation in carbon isotopes than wCC4. The depleted oxygen values of wCC1 are probably the result of resetting of the oxygen isotopic signatures by diagenetic fluids. Therefore, these values do not represent the freshwater phreatic conditions interpreted from petrography and paragenetic relations. The $\delta^{13}C$ values are more slighlty negative than Mississippian marine carbonate values (~4‰; Meyers and Lohmann, 1985) and appear in a range that suggest the incorporation of carbon derived from organic matter decomposition.

Fluid inclusion microthermometry by King (2012) indicates that wCC4 precipitated at temperatures ranging from 93.0 to 103.5°C, which are interpreted as hydrothermal signatures.

Thus, the negative $\delta^{18}O$ values are representative of the high-temperatures of precipitation. Little change was observed in the $\delta^{13}C$. The values suggest that most of the carbon was supplied from nearby carbonates with some minor influence of organic matter-derrived carbon.

Delaney area calcites

Core: Delaney No. 1

Two generations of calcite cements from the *Delaney No. 1* core were sampled for stable isotope analysis. The first calcite generation sampled is found as fringing rims of cloudy radiaxial syntaxial calcite cement in interparticle voids (stage 4; dRSCC). dRSCC have $\delta^{18}O$ values ranging from $^{-}5.24$ to $^{-}4.32$‰ PDB and $\delta^{13}C$ values ranging from $^{+}4.29$ to $^{+}4.79$‰ PDB (Fig. 47). The second generation of calcite analyzed occurs as a drusy void-filling calcite cement (stage 5; dCC1). dCC1 have $\delta^{18}O$ values ranging from $^{-}7.14$ to $^{-}5.40$‰ PDB and $\delta^{13}C$ values ranging from $^{+}2.89$ to $^{+}4.15$‰ PDB (Fig. 47).

From petrographic observations, dRSCC pre-dates dCC1 and they occur under marine and meteoric conditions respectively. Both cements help preserve the rather delicate framework of bryozoan fronds that would have broken apart if not cemented early. $\delta^{13}C$ values from dRSCC approximate the Mississippian marine carbonate values ($\sim^{+}4$‰; Meyers and Lohmann, 1985). However dRSCC have $\delta^{18}O$ values that are depleted relative to Mississippian marine carbonate values ($\delta^{18}O \sim^{-} 1.5$‰ PDB; Meyers and Lohmann, 1985). It is possible that dRSCC had an original metastable mineralogy (i.e. high-Mg calcite or aragonite) and had been altered to a more stable mineralogy (i.e. low-Mg calcite) by freshwater alteration during meteoric stages. This is consistent with neomorphic alteration suggested from patchy luminescence observed under cathodoluminescence. The original mineralogy of radiaxial calcites has long been in dispute. Lohmann and Meyers (1977) interpreted that radiaxial calcites had an original high-Mg calcite

mineralogy based on the abundance of microdolomite inclusions. However microdolomite inclusions are not found on dRSCC. In the other hand, dCC1 has slightly more negative $\delta^{13}C$ and $\delta^{18}O$ values than dRSCC. These values are consistent with an influence lighter oxygen isotopes from freshwaters and influence of lighter carbon isotopes from degrading organic matter. Thus, stable isotopes support petrographic interpretations which suggested that dCC1 precipitated under meteoric phreatic conditions after dRSCC.

Rhodes field Dolomites

Cores: Harbaugh UB 15 and George Michael 1-8

Dolomites from stage 7-8 and baroque dolomites from stage 26 on the paragenesis of the Cowley Formation were analyzed for major- and trace-element concentrations. The two stages can be divided into five different dolomite phases based on backscattered electron images (BSE): cD1, cD2, cD3, cD4 and baroque dolomite (cBD); in order of precipitation. A total of 71 points were analyzed on the different dolomite phases.

cD1, cD2, cD3 and cD4

The first phase of dolomite precipitation corresponds to cD1 (Fig. 48) and is characterized by the darkest gray layer on dolomite crystals on BSE images. Dissolution of this dolomite removed the cores and part of its outer surfaces leaving irregular voids that were subsequently filled, cemented and overgrown with later phases of dolomite. In some areas dissolution of the outer surfaces of cD1 generated open cavities that reached the core of the dolomite crystals cD1. This indicates that dissolution of the outer surfaces and dolomite cores occur at the same time. The second phase of dolomite corresponds to cD2 (Fig. 48) and is characterized by the lightest gray layer on dolomite rhombs on the BSE images. cD2 precipitated in the dissolved cores of cD1. cD2 has an irregular outline that reflects the topographical

irregularities that existed on the inner surfaces of the once hollow cD1 crystals. Access for the fluids that precipitated dolomite cD2 would have been through the same openings that allowed the aggressive fluids to enter and dissolve the cores of dolomite cD1. The third phase of dolomite precipitation corresponds to cD3 (Fig. 4). cD3 forms as an overgrowth on dolomite cD1. cD3 typically infill dissolved cavities in the surfaces of cD1 and continuous growth results in the formation of a relatively euhedral dolomite rhombs. Of all dolomites, cD3 is the thinnest zone. The fourth phase of dolomite precipitation corresponds to cD4 (Fig. 48). cD4 occurs as a subsequent overgrowth of cD3 and further improves the euhedral shape of individual rhombohedra. cD2, cD3 and cD4 corresponds to the non-luminescent and ferroan phases (as revealed from staining) discussed in section 3. cD1 corresponds to non-ferroan (as revealed from staining) and dull to bright luminescent phase described in section 3.

None of the dolomite phases was found as an individual crystal. All dolomite crystals contain at least more than one of different phases described. This suggests that after the precipitation of dolomite cD1, most of the subsequent phases of dolomite nucleated on previous dolomite crystals. None of the dolomites was found replacing calcareous or siliceous fossils either. This can indicate a preferential replacement of the matrix due to mineralogical composition (i.e. high-Mg calcite) or abundance of nucleation sites on the matrix.

All dolomite phases are non-stochiometric, calcian dolomite (>55%Ca; Fig. 49 and 50). There are, however, noticeable changes in the Fe and Mn concentrations (Table 2). A significant difference in Fe concentrations exists between cD1 (average 1,174 ppm) and cD2 (average 81,122 ppm). Relatively similar Fe concentrations exist between cD3 (average 54,770 ppm) and cD4 (average 49,187 ppm) but they are still much higher than cD1. The Mn concentration increases in order of precipitation from cD1 to cD4 (Table 1, Fig. 50). These values are

consistent with the luminescence observed on each phase under the CL microscope. In dolomite, Mn^{2+} concentrations as low as 100 ppm are sufficient to activate luminescence while Fe^{2+} quenches the luminescence at concentrations above 10,000 ppm (Pierson, 1981; Hemming et al., 2006). Even though cD1 has the lowest Mn concentrations (average 357 ppm), it also has the lowest Fe concentrations (average 1174 ppm) allowing luminescence from Mn to occur. In contrast, the Fe concentrations in cD2, cD3 and cD4 are well above 15,000 ppm where total extinction of luminescence should occur (Pierson, 1981).

Sr and Na concentrations showed no linear trends in concentrations. The highest Sr concentrations occur on cD3 (average 516 ppm) and cD4 (average 648 ppm). The Na concentrations in cD1 (average 696 ppm) appear to be nearly twice as high as later dolomite phases. It is possible that with Na concentrations one can differentiate cD1 from later phases; however, these values are relative and not absolute. As it is still unclear where Na is located in a crystal of dolomite: either substituting for cations or trapped in fluid inclusions (Land, 1980).

Stable isotopes from these dolomite phases were not obtained due to their presence on a calcareous matrix, their finely crystalline size and the presence of more than one dolomite phase with very variable thicknesses within a single crystal.

Baroque dolomite (cBD)

As predicted from cathodoluminescence, baroque dolomite (cBD) showed no evidence of compositional zoning or multiphase precipitation on BSE images (Fig. 48). cBD have similar concentrations in Fe (average 54450 ppm) and Mn (average 3385 ppm) to that of cD3 and cD4. Also the lowest concentrations of Na (average 134 ppm) are found in cBD. Only one of the two

samples of cBD was suitable for micro sampling and stable isotope analysis. The isotopic values obtained were: $\delta^{18}O$ of ~ ⁻7.20‰ and a $\delta^{18}C$ of ~ ⁻1.33‰ (Fig. 45).

Geochemical and petrographic implications for timing and origin of dolomitization: Rhodes field dolomites

From cathodoluminescence and BSE imaging it should be clear that cD2, cD3 and cD4 are all related to dissolution/re-precipitation and overgrowth of cD1. Since it is a dolomite-to-dolomite recrystallization process, an external source of Mg is not required for precipitation of the later phases (Warren, 2000). The fact that most of the dolomites are still Ca-rich (>55%Ca; Table 2) and all the phases can be recognized by different, yet seemingly consistent elemental concentrations, suggests that the dolomites have not stabilized completely through diagenetic alteration. These provide some evidence that the trace elemental concentrations are still relatively representative of the precipitation conditions.

Dolomitization in the Cowley Formation is considered to be selective because it only replaces the matrix in the sediments but none of the calcareous or siliceous fossils. Selective dolomitization and lack of a pervasive replacement textures suggest that the diagenetic fluid was poorly saturated with respect to dolomite (Sibley and Gregg, 1987). The idiotopic planar-e mosaic suggests precipitation below the critical roughening temperature (CRT), assumed to range from 50 to a 100 °C according to Sibley and Gregg (1987). Also, petrographic cross cutting relationships (see section 3) suggest that dolomitization occurred before meteoric conditions. All these observations indicate that dolomitization replaced the sediments relatively early after their deposition.

The very low Fe and Mn concentrations on cD1 relative to all dolomite phases, along with petrographic observations suggesting that the earliest crystal of dolomite was precipitated

prior subaerial exposure and burial compaction, indicates that Dolomite cD1 was precipitated in a near-surface environment. The relatively high Na concentrations in cD1 may indicate precipitation from a seawater-derived fluid, which is also consistent with dolomite precipitation prior meteoric conditions. In general, the concentration of Fe and Mn from successive dolomite stages suggests increasing reducing-meteoric and/or burial conditions relative to cD1. The very high Fe and Mn concentrations of cD2 strongly suggest precipitation on reduced burial conditions. Possible sources for Fe can be found on clays, shales and overlying Pennsylvanian terrigenous strata. The similar concentrations of Fe and Mn between cD3, cD4 and cBD may suggest that they precipitated from similar fluids during burial conditions. The depleted $\delta^{18}O$ from baroque dolomite (cBD) is also consistent with a high-temperature precipitation during burial conditions. Overall petrography and elemental concentrations support the idea that dolomitization started early, possibly under the influence of seawater-derived fluids (source of Mg) and continued later with dolomite precipitation and overgrowths from connate waters rich in divalent cations (Fe^{2+} and Mn^{2+}; Banner et al., 1988; Warren, 2000).

Wellington field Dolomites

Core: Wellington 1-32

Dolomites from stage 8-9 (wD1a and wD1b) and stage 13-14 (wD2) on the paragenesis of the Wellington field were analyzed for major- and trace-element concentrations. A total of 93 points were analyzed on the different dolomite phases. All dolomite phases were described under BSE imaging and the petrographic observations are discussed below.

The first phase of dolomitization corresponds to wD1a. wD1a is characterized by a dark gray color in BSE imaging (Fig. 51A and 51B). It typically contains micron-sized solid inclusions that are rounded and exhibit lights gray colors in BSE imaging (Fig. 51B). wD1a is

accompanied by an overgrowth that corresponds to a secondary stage of dolomitization, wD1b (Fig. 51B). wD1b has a light gray color on BSE imaging and corresponds to the ferrous overgrowths of dolomite rhombs observed on stained thin sections. Not all dolomite crystals may show a good development of wD1b overgrowth and it tends to vary a lot in thickness from crystal to crystal. The wD1a phase dominates most of the dolomite rhombs throughout the Mississippian section in the *Wellington 1-32*.

A textural difference was observed on dolomites from different depths. Dolomite rhombs of the *cherty sucrosic dolomite* (CSD) facies found below the "chat" equivalent facies and the pre-Pennsylvanian unconformity in the *Wellington 1-32* contained the wD1b ferroan dolomite overgrowth. Dolomite rhombs lower in the section lack any visible zonation on BSE images. The wD1a phase in the CSD facies also contains a larger amount of pits mostly found in the cores of individual dolomite rhombs.

A third phase of dolomite corresponds to wD2 (Fig. 51C). The wD2 phase only occurs as a void-filling euhedral dolomite cement in open cavities. It is generally coarser than the rest of the dolomite rhombs. The wD2 phase showed no evidence of compositional zoning as predicted from petrography, staining and cathodoluminescence; and it occurs as a single phase separate from wD1a and wD1b.

Contrary to the dolomite phases in the Cowley Formation, all dolomite phases in the Wellington field approach a low-Ca dolomite (<55% Ca; Table 3; Fig. 52 and 53). Fe concentrations between all dolomite phases appear to differ the most (Table 3). Fe concentrations of wD1b (average 48885 ppm) are much higher than wD1a (average 2817 ppm) and wD2 (average 6819 ppm). wD1b also has the highest concentration of Mn (average 1114 ppm). No

significant variation was found in Sr and Na concentrations. The rounded inclusions in wD1a are variable in composition but they generally show higher Ca concentrations (up to 97.6 mol%) than the host dolomite. The large amount of Ca content suggests that the inclusions are relics of the $CaCO_3$ precursor.

The size of dolomite rhombs was too small to sample individual phases for stable isotopes analysis. As a result the stable isotope measurements obtained are weighted averages of the zoned crystals. Whole-rock dolomite samples were obtained from different depths where inter-crystalline porosity dominated or where it was filled with non-calcareous material. From petrography it is assumed that wD1a constitute the largest portion of the dolomite sampled, and in many cases it is the only one present. The dolomite samples have $\delta^{18}O$ values ranging from $^{-}5.48$ to $^{-}3.76$ ‰ PDB and $\delta^{13}C$ values ranging from $^{+}0.78$ to $^{+}2.55$‰ PDB (Fig. 46).

Geochemical and petrographic implications for timing and origin of dolomitization: Wellington field dolomites

It was deduced from petrographic interpretations (section 3) that dolomitization started early. The dissolution of dolomite along stylolites and dissolution seams and the absence of dolomite in cements interpreted to occur after meteoric diagenesis (i.e. wCDN and wCC1) confirmed an origin prior to burial diagenesis. The presence of scattered dolomite rhombs enclosed inside chert nodules indicates that dolomitization occurred at some time close to chertification. Therefore dolomitization was interpreted as an early event that occurred before subaerial exposure.

In addition to readily observable petrographic characteristics, it is assumed that the presence of undissolved relics of precursor $CaCO_3$ inside dolomite rhombs indicates that the dolomitizing fluid had lower saturations with respect to dolomite. Replacement of all

components in the sediment, regardless of mineralogy, would be expected from a highly saturated fluid with respect to dolomite (Sibley and Gregg, 1987). Also the presence of planar-e idiotopic mosaic fabrics on the dolomitized facies suggests precipitation below the critical roughening temperature (50 to a 100°C; Sibley and Gregg, 1987), which is also consistent with an early origin.

The most abundant of all dolomite phases is wD1a and is interpreted as the first stage of dolomitization. This is consistent with low Fe and Mn concentrations relative to wD1b and wD2. The second stage of dolomite precipitation is wD2 because it contains slightly higher concentrations of Fe and Mn and occurs along fractures and open cavities that are interpreted to occur during subaerial exposure. Fe and Mn concentrations obtained for wD1b are significantly higher (more than twice) than wD1a and wD2. This suggests that precipitation occurred under increasing reducing conditions where divalent cations were readily available for incorporation into the dolomite crystal. The positive correlation of the dolomite overgrowth wD1b and terrigenous siliciclastics beds above the pre-Pennsylvanian unconformity suggest that the siliciclastics where a source for divalent cations (Fe^{2+} and Mn^{2+}) during dolomitization. An alternative to this hypothesis is that wD1b precipitated from hydrothermal related fluids that also precipitated baroque dolomite. King (2012) suggested that the entire stratigraphic interval in the Wellington 1-32 works as a vertically connected regional aquifer system for hydrothermal fluids in which the highest temperatures recorded occurred on top of the Mississippian rather than on the bottom. Divalent cations in this case could have been sourced from clay minerals and underlying shales.

The low positive range in $\delta^{13}C$ of dolomite suggests normal marine water. The low negative range in $\delta^{18}O$ is not consistent with dolomite precipitation from Mississippian normal

seawater (Banner et al., 1988; Fig. 46). Negative oxygen values can result from an influx of freshwater into the dolomitizing fluid or an increment in temperature during dolomite precipitation. Both of these scenarios seem plausible based on implications discussed below.

Dolomitization occurs pervasively in the matrix of fine-grained facies (mudstones and wackestones). Most of the pervasive dolomites in the ancient rock record show some evidence of multiple periods of dolomitization (Banner et al., 1988; Warren, 2000). Petrographic descriptions suggest that dolomite size increases with increasing content of dolomite in the matrix. It was also suggested from petrography that at least 4 events of dolomitization occurred (wD1a, wD2, wD1b and wBD). It is thus very likely that dolomite growth continued after its primary precipitation. Dolomite rhombs with cloudy cores and limpid rims that are typically found on tight hypidiotopic dolomite fabrics in argillaceous facies in the *Wellington 1-32* core supports this idea. As dolomite growth continues, it does so under the influence of more dilute solutions that dissolve pre-existing calcite and precipitate dolomite. Increased fluid temperatures during progressive dolomitization could have affected isotopic composition of dolomite, shifting the $\delta^{18}O$ values towards the negatives. It is also possible that depleted $\delta^{18}O$ could be sourced from freshwater during subaerial exposure at the end of the Mississippian. A combination of these events could explain the low negative values of $\delta^{18}O$ in dolomite.

Considering the timing of dolomite precipitation, it is likely that seawater was a principal source of Mg for dolomititzation. In addition to seawater, the dolomitizing fluid may have been enriched with Mg from the dissolution of high-Mg calcite. The persistent low Sr concentrations in replacive dolomites (<500 ppm) and no evidence of recrystallization of the calcareous matrix beyond the micrite stage supports a high-Mg calcite precursor. Preservation of low-Mg calcite fossil fragments (i.e. crinoids) within pervasively dolomitized facies also supports this idea. In

addition to the Mg source an effective transport of diagenetic fluids within the sediment is necessary for pervasive replacement with dolomite. The precipitation of evaporite nodules in subtidal sediments and their presence along burrowed sections, suggests that an effective transport of fluids existed within the sediments very early. It is possible that the similar pathways were transporting the dolomitizing fluid during dolomite precipitation. Moreover, an important by-product of calcium-sulfate precipitation is the production of residual brines enriched in magnesium, which can also be available for reflux into adjacent facies and precipitate dolomite (Deffeyes et al. 1965, Chowns and Elkins, 1974; Maliva, 1987).

The exact model in which dolomitization occurred is still unclear and clearly merits more study beyond the scope of this research. Nonetheless, the integration of petrographic, stratigraphic and geochemical data leads us to believe that dolomititzation of the Mississippian section in the Welington field started early prior to subaerial exposure and was followed by various episodes of dolomitization that resulted in the pervasive replacement of the sediment.

Origin of early megaquartz (MGQZ-1) precipitation on silicified evaporite nodules in the Cowley Formation: implications from fluid inclusion petrography and salinity

SEN's have been described on the Cowley Formation and Mississippian strata in the *Wellington 1-32* core. The presence of lath-like anhydrite inclusions on early megaquartz crystals (cMGQZ-1 and wMGQ-1) found in round, translucent to milky white silica nodules is evidence that evaporites precipitated in Mississippian before silicification occurred. Determining the timing and condition of replacement of evaporites with silica is important to constrain paragenetic relations between anhydrite precipitation and silicification. Fluid inclusion analysis

is used to estimate the temperature of early megaquartz (cMGQZ-1) precipitation, the salinity of the fluid from which it precipitated, and the diagenetic environment of its formation.

Petrograpy:

SEN's are not restricted to a particular lithology, but most commonly occur on finer grained facies at all depths within the Mississippian strata. They tend to displace the sediments around them and an array of these nodules result in the typical chicken wire texture. They can be autobrecciated and sometimes they are found within the Mississippian karst breccias. This suggests that the evaporites precipitated before the sediments were lithified, but that silicification (and thus early megaquartz precipitation) occurred before karst breccias formed.

Fluid inclusions on early megaquartz have highly variable ratios of liquid to vapor (Fig. 54). Very liquid rich to very liquid poor, and all liquid inclusions may be found in a single field of view. They occur on a three-dimensional array of variable size (5 μm to 50 μm), isolated fluid inclusions. This petrographic distribution of fluid inclusions with highly variable phase ratios and the presence of all liquid inclusions cannot have occured during necking down. Fluid inclusions with a similar phase ratios along with petrographically-paired inclusions that have contrasting phase ratios would be expected on necked down fluid inclusion assemblages. Therefore, isolated fluid inclusions in a three dimensional array are interpreted as primary. The presence of anhydrite accidentals in some of the inclusions vacuole also indicates that the inclusions are primary (Fig. 54D).

Microthermometry:

Due to the highly variable ratios of liquid to vapor of the fluid inclusions Th measurements were not performed. Such values wouldn't represent the temperature of early

megaquartz formation (Goldstein and Reynolds, 1994). Salinity of the liquid phase present in each inclusion vacuole was obtained by freezing the liquid and determining the final melting temperature of ice (Tm_{ice}). The H_2O-NaCl system was selected as a representative model for the interpretation of Tm_{ice} data based on the persistence of eutectic temperatures (Te) between ¯21 and ¯33°C (Fig. 55).

Most of the fluid inclusions showed salinities representative of seawater (3.5 wt% salts) and evaporated seawater (hypersaline conditions, > 3.5 wt% salts). Petrography shows that the evaporite replacement with megaquartz formed early, even before subaerial exposure or significant burial occurred. It is therefore inferred that a source of seawater must have been close to the system that precipitated megaquartz. In other to interpret the diagenetic system correctly, a seawater model was applied for fluid inclusions that range from brackish to less than twice the salinity of seawater. This is a critical step because salinity values calculated with the H_2O-NaCl model have an 8% difference than those calculated with a seawater model. This kind of error can be geologically significant. After applying the seawater model, salinity values of the precipitating fluid ranged from 3.15 to 21.19 wt% salts (Fig. 56).

Interpretation:

The variable liquid to vapor ratio on primary fluid inclusions without evidence of necking down suggest heterogeneous entrapment. The presence of all-liquid primary inclusions indicates the formation of megaquartz at less than 50°C. Salinity values suggest that the liquid-phase was predominantly derived from seawater and evaporated seawater (Fig. 56). It is still unclear what causes the range of salinity in primary fluid inclusions. It is possible that the range is a result of fluid evolution trough the dissolution of precursor anhydrites. After the outer part of evaporite

nodules is replaced by quartz the pore waters become less saline resulting in dissolution of remaining anhydrite (Maliva, 1987). This is also what produces the characteristic central cavity in which megaquartz with anhydrite inclusions precipitates.

The occurrence of seawater-derived fluids on megaquartz has an important implication on the origin of SEN. Deepwater evaporites have been interpreted to form by dense sulfate-rich brines that are heavy enough to displace connate waters and seep slowly downward from evaporitic shelfal areas and precipitate evaporates in deep-water sediments (Dean, 1975; Scholle and Scholle, 2003; Milliken, 1979). The hypersaline and generally high-pH environment of evaporite deposition permits silicon concentrations in solution to build up to high levels (Hesse, 1990). Thus it is not surprising to find nodular evaporites replaced with silica shortly after they formed.

Hypersaline or seawater restricted conditions might have existed in the shallower regions of the Mississippian ramp (Franseen, 2006). Such conditions can occur during early stages of a transgression when the sea migrates in-land and shallow sea-water restricted zones are formed. Mazzullo and others (2009) identified short-time changes of sea-level during the Mississippian time interpreted from subaerial exposure surfaces in the Cowley Formation. These changes in sea-level could have triggered short-term hypersaline conditions in proximal sections of the ramp. These fluids could be pushed down section by changes in fluid density and reach mid- and outer-ramp sediments where they precipitate evaporite minerals; and later-on silica minerals.

Dissolution of siliceous sponge-spicules probably provides a major source of silica for megaquartz precipitation. Opal-A from siliceous sponge-spicules is readily dissolved in seawater due to the low concentration of silicon in seawater. The chemical instability of these particles can

drive dissolution-reprecipitation reactions in subbottom marine sediments (Mazzullo et al. 2009). It is possible that the same fluids responsible for anhydrite precipitation where dissolving the available silica on sponge-spicules. Once the system overloads, the excess silica can be reprecipiated as a more stable form of silica such as Opal-CT (hydrated silicon dioxide) or quartz.

Heterogeneous entrapments on near surface environments are commonly associated with the vadose zone. However, on such an environment seawater is unlikely to dominate the pore fluids. It is possible that the gas-phase in the inclusions is methane derived from methanogenic reactions in anoxic and sulfate-depleted sediments. In addition, evaporite nodules can also be found in sediments that occur within strata that show no evidence of subaerial exposure. This is the case of the Mississippian section in the *Wellington 1-32* where the largest concentrations of silicified evaporite nodules are found 140 ft below the only evidence of sub aerial exposure (pre-Pennsylvanian unconformity). Preferred concentration of such nodules in this interval might suggest that the diagenetic fluids most easily penetrated them. This interval is moderately bioturbated and nodules are commonly found within burrows. The bioturbated network would have increased the permeability of the sediments making this particular facies a favorable pathway for the diagenetic fluids.

Silica replacement of evaporite nodules corresponds to the first stages of silicification of Mississippian carbonate strata. Petrography and interpretation of fluid inclusion data on early megaquartz (cMGQZ-1) confirms that silicification started early before lithification and before sub-aerial exposure. Megaquartz replacement of evaporites occurred at shallow depths, below 50°C, and in the presence of seawater and evaporated-seawater within the sediment column.

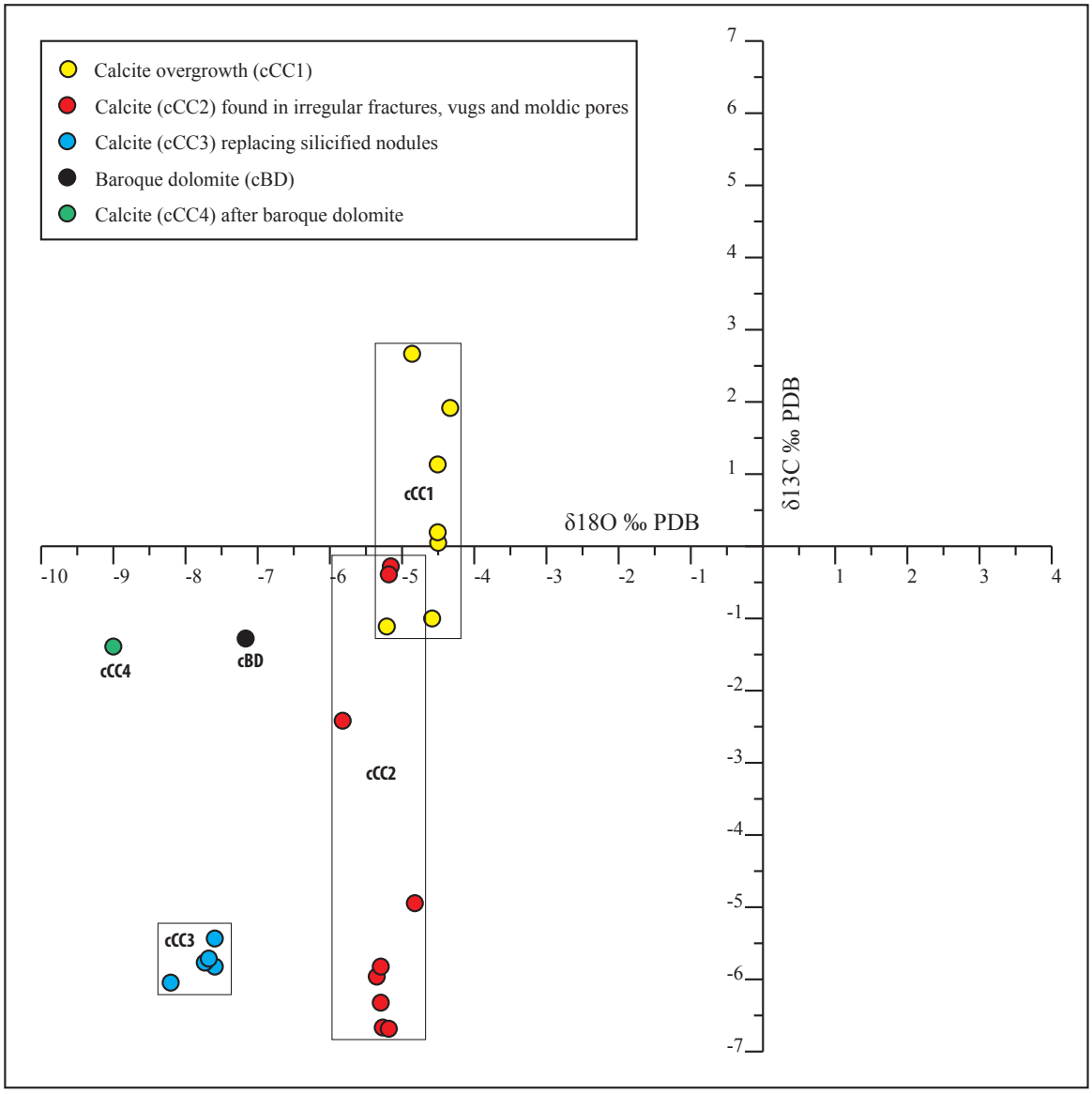

Figure 45. Cross plot of oxygen and carbon isotope data from the different calcite cements (cCC1, cCC2, cCC3 and cCC4) and baroque dolomite (cBD) in the Mississippian Cowley Formation.

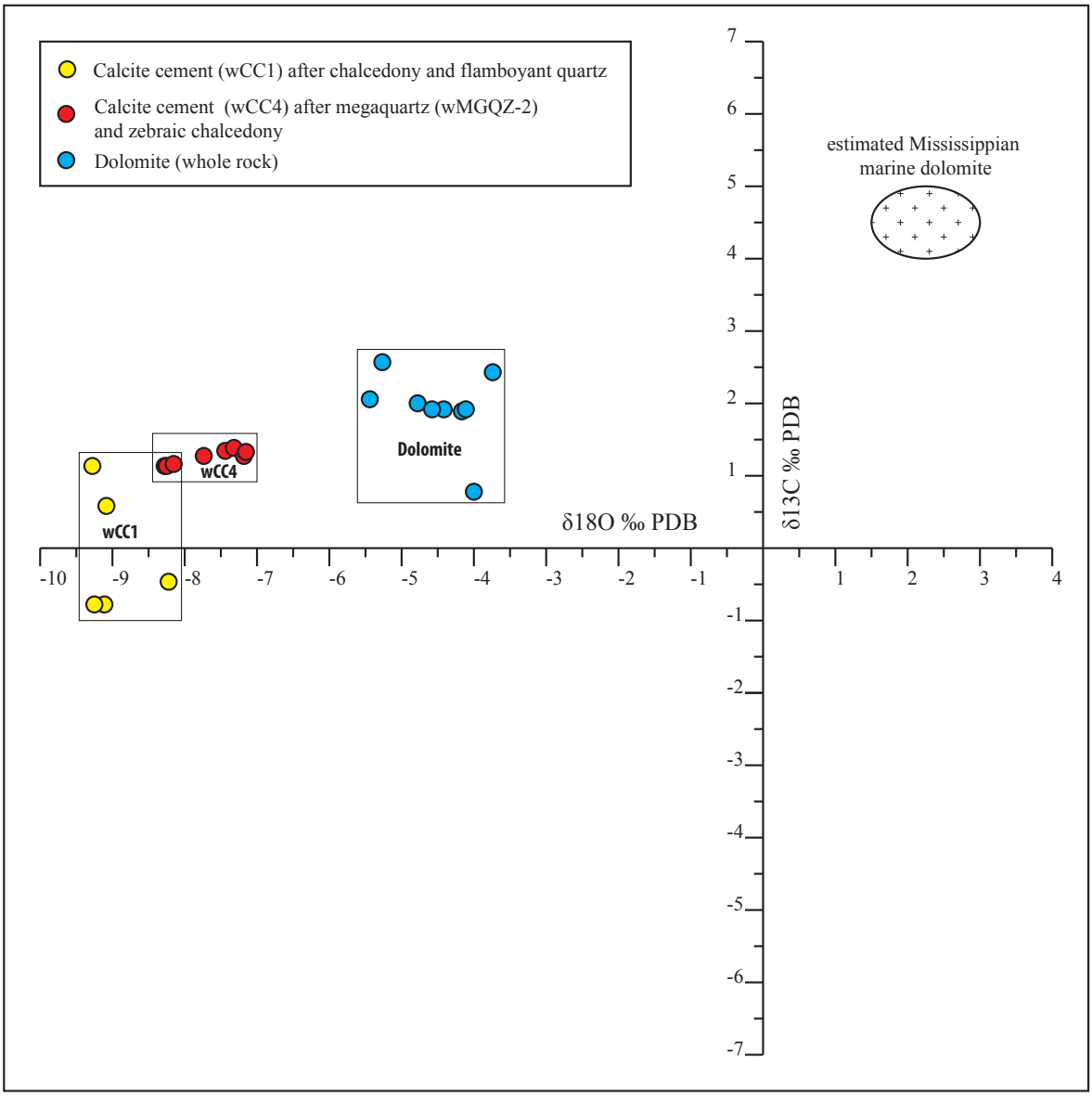

Figure 46. Cross plot of oxygen and carbon isotope data from different calcite cements (wCC1 and wCC4) and whole rock dolomite in the Mississippian section of the *Wellington 1-32* core. Estimated isotopic values for Mississippian marine dolomite are from Banner and others (1988).

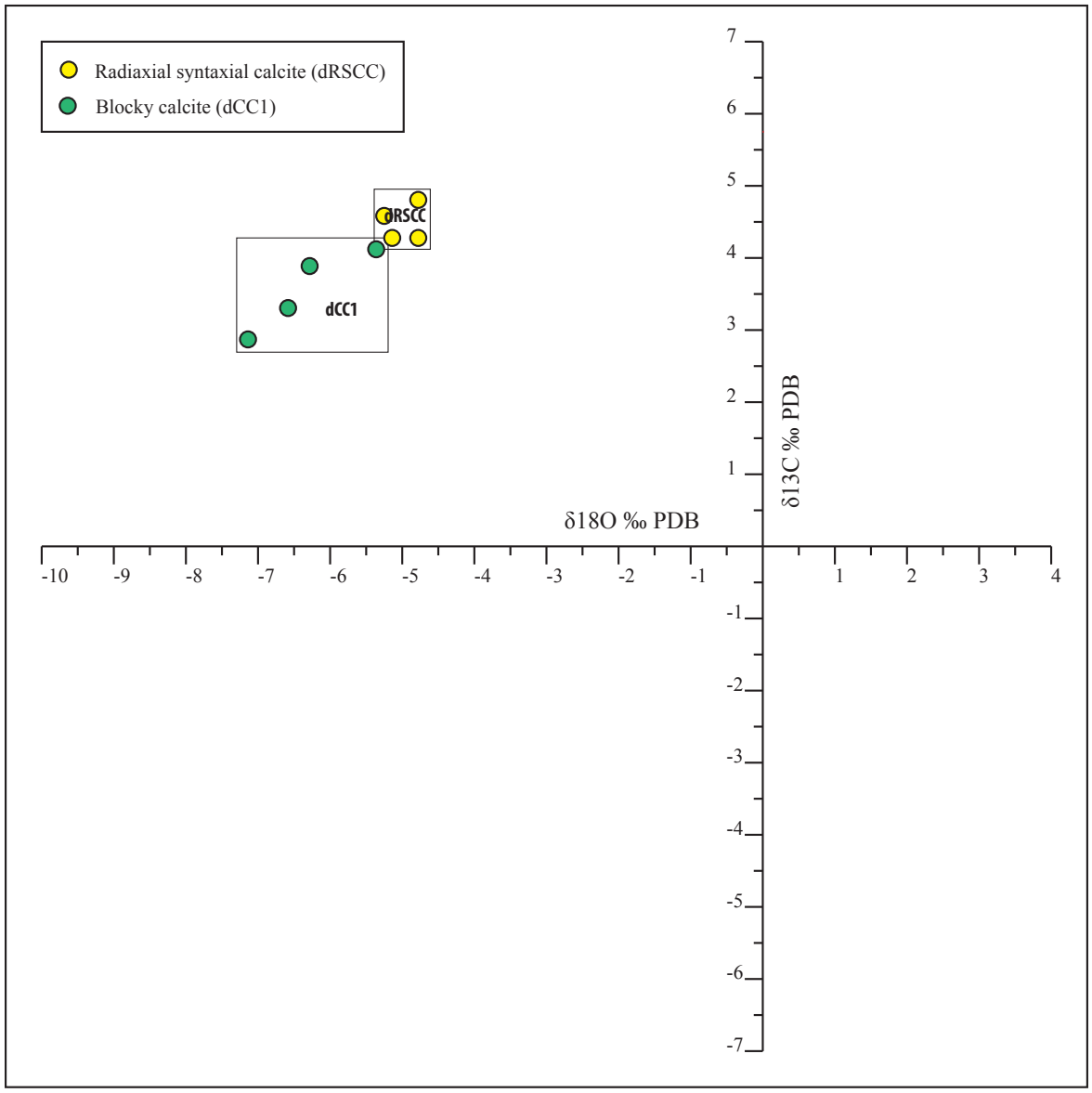

Figure 47. Cross plot of oxygen and carbon isotope data from calcite cements (dRSCC and dCC1) in the Mississippian section of the *Delaney No. 1* core.

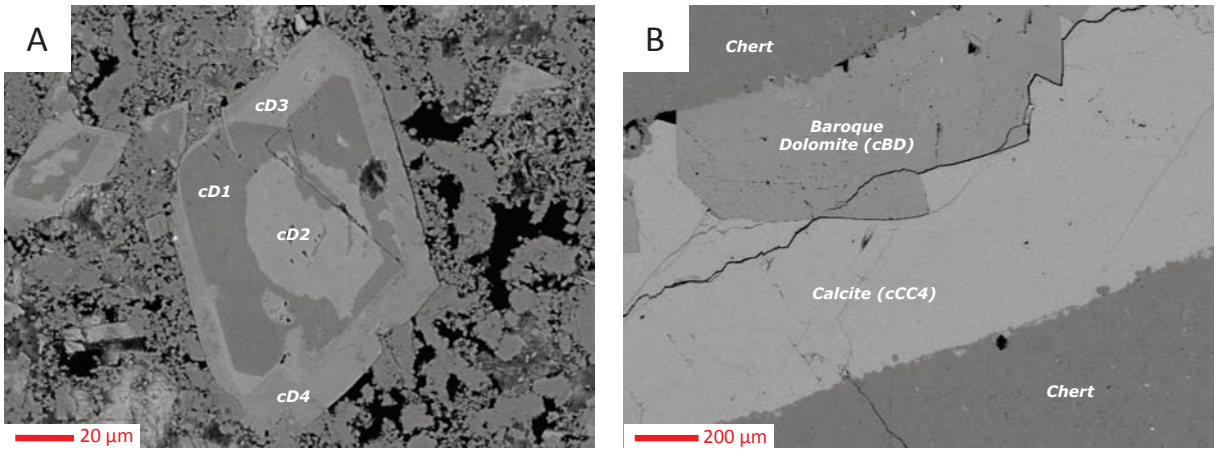

Figure 48. A) Backscattered electron (BSE) photomicrograph of a finely crystalline dolomite rhomb in the Cowley Formation showing the zoning pattern associated with dolomite phases cD1, cD2, cD3 and cD4. Note that cD2 is restricted to the dissolved cores of the dolomite crystal cD1. cD3 and cD4 occur as an overgrowth of cD2. Also note that surrounding dolomite crystals follow the same pattern regardless of crystal size. (*George Michael 1-8, 4610 ft*). **B)** BSE photomicrograph of baroque dolomite (cBD) found on a chert fracture that is also cemented with calcite (cCC4). Note the absence of compositional zoning or any evidence of multiphase precipitation. (*Harbaugh U.B. 15, 4620 ft*). A and B are both examples of crystals analyzed with the EMP. Individual sheets of the EMP analysis

Cowley Formation Dolomite

		Trace Elements							
		mol%		ppm*					
Dolomite phase	Cathodoluminescence	Ca	Mg	Ca	Mg	Fe	Mn	Sr	Na
cD1	Dull to bright luminescent	55.4	44.2	238141	115416	1174	357	251	696
cD2	Non-luminescent	55.8	29.8	229041	74170	81122	907	342	303
cD3	Non-luminescent	55.9	35.1	233358	89145	54770	2869	516	345
cD4	Non-luminescent	55.6	35.2	232209	89113	49187	3666	648	226
cBD (Baroque Dolomite)	Non-luminescent	55.3	34.7	230403	87716	54450	3385	372	134

*Average concentration in ppm. Analyses that gave values below detection limits were not included in these calculations.

Table 2. Cathodoluminescence intensities along with major- and trace-element concentrations obtain from EMP data of the different dolomite phases in the Cowley Formation (Rhodes Field).

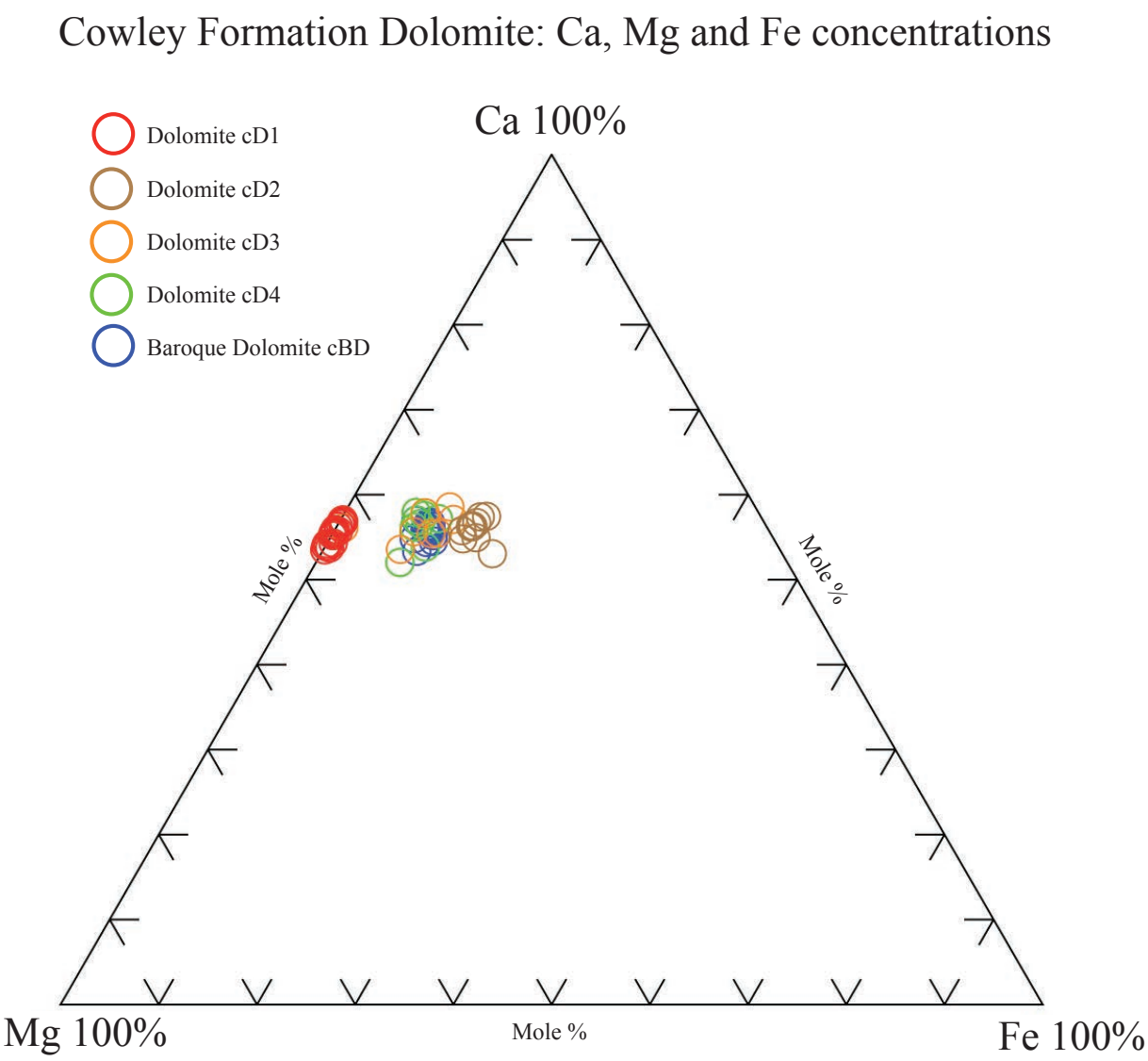

Figure 49. Ternary plot illustrating the Mole % of Ca, Mg and Fe from the different dolomite phases in the Cowley Formation.

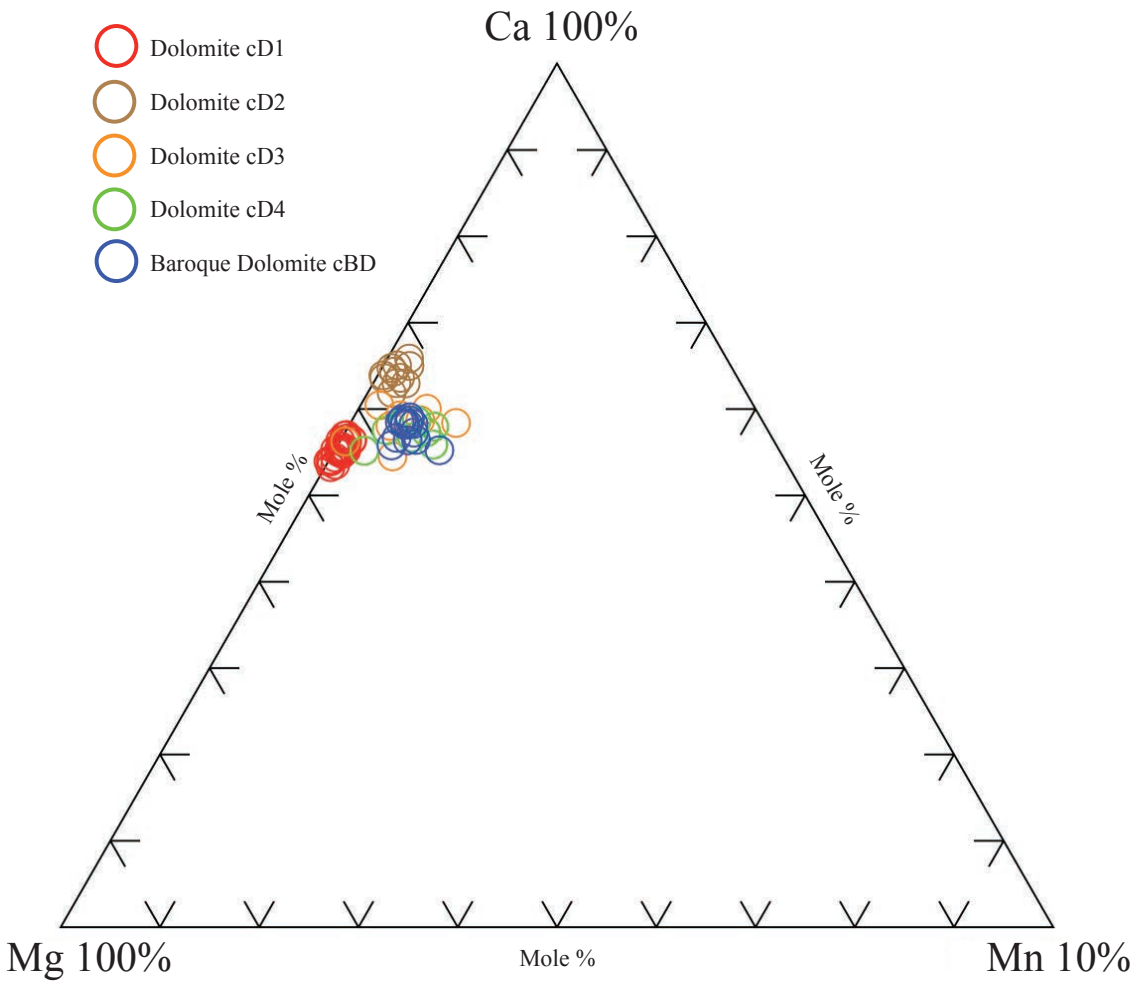

Figure 50. Ternary plot illustrating the Mole % of Ca, Mg and Mn from the different dolomite phases in the Cowley Formation. Note that the values of Manganese have been multiplied by 10 in other to observe the small changes in concentrations that would be observed on a 100% scale.

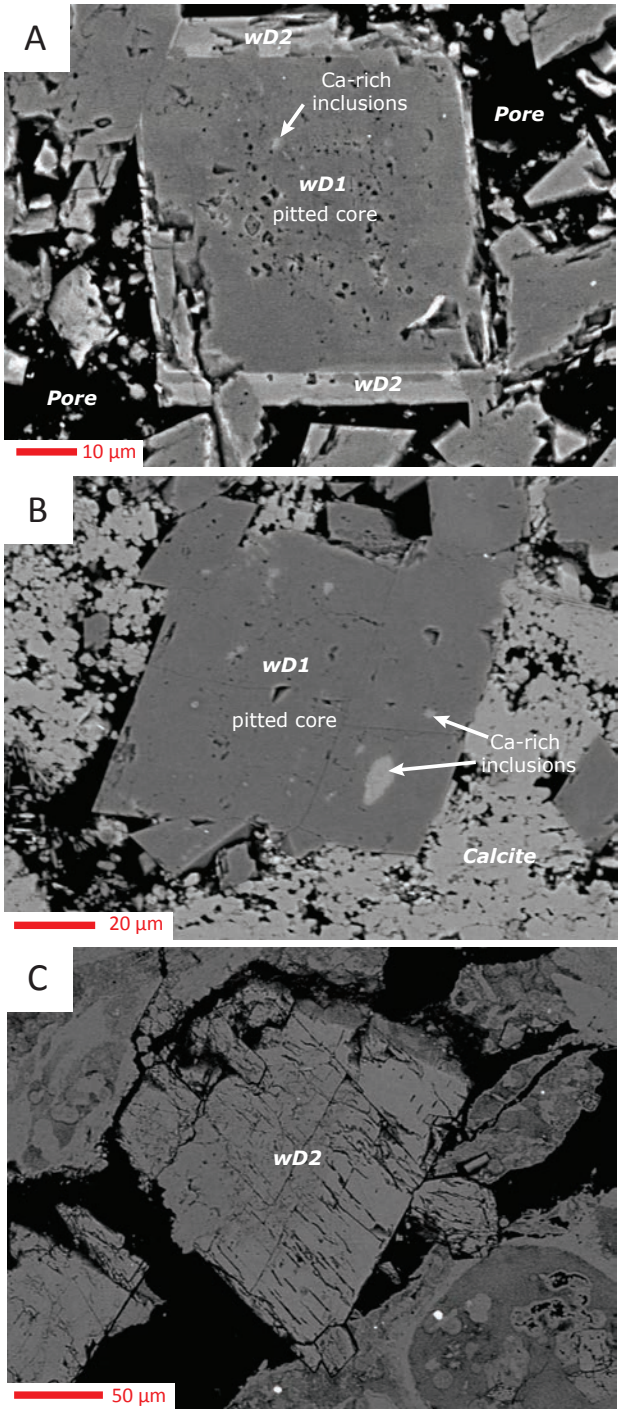

Figure 51. A) BSE photomicrograph of a finely crystalline dolomite rhomb in the Wellington field showing the zoning pattern associated with dolomite phases wD1 and wD2. Note the pitted texture of wD1 and the abundance of Ca-rich inclusions, as determined from EMP data. (*Wellington 1-32, 3671.6 ft*). **B)** BSE photomicrograph of a finely crystalline dolomite rhomb in the Wellington field. Note the relatively uniform wD1 Dolomite crystal with no visible zoning or wD2 phase. Also note the abundance of Ca-rich inclusions, much larger than in image A. (*Wellington 1-32, 3883 ft*) **C)** BSE photomicrograph of a medium crystalline dolomite rhomb from wD2 phase. (*Wellington 1-32, 3883 ft*).

Wellington Field Dolomite

		Trace Elements							
		mol%		ppm*					
Dolomite phase	Cathodoluminescence	Ca	Mg	Ca	Mg	Fe	Mn	Sr	Na
wD1a	Non-luminescent	52.8	46.7	228021	122376	2817	388	396	264
wD1b	Non-luminescent	52.3	39.0	220066	99666	48885	1114	641	255
wD2	Non-luminescent	53.2	45.6	228911	118940	6819	481	484	276

*Average concentration in ppm. Analyses that gave values below detection limits were not included in these calculations.

Table 3. Cathodoluminescence intensities along with major- and trace-element concentrations obtain from EMP data of the different dolomite phases in the Wellington field.

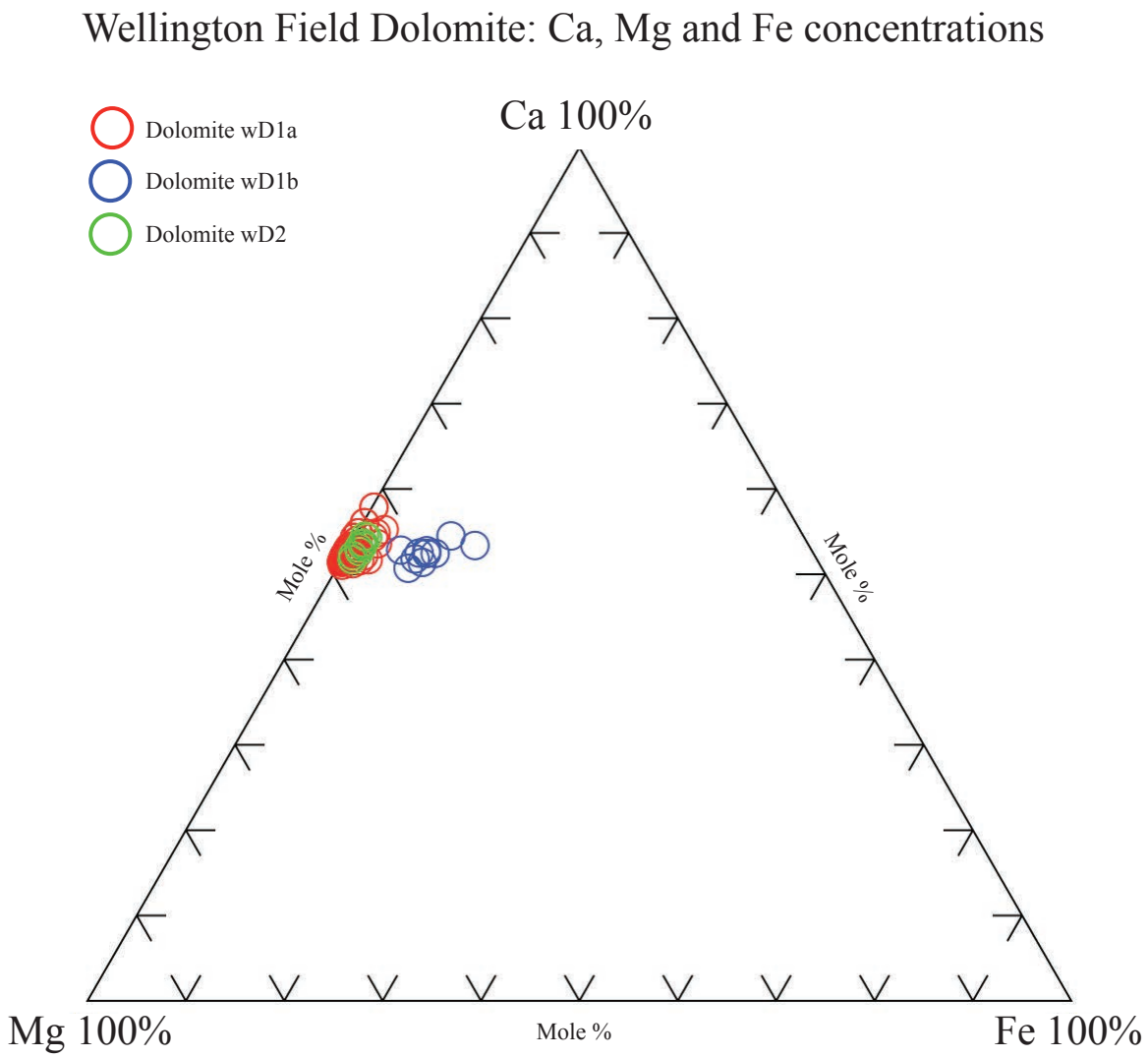

Figure 52. Ternary plot illustrating the Mole % of Ca, Mg and Fe from the different dolomite phases in the Wellington Field.

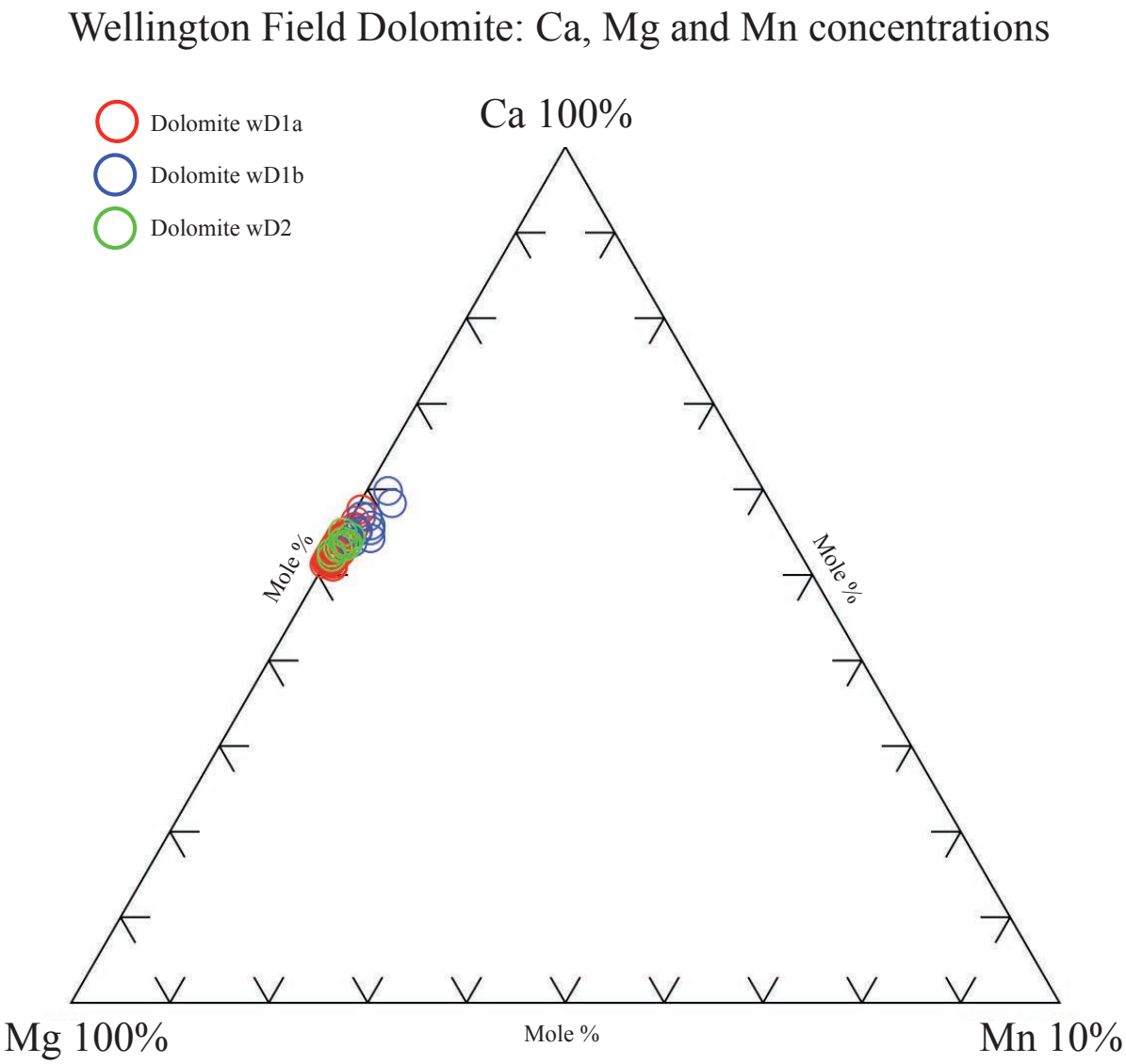

Figure 53. Ternary plot illustrating the Mole % of Ca, Mg and Mn from the different dolomite phases in the Wellington Field. Note that the values of Manganese have been multiplied by 10 in other to observe the small changes in concentrations that would be observed on a 100% scale.

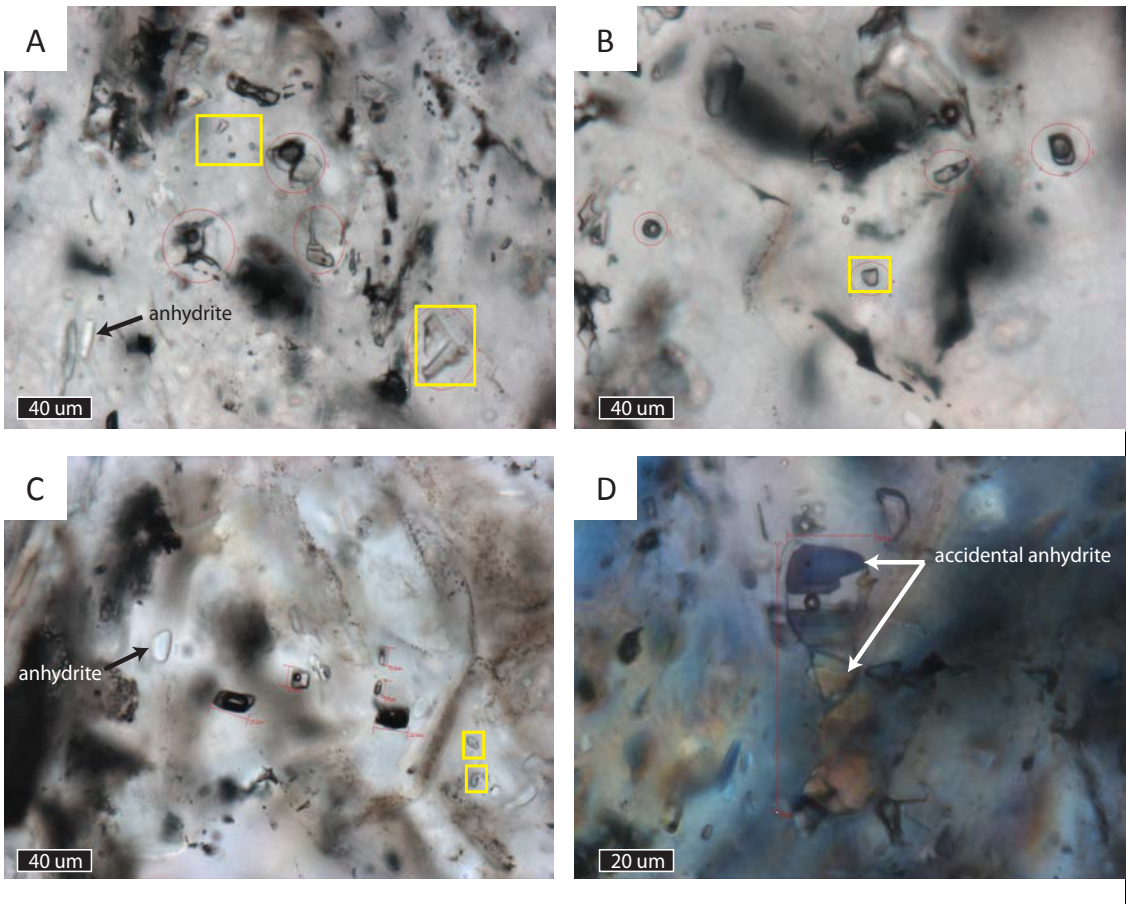

Figure 54. A) Thin section photomicrograph illustrating the three-dimensional arrangement of primary fluid inclusions with variable liquid to vapor ratios. Note the presence of liquid-rich and vapor-rich inclusions with varying sizes. Yellow squares indicate all-liquid inclusions. Anhydrite inclusions are also illustrated for comparison since they can be easily misinterpreted as all-liquid inclusions. (Harbaugh UB 15 4564.5) B) Same as A, but in another field of view (Harbaugh UB 15 4564.5). C) Same as A, but in another field of view. (Harbaugh UB 15 4564.5). D) Thin section photomicrograph illustrating the presence of an accidental anhydrite crystal inside a fluid inclusion. The presence of accidentals of precursor minerals is evidence of primary entrapment. This fluid inclusion gave the highest salinities of all fluid inclusions measured. (Harbaugh UB 15 4564.5)

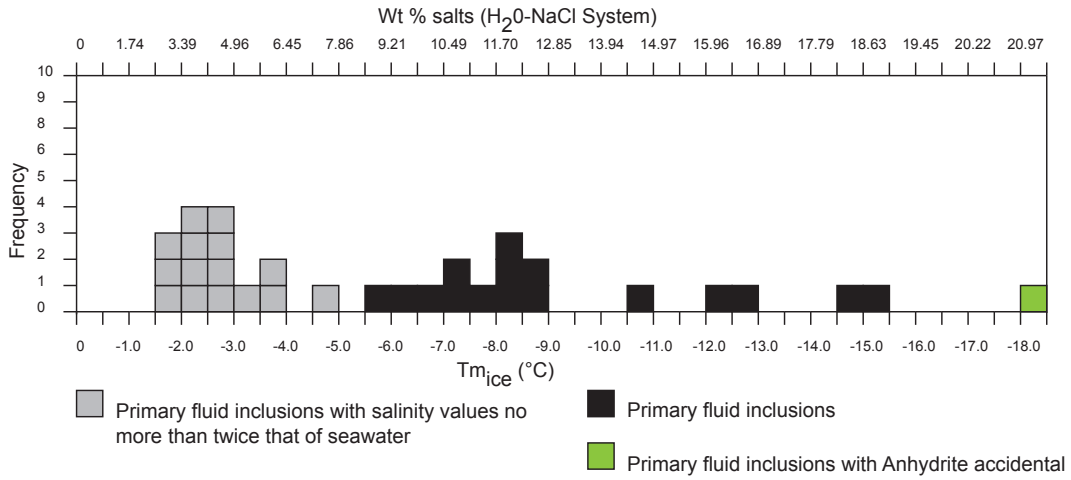

Figure 55. This histogram illustrates the final melting temperature of ice (Tm_{ice}) and respective mass percentage of salts (wt% salt) on the liquid phase of primary fluid inclusions. Calculations are based on the H_2O-NaCl model. Fluid inclusion data that was interpreted using a seawater model are shown in grey and the corrected values are illustrated in figure 6. Data of the fluid inclusion with an anhydrite accidental that showed the highest salinity is illustrated with a green square. The rest of the inclusions are illustrated with a black square.

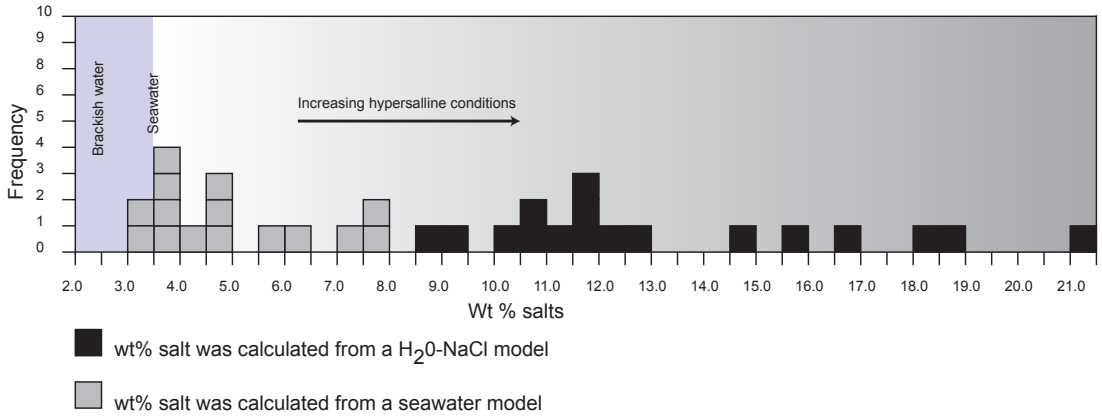

Figure 56. This histogram illustrates the calculated mass percentage of salts (wt% salt) on the liquid phase of primary fluid inclusions after the seawater model was applied to those inclusions with salinities less than twice that of seawater. Note that the salinity values suggest that the liquid-phase was predominantly derived

SECTION 5. DISCUSSION

Silicification and dolomitization

Silica (mostly chert) and dolomite are the two mineral phases that account for most of the present diagenetic textures described in Mississippian strata. Dolomitization, like silicification, ranges in degree from partial to complete recrystallization of the original limestone. Observable paragenetic relationships and geochemical interpretations indicate that these events occur early in the diagenesis at relatively close times before karstification at the end of the Mississippian and prior to mechanical compaction textures formed. Others have made similar interpretations in Mississippian strata adjacent to south-central Kansas. Franseen (2006) noted a close temporal association of dolomite, evaporites and silicification in Mississippian strata on Ness County, Kansas; all occurring early and perhaps simultaneously. Ramaker and others (2014) found evidence for dolomitization prior and after chertification in Mississippian strata in Cherokee County, Kansas. In all cases, dolomite does not appear to be replaced with any of the silica phases and chert nodules appear to engulf dolomite rhombs rather than replace them. It is possible that chert and dolomite occur simultaneously (Hesse, 1990).

The change-over from dolomitization and silicification may occur several times in the diagenetic history of a sediment (Swett, 1965; Batchelder, 1985; Hesse, 1990; Nolte and Benson, 1998). The close resemblance to each other in early paragenetic trends is linked to the precipitation under similar conditions, involving but not constrained to, the mixing zone of meteoric and marine pore waters. In these environments the pore fluids may become undersaturated with respect to calcite, and consequently supersaturated with respect either dolomite (Badiozamani, 1973) or silica (Knauth, 1979). Nonetheless the required conditions for precipitating dolomite and/or silica can be met under the sole influence of marine, meteoric or

hypersaline pore-fluids (Warren, 2000). Fluid inclusions in early megaquartz (MGQZ-1) indicated the presence of seawater and evaporated seawater (hypersalinity) during silica precipitation. Petrographic cross-cutting relationship also suggest that silica cements precipitated during various stages in the diagenesis (marine, meteoric and burial stages).

Mazzullo and others (2008) interpreted isotopic data in chert nodules from the Cowley Formation and concluded that chert first precipitated syndepositionaly from marine pore-fluids and continued precipitating from mixed meteoric-marine groundwaters, during periods of sea-level fall and eventual sub-aerial exposures. If siliceous shells are available in the coastal sediments, meteoric waters percolating trough the sediments can become supersaturated with respect to opaline silica upon dissolution of biogenic silica (in this case sponge-spicules; Hesse, 1990). Once this water gets mixed with marine connate water, it will immediately become under saturated with respect to Opal-A because of the low silicon concentration in seawater (Knauth, 1979; Hesse, 1990). However, the resulting mixing water may not become undersaturated with respect to Opal-CT and quartz (Knauth, 1979). Therefore, the siliceous sponge-spicules, which had an Opal-A composition, can be dissolved and the resulting silica be precipitated down section as Opal-CT (i.e. chalcedony) or quartz (i.e. chert). Dissolution of opaline silica from monaxon spicules can occur by an increase in pH of the pore-fluid (Flügel, 2004). An increase in pH can occur if CO_2 is removed from the pore-fluids by increasing the fluid temperature or decreasing the CO_2 partial pressure. In turn, lowering the pH of pore-fluids encourages the precipitation of silica. Bacterial decay of organic matter, including desulfurization triggered by sulfur reducing bacteria, generates CO_2, causing the dissolution of calcium carbonate and decreasing the pH of pore-fluids. Organic matter decay can thus result in a simultaneous precipitation of silica and dissolution of calcium carbonate (Eley and Jull, 1982). The occurrence

of framboidal pyrite within chert nodules can support the later case.

In other spiculitic sequences, sponge-spicules have consistently been interpreted as one important source for silicification trough dissolution and remobilization of silica from siliceous sponge-spicules by processes described above (Eley and Jull, 1982; Maliva, 1987; Nolte and Benson, 1998; Ehrenberg et al. 2001; Saller et. al 2001; Kopaska-Merkel et al., 2013). Nearly all of the chert nodules examined under thin-section contained an evidence for a former presence of sponge-spicules, either preserved (recrystallized spicules) or un-preserved (molds). The preservation of siliceous sponge-spicules in chert nodules indicates that spicule-rich sediments were preferential sites for pervasive silicification, provided that silica-bearing fluids were present. In addition to siliceous sponge-spicules, other possible sources of silica have been suggested in geologic literature, such as: the dissolution of detrital silicate minerals, weathering of clay minerals and shale dewatering. Large quantities of detrital silicate minerals would be necessary to produce massive silica replacement of carbonates making this an unlikely source of silica. Dissolution of clay minerals and shale dewatering seems logical due to the association between shale, clay and calcareous sediments in the Mississippian. However no consistent trend is observed in chert content adjacent to shaly or argillaceous units. Novaculite deposits of Mississippian age, a radiolarian-rich sedimentary rock, are found on deeper areas of the Anadarko basin (Lane and De Keyser, 1980) and could have been a tremendous source of silica by upwelling processes suggested by Lowe (1975).

Finer grained facies appeared to be more susceptible to pervasive dolomitization and silicification. Meyers (1977) has indicated that the susceptibility to replacement of various carbonate constituents by microquartz is controlled by the calcium carbonate mineralogy and particle size. Sibley and Gregg (1987) also found similar implications for replacement of

carbonate constituents by dolomite. In most of the facies, low-Mg calcite constituents such as crinoids, brachiopods and syntaxial cements are preserved. The bryozoan mound facies and crinoidal grainstones preserve most of their calcium carbonate mineralogy, and only contain minor amounts of chert and/or silica cements.

The widespread distribution of dolomitic and cherty facies is difficult to explain by a single diagenetic event. Pervasive replacement textures are usually the result of continuous rock alterations trough time. Differentiation of chert types from petrographic characteristics and isotopic compositions according to Mazzullo and others (2008) is also evident of multiple chertification events. The presence of various dolomite phases and variable dolomite fabrics is evident of multiple dolomitization events.

Although it is still unclear what was the exact environment for dolomitization; petrographic observations, paragenetic timing and geochemical analyses, leads us to believe that the first crystals of dolomites (cD1 and wD1a) precipitated in a near-surface environment from potentially seawater-derived fluids. Secondary dolomite precipitation (cD2, cD3, cD4 and wD1b) resulted from dolomite overgrowth and dissolution/re-precipitation of the primary dolomite phases. Secondary dolomite precipitation most likely occurred on the meteoric and subsurface realms as indicated by elevated trace-element concentrations and void-filling textures. Other phases of dolomite precipitation occurred under high temperatures in the subsurface, this is evident by the presence of late stage baroque dolomite cementation (cBD and wBD).

Silicification and dolomitization are both regionally abundant events but their relative abundance vary locally. This is clearly indicated by the different dolomite textures and patterns of dolomitization between the Mississippian section in the Wellington and Rhodes field. Textural and paragenetic differences can be a factor of paleoenviromental controls, and the local extent

and permeability of the facies facilitating exchange of pore waters. Thus, facies prone to a particular diagenetic texture may also vary by the timing, volume and duration that diagenetic fluids had access to.

Paragenetic assimilations between the studied Mississippian sections

The paragenetic sequences in the *Wellington* and *Rhodes* field show very similar trends in the early diagenetic stages. In addition to early dolomitization and chertification; evidence for the precipitation of evaporite nodules was found in both fields. Early evaporite nodules are also documented in other Mississippian sections at locations kilometers north of the study area on what is interpreted as a shelf setting (Franseen, 2006). It is possible that the coincident presence of evaporite nodules in marine subtidal sediments represent a regional-scale event that transported sulfate-enriched fluids through the sediments from adjacent areas where seawater was evaporating. However, no evidence of sabhka deposits have been documented in overlying Mississippian sections. Other alternatives to explain their occurrence are clearly possible. All the evaporite nodules appear to be replaced with a similar sequence of silica cements: beginning with quartzine and follwed by a mosaic of megaquartz and microflamboyant quartz. This sequence of silica cements in a nodular shape has been documented as a predictive texture of evaporite replacement with silica (Milliken, 1979) and should be expected. The timing of evaporite precipitation and silica replacement of the nodules is paragenetically similar in all areas where they were found, suggesting a widespread event that affected the ramp locations covered in this study.

Similarities were also observed in the mineral assemblage of late cements which includes: megaquartz, chalcedony (zebraic), baroque dolomite and late stage calcite cements. This mineral assemblage has been described by King (2012) in the *Wellington field* and by

Ramaker (2014) in Mississippian strata in the subsurface of south-east Kansas. The assimilation between the late stage cements in Mississippian strata and adjacent units (Arbuckle Group and Pennsylvanian System) in different locations in the mid-continent has been interpreted as a regional-scale precipitation associated to the migration of hydrothermal fluids during Ouachita and Laramide orogeny (Wojcik et al., 1997; King, 2012; Ramaker, 2014). The presence of a similar assemblage of late cements in the *Rhodes* field leads to believe that they also precipitated from genetically related hydrothermal fluids.

The facies and paragenetic relations found in the *Delaney no. 1* are very different from the ones found in the *Wellington* and *Rhodes* field. The contrasting paragenetic sequence is related to the location within the ramp, the depositional environment and primary mineralogical composition of the sediments. All of the facies in the *Delaney no. 1* underwent a large amount of early cementation with various calcite phases. Most of the calcite cements precipitated under marine and meteoric-phreatic conditions. Nontheles, silica replacement occured as small patches of chert replacing skeletal fragments.

Development of porosity

Diagenetic alterations of the Mississippian limestone also resulted in porosity development after deposition. The processes that seemed to be regionally important in the development of porosity are: dissolution of sponge-spicules, matrix dissolution (lime-mud, micrite or chert), and brecciation. Of the cores described the most easily observed porosity occurs as molds after sponge-spicule dissolution that resulted in large porosities of up to 15% (based on visual estimates). Very high porosities where also observed in dolomitizied facies where intercrystalline porosity has been calculated to reach up to 30% (Watney et al. 2013). A lot of matrix porosity observed occurs as microporosity in tripolitized chert nodules.

Microporosity was also observed along cements of chalcedony. Fracture porosity is locally important along brecciated intervals where large fractures are interconnected.

Petrographic observation suggest that most of the porosity was generated by subaerial weathering. Vuggy, fracture and microcrystalline porosity is closeley associated with sub-aerial exposure surfaces and this association has led to an interprettion of a meteoric origin for much of the porosity observed. Some of this porosity is cemented with calcite and chalcedony phases that precipitated in meteoric-phreatic conditions. Sediment infill of fractures and vugs along chert nodules also indicate that porosity was generated before compaction and lithification of the sediments. Similar interpretations have been observed throughout the Mississippian that indicates dissolution during subaerial weathering (Rogers et al., 1995; Montgomery et al., 1998; Rogers, 2001; Watney et al., 2001; Mazzullo et al., 2009; Mazzullo et al., 2011; Ramaker et al., 2014). Generation of porosity after the onset of burial diagenesis was inferred from the presence of moldic porosity after dissolution of crinoids, some of which was cemented with late stage megaquartz cements. Recent research in the Mississippian also suggested that porosity was enhanced by late events of silica dissolution associated with hyrothermal fluids (Ramaker, 2014; King, 2012). The presence of an assemblage of late stage cements associated with hydrothermal fluid migration, and the presence of open pore spaces after their precipitation, leads to infer that some of the porosity was generated later in the paragenesis and possibly hydrothermaly induced. However it is difficult to specify how much of the porosity observed is related to dissolution during subaerial exposure and dissolution during hydrothermal fluid migration.

Implications for hydrocarbon exploration

Petrographic observations lead to the conclusion that potential hydrocarbon reservoirs can be found in sponge-spicule rich facies and dolomitized facies. Typically, where any of both

constituents are found, porosity is visualy high and associated to moldic porosity after sponge-spicule dissolution and intercrystaline porosity after dolomitization. Sponge-spicule-rich facies occur where siliceous sponges colonized the sea floor and their remains accumulated into lenticular shaped pods within a calcareous or shaly matrix. Such facies are interpreted as biohermal deposits of siliceous-sponges in mid- to outer-ramp settings where upwelling of cool, nutrient-rich and silica-bearing waters provided adequate conditions for prolific sponge growth. Dolomite seems to be more abundant on fine-grained facies (mudstones and wackestones) typically related to quieter environments. However, since dolomitization was not syndepositional, the distribution of dolomitic facies is not a factor in constraining the interpretation of the depositional environment. A dominant presence of moldic and intercrystalline porosity was found on the *cherty sucrosic dolomite* facies in the *Wellington 1-32*. This facies contained the higest porosity observed in thin section samples (up to 30%). Other types of porosity (vuggy, fracture and micro-porosity) can play an important role locally. The *Bedded nodular chert* facies also contained a large amount of vuggy and micro-porosity. Mazullo and others (2009) interpreted this facies as the main reservoir in the Cowley Formation. Therefore it is clear that vuggy and microporosity greatly enhance the net porosity values within a given facies. Many studies prior this one have also suggested enhanced porosity in the "chat" facies. This incremental porosity is the result of an extensive paleokarst were all the previously desicribed porosities tend to dominate (Montgomery, 1998; Watney et al., 2001; Mazullo et al. 2009; Ramaker et al., 2014).

CONCLUSION

Mississippian strata described in three different locations: *Rhodes* field, *Wellington* field and *Delaney* wildcat area, comprises a series of lithofacies that where deposited on normal marine subtidal conditions in the inner-, mid- and outer-ramp depositional environments. Thirteen lithofacies were described including: *lenticular spiculite wacke-packestone, bioclastic crinoidal packe-grainstone, nodular and bedded cherty spiculite, porcelaneous chert, cherty sucrosic dolomite, bioclastic mudstone-wackestone, cherty and dolomitized argillaceous mudstone-wackestone, nodular and bedded dolomitized argillaceous wackestone, dolomitized lenticular bioclastic wacke-packestone, argillaceous dolomite, chert breccia, bryozoan bafflestone and bryozoan packe-grainstone*. Much of the deposition consisted of sponge-spicule debris from in-situ sponge colonies (demosponges) and/or reworking of these particles by wave action. Spiculites where deposited in quiet, nutrient-rich, well oxygenated waters as indicated by moderate bioturbation and interbedding with shales and clays. Cross stratification and laminations found on some spiculitic facies indicated periods of higher energy and possibly shallower conditions associated to inferred relative sea-level falls discussed in literature. Accumulation of spiculites was interrupted by brief episodes of calcareous skeletal debris deposition during storms. Most of the calcareous debris was transported from shallower inner-ramp settings. Facies associated with bryozoan mounds were described, but they most likely represent local structures that are not regionally widespread. Bryozoan mounds are a potential source for the calcareous debris found in mid- and outer-ramp settings. Facies associated with karstification were found on top of the Mississippian as variable solution-collapse and residual chert breccias that correspond to the Mississippian “chat” reservoirs. In addition, residual chert breccias are also found beneath surfaces of subaerial exposure that cap high-frequency cycles of

the Mississippian in the shallow ramp settings as Spivey-Grabs Field that lies north of the *Harbaugh UB 15* and *George Michael 1-8* cores (Watney et al., 2001).

The Mississippian sediments were altered many times by cementation and replacement with various diagenetic minerals, and dissolution of depositional and diagenetic constituents. Three paragenetic sequences, one for each location, was developed to compare and highlight local and regional differences. The most important and abundant diagenetic mineral phases are chert and dolomite, which partially to pervasively replaced the Mississippian sediments. They both occurred early before subaerial exposure and mechanical compaction of the sediments. Remobilization of unstable silica from the dissolution of monaxon sponge-spicules most likely explains the pervasive replacement with chert. The consistent presence of sponge-spicules in chert nodules indicates that spiculitic facies are preferentially chertified. Salinity measurements conducted on fluid inclusions of early megaquartz, a silica phase that predates chert and replaces evaporite nodules, revealed values that are consistent with seawater and evaporated seawater (early hypersalinity). This finding further lead to the conclusion that silicification processes (including chertification) began shortly after deposition of the sediments, and before complete lithification.

Dolomitization in the *Rhodes* field is texturally different than dolomitization in the *Wellington* field. Dolomites in the *Rhodes* field occur as scattered rhombs in the matrix of lenticular spiculites, while in the *Wellington* field entire lithofacies have been pervasively dolomitized. Multiple phases of dolomite were described. In both fields, primary dolomite (cD1 and wD1a) precipitation occurred in near-surface environments from potentially seawater-derived fluids and temporally associated with nodular cherts. Elevated concentrations of iron and manganese and void-filling textures characteristic of secondary dolomite phases indicate that

secondary dolomitization occurred in the meteoric or subsurface realms. Dolomitization is a complex process that altered the Mississippian strata in different magnitudes and merits further investigation to understand its origin. In particular the geometry of the dolomite body in local fields can provide an important key to understand the exact model of dolomitization (Warren, 2000). Even though the dolomite textures are different, the paragenetic timing of dolomitization in both fields seems to be very similar.

In addition to dolomite and chert, similar mineral assemblages that are temporally associated were found in different locations. The presence of early evaporite nodules in subtidal sediments seems to be a consistent phenomenon in many Mississippian locations (*Wellington* field and *Rhodes* field – this study; *Schaben* field – Franseen, 2006) and probably represents a regional-scale event. A similar case of regional-scale precipitation is inferred from a mineral assemblage of late stage cements comprising megaquartz, chalcedony (zebraic), baroque dolomite and late stage calcite which has been indicated as a predictive mineral series to indicate hydrothermal fluid migration on Mississippian and adjacent units in the mid-continent. This assemblage of late stage cements was previously found in Mississippian strata in the *Wellington* field by King (2012) and in southwest Cherokee County by Ramaker and others (2014); and this study reveals it is present in the Mississippian Cowley Formation in *Rhodes* field.

Potential reservoir porosities may be abundant in various lithofacies but highest porosities where observed in *lenticular spiculite wacke/packestone, nodular and bedded cherty spiculite and cherty sucrosic dolomites.* Visually high porosities are associated with dissolution of sponge-spicules, solution-enlarged vugs and intercrystalline porosity after dolomitization. In addition to this, microporosity was observed in many thin-sections and it is known that it further improves porosity in Mississippian chert reservoirs (Montgomery, 1998; Watney et al. 2001).

None of the calcareous facies (*bioclastic crinoidal packe/grainstone, bryozoan bafflestone and bryozoan packe/grainstone*) show potential reservoir quality. The tight nature of the calcareous facies is in part associated to early calcite cementation and large quantities of skeletal components with a more stable mineralogy. In light of this paper, prospective hydrocarbon reservoirs involve facies rich in sponge-spicule debris that had undergone dissolution (either meteoric or hydrothermal), or pervasively dolomitized facies where intercrystaline porosity dominates.

REFERENCES CITED

Abassi, R., M. H. Adabi, 2009, Application of cathodoluminescence to recognize diagenetic trends of carbonate rocks *in* A. Gucsik, eds., Micro-Raman spectroscopy and luminescence studies in the Earth and planetary science, p. 177–186.

Banner, J.L., Hanson, G.N., and Meyers, W.J., 1988, Water-rock interaction history of regionally extensive dolomites, of the Burlington-Keokuk Formation (Mississippian): Isotopic evidence, *in* Shukla, V., and Baker, P. A., eds., sedimentology and geochemistry of dolostones: Society of economic paleontologists and mineralogists special publication, n. 43, p. 97-113.

Badiozamani, K., 1973, The Dorga dolomitization model-application to the middle Ordovician of Wisconsin: Journal of sedimentary petrology, v. 43, no. 4, p. 965-984.

Batchelder, E.C., 1985, Diagenesis of Knox group (Cambro-Ordovician) carbonates exposed along Alligator creek, Bibb County, Alabama: Gulf Coast Association of Geological Societies Transactions, V. 35, p. 309-316.

Boggs, Sam and David Krinsley, 2006, Luminescence characteristics and diagenesis of carbonate sedimentary rocks *in* Boggs, Sam and David Krinsley, eds., Application of cathodoluminescence imaging to the study of sedimentary rocks, p. 109-133.

Bourque, P.A., F. Boulvain, 1993, A model for the origin and petrogenesis of the red stromatactis limestone of Paleozoic carbonate mounds: Journal of sedimentary petrology, v. 63, p. 607-619.

Brasher, J.E., and K.R. Vagle, 1996, Influence of lithofacies and diagenesis on Norweigan North Sea chalk reservoirs: AAPG Bulletin, v. 80, no. 5, p. 746–769.

Burke, R.B. and Z. Lasemi, 1995, A preliminary comparison of Waulsortian mound facies in the Williston and Illinois basins: *in* Montana geological society – Seventh international Williston basin symposium, p. 115-128.

Chowns, T. M., and J. E. Elkins, 1974, The origin of quartz geodes and cauliflower cherts through the silicification of anhydrite nodules: Journal of Sedimentary Petrology, v. 44, no. 3, p. 885-903.

Colleary, W.M., E.D. Dolly, M.W. Longman, and J.C. Mullarkey, 1997, Hydrocarbon production from low resistivity chert and carbonate reservoirs in the Mississippian of Kansas: AAPG, Rocky Mountain Section Meeting, Program Book and Expanded Abstracts Volume, p. 47-51.

Costello, D., M.K. Dubois, R. Dayton, 2013, Core characterization and modeling of the Mississippian. North Alva area, Woods and Alfalfa counties, Oklahoma: *in* M.K. Dubbois and W.L. Watney, eds., Mid-Continent Core Workshop: From source to reservoir seal; Kansas Geological Survey and Kansas Geological Society publication, p. 165-174.

Dean E., Walter, 1975, Shallow-water versus deep-water evaporates: discussion: AAPG Bulletin, v. 59, no. 3, p. 534-535.

Deffeyes, K.S., F.J. Lucia, P.K. Weyl, 1965, Dolomitization of recent and plio-Pleistocene sediments by marine evaporite waters on Bonaire, Netherlands Antilles: *in* Dolomitization and limestone diagenesis: SEPM Special Publication no. 13, p. 71-88.

Dickson, J.A.D., 1965, A modified staining technique for carbonates in thin section: Nature, v. 205, p. 587.

Dunham, R.J. 1962, Classification of carbonate rocks according to depositional texture, *in* Ham, W.E., ed., Classification of carbonate rocks: AAPG Memoir 1, p. 108-121.

Ehrenberg, S.N., N.A.H. Pickard, L.B. Henriksen, T.A. Svana, P. Gutteridge, and D.Macdonald, 2001, A depositional and sequence stratigraphic model for cold-water, spiculitic strata based on Kapp Starostin Formation (Permian) of Spitsbergen and equivalent deposit from the Barents Sea: AAPG Bulletin, v. 85, no. 12, p. 2061-2087.

Eley, Betty, E. and Robert K. Jull, 1982, Chert in the middle Silurian Fossil Hill Formationof Manitoulin island, Ontario: Bulletin of Canadian Petroleum Geology, v. 30, no. 3, p. 208-215.

Evans, C.S., K.D. Newell, 2013, The Mississippian limestone play in Kansas: oil and gas in a complex geologic setting: *in* Kansas Geological Survey: Public information circular 33, p. 1-6.

Flügel, Erik, 2004 b, Silicification of carbonates: authigenic feldspar and glauconite *in* Flügel, Erik, ed., Microfacies of Carbonate Rocks: Analysis, interpretation and application, Chapter 13: Integrated facies analysis, Section 13.1.2.1, p. 644-646.

Franseen, E.K., 2006, Mississippian (Osagean) Shallow-water, mid-latitude siliceous sponge spicule and heterozoan carbonate facies: An example from Kansas with implications for regional controls and distribution of potential reservoir facies: Current Research in Earth Sciences, Bulletin 252, part 1.

Friedman, Gerald M., 1959, Identification of carbonate minerals by staining methods: Journal of sedimentary petrology, v. 29, no. 1, p. 87-97.

Johnson, R.A., and D.A. Budd, 1994, The utility of continual reservoir description—An example from Bindley field, western Kansas: AAPG Bulletin, v. 78, p.722-743.

Gammon, P.R., N.P. James, and A. Pisera, 2000, Eocene spiculites and spongolites in southwestern Australia-Not deep, not polar, but shallow and warm: Geology, v. 28, p. 855-858.

Goebel, E. D., 1968, Mississippian rocks of western Kansas: AAPG Bulletin, v. 52, no. 9, p. 1732-1778.

Goldstein, R.H., and T.J. Reynolds, 1994, Systematics of fluid inclusions in diagenetic minerals: SEPM Short Course 31, SEPM, Tulsa, OK.

Gutschick, R.C., and C.A. Sandberg, 1983, Mississippian continental margins of the conterminous United States, *in* D.J. Stanley and G.T. Moore, eds., The shelfbreak: Critical interface on continental margins: SEPM Special Publication no. 33, p. 79–96.

Harbaugh, J.W., 1957, Mississippian bioherms in northeast Oklahoma: AAPG Bulletin, v. 41, p. 2530-2544.

Hemming, G.N., W.J. Meyers, J.C. Grams, 2014, Cathodoluminescence in diagenetic calcites; the roles of Fe and Mn as deduced from electron probe and spectrophotometric measurements: Journal of sedimentary research, v. 59, No. 3, p. 404-411.

Hesse, R., 1990, Origin of chert: Diagenesis of biogenic siliceous sediments, *in* I. A. McIlreath and D. W. Morrow, Diagenesis: Geoscience Canada Reprint Series 4, p. 227–251.

James, N.P., D.A. Feary, F. Surlyk, J.A. Toni Simo, C. Betzler, A.E. Holbourn, Q. Li, H. Matsuda, H. Machiyama, G.R. Brooks, M.S. Andres, A.C. Hine, M.J. Malone, 2000, Quaternary bryozoan reef mounds in cool-water, upper slope environments: Great Australian Bight: Geology, v. 28, no. 7, p. 647-650.

Jobe, H. and A. Saller, 1995, Oil reservoirs in grainstone aprons around bryozoan mounds, upper Harrodsburg Limestone, Mississippian, Illinois basin: AAPG Bulletin, v. 79, No 6., p. 783-800.

King, Bradley, 2013, Fluid Flow, Thermal History, and Diagenesis of the Cambrian-Ordovician Arbuckle Group and Overlying Units in South-Central Kansas, Master's Thesis, University of Kansas, Lawrence, Kansas, 198 p.

Knauth, L. Paul, 1979, A model for the origin of chert in limestone: Geology, v. 7, p. 274-277.

Kopaska-Merkel, D. C., S.D. Mann, J.C. Pashin, 2013, Sponge-microbial mound facies, in Mississippian Tuscumbia Limestone, Walker County Alabama: AAPG Bulletin, v. 97, no. 11, p. 1871-1893.

Land, L.S., 1980, The isotopic and trace element chemistry of dolomite: The state f the art, *in* Zenger, D.H., Dunham, J.G., Ethintong, R.L., eds, Concepts and models of dolomititzation: Society of economic paleontologists an mineralogists special publication, No. 28, p. 87-110.

Lane, H.R., and R.L. DeKeyser, 1980, Paleogeography of late Early Mississippian (Tournaisian 3) in the central and southwestern United States, *in* T.D. Foutch, and E.G. Magathan, (eds.) Paleozoic Paleostratigraphy of the West-Central United States: West-Central U.S. Paleogeography Symposium 1, Rocky Mountain Section, SEPM, p. 149-162.

Lazar, I., C.E. Panaiotu, D. Grigore, M.R. Sandy, J. Peckmann, 2011, An unusual brachiopod assemblage in a Late Jurrasic (Kimmeridgian) stromatactis mud-mound of the Eastern Carpathians (Haghimas¸ Mountains), Romania: Springer Verlag, Facies, v. 57, p. 627-647.

Lohmann, K.C., and W.J., Meyers, 1977, Microdolomite inclusions in cloudy prismatic calcites – a proposed criterion for former high magnesium calcites: Journal of sedimentary petrology, v. 47, p. 1078-1088.

Lohman, K.C., 1988, Geochemical patterns of meteoric systems and their application to studies of paleokarst, *in* James, N.P., and Choquette, P.W., eds., Paleokarst: New York, Springer, p. 58-80

Lowe, D. R., 1975, Regional controls on silica sedimentation in the Ouachita System: Geological Society of America, Bulletin, v. 86, p. 1,123-1,127.

MacIntyre, I. G., L. Prufert-Bebout, R.P. Reid, 2000, The role of emdolithic cyanobacteria in the formation of lithified laminae in Bahamian stromatolites: Sedimentology, v. 47, p. 915-921.

Maliva, Robert G., 1987, Quartz geodes: early diagenetic silicified anhydrite nodules related to dolomitization: Journal of Sedimentary Petrology, v. 57, no. 6., p. 1054-1059.

Mazzullo, S.J., 2000, Organogenicdolomitization in peritidal to deep sea sediments: Journal of sedimentary research: v. 70, no. 1, p. 10–23.

Mazzullo, S.J., C. Hongsheng, and B.W. Wilhite, 2008, Chert reservoirs in the Cowley Formation (Mississippian), south-central Kansas: paragenesis, oxygen and silicon isotope geochemistry, and timing of silicification and porosity formation: Kansas Geological Society Bulletin, v. 83, no. 2, p.14–20.

Mazzullo, S.J., B.W. Wilhite, and I.W. Woolsey, 2009, Petroleum reservoirs within a spiculite dominated depositional sequence: Cowley Formation (Mississippian: Lower Carboniferous), south-central Kansas: AAPG Bulletin, v. 93, no.12, p.1649–1689.

Mazzullo, S.J., B.W., Wilhite, D. R., Boardman, 2011, Lithostratigraphic architecture of the Mississippian Reeds Spring Formation (middle Osagean) in southwest Missouri, northwest Arkansas, and northeast Oklahoma: outcrop analog of subsurface petroleum reservoir: Shale Shaker: The journal of the Oklahoma City geological society, v. 61, no. 5, p. 254–268.

Merriam, D.F., 1963, The Geologic History of Kansas, Kansas Geological Survey Bulletin, v. 162, 317 p.

Meyers, W.J., 1977 Chertification in the Mississippian Lake Valley Formation, Sacramento mountains, New Mexico: Sedimentology, v. 24, p. 862-867.

Meyers, W.J. and K.C., Lohmann, 1985, Isotope geochemistry of regionally extensive calcite cement zones and marine components in Mississippian limestones, New Mexico, *in* N. Schneidermann and P.M. Harris, eds., Carbonate Cements, Society of economic paleontologists an mineralogists special publication, no. 36, p. 223-239.

Milliken, Kitty Lou, 1979, The silicified evaporate syndrome – two aspects of silicification history of former evaporate nodules from southern Kentucky and northern Tennessee: Journal of sedimentary petrology, v. 49, no 1, p. 245–256.

Montgomery, S.L., J.C. Mullarkey, M.W. Longman, W.M. Colleary, and J.P. Rogers, 1998, Mississippian chat reservoirs, south Kansas-Low-resistivity pay in a complex chert reservoir: AAPG Bulletin, v. 82, p. 187-205.

Neuweiler, F., P.A. Bourque, F. Boulvain, 2001, Why is stromatactis so rare in Mesozoic carbonate mud mounds?: Terra Nova, V. 13, p.338-346.

Nolte, Ralph A. and D. Joe Benson, 1998, Silica diagenesis of Mississippian carbonates of northern Alabama: Gulf Coast Association of Geological Societies Transactions, v. 48, p. 301-310.

Pierson, J. B., 1981, The control of cathodoluminescence in dolomite by iron and manganese: Sedimentology, v. 28, no. 5, p. 601-610.

Radke, B.H. and R.L. Mathis, 1980, On the formation and occurrence of saddle dolomite: Journal of sedimentary petrology, v. 50, p. 1149-1168.

Ramaker, E.M., R.H. Goldstein, E.K. Franseen and L.W. Watney, 2014, What controls porosity in cherty fine-grained carbonate reservoir rocks? Impact of stratigraphy, unconformities, structural setting and hydrothermal fluid flow: Mississippian, SE Kansas: *in* S. Agar and S. Geiger, eds., Fundamental Controls on Fluid Flow in Carbonates: Current Workflows to Emerging Technologies, Geological Society London, Special publication, v. 406

Rankey, Eugene C., 2003, Carbonate-filled channel complexes on carbonate ramps: an example from the Peerles Park Member [Keokuk Limestone, Visean, lower Carboniferous (Mississippian)], St Louis, MO, USA: Sedimentary Geology, v. 155, p Scotese 45-61.

Reid, R.P. and I.G. MacIntyre, 2000, Microboring versus recrystallization: further insight into the micritization process: Journal of sedimentary research, v. 70, p. 24-28.

Rogers, J.P., M.W. Longman and R.M. Lloyd, 1995, spiculitic chert reservoir in Glick field, south-central Kansas: The mountain geologist, v. 32, p. 1-22.

Rogers, S.M., 2001, Deposition and diagenesis of Mississippian chat reservoirs, north-central Oklahoma: AAPG Bulletin, v. 85, no.1, p. 115-129.

Ruppel, S.C., and S.D. Hovorka, 1995, Controls on reservoir development in Devonian chert: Permian Basin, Texas: AAPG Bulletin, v. 79, p. 1757-1785.

Saller, A.H., D. Van Horn, J.A. Miller, and B.T. Guy, 1991, Reservoir geology of Devonian carbonates and chert—implications for tertiary recovery, Dollarhide field, Andrews County, Texas: AAPG Bulletin, v. 75, p. 86-107.

Saller, A., B. Ball, S. Robertson, B. McPherson, C. Wene, R. Nims, J. Gogas, 2001, Reservoir characteristics of Devonian cherts and their control on oil recovery: Dollarhide field, West Texas; AAPG Bulletin, v. 85, No. 1, p. 35-50.

Sibley, D.F. and J.M. Greg, 1987, Classification of dolomite rock textures: Journal of sedimentary research, v.57, p. 967-975.

Scholle, Peter A. and Dana S. Scholle, 2003, Ch 28: Silica replacement and cementation *in* Scholle, Peter A. and Dana S. Scholle, eds., A color guide to the petrography of carbonate rocks: grains, textures, porosity, diagenesis: AAPG Memoir 77, p. 414.

Scotese, C.R., 1999, Paleomap project: http://www.scotese.com (accessed October 2014).

Swett, Keene, 1965, Dolomititzation, silicification and calcitization patterns in Cambro-Ordovician oolites from northwest Scotland: Journal of sedimentary petrology, v. 35, no. 4, p. 928-938.

Taylor, K.G. and J.H.S. Macquaker, 2000, Early diagenetic pyrite morphology in a mudstone-dominated succession: the Lower Jurassic Cleveland Ironstone Formation, eastern England: Sedimentary Geology, v. 131, p. 77-86.

Thomas, M.A., 1982, Petrology and diagenesis of the Lower Mississippian, Osagean Series, western Sedgwick basin, Kansas: Master's thesis, University of Missouri-Columbia, p. 87.

Watney, W. L., W.J. Guy, and A.P. Byrnes, 2001, Characterization of the Mississippian chat in south-central Kansas: AAPG Bulletin, v. 85, no.1, p. 85–113.

Watney, W. L., J. Rush, D. Wreath, J. Doveton, M. Fazelalavi, E. Holubnyak, D. Newell, J. Victorine, S. Datta, J. Roberts, D. Fowle, 2013, Paleozoic anchor core in south-central Kansas-Berexco Wellington KGS #1-32, Sumner County: *in* M.K. Dubbois and W.L. Watney, eds., Mid-Continent Core Workshop: From source to reservoir seal; Kansas Geological Survey and Kansas Geological Society publication, p. 177-184.

Warren, John, 2000, Dolomite: Occurrence, evolution and economically important associations: Earth-Science Reviews, v. 52, p. 1–82.

Witzke, B.J., 1990, Paleoclimatic constraints for Paleozoic paleolatitudes of Laurentia and Euramerica, *in* W.S. McKerrow and C.R. Scotese, eds., Paleozoic paleogeography and biogeography: London, Geological Society Memoir 12, p. 57-73.

Wilson, J.L., 1975, The Lower Carboniferous Waulsortian facies: *in* Wilson, J.L. ed., Carbonate facies in geologic history, Springer Verlag, New York, p. 148-168.

Wojcik, K.M., R.H. Goldstein, and A.W. Walton, 1997, Regional and local controls of diagenesis driven by basin-wide flow system: Pennsylvanian sandstones and limestones, Cherokee basin, southeastern Kansas, *in* I.P. Montaneez, J.M. Gregg, and K.L. Shelton, eds., Basin-wide diagenetic patterns; integrated petrologic, geochemical, and hydrologic considerations: SEPM Special Publication no. 57, p. 235-252.

Young, E.M., 2010, Controls on reservoir character in carbonate-chert strata, Mississippian (Osagean-Meramecian), southeast Kansas, Master's Thesis, University of Kansas, Lawrence, Kansas, 198 p.

APPENDIX

Trace Elemental Concentrations in Dolomite: Rhodes Field

Core: George Miachael 1-8
Depth: 4610 ft

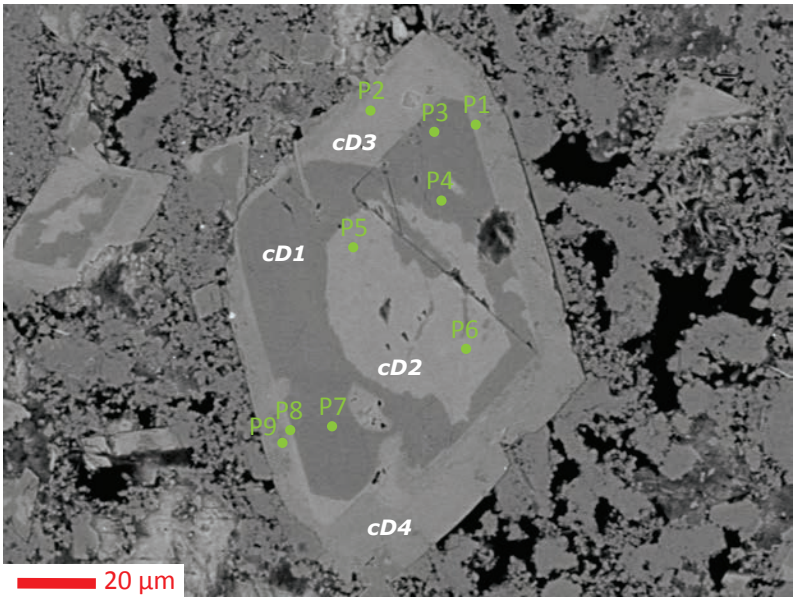

GM4610 Dolomite Sample 1

Averages cD1

Na	Fe	Ca	Mg	Mn	Sr
650	983	235457	117587	368	81

Averages cD2

Na	Fe	Ca	Mg	Mn	Sr
152	76217	229957	76469	1013	0

Averages cD3

Na	Fe	Ca	Mg	Mn	Sr
249	62183	236657	77622	4824	136

Averages cD4

Na	Fe	Ca	Mg	Mn	Sr
629	54436	220452	95218	1892	685

Zones: Point

cD1: P3, P4, P7
cD2: P5, P6
cD3: P2, P8
cD4: P1, P9

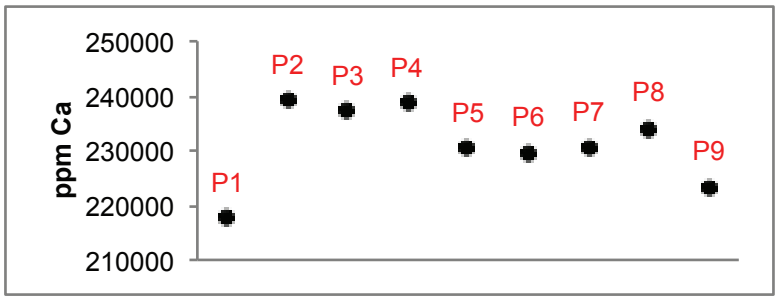

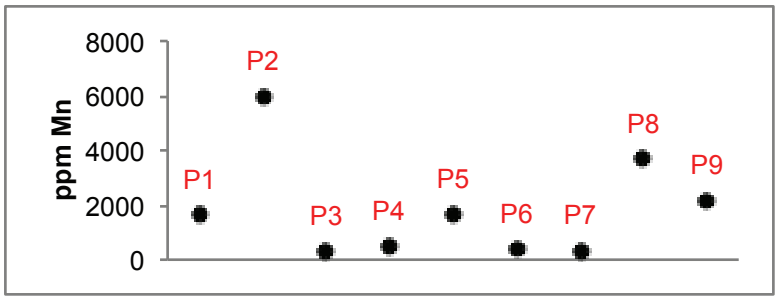

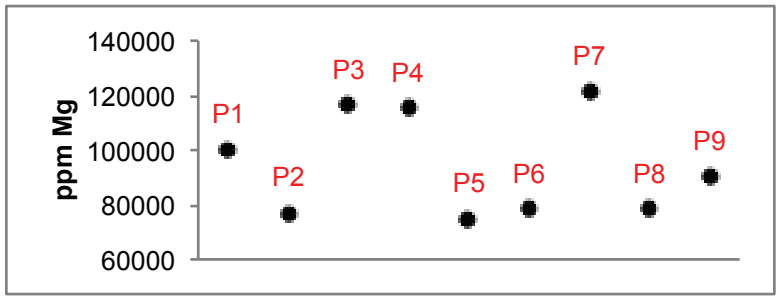

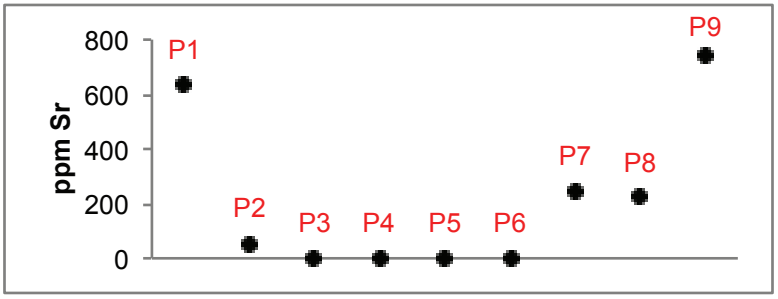

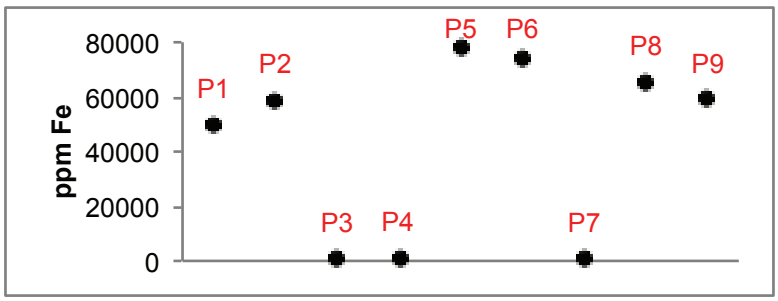

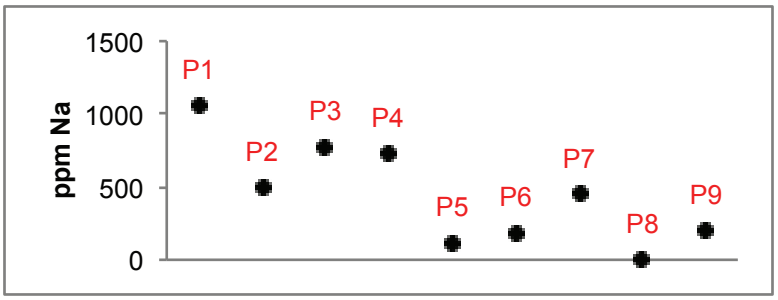

Trace Elemental Concentrations in Dolomite: Rhodes Field

Core: George Miachael 1-8
Depth: 4610 ft

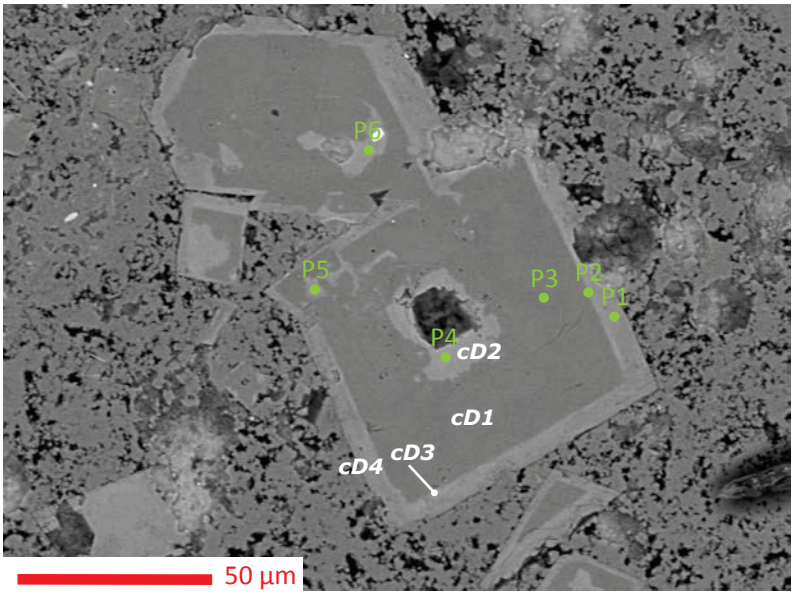

GM4610 Dolomite Sample 2

Averages cD1

Na	Fe	Ca	Mg	Mn	Sr
401	0	233551	119670	95	449

Averages cD2

Na	Fe	Ca	Mg	Mn	Sr
452	85491	225193	74173	919	148

Averages cD3

Na	Fe	Ca	Mg	Mn	Sr
104	4685	240376	111995	314	425

Averages cD4

Na	Fe	Ca	Mg	Mn	Sr
212	56488	234829	82052	4803	805

Zones: Point

cD1: P3
cD2: P4, P5, P6
cD3: P2
cD4: P1

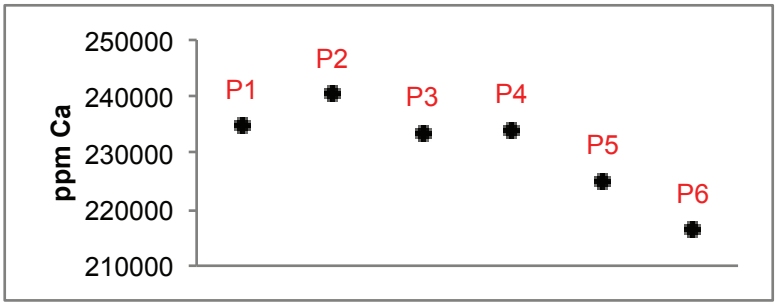

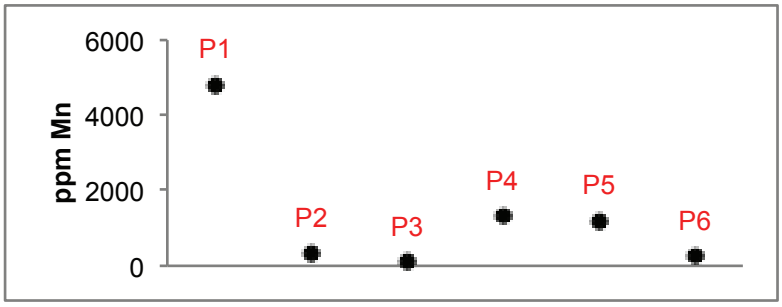

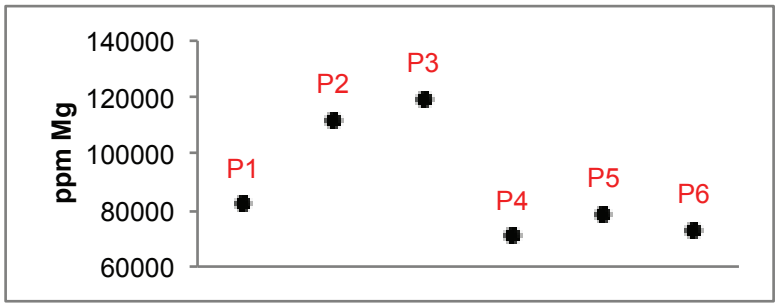

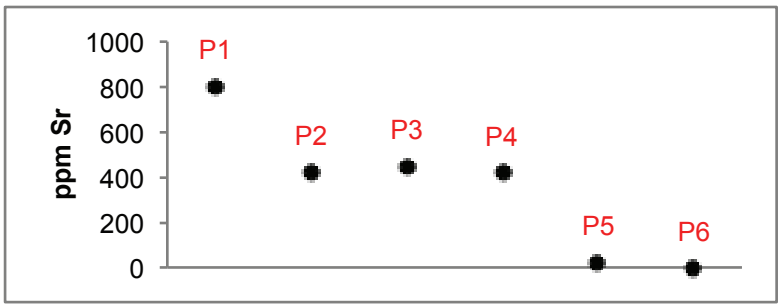

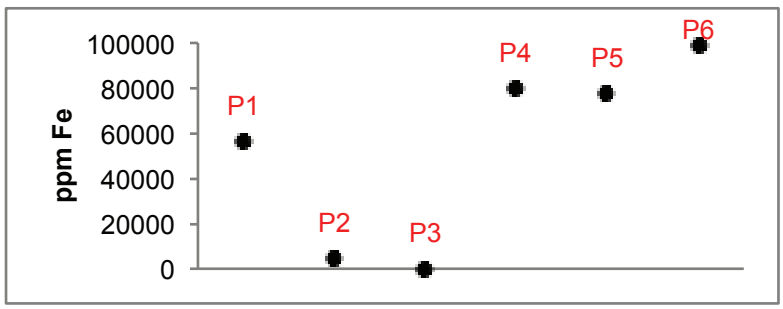

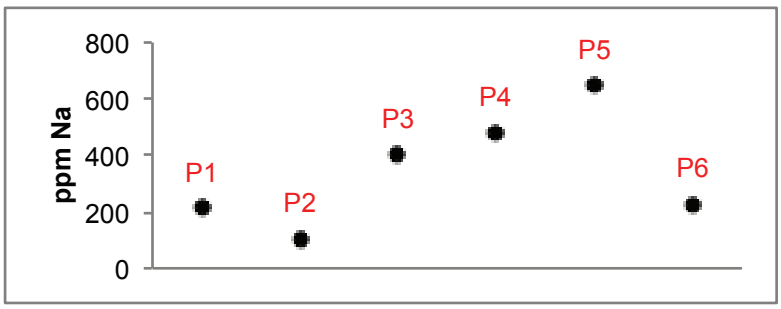

Trace Elemental Concentrations in Dolomite: Rhodes Field

Core: George Miachael 1-8

Depth: 4616 ft

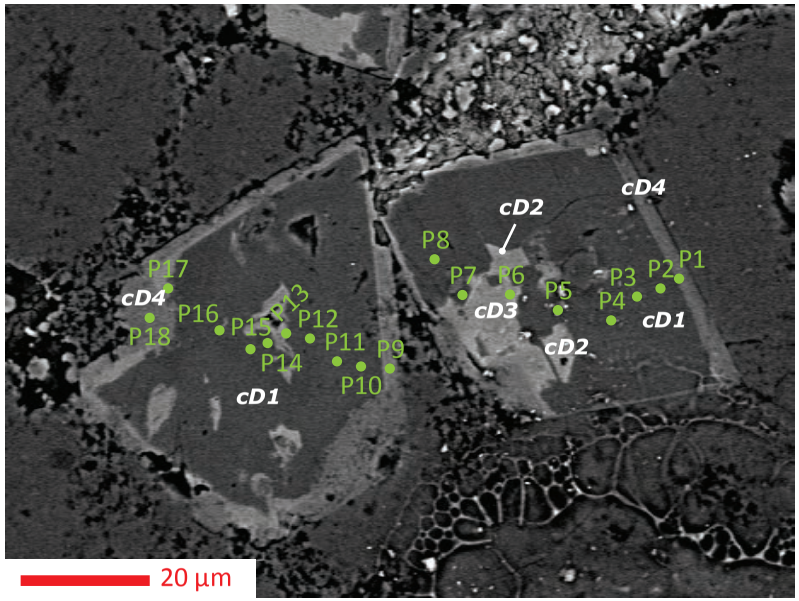

GM4616 Dolomite Sample 1

Averages cD1

Na	Fe	Ca	Mg	Mn	Sr
511	5550	238680	112184	790	436

Averages cD2

Na	Fe	Ca	Mg	Mn	Sr
154	74807	229582	77075	1559	367

Averages cD3

Na	Fe	Ca	Mg	Mn	Sr
0	83968	230108	71759	618	591

Averages cD4

Na	Fe	Ca	Mg	Mn	Sr
256	33808	227479	103344	1182	244

Zones: Point

cD1: P2, P3, P4, P5, P7, P8, P10, P11, P12, P14, P15, P16
cD2: P13, P17
cD3: P6
cD4: P1, P9, P18

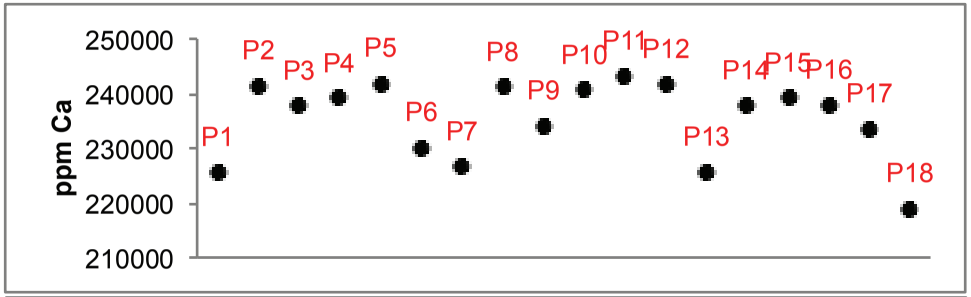

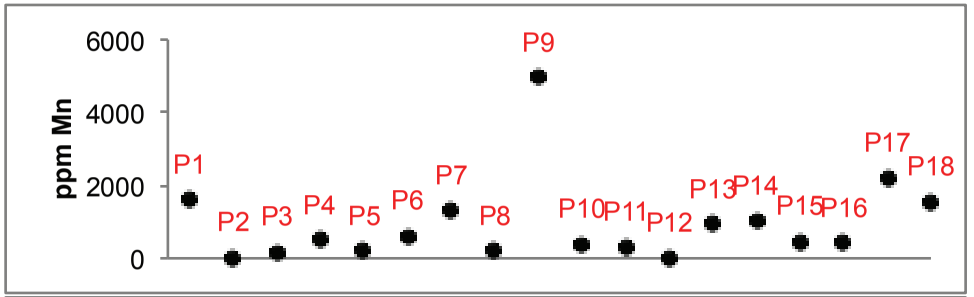

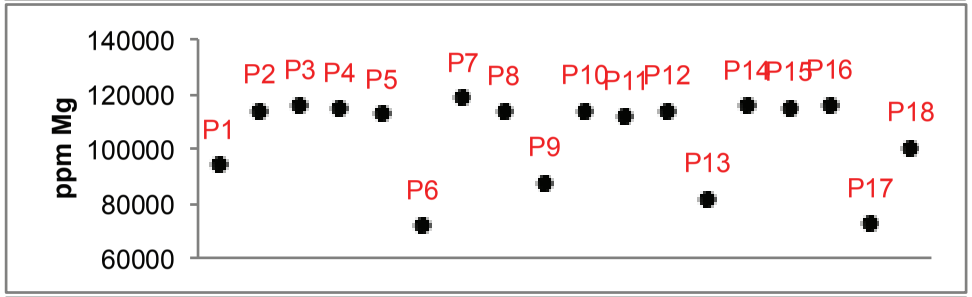

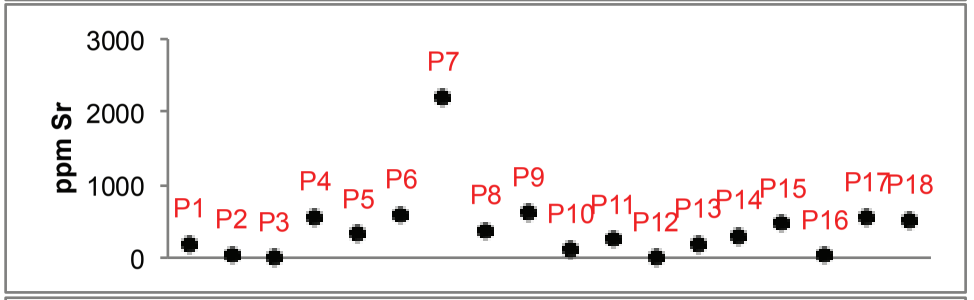

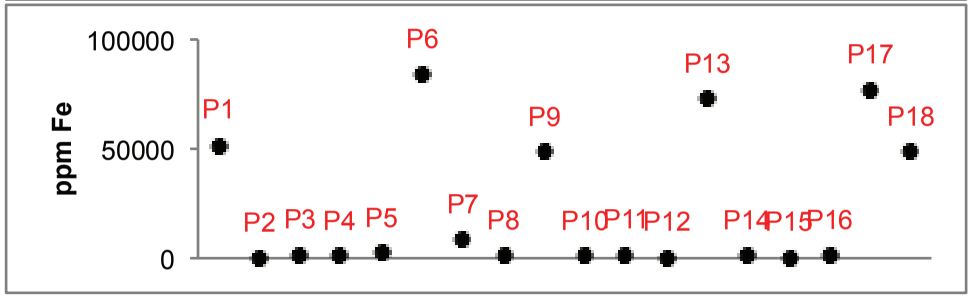

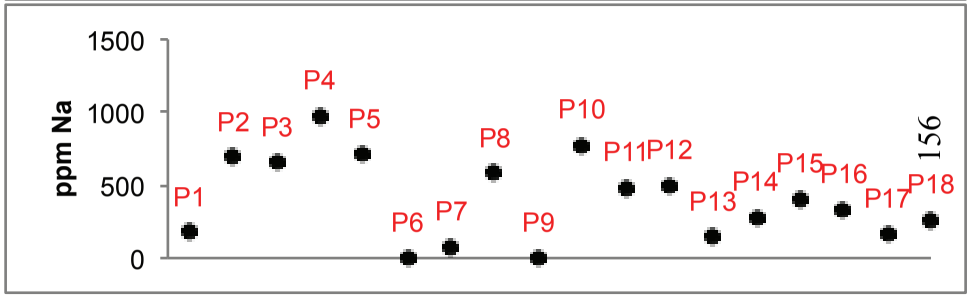

Trace Elemental Concentrations in Dolomite: Rhodes Field

Core: George Miachael 1-8
Depth: 4616 ft

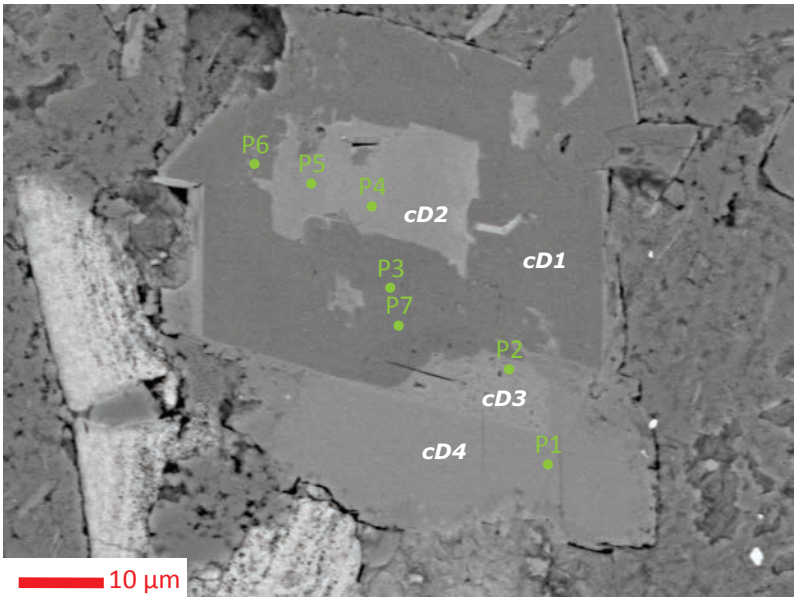

GM4616 Dolomite Sample 2

Averages cD1

Na	Fe	Ca	Mg	Mn	Sr
517	482	159612	76565	193	83

Averages cD2

Na	Fe	Ca	Mg	Mn	Sr
798	99760	339637	126378	1836	723

Averages cD3

Na	Fe	Ca	Mg	Mn	Sr
541	61195	228977	84804	2404	627

Averages cD4

Na	Fe	Ca	Mg	Mn	Sr
167	48103	234850	88385	2897	479

Zones: Point

cD1: P3, P7
cD2: P4, P5, P6
cD3: P2
cD4: P1

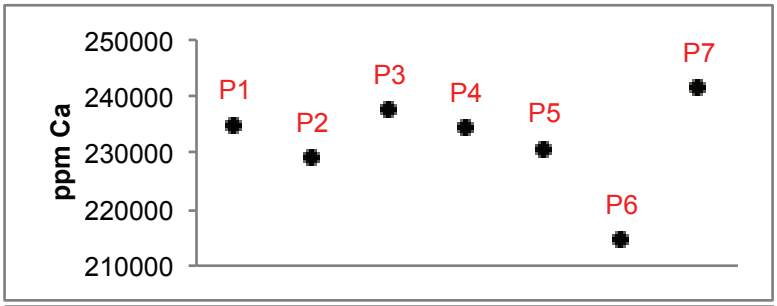

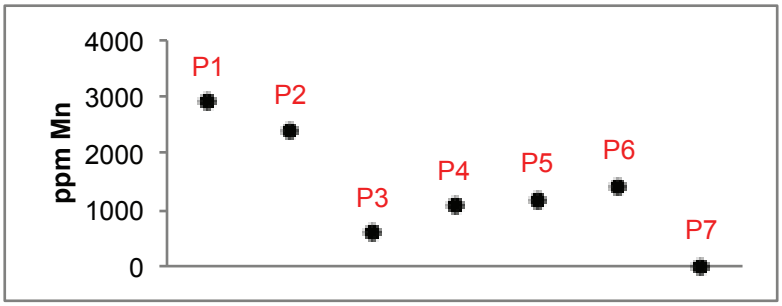

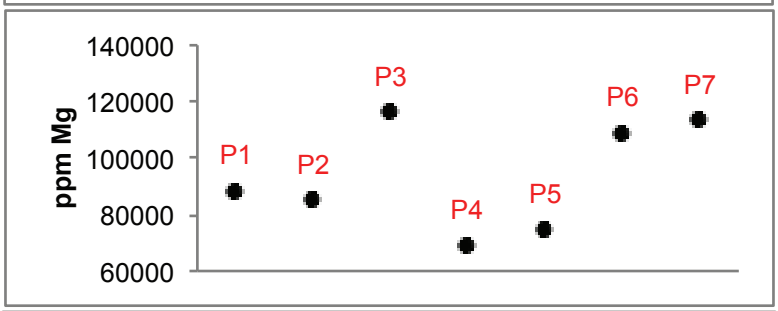

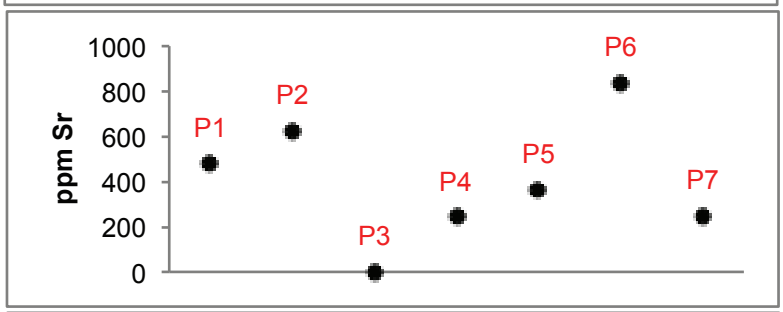

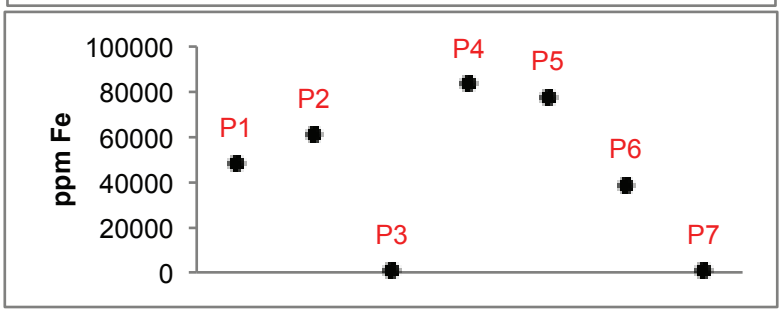

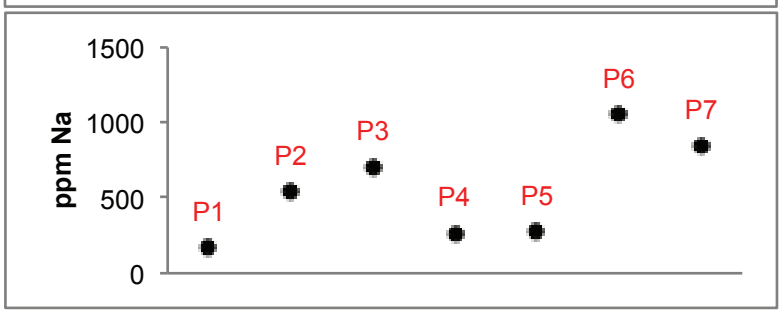

Trace Elemental Concentrations in Dolomite: Rhodes Field

Core: George Miachael 1-8

Depth: 4617 ft

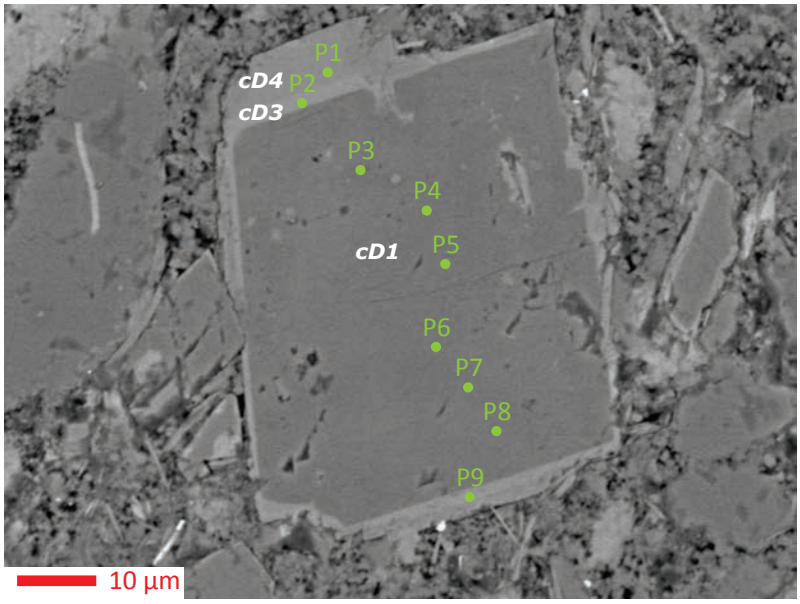

GM4617 Dolomite Sample 1

Averages cD1					
Na	Fe	Ca	Mg	Mn	Sr
750	991	237786	115848	234	253

Averages cD3					
Na	Fe	Ca	Mg	Mn	Sr
305	52585	234793	86089	2413	217

Averages cD4					
Na	Fe	Ca	Mg	Mn	Sr
351	45752	232825	90262	3959	987

Zones: Point

cD1: P3, P4, P5, P6, P7, P8
cD3: P2, P9
cD4: P1

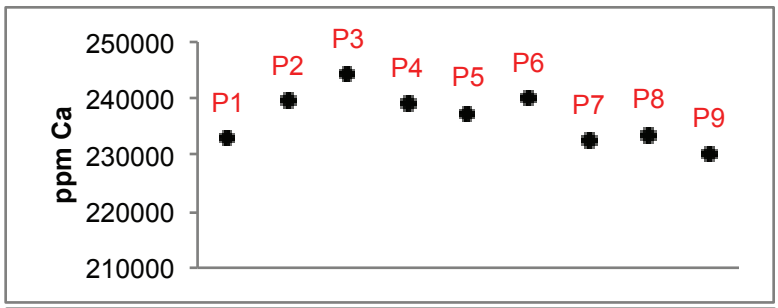

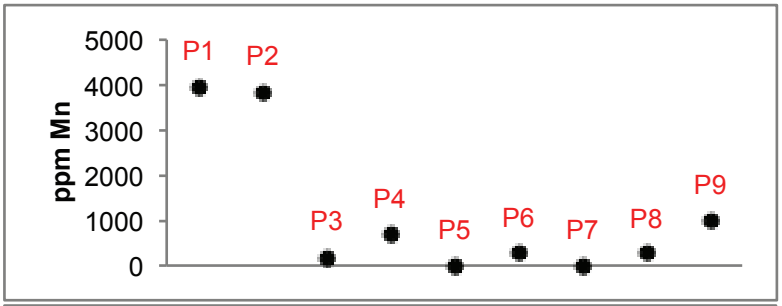

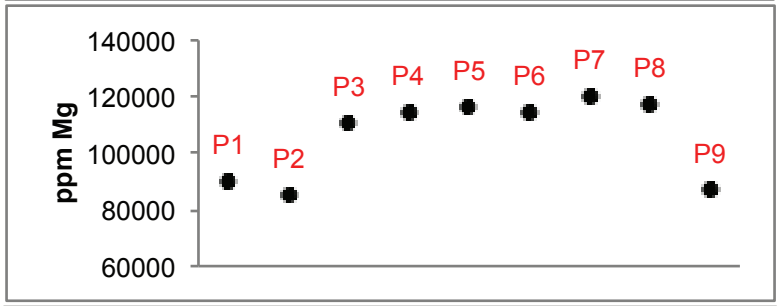

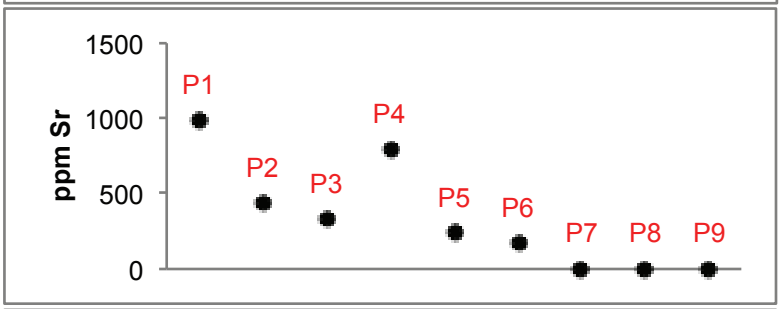

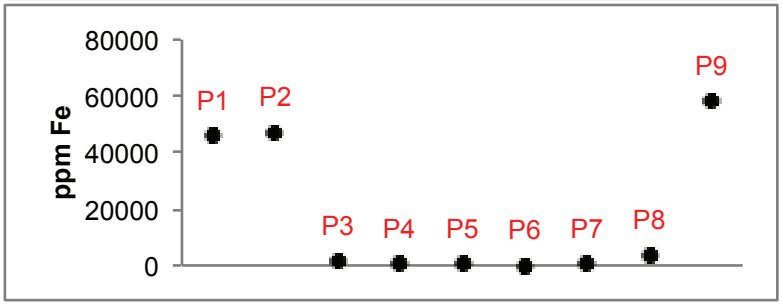

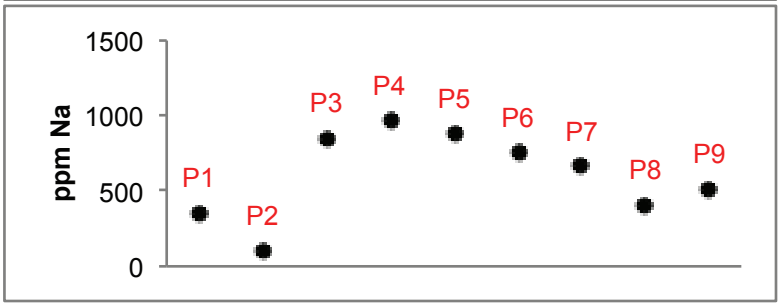

Trace Elemental Concentrations in Dolomite: Rhodes Field

Core: George Miachael 1-8

Depth: 4617 ft

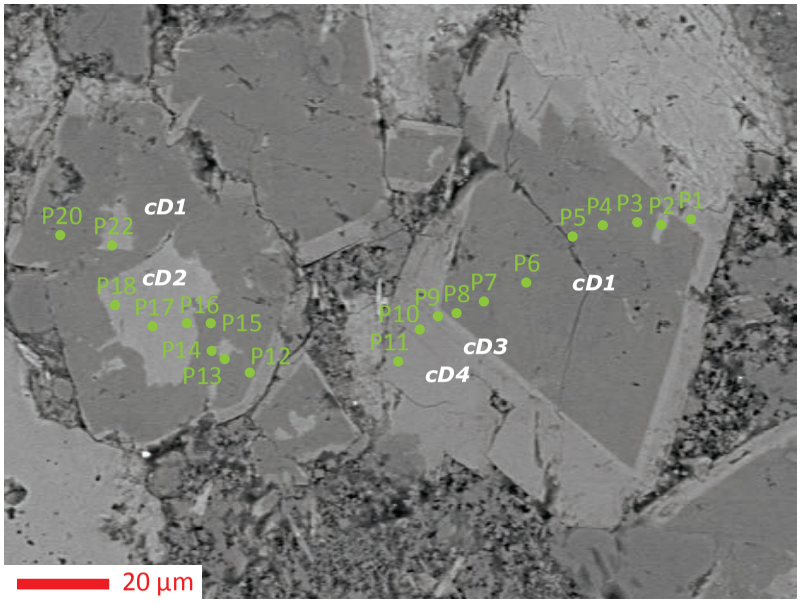

GM4617 Dolomite Sample 2

Averages cD1					
Na	Fe	Ca	Mg	Mn	Sr
628	1596	217603	103813	372	207

Averages cD2					
Na	Fe	Ca	Mg	Mn	Sr
79	70865	230574	79200	1078	56

Averages cD3					
Na	Fe	Ca	Mg	Mn	Sr
1005	46328	227307	94471	2879	394

Averages cD4					
Na	Fe	Ca	Mg	Mn	Sr
67	44761	238088	87256	4627	83

Zones: Point

cD1: P3, P4, P5, P6, P7, P8, P12, P14, P15, P20
cD2: P13, P16, P17, P18, P22
cD3: P1, P2
cD4: P9, P10, P11

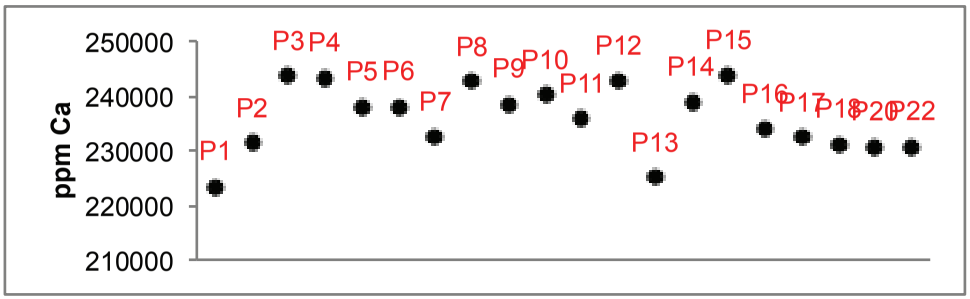

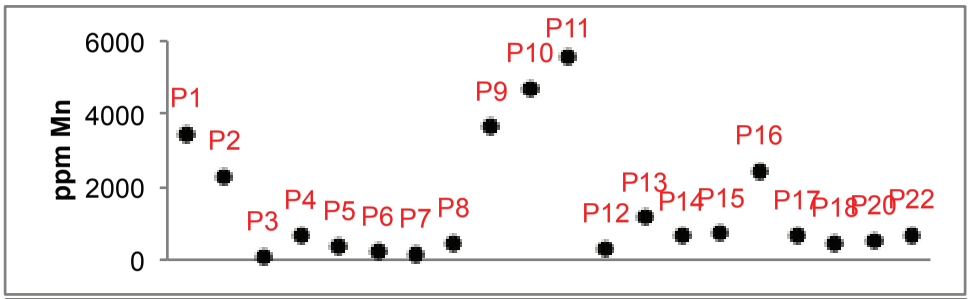

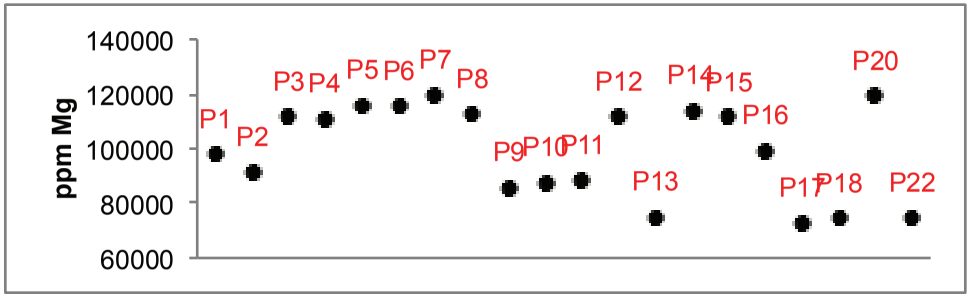

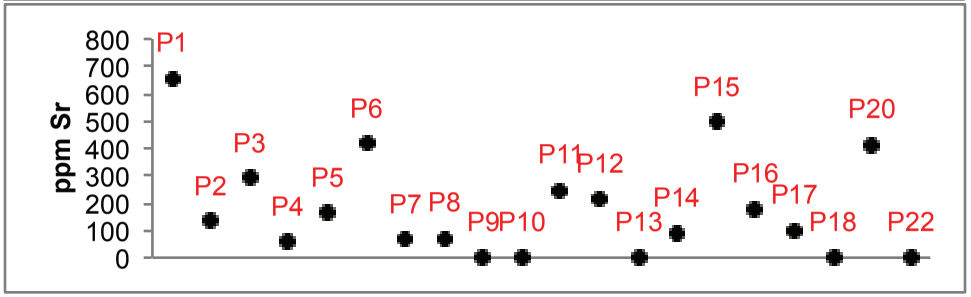

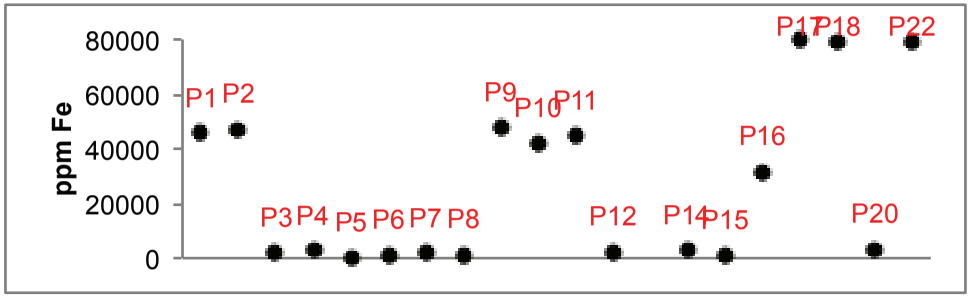

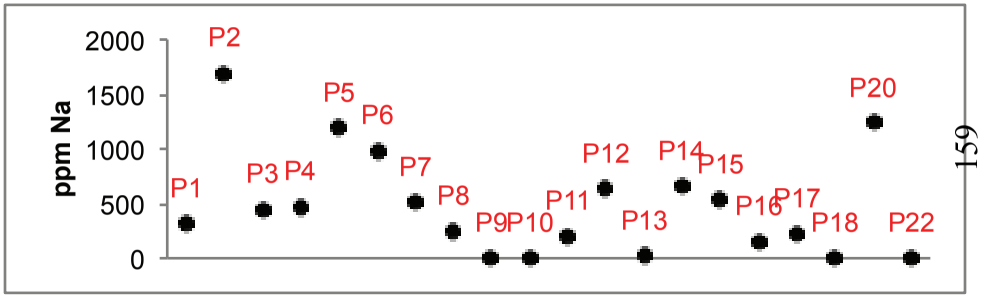

Trace Elemental Concentrations Baroque Dolomite (cBD): Rhodes Field

Core: Harbaugh U.B. 15

Depth: 4620 ft

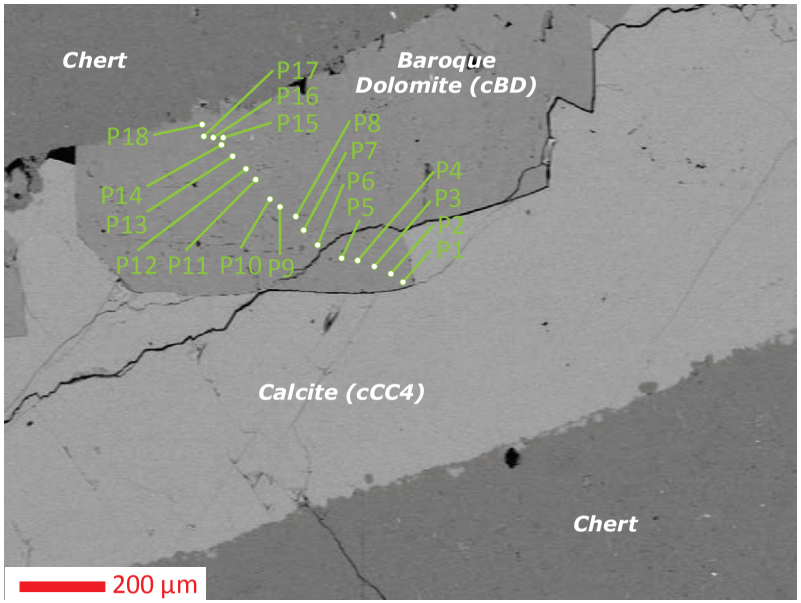

HB4620 Saddle Dolomite (cBD)

Averages cBD					
Na	Fe	Ca	Mg	Mn	Sr
38	53470	229921	87315	5609	155

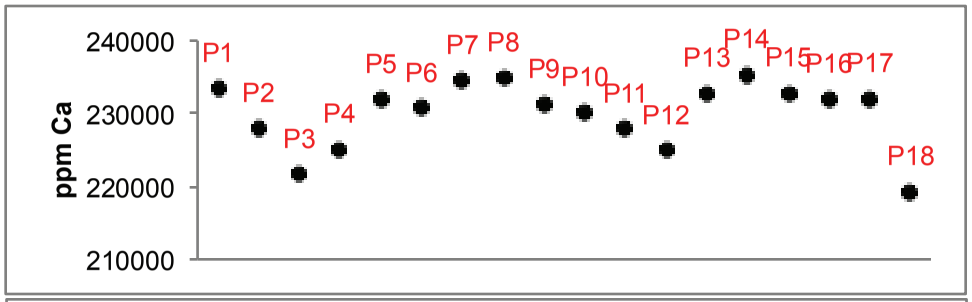

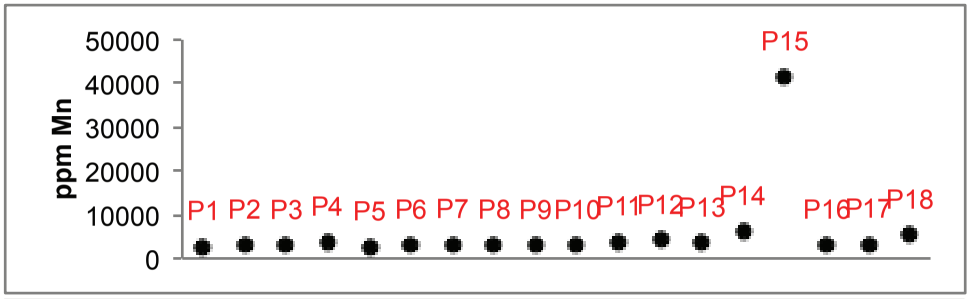

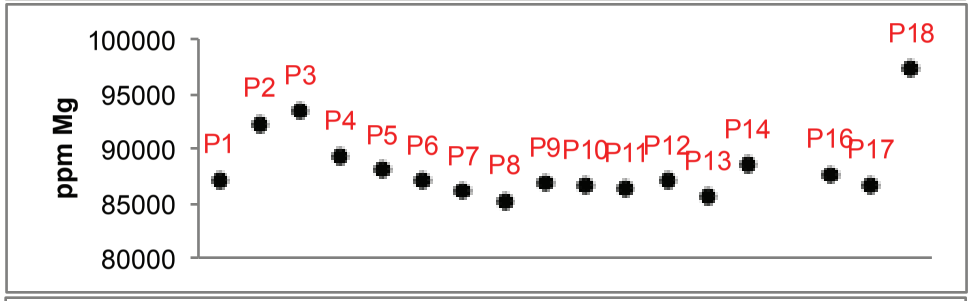

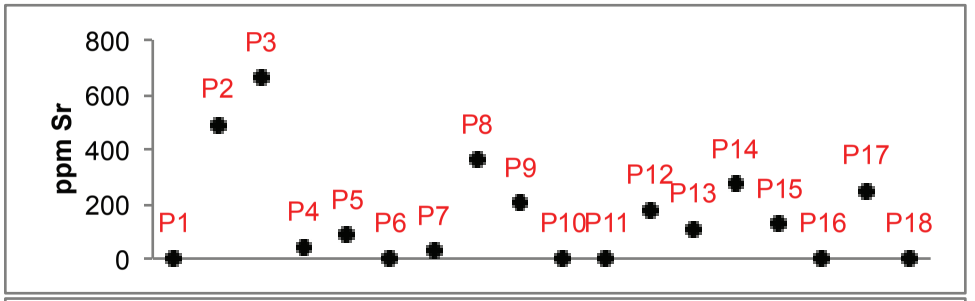

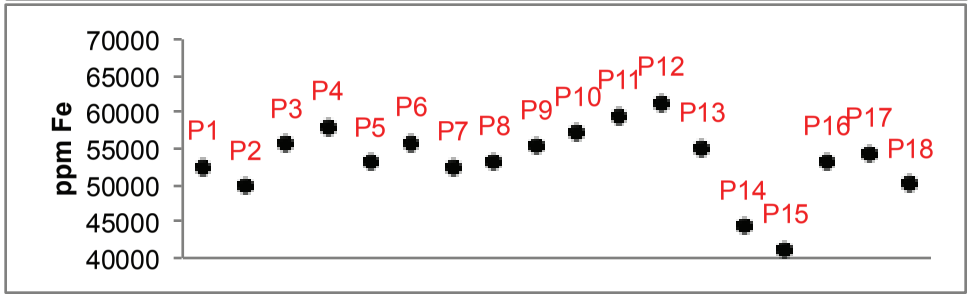

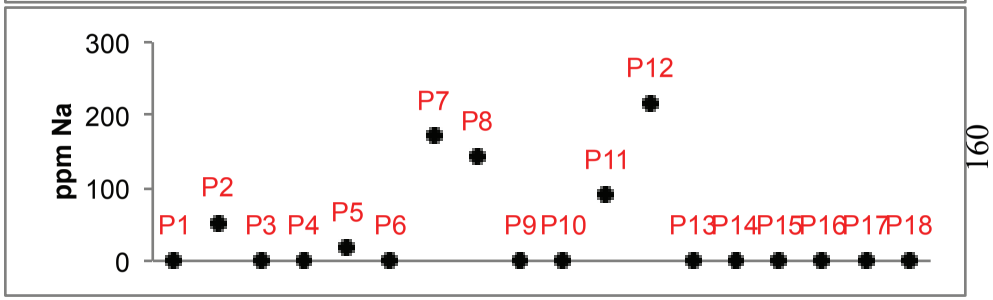

Trace Elemental Concentrations in Dolomite: Wellington Field

Core: Wellington 1-32
Depth: 3671 ft

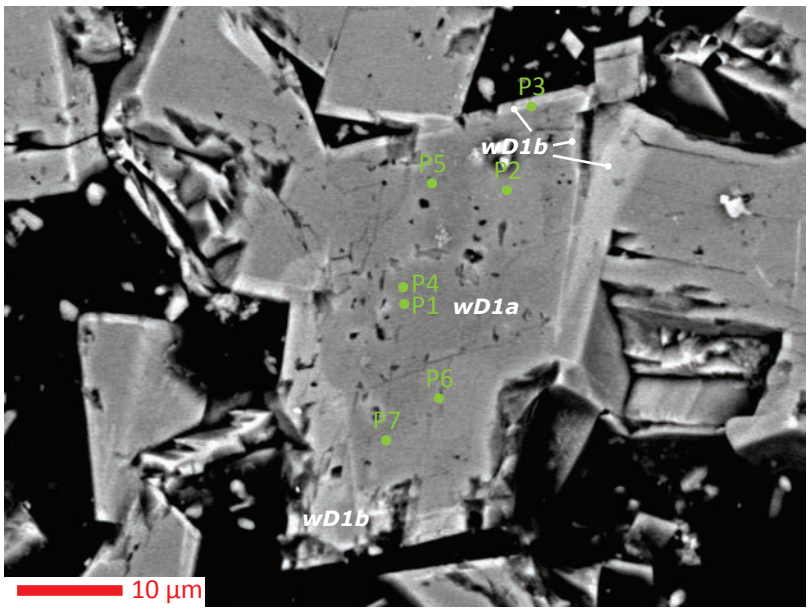

WL3671 Dolomite Sample 1

Averages wD1a					
Na	Fe	Ca	Mg	Mn	Sr
390	6567	225681	121395	381	135

Averages wD1b					
Na	Fe	Ca	Mg	Mn	Sr
493	1920	233831	118247	494	0

Zones: Point
wD1a: P1, P2, P4, P5, P6, P7
wD1b: P3

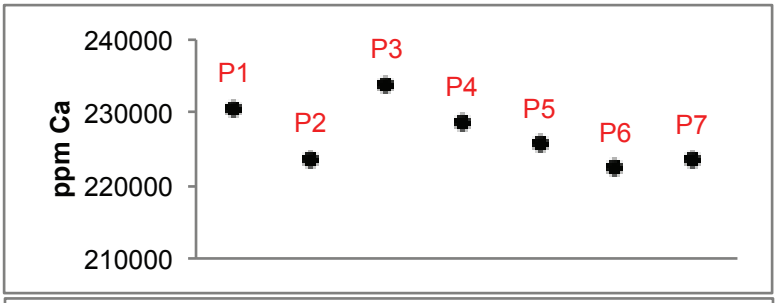

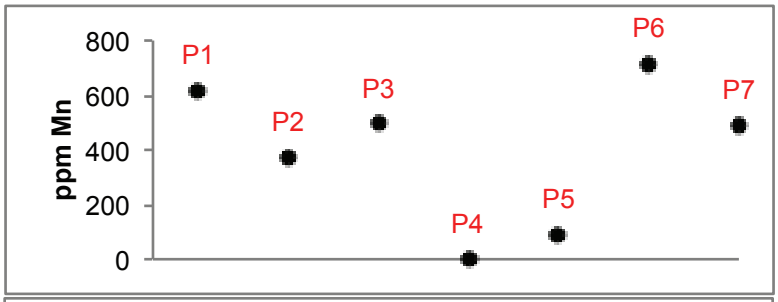

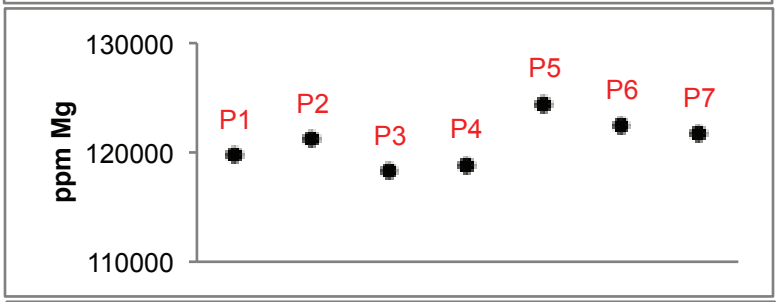

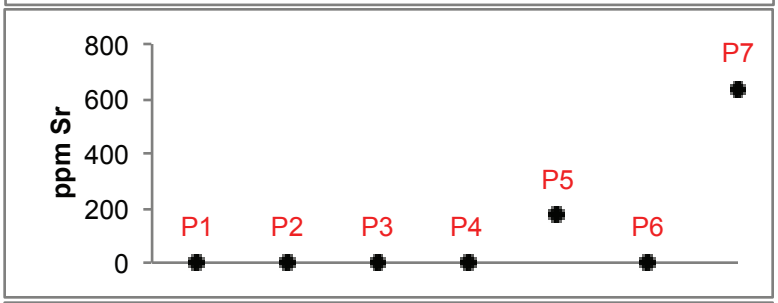

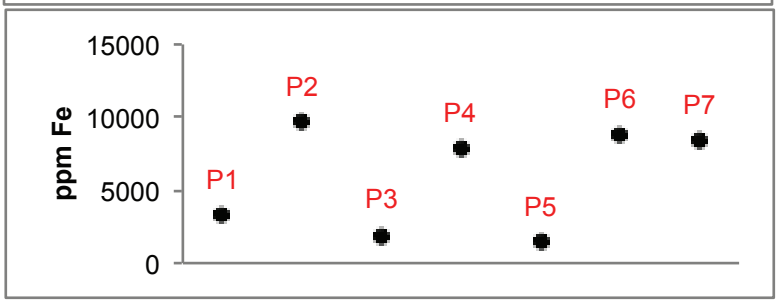

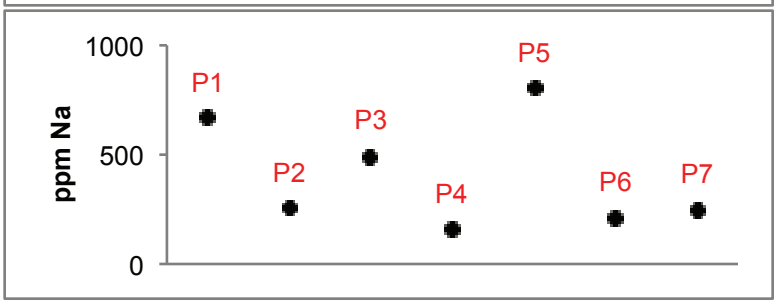

Trace Elemental Concentrations in Dolomite: Wellington Field

Core: Wellington 1-32
Depth: 3671 ft

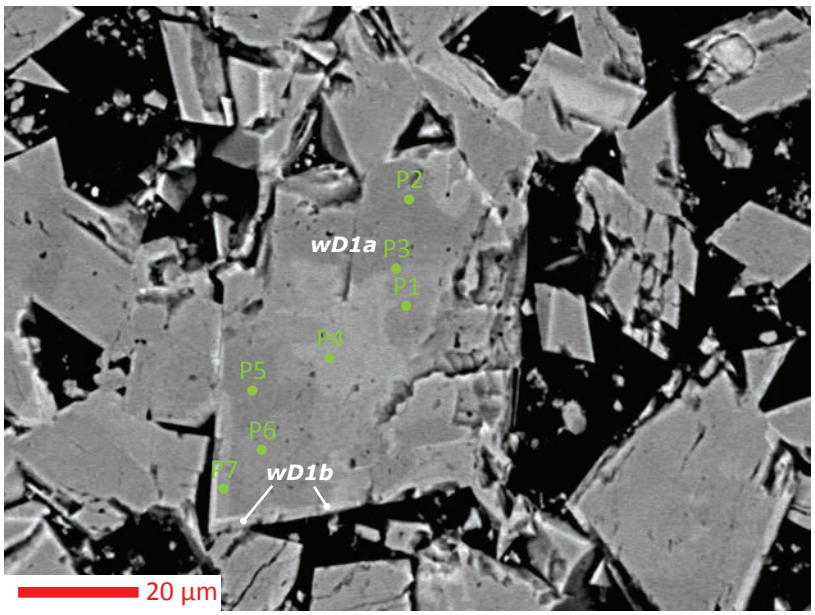

WL3671 Dolomite Sample 2

Averages wD1a					
Na	Fe	Ca	Mg	Mn	Sr
163	17285	224966	115031	1317	189

Zones: Point
wD1a: P1, P2, P3, P4, P5, P6, P7

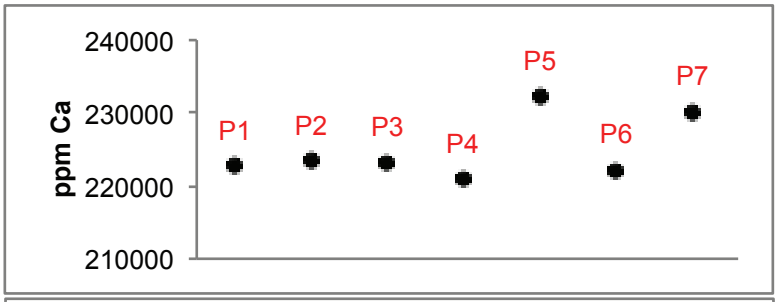

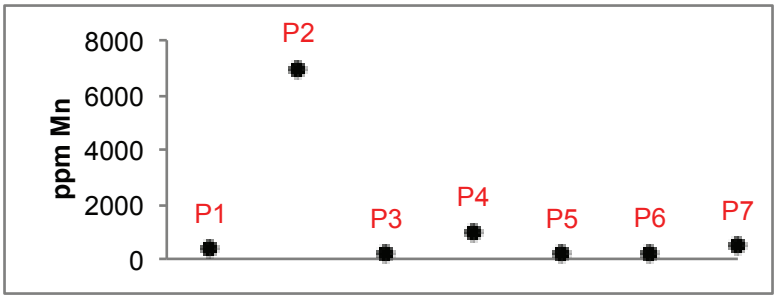

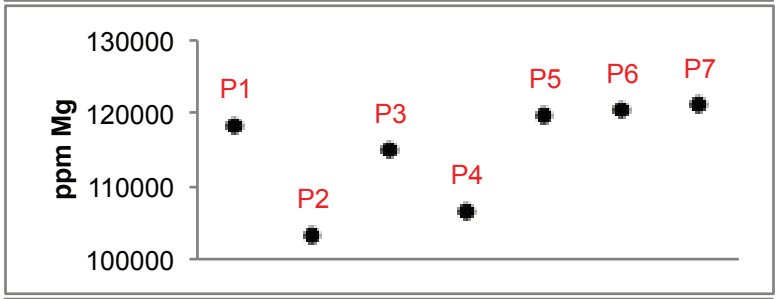

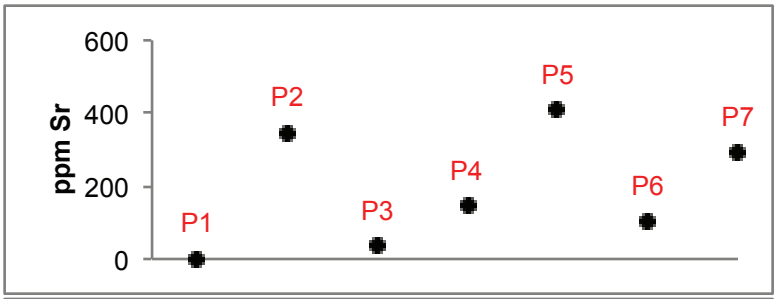

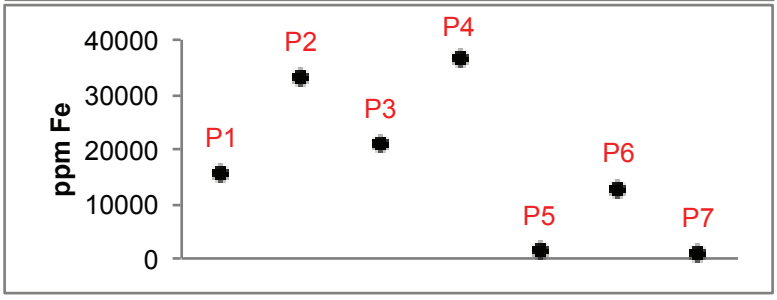

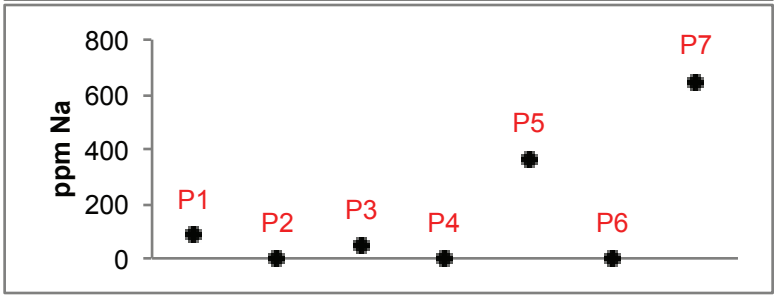

Trace Elemental Concentrations in Dolomite: Wellington Field

Core: Wellington 1-32

Depth: 3671 ft

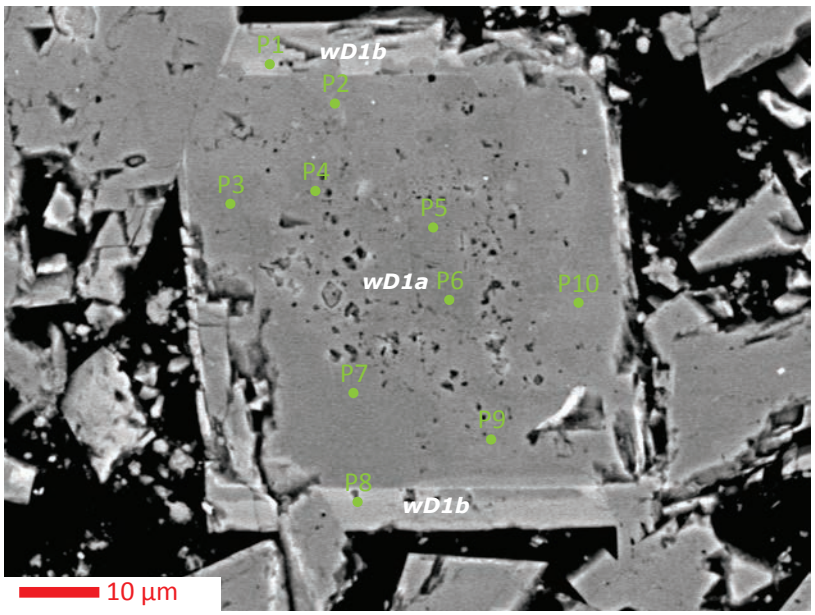

WL3671 Dolomite Sample 3

Averages wD1a					
Na	Fe	Ca	Mg	Mn	Sr
402	5156	223320	123702	673	245

Averages wD1b					
Na	Fe	Ca	Mg	Mn	Sr
173	39685	222579	103463	632	801

Zones: Point
wD1a: P2, P3, P4, P5, P6, P7, P9, P10
wD1b: P1, P8

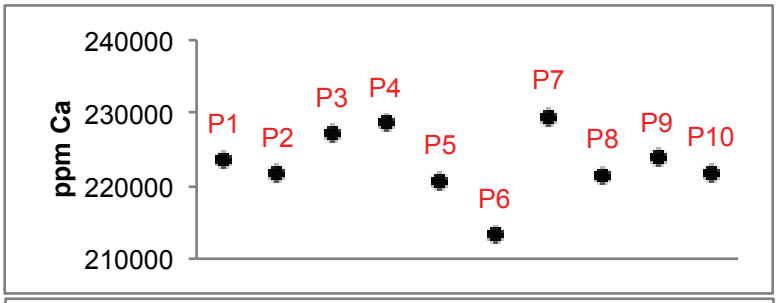

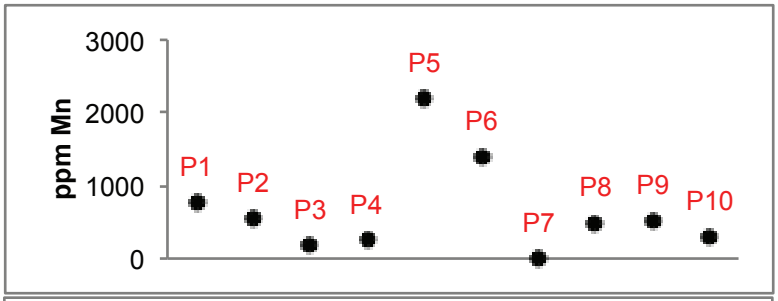

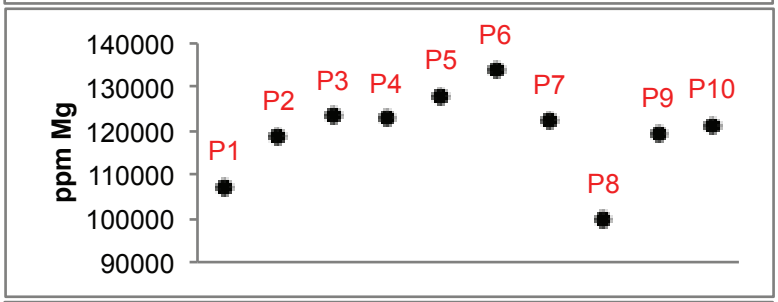

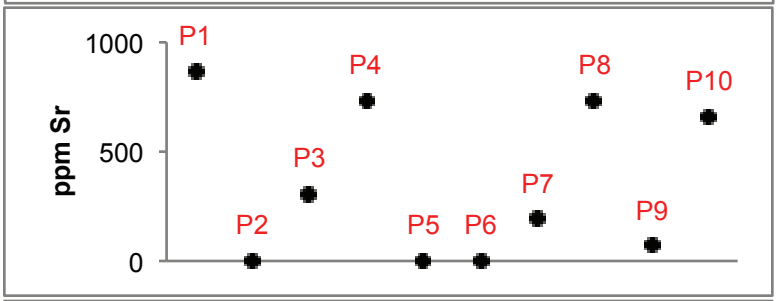

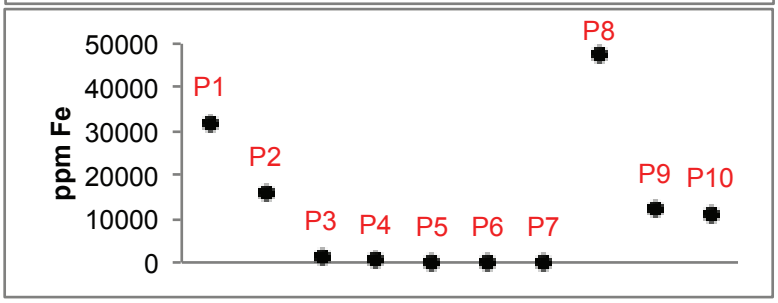

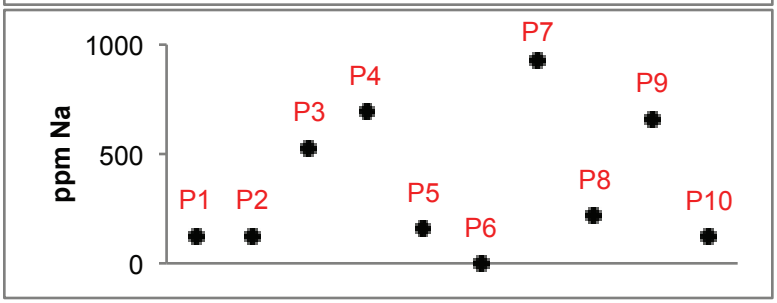

Trace Elemental Concentrations in Dolomite: Wellington Field

Core: Wellington 1-32
Depth: 3724 ft

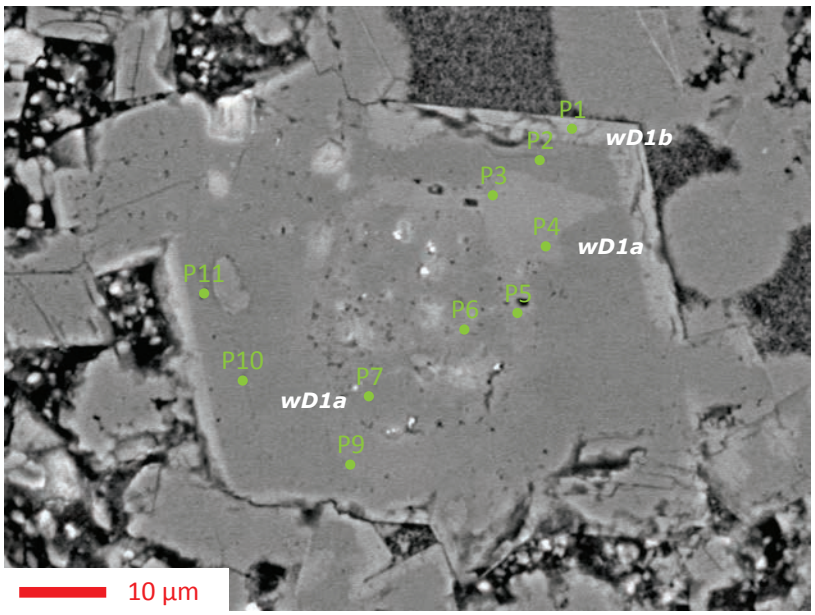

WL3724 Dolomite Sample 1

Averages wD1a					
Na	Fe	Ca	Mg	Mn	Sr
50	6573	228824	119344	201	297

Averages wD1b					
Na	Fe	Ca	Mg	Mn	Sr
682	53173	219496	97580	871	0

Zones: Point
wD1a: P1, P2, P3, P4, P5, P6, P7, P9, P10, P11
wD1b: P1

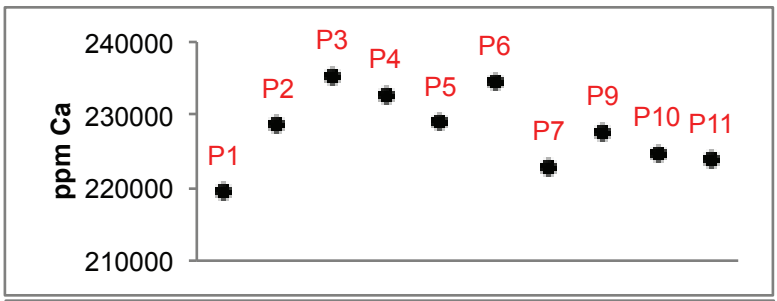

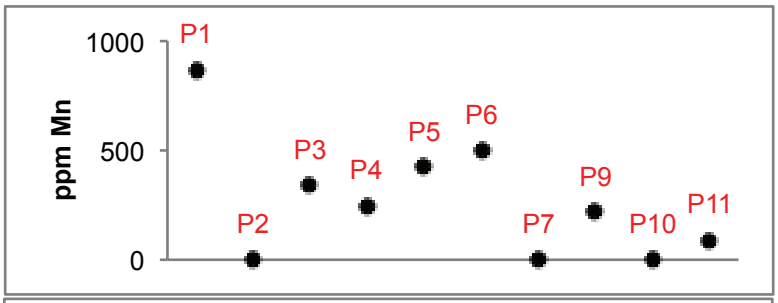

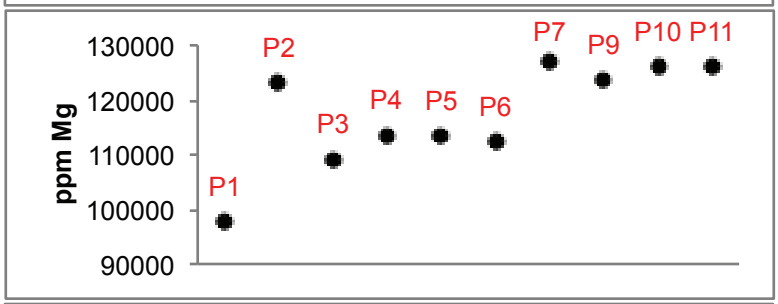

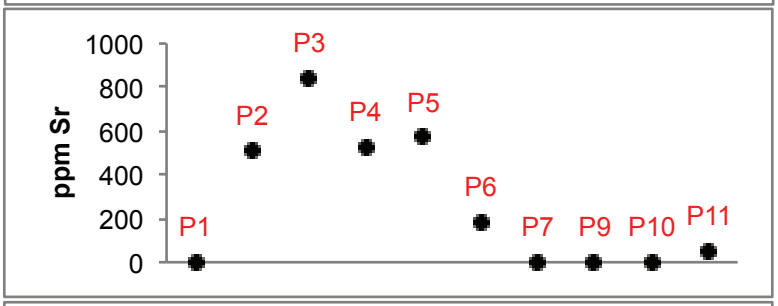

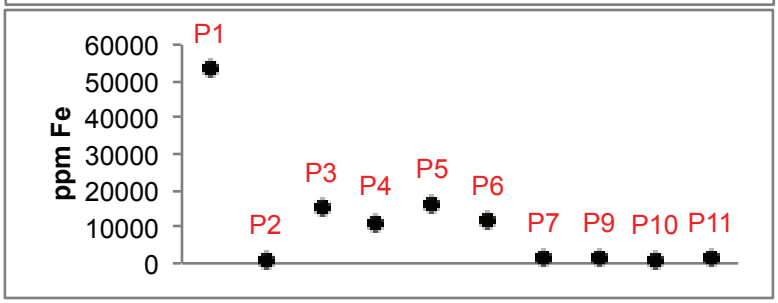

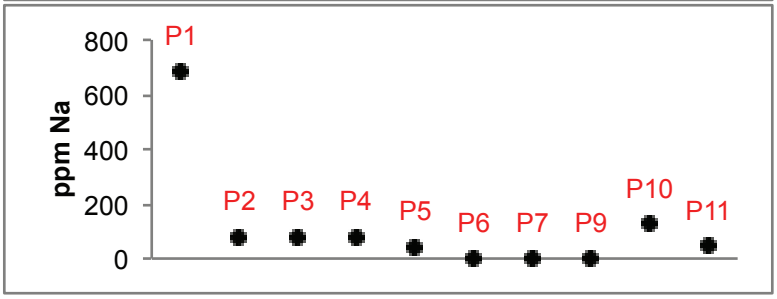

Trace Elemental Concentrations in Dolomite: Wellington Field

Core: Wellington 1-32

Depth: 3724 ft

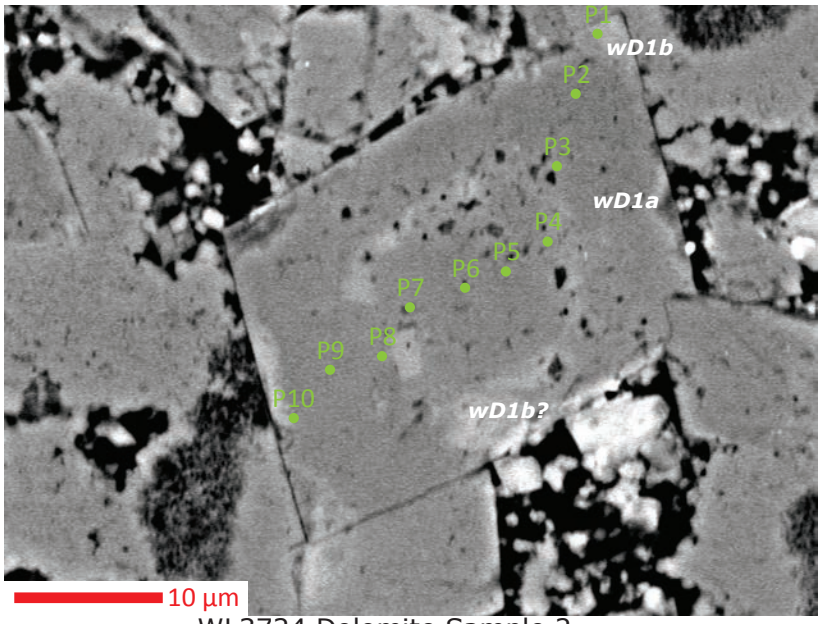

WL3724 Dolomite Sample 2

Averages wD1a					
Na	Fe	Ca	Mg	Mn	Sr
281	2077	227260	123105	225	117

Averages wD1b					
Na	Fe	Ca	Mg	Mn	Sr
47	13506	227617	115928	323	433

Zones: Point
wD1a: P2, P3, P4, P5, P6, P7, P8, P9, P10
wD1b: P1

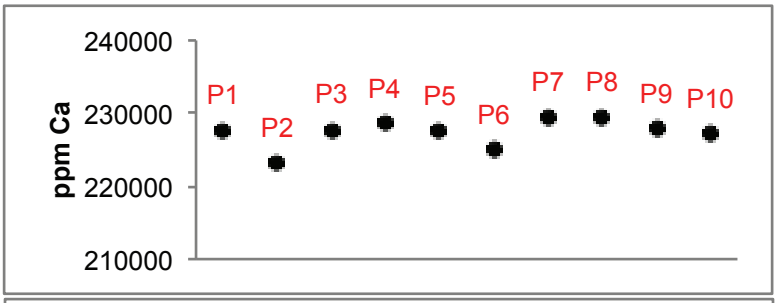

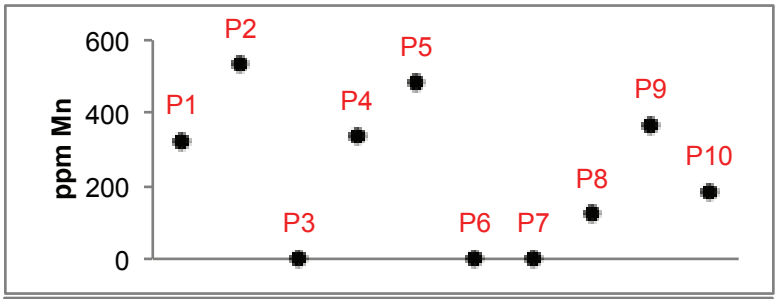

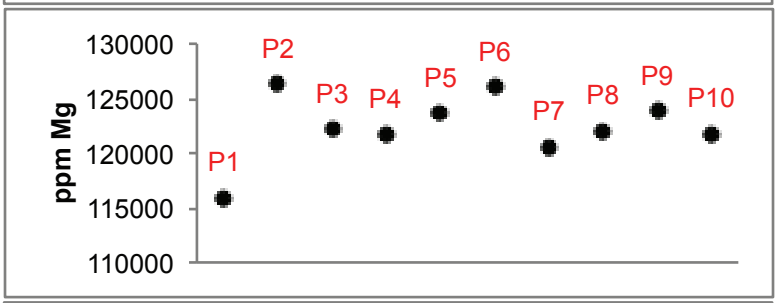

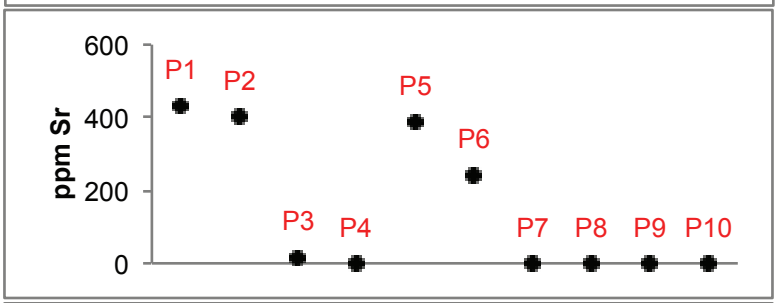

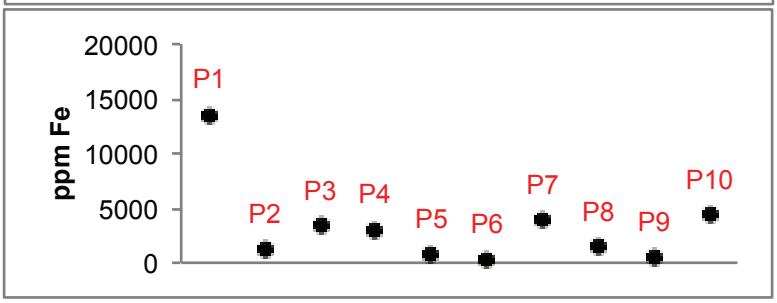

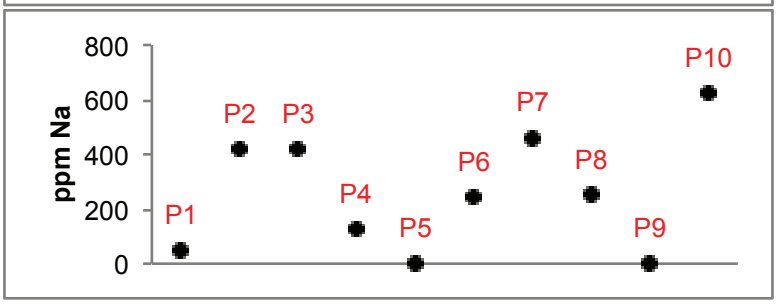

Trace Elemental Concentrations in Dolomite: Wellington Field

Core: Wellington 1-32

Depth: 3724 ft

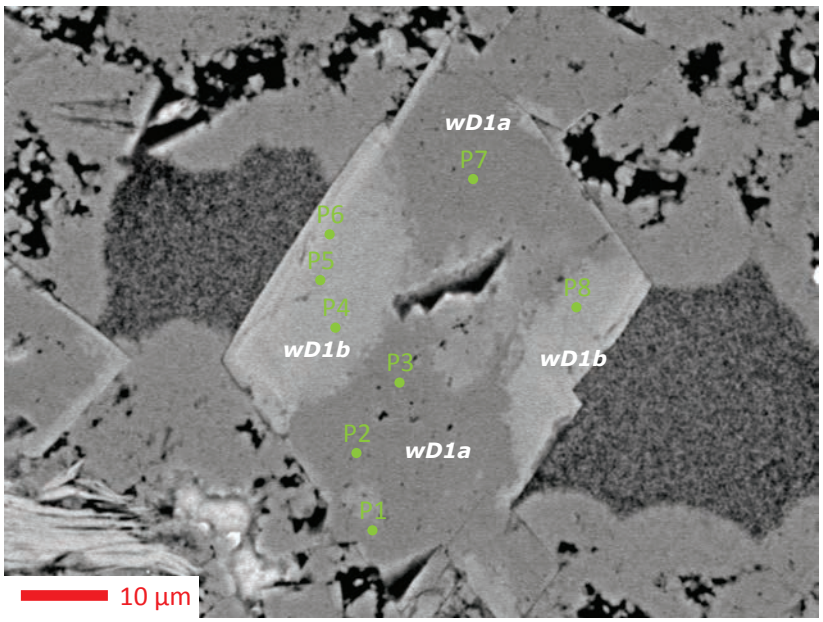

WL3724 Dolomite Sample 3

Averages wD1a					
Na	Fe	Ca	Mg	Mn	Sr
164	1830	225786	124397	129	199

Averages wD1b					
Na	Fe	Ca	Mg	Mn	Sr
112	49251	220679	98724	1562	506

Zones: Point
wD1a: P1, P2, P3, P7
wD2b: P4, P5, P6, P8

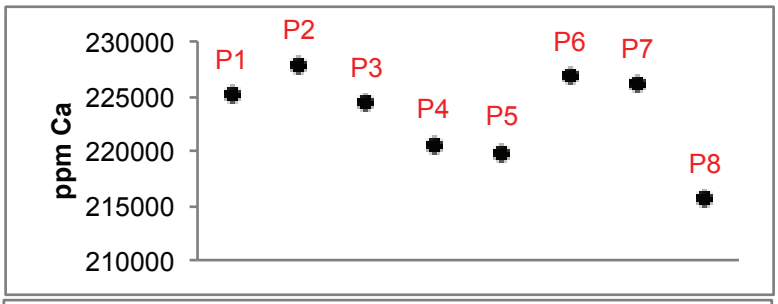

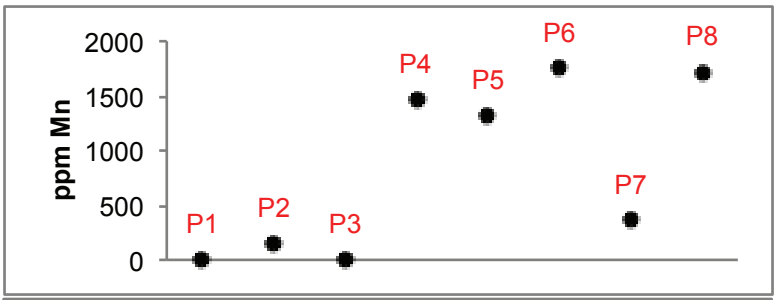

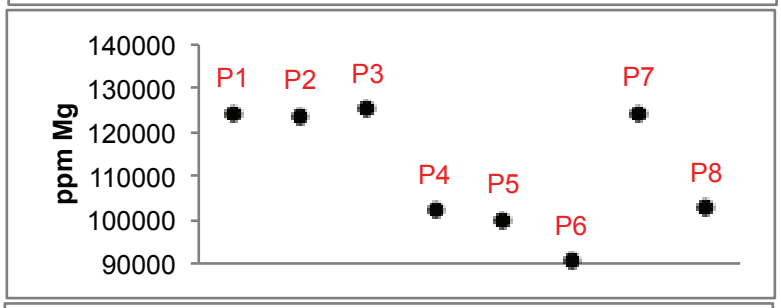

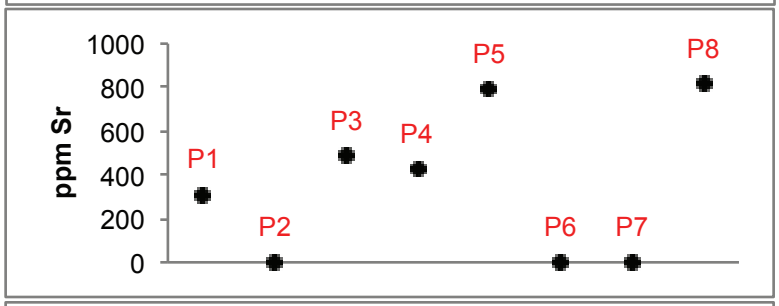

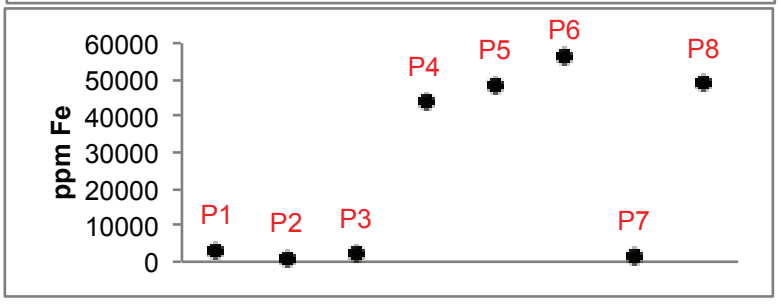

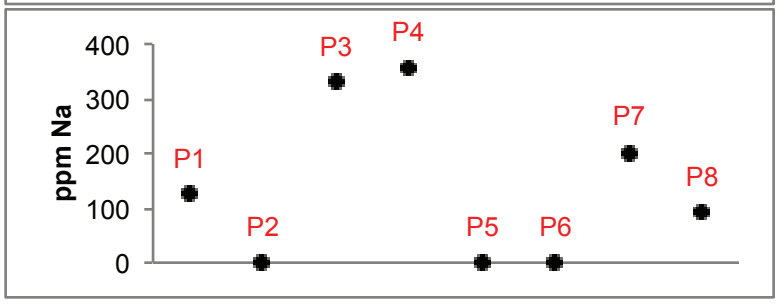

Trace Elemental Concentrations in Dolomite: Wellington Field

Core: Wellington 1-32
Depth: 3724 ft

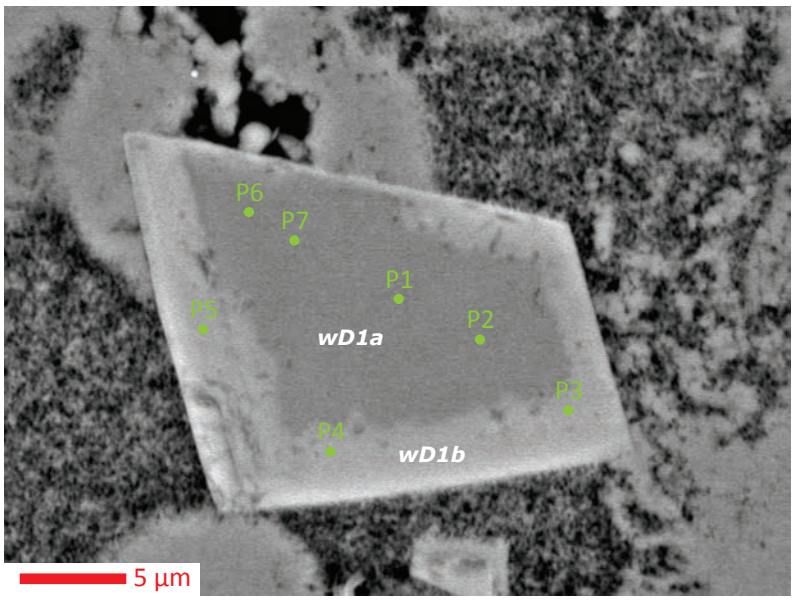

WL3724 Dolomite Sample 4

Averages wD1a					
Na	Fe	Ca	Mg	Mn	Sr
213	1432	223967	126045	69	10

Averages wD1b					
Na	Fe	Ca	Mg	Mn	Sr
104	53099	217764	99085	920	152

Zones: Point
wD1a: P1, P2, P6, P7
wD1b: P3, P4, P5

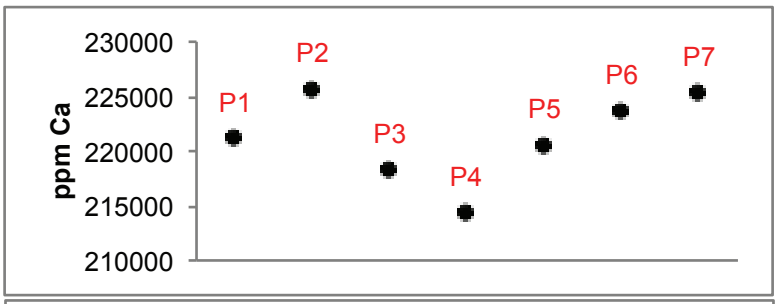

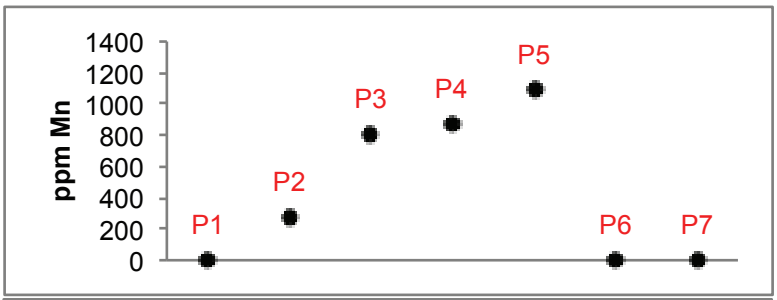

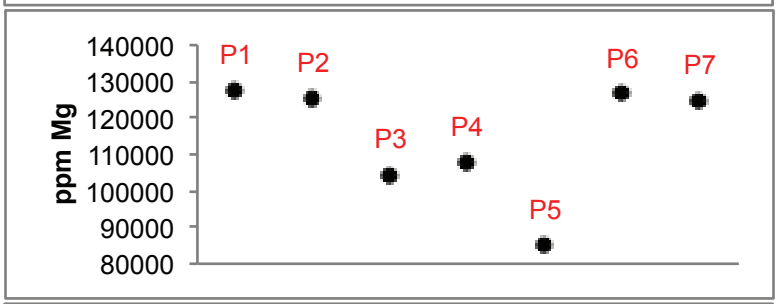

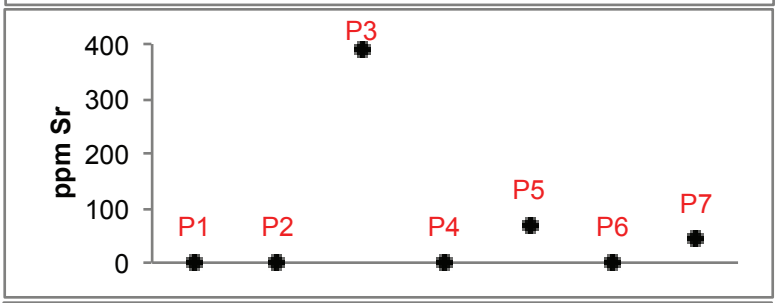

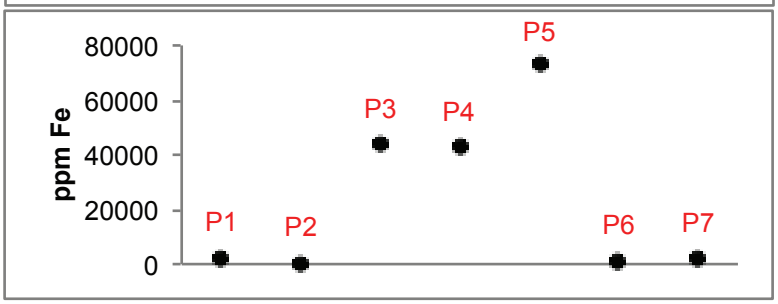

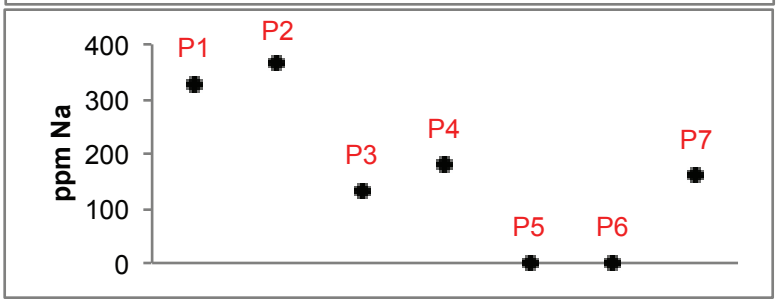

Trace Elemental Concentrations in Dolomite: Wellington Field

Core: Wellington 1-32

Depth: 3876 ft

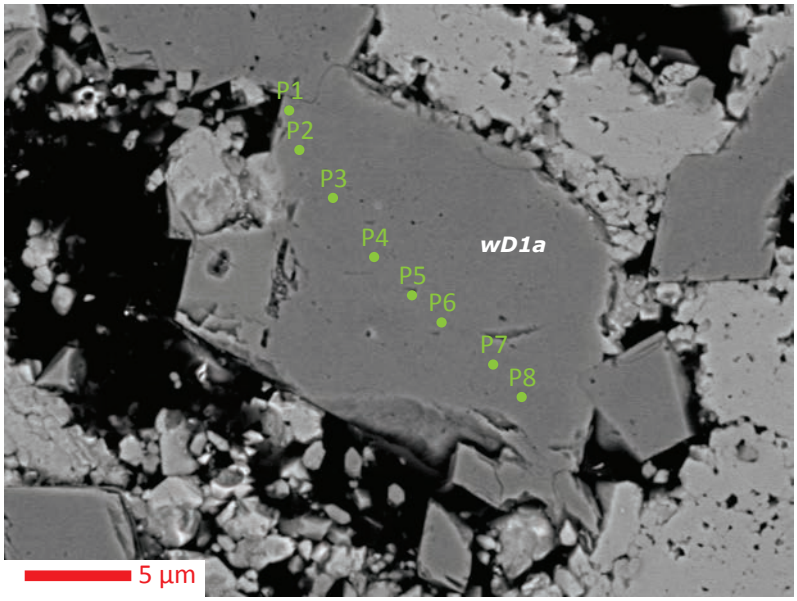

WL3876 Dolomite Sample 1

Averages wD1a					
Na	Fe	Ca	Mg	Mn	Sr
80	1182	226355	124461	102	151

Zones: Point

wD1a: P1, P2, P3, P4, P5, P6, P7, P8

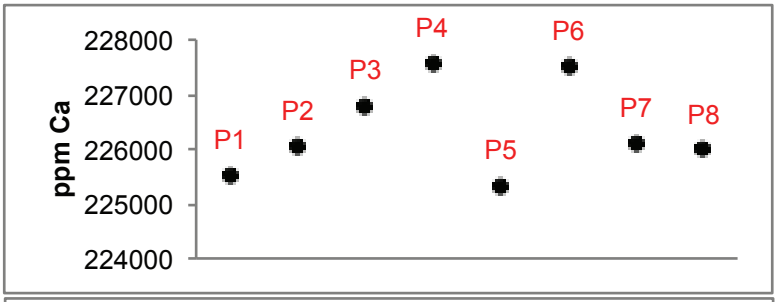

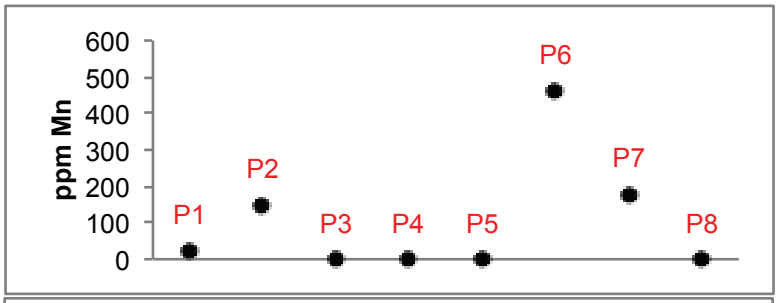

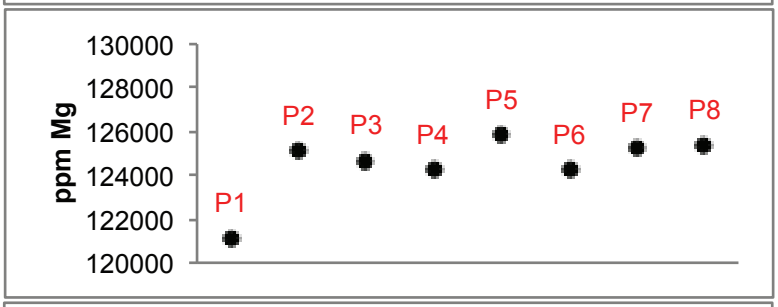

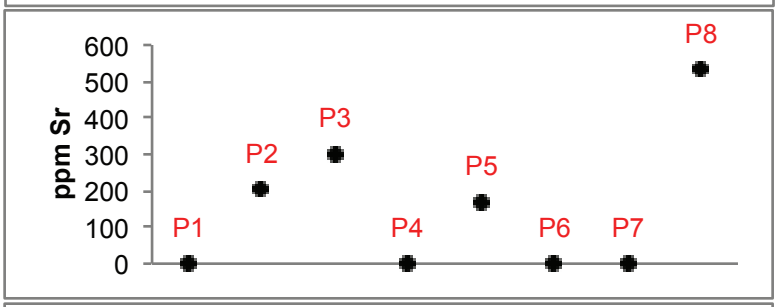

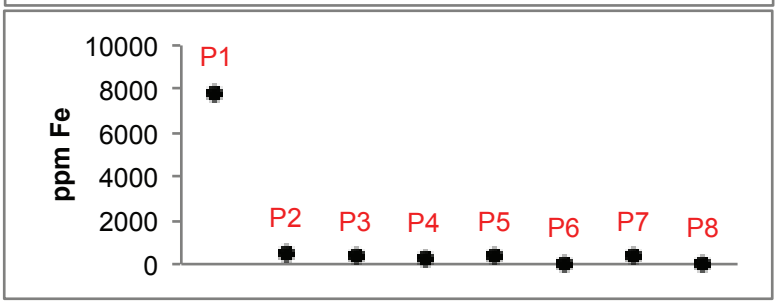

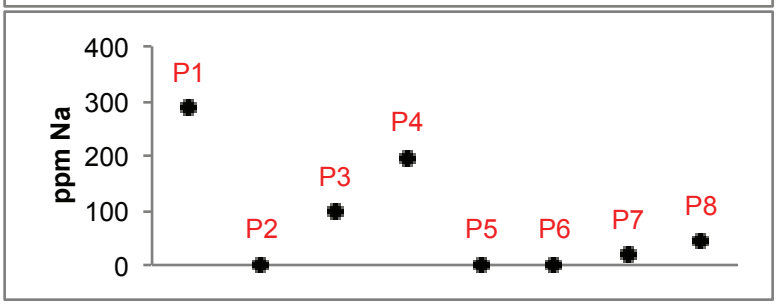

Trace Elemental Concentrations in Dolomite: Wellington Field

Core: Wellington 1-32
Depth: 3876 ft

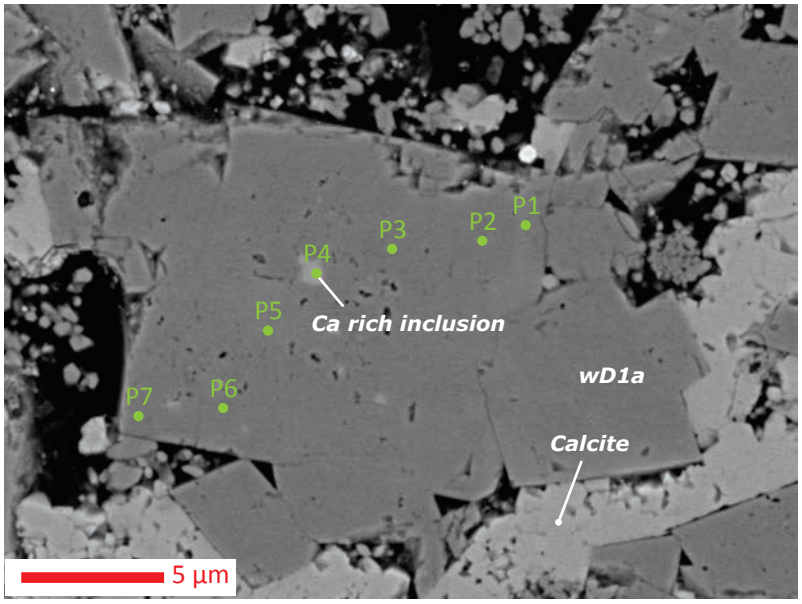

WL3876 Dolomite Sample 2

Averages wD1a					
Na	Fe	Ca	Mg	Mn	Sr
214	2832	231059	120010	52	219

Calcium rich Inclusion					
Na	Fe	Ca	Mg	Mn	Sr
96	1029	290853	78009	0	474

Zones: Point

wD1a: P1, P2, P3, P5, P6, P7
Ca: P4

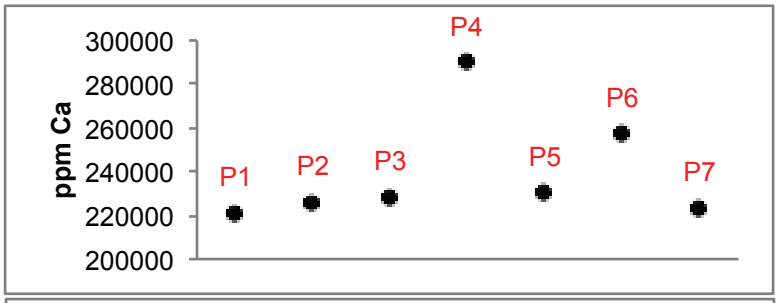

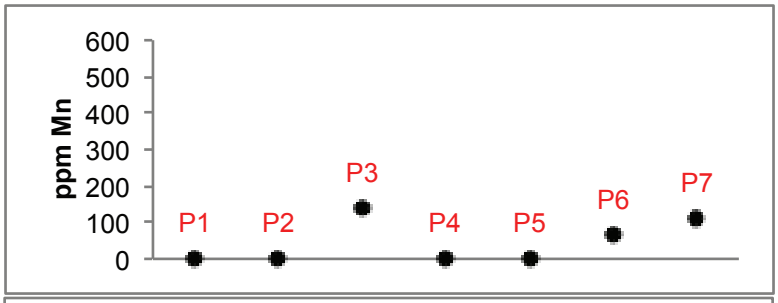

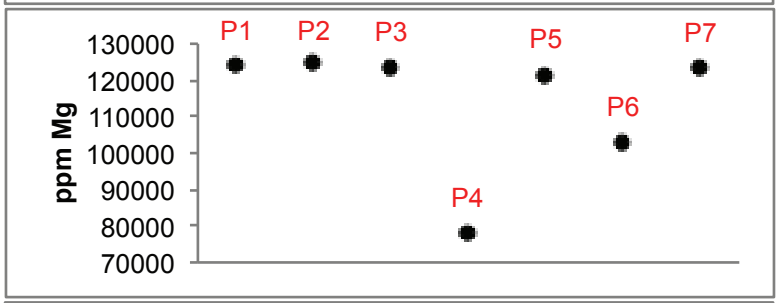

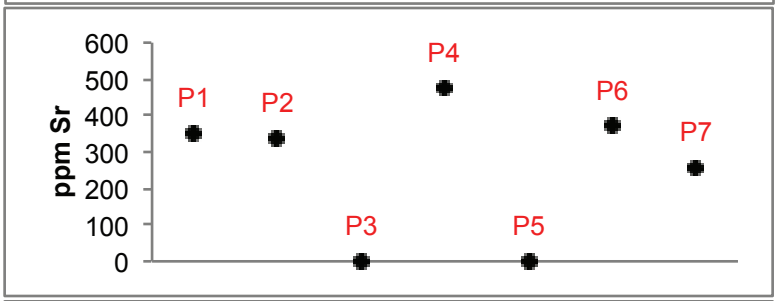

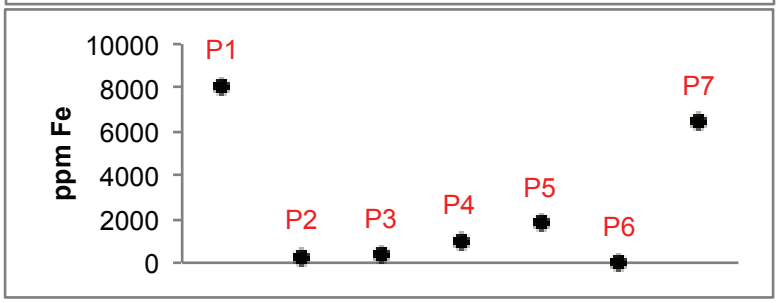

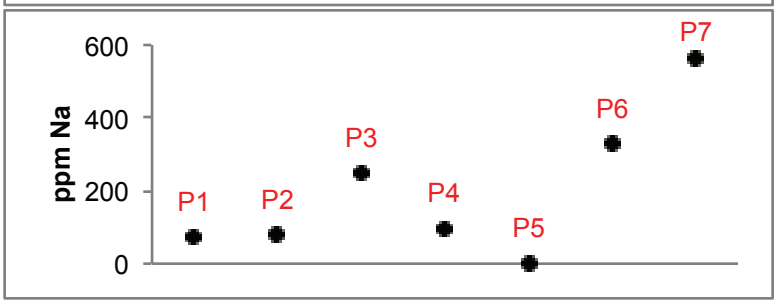

Trace Elemental Concentrations in Dolomite: Wellington Field

Core: Wellington 1-32
Depth: 3883 ft

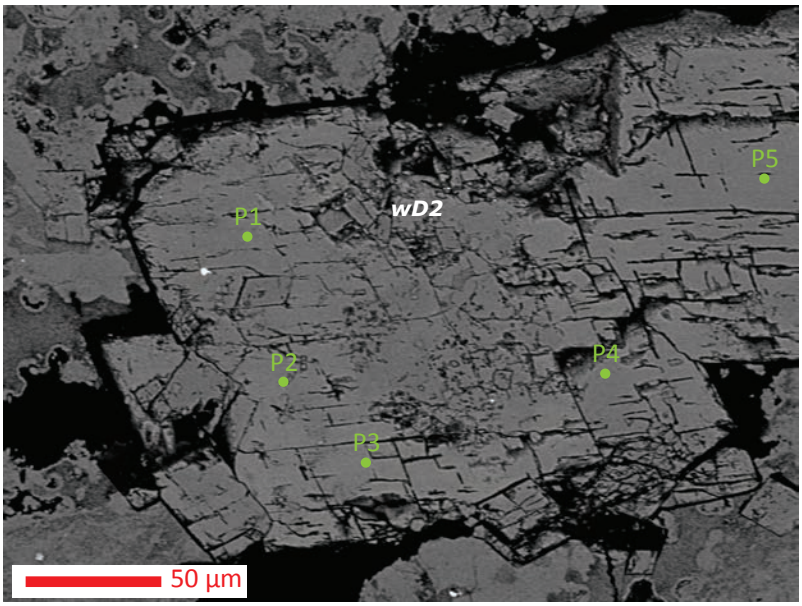

WL3883 Dolomite Sample 1

Averages wD2					
Na	Fe	Ca	Mg	Mn	Sr
218	6693	227467	120030	442	258

Zones: Point
wD2: P1, P2, P3
P4, P5

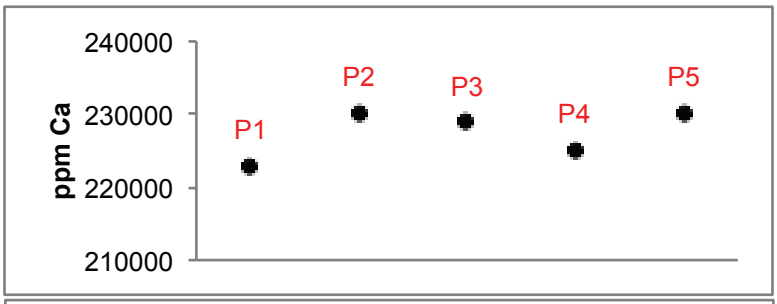

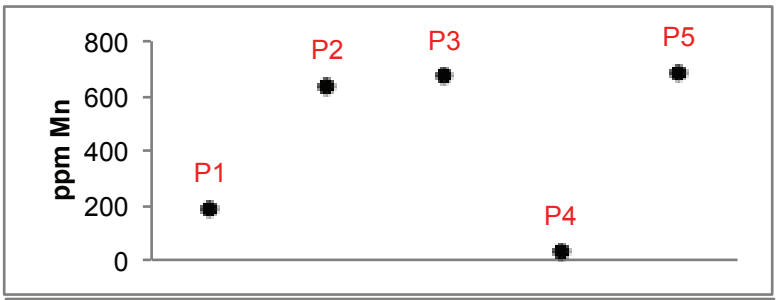

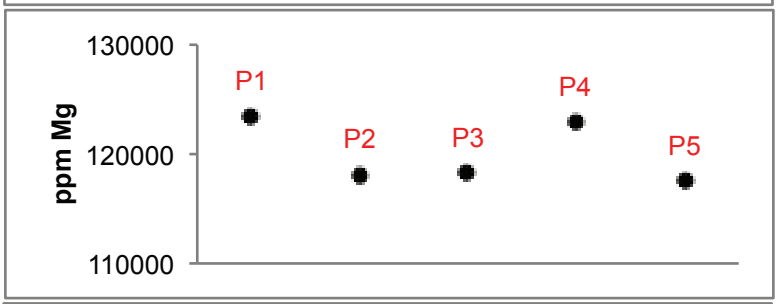

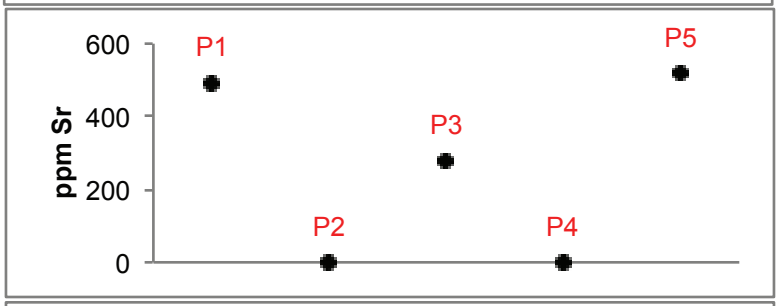

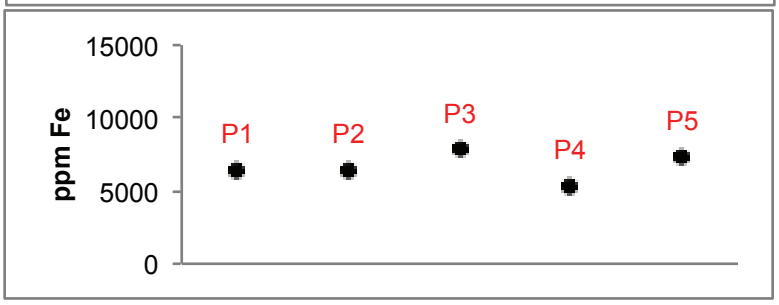

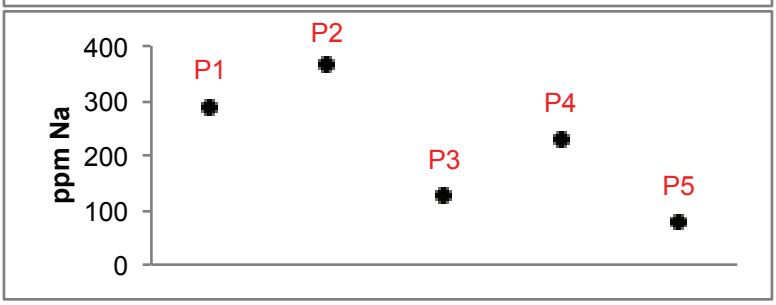

Trace Elemental Concentrations in Dolomite: Wellington Field

Core: Wellington 1-32
Depth: 3883 ft

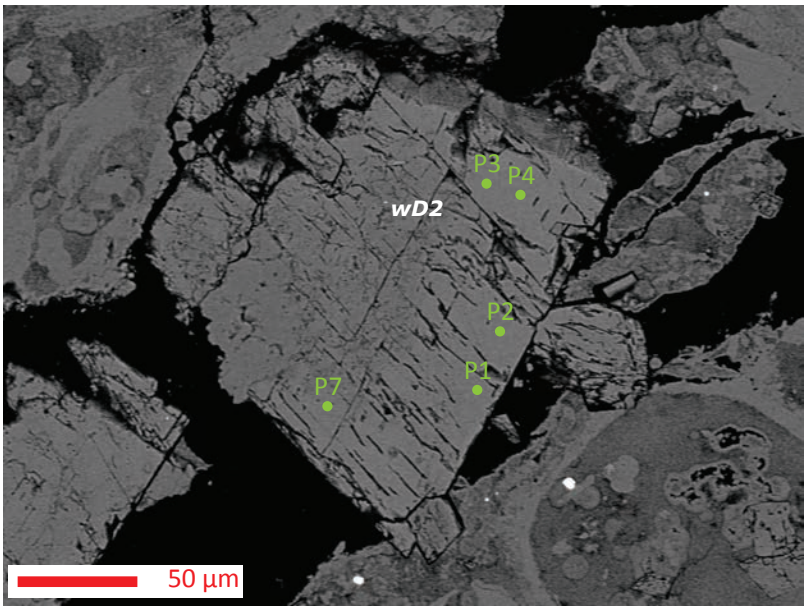

WL3883 Dolomite Sample 2

Averages wD2					
Na	Fe	Ca	Mg	Mn	Sr
279	6945	230355	117849	333	226

Zones: Point
wD2: P1, P2, P3
P4, P7

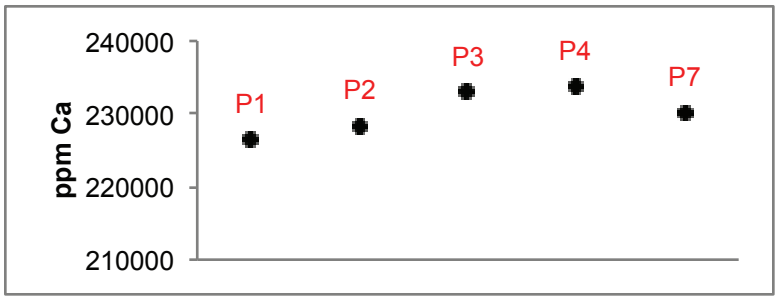

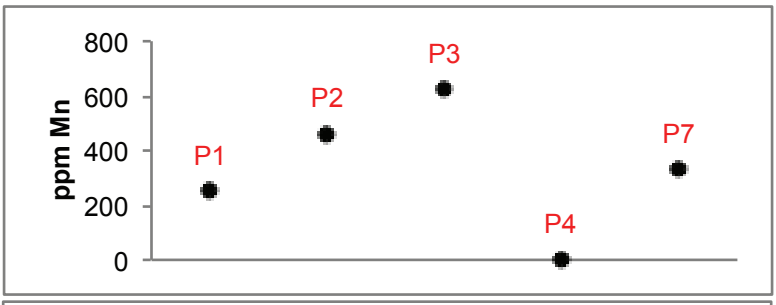

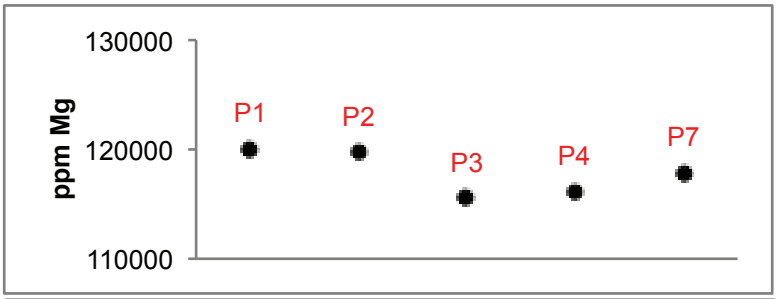

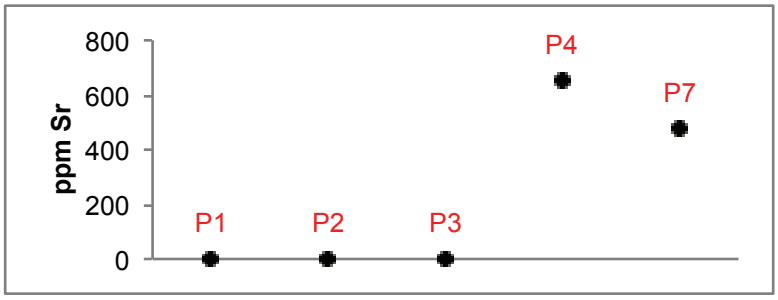

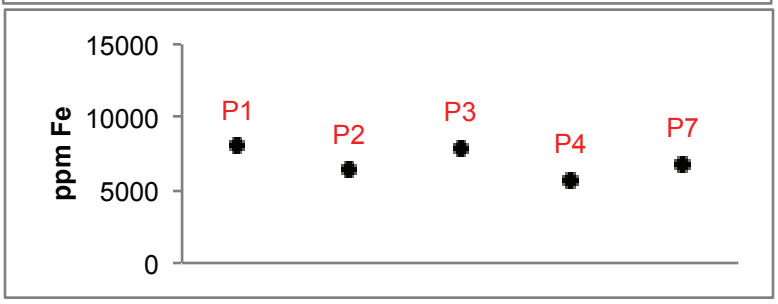

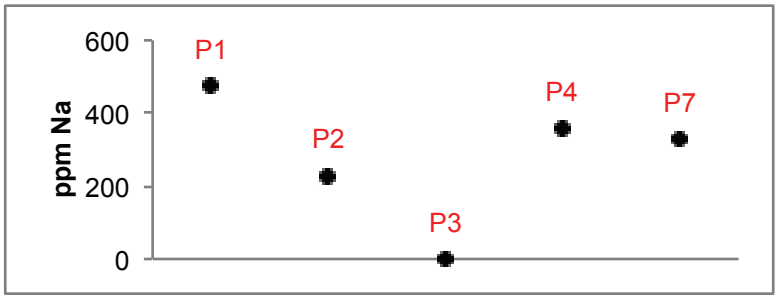

Trace Elemental Concentrations in Dolomite: Wellington Field

Core: Wellington 1-32
Depth: 3892 ft

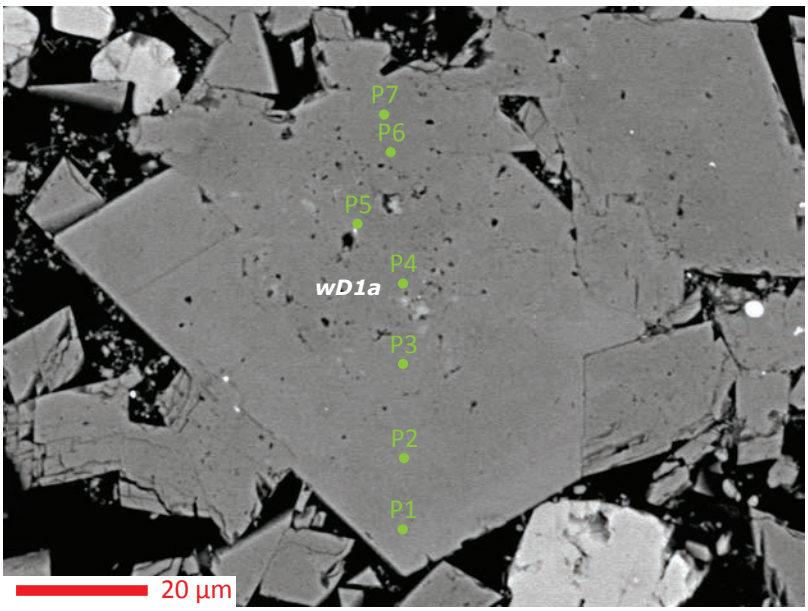

WL3892 Dolomite Sample 1

Averages wD1a					
Na	Fe	Ca	Mg	Mn	Sr
69	781	226669	124465	201	60

Zones: Point
wD1a: P1, P2, P3
P4, P5, P6, P7

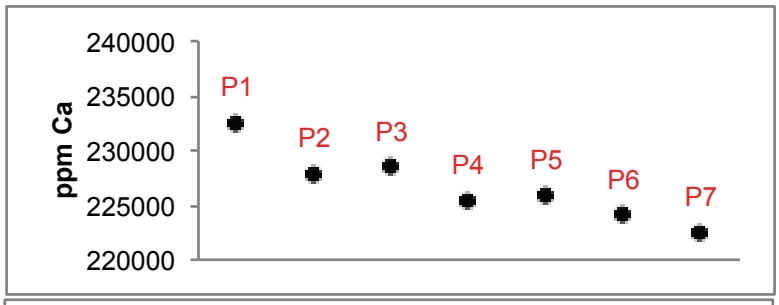

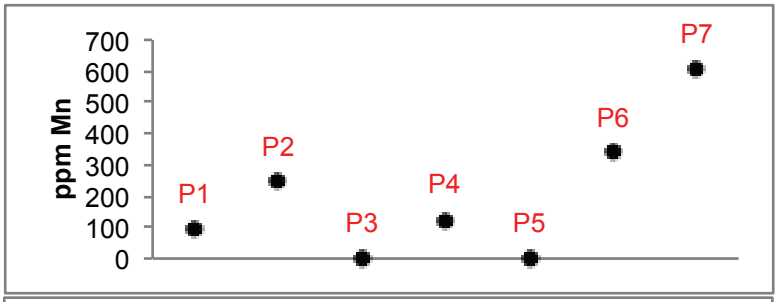

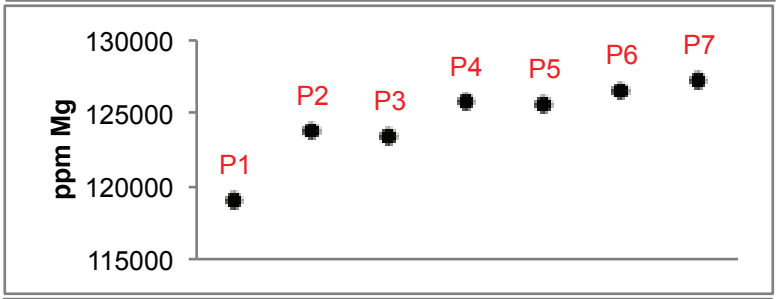

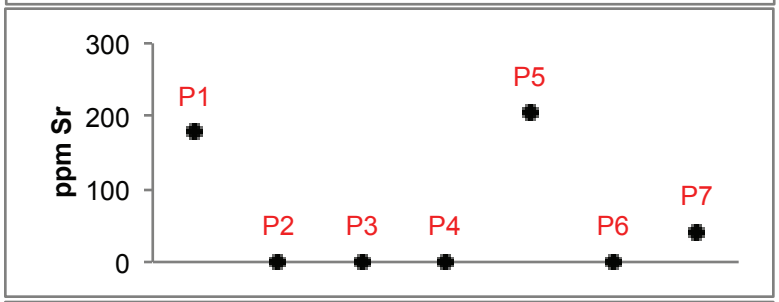

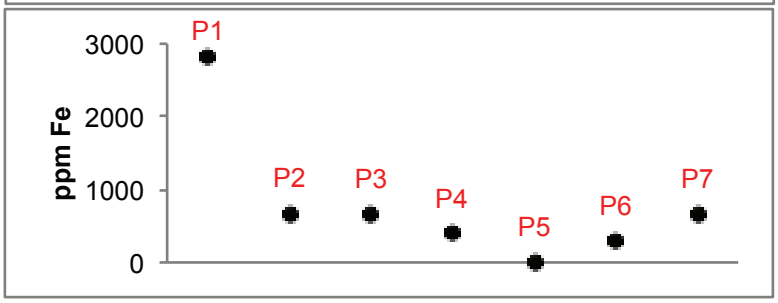

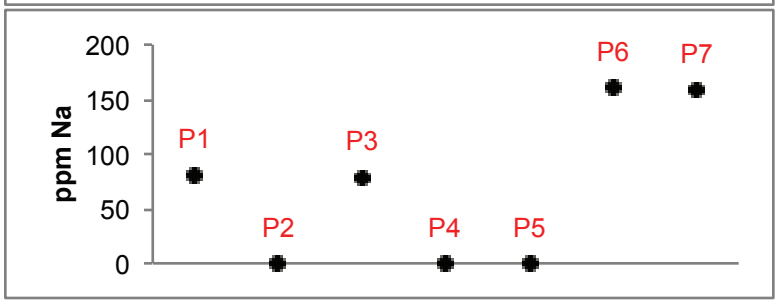

Trace Elemental Concentrations in Dolomite: Wellington Field

Core: Wellington 1-32
Depth: 3892 ft

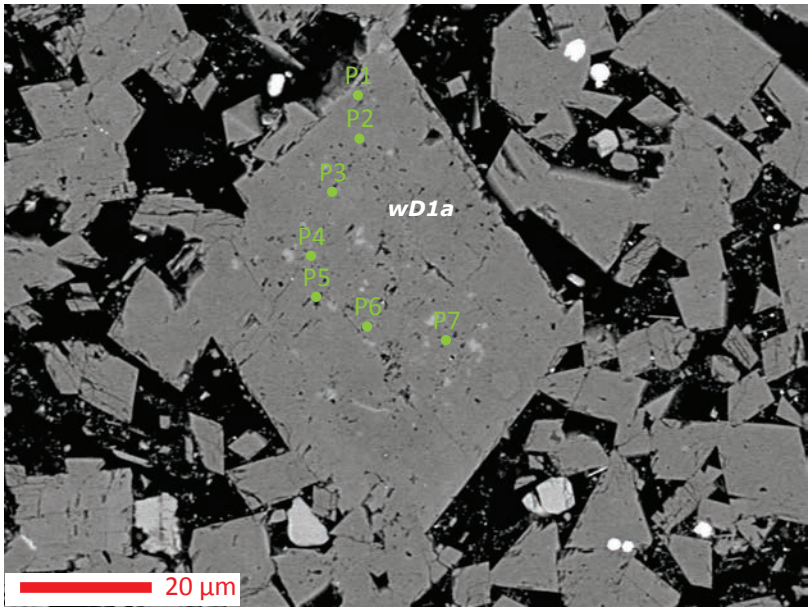

WL3892 Dolomite Sample 2

Averages wD1a					
Na	Fe	Ca	Mg	Mn	Sr
193	771	233990	119025	290	169

Zones: Point
wD1a: P1, P2, P3
P4, P5, P6, P7